Characterisation of Quantum Well Solar Cells for Low Temperature Thermophotovoltaic Applications

by

Paul Abbott

A thesis submitted for the degree of

Doctor of Philosophy

in

Physics

at the

University of London

Imperial College London

May 2004

BIBL. LONDIN. UNIV.

Abstract

Lattice-matched and strain-compensated multi-quantum-well solar cells based on InP substrates are designed and characterised for incorporation into two thermophotovoltaic electricity generators. The photovoltaic devices within the two systems are illuminated by radiation from selective emitters of the materials erbium oxide and thulium oxide, chosen for being well matched to the combustion temperature. Optimisation is carried out to match the devices to the respective incident spectrum. Structures are analysed that are successful in exhibiting an absorption range extended to longer wavelengths compared to lattice-matched structures, whilst simultaneously possessing a lower dark current. A rear surface reflection is seen to greatly enhance the quantum efficiency of certain devices, while its absence can be used to explain lower quantum efficiency in others. The magnitude of this reflection is determined by two separate models and figures of 45-65% are found, with good agreement between the two models. Large area devices are found to have poorer characteristics than smaller devices of the same structure, particularly with regards to parasitic resistances. High intensity light I-V measurements conducted on the better devices, using electronics constructed by the author, illustrate the effects of these resistances on device performance and highlight the need for optimisation of the front contact mask design for a given light intensity within the system.

The feasibility and potential benefits of processing device wafers in an inverted configuration are investigated. Absorption measurements of InP and lattice-matched $In_{0.53}Ga_{0.47}As$ conclude that photocurrent losses due to illumination through the substrate will amount to no more than 4%. Measurements on devices produced specifically to investigate the structure suggest that the loss is between 10-20%. Comparable dark currents are also shown in the inverted devices. As a further advantageous processing technique, anti-reflection coatings are modelled and investigated, with the additional considerations of material availability and system requirements.

Contents

ABSTRACT 2

CONTENTS 3

LIST OF FIGURES 8

LIST OF TABLES 15

LIST OF ABBREVIATIONS (IN ORDER OF APPEARANCE) 16

ACKNOWLEDGEMENTS 18

1. INTRODUCTION 19

1.1. Photovoltaics 21

1.1.1. Diode Characteristics 23

1.1.2. Photocurrent 25

1.2. Quantum Wells 27

1.3. Thermophotovoltaics 28

1.3.1. A TPV System 29

1.3.1.1. Heat Source 30

1.3.1.2. Selective Emitter 30

1.3.1.3. Photovoltaic Cells 32

1.3.1.4. Other System Considerations 33

1.3.2. General TPV Considerations 34

1.4. Strain Compensation 35

1.4.1. The Problem of Strain 36

1.4.2. Strain compensation 38

1.5. References **40**

2. EXPERIMENTAL METHODS **44**

2.1. Origin and Production of Samples **44**

2.1.1. Device Processing 46

2.2. Characterisation Methods **47**

2.2.1. Current-Voltage (I-V) characteristics in the dark 47

2.2.2. Current-Voltage (I-V) characteristics under illumination 50

2.2.3. Quantum Efficiency 51

2.2.4. Monochromatic I-V 53

2.2.5. Reflectivity and Transmission 54

2.2.6. Modelling of Reflectivity, Transmission and Absorption 55

2.2.7. X-ray diffraction analysis 58

2.2.8. Further measurement techniques 58

2.3. References **59**

3. RESULTS ON LATTICE-MATCHED STRUCTURES **60**

3.1. Initial Characterisation **60**

3.1.1. Wafers E004 and E006 60

3.1.2. Wafers E005 and E007 67

3.1.3. Wafer E008 69

3.1.4. Wafer E014 73

3.1.5. Wafer E015 76

3.1.6. Wafer E042 80

3.2. Light I-V comparisons **86**

3.2.1. Results 88

3.3. Conclusions **92**

3.4. References **94**

4. RESULTS ON STRAIN-COMPENSATED STRUCTURES **95**

4.1. IQE grown structures **95**
4.1.1. Wafers E010 and E011 – Absorption edge: 1830nm 95
4.1.2. Wafers E012 and E013 – Absorption edge: 1800nm 96
4.1.2.1. Material Characterisation 101
4.1.3. Wafer E016 – Absorption edge: 1750nm 104
4.1.4. Wafers E1054, E1055 and E1057 – Absorption edges 1900-1940nm 107

4.2. Sheffield grown structures **111**
4.2.1. MR1665 – Absorption edge: 1800nm 112
4.2.2. MR1674 – Absorption edge: Beyond 2000nm 115
4.2.3. MR1845 – Absorption edge: 1840nm 116

4.3. Light I-V characterisation **120**
4.3.1. Results 121

4.4. Quantum Well Carrier Escape **123**
4.4.1. Theory 124
4.4.2. Experimental Details 124
4.4.3. MR1674 125
4.4.4. E1055 127

4.5. A Study of Strain-Compensated Quantum Well Structures **129**
4.5.1. Summary on quantum well structures 132

4.6. Conclusions **132**

4.7. References **134**

5. ALTERNATIVE PROCESSING TECHNIQUES **135**

5.1. Inverted Cell Processing **135**
5.1.1. The Present Design 135
5.1.2. The Inverted Cell Design 137

5.2. Below Band-Gap Absorption Considerations **139**
5.2.1. Sample Descriptions 139
5.2.2. Theory 140

5.2.3. InP and InGaAs absorption results 142
5.2.4. Summary On Absorption Measurements 145

5.3. Investigation of the Inverted Structure 146
5.3.1. MR1020 and E012 146
5.3.1.1. Experimental Details 147
5.3.1.2. MR1020 Results 148
5.3.1.3. E012 Results 152
5.3.2. MR1091 155
5.3.2.1. MR1091 Results 156
5.3.3. Final THE REV material 159
5.3.3.1. Results on final THE REV material 159
5.3.4. Conclusions on inverted structure 162

5.4. Anti-Reflection Coatings 164
5.4.1. Basic Theory 164
5.4.2. Single layer AR coats 166
5.4.3. Double layer AR coats 168
5.4.4. System Considerations 170
5.4.5. Summary of AR coats 171

5.5. Conclusions 171

5.6. References 173

6. CONCLUSIONS AND DISCUSSION 175

APPENDIX A: SAMPLE DESCRIPTIONS 179

A.1. IQE Grown Samples 179
A.1.1. Lattice-Matched InGaAs Samples 179
A.1.2. Strain-balanced InGaAsP samples 183

A.2. Sheffield Grown Samples 188

APPENDIX B: HIGH INTENSITY LIGHT I-V ELECTRONICS 190

B.1. Operation of the Electronics **191**

B1.1. Multiplexer 191

B1.2. 4-point measurement 192

B1.3. Open-circuit voltage 193

APPENDIX C: SOL DEVICE MODELLING **194**

APPENDIX D: THE REV PROJECT **197**

List of Figures

Figure 1.1: Fossil fuel dependency in OECD countries in the year 2000 [1]. Source - International Energy Agency. 19

Figure 1.2: A p-n junction in operation, illustrating absorption, thermalisation and collection. 22

Figure 1.3: Dark current curves illustrating the effects of non-ideal series and parallel resistances. 24

Figure 1.4: Dark and Light I-V characteristics. 26

Figure 1.5: Quantum Well Solar Cell. 27

Figure 1.6: Quantum wells in device QT1227 have extended the absorption to longer wavelengths compared to the bulk device QT1228. 28

Figure 1.7: A functioning TPV system (left) and a drawing of THE REV system (right). The red layer denotes the selective emitter while the green layer is the photovoltaic cells. 30

Figure 1.8: Pictures of the arrays produced for THE REV system. The close-up on the right shows
the series connections between devices. 33

Figure 1.9: Band-gap vs lattice parameter for the InGaAsP material system. Superimposed are the expected peak emission wavelengths for the selective emitters Erbia and Thulia. 37

Figure 1.10: A schematic diagram of the materials involved in a strain-compensated structure. The quantum wells have a natural lattice parameter larger than that of the substrate. Therefore, the barriers have a smaller natural lattice parameter to 'compensate' the strain. It must be remembered that in the actual structure all the layers possess the same lattice parameter as the substrate. 38

Figure 2.1: Plan views of six 1mm mesa devices mounted on a TO5 header (left) and a 1cm device mounted on a copper disc (right). For the 1cm device the rear contact is the copper disc itself. For the 1mm devices the rear contact is the base of the header, which is bonded to the pin next to the tab, in the top right of the figure. 45

Figure 2.2: Schematic depictions of a) two-point, and b) four-point measurements using a source-measure unit (SMU). By sensing the voltage between points A and B with the high impendance voltmeter facility on the SMU the resistance of the cables is not measured. However, by joining the circuits at points A and B any resistances between these points and the device would still be detected. 49

Figure 2.3: Quantum efficiency set-up. The purple box indicates extra equipment used only for reflectivity measurements, see Section 2.2.5. 52

Figure 2.4: Illustration of the effect of background doping on monochromatic I-V. The associated electric field profiles shown inset refer to a point in reverse bias around –0.5V. 54

Figure 2.5: Schematic diagram of the infinite pass model, using a single material. Different reflected components sum to give the total reflectivity (R_{total}) and transmission (T_{total}), or the total absorption. 56

Figure 3.1: Dark current densities of wafers E004 and E006. 61

Figure 3.2: Quantum efficiencies of wafers E004 and E006 AR and non-AR samples. 62

Figure 3.3: Reflectivities of wafers E004 and E006 AR and non-AR samples. The expected reflectivity from the InP front surface is included for reference. E004 AR is not present as the device had been sent to Italy for further characterisation. 64

Figure 3.4: E004 quantum efficiency modelled with the programme SOL. A rear surface reflection of 45% and good minority carrier transport can produce a modelled quantum efficiency that is consistent with the experimental quantum efficiency. 65

Figure 3.5: Varying intensity light I-Vs of E004 under Erbia-like illumination, with their fill factors. Also included is a light I-V predicted for the highest short-circuit current, using the fitted dark current. 66

Figure 3.6: Efficiency of E004 at varying incident power densities. The left-hand axis is measured efficiency of small area devices. The right-hand axis gives a predicted efficiency for large area devices, which have around three times less metal coverage. 67

Figure 3.7: Dark currents of wafers E005 and E007 compared to E004. 68

Figure 3.8: Light I-Vs of E005 and E007 devices under 3000K black-body illumination. 69

Figure 3.9: E008 dark currents compared to E004. 70
Figure 3.10: Monochromatic I-V of E008 at 1200nm. Compared to E004 there is poor carrier collection indicative of a failure to maintain the electric field in the active region. 71
Figure 3.11: E008 quantum efficiencies at varying applied biases. 72
Figure 3.12: E014 dark current densities. 74
Figure 3.13: Quantum efficiency comparison of E014 and E006. 75
Figure 3.14: 3000K black-body light I-Vs of E014 small area devices. The fill factors are much lower than from E004. 76
Figure 3.15: Dark currents of all the sizes of E015 devices, compared to E004. 77
Figure 3.16: Quantum efficiency comparison of E015 with E006, the original structure. 78
Figure 3.17: 3000K black-body light I-V of small area E015, compared with previous E014 and E004. The quality of devices has been regained after the poor E014. 79
Figure 3.18: Reflectivity comparison between E006, E014 and E015. Apart from slight differences in layer thickness, the AR coats are all of good quality. 80
Figure 3.19: Dark currents of E042 large area devices, compared to E004 and E015. The average dark current of a single 1cm device from within the final system array is also shown. 81
Figure 3.20: E042 quantum efficiency compared with E006. The E042 line lies between the AR and non-AR devices from E006. 83
Figure 3.21: Reflectivity comparison of E042 and E006 devices. Also included is a modelled two layer AR coat of TiO_2 and Al_2O_3 optimised at 1200nm. 85
Figure 3.22: Light I-V measurements of the two TPV system arrays. Illumination is provided by the Erbia selective emitter at 1025°C. The cell temperature was 40°C. 86
Figure 3.23: Measured Erbia emission spectrum. 87
Figure 3.24: Light I-V measurement results under varying incident power density for E004 (non-AR) and E006 (AR), plus results modelled from the fitted dark currents of the two devices. 88
Figure 3.25: E042 high intensity light I-Vs. One of the curves is compared to a more ideal light I-V with the same short-circuit current. 91

Figure 3.26: Efficiency and fill factors of E042 1cm device at varying light intensities. Both efficiency and intensity are shown in arbitrary units as the absolute intensity cannot be calculated. 92
Figure 4.1: Dark currents of E012, E013 and the previous sample MR1288 compared to E004. 96
Figure 4.2: Quantum efficiency of E012, illustrating the extension in absorption achieved by the quantum wells compared to E004. 97
Figure 4.3: E012 reflectivity. As was seen with E004, beyond the absorption edge the reflectivity rises above that from purely front surface reflection. This can be attributed to a rear surface mirroring effect. 98
Figure 4.4: E012 quantum efficiency modelled with the programme SOL. A rear surface reflection of 65% increases the quantum efficiency such that the continuum level, at energies above the exciton, matches the experimental data. 99
Figure 4.5: 3000K black-body light I-Vs of E012 devices. The fitted light I-V shows the devices performing much worse than predicted. 100
Figure 4.6: Cross-sectional TEM of E012 taken by collaborators in Parma, Italy. The quantum wells in this region do not appear to have relaxed, but there is clear compositional modulation within the quaternary layer. 102
Figure 4.7: Reciprocal space map of wafer E012 about the point [2 2 4]. The lack of lateral features indicates high quality quantum wells. 103
Figure 4.8: Dark currents of E016 devices compared with E004, E012 and a small area device from E016 measured at NMRC prior to delivery. 105
Figure 4.9: E016 quantum efficiencies. Despite an almost identical nominal quantum well region the absorption falls short of E012 by about 50nm. 106
Figure 4.10: 3000K black-body light I-Vs of E016 devices. Also shown is a modelled light I-V of the 1cm device. 107
Figure 4.11: Dark currents of E1054, E1055 and E1057 devices compared to E012 and E004. 108
Figure 4.12: Quantum efficiency comparison between E1054, E1055, E1057 and E012. 109
Figure 4.13: E1054, E1055 and E1057 reflectivity comparison. 110
Figure 4.14: SOL modelled longer wavelength quantum efficiency of AR coated E1055 with no rear surface reflection. 111

Figure 4.15: Dark currents of MR1665 devices compared with E012 and MR1288. The quantum wells in all the structures are identical in composition and thickness. 112
Figure 4.16: MR1665 AR and non-AR quantum efficiencies compared to E012. 114
Figure 4.17: Reflectivity comparison between MR1665 AR and non-AR devices and E012 non-AR. 114
Figure 4.18: MR1674 dark currents compared with MR1665 and E012. 115
Figure 4.19: Bias and temperature dependent quantum efficiency of an AR coated MR1674 sample. The level is clearly much reduced compared with MR1665 and E012 as there are fewer wells. However, the signal becomes so small that the quantum efficiency cannot be accurately determined at longer wavelengths. 116
Figure 4.20: MR1845 dark currents compared to E012. 117
Figure 4.21: Monochromatic I-V of MR1845 samples. The flatness of the curves indicates low background doping in the quantum well region. 118
Figure 4.22: MR1845 compared with E012. Again, apart from a rear surface mirror, the response at the exciton wavelength is as good as E012. 119
Figure 4.23: MR1845 and E012 reflectivities. The MR1845 devices do not appear to have a rear surface mirror because, unlike E012, there is no rise in reflectivity beyond the absorption edge. 120
Figure 4.24: Measured Thulia emitter spectrum, cut off at 2100nm. 121
Figure 4.25: Light I-V measurements for E1055, MR1665 and MR1845, plus results modelled from the fitted dark currents of MR1665 and MR1845. 122
Figure 4.26: Arrhenius plot of normalised photocurrent against inverse temperature for MR1674 at 1800nm. The choice of axes aids the calculation of the activation energy for escape. 127
Figure 4.27: Temperature dependent quantum efficiency of E1055 at -2V applied bias. 128
Figure 4.28: Arrhenius plot of normalised photocurrent against inverse temperature for E1055. 129
Figure 5.1: An illustration of the overlap between the Thulia spectrum and InGaAs absorption, here represented by E004. Much of the high energy spectrum would be lost if there was an InGaAs layer over the optical window. 137

Figure 5.2: The current 'normal' structure of processed devices, a), is compared with the proposed inverted structure, b). The thick substrate allows the carriers moving laterally upwards to the finger contacts to move along a path of lower resistance. The figures are not to scale. 138

Figure 5.3: The measured transmission of the InP wafer yields the absorption coefficient (right-hand axis). The theory also predicts the reflectivity of the wafer, which is confirmed by experiment. Also included is tabulated data from Ref. 7, although only two data points are available over the range of the experiment. 143

Figure 5.4: Measured transmission of MR1181. The expected reflection is also shown compared to the measured reflection. 144

Figure 5.5: Calculated InGaAs absorption coefficient. This is compared with three data sets where the internal InP/InGaAs boundary was ignored (Ref. 4), and another using a different thin-film theory (Ref. 8). The calculated absorption if the internal boundary is ignored is also shown for comparison. 145

Figure 5.6: Reflectivity and transmission of MR1020 taken from the front and the rear of the wafer. 148

Figure 5.7: Diagram of the MR1020 wafer mounted on a copper disc. The region of the wafer without the contact layer hangs over the hole in the disc. The contact region is directly above the wafer such that when the illumination moves horizontally any change in the distance between the illuminated point and the contact is minimal. 149

Figure 5.8: Quantum efficiency scans taken from various positions in a horizontal line on the front of wafer MR1020. 150

Figure 5.9: Quantum efficiencies of wafer MR1020 taken from the front and the rear. The right-hand axis shows the response of the rear as a fraction of that from the front. Also included is an original measurement on an MR1020 small area non-AR device. 151

Figure 5.10: Front and rear reflectivity and transmission of wafer E012. 152

Figure 5.11: Front and rear photocurrents of wafer E012. The rear signal as a fraction of the front is given along with the fraction of light intensity unabsorbed after passing through 2μm of InGaAs. 153

Figure 5.12: Wafer E012 transmission comparison. The experimental measurements are compared with the modelled transmission of the wafer using the author's model (blue line). The black line is the SOL modelled transmission of E012 if the 2μm thick InGaAs below the quantum wells is replaced with lattice-matched quaternary of the composition used elsewhere in the structure... 155
Figure 5.13: Dark current comparison of MR1091 normal and inverted devices processed by the author and an original AR coated device processed in Sheffield. 157
Figure 5.14: Quantum efficiency measurements of normal and inverted processed MR1091 devices. The quantum efficiency of the inverted structure as a percentage of the normal structure, using the same axis, shows a loss of around 20%. Also shown for comparison is a quantum efficiency of one of the original normally processed non-AR devices from Sheffield. 158
Figure 5.15: Dark current comparison of normal and reverse processed devices produced from the final THE REV material. 160
Figure 5.16: Quantum efficiencies of normal and reverse processed devices from the final THE REV material. The ratio between the reverse and the normal quantum efficiencies shows a 30% drop in signal with the inverted device. 161
Figure 5.17: Light I-Vs of one normal and one inverted device from THE REV final material. 162
Figure 5.18: Modelled angular reflectivity of an Al_2O_3 coat optimised at 1700nm. 167
Figure 5.19: Modelled angular reflectivity of a MgF_2/ZnS AR coat optimised for 1800nm. 169
Figure 5.20: Modelled angular reflectivity of the RWE double layer Al203/TiO2 coat optimised at 1800nm. 170
Figure B.1: Circuit diagram of the high current pulsed source-measure unit. 190
Figure B.2: DG508 multiplexer pin layout. 192

List of Tables

Table 2.1: Summary of THE REV characterisation techniques performed outside Imperial. 59
Table 3.1: Results of fitting the best E004 and E006 small area non-AR dark currents. 61
Table 3.2: Results of fitted dark currents of E015 devices from Figure 3.16. 77
Table 3.3: Results of fitting E042 1cm device dark currents and the average array device. 82
Table 5.1: Nominal structure of MR1181, which contains 1927nm of InGaAs lattice-matched to InP. 140
Table 5.2: Nominal structure of MR1020. Q1.1 and Q1.6 are InGaAsP lattice-matched to InP with the given band-edge in μm. 147
Table B.1: DG508 multiplexer truth table. 192

List of Abbreviations (In order of appearance)

IQE – Commercial epitaxial growth company based in Wales, the supplier of all grown wafers for this European project.

NMRC – National Microelectronics Research Centre. Irish research institute responsible for processing of test devices for this thesis.

EPSRC – Engineering and Physical Sciences Research Council. British funding council responsible for the survival of the author.

TEM – Transmission Electron Microscopy. Characterisation method employed during the course of the project.

IMEM CNR – Italian research centre responsible for transmission electron microscopy of wafers.

OECD – Organisation for Economic Co-operation and Development. International group of 30 countries.

PV – Photovoltaics. The physical effect that is the basis for converting light directly into electricity.

TPV – Thermophotovoltaics. The general method of converting heat radiation into electricity, of which photovoltaics is a special case. The main topic of this thesis.

QE/EQE – External Quantum Efficiency. A measure of how successfully light striking the device is converted into current.

THE REV – European collaboration to construct a range extender for an electric car.

MIMs – Monolithic Interconnected Modules – A method of series-connecting devices in order to reduce resistive losses.

MOVPE – Metal-Organic Vapour Phase Epitaxy. The growth method by which all structures in this thesis are made.

TO5 – Code number for a particular size of mount used for small-area devices within this thesis.

SMU – Source-Measure Unit. Laboratory equipment used for I-V measurements.

SOL – Quantum efficiency modelling programme designed and written at Imperial College.

AR – Anti-reflection. A coating applied to the front of devices to maximise the amount of light entering.

SI – Semi-insulated. The kind of non-conducting substrate used for top-contacting to devices. The chemical symbol for silicon is not used in this thesis.

EBIC – Electron Beam Induced Current. Characterisation technique used to identify dislocations at the surface of devices.

MASPEC – Italian research centre and part of the European project.

PL – Photoluminescence. Characterisation technique used to assess the absorption edge of a sample.

RWE – German commercial company responsible for processing the final devices for the project.

CL – Cathodoluminescence. Characterisation technique as photoluminescence.

Acknowledgements

The first thanks must go to my supervisor Keith Barnham, who has given me all the support I could have wished for. I am in no doubt as to how much more difficult my three years would have been without regular contact from up on high. For making my term at Imperial run that much smoother, great thanks also go to the other members of the group: Carsten, Ian, James, Dave B, Ned and Tom. I am also grateful to these guys, along with Dave G, Adrian, Alex, James and Anthony, for sharing the social side of the college and helping to dispel my preconceptions about physics departments. I also must thank Jenny Nelson for giving a seminar at Cambridge during my fourth year project which convinced me that I wanted to be involved in solar cells and renewable energy.

The growth and processing of samples is a vital component indeed in an experimental thesis, and for this I wish to thank to thank two groups of people. The majority of samples came courtesy of Graham Clarke from IQE in Wales, and Ravin Ginige from NMRC in Ireland. I was also supplied by the EPSRC Central Facility for III-V semiconductors, and would thus like to thank John Roberts and Andrey Krysa for growth and Geoff Hill and Rob Airey for processing. Massimo Mazzer is thanked for co-ordinating the European Framework V project of which my thesis is part.

This thesis contains characterisation not performed at Imperial. For TEM pictures I wish to thank Lucia Nasi and Laura Lazzarini at IMEM CNR in Parma, Italy. I would also like to thank Antonio Licciulli and Daniela Diso for fabricating and measuring the emission spectra of the erbia and thulia selective emitters.

My lasting thanks go to my family for the constant support and encouragement they have always given me, particularly during the extended periods when I had not a clue about what I wanted to do with my life.

1. Introduction

Fossil fuels currently dominate the energy market. By way of illustration, in the year 2000 fossil fuels supplied the UK with 88.8% of its energy, with renewables providing only 2.8% of its electricity [1]. Figure 1.1 shows the extent to which many countries rely upon fossil fuels for their energy. 'Primary energy' refers to the total energy use of a country, not only for electricity generation, but also domestic heating and transport fuels. Figure 1.1 clearly demonstrates the progress that must be made if sustainability is to be achieved.

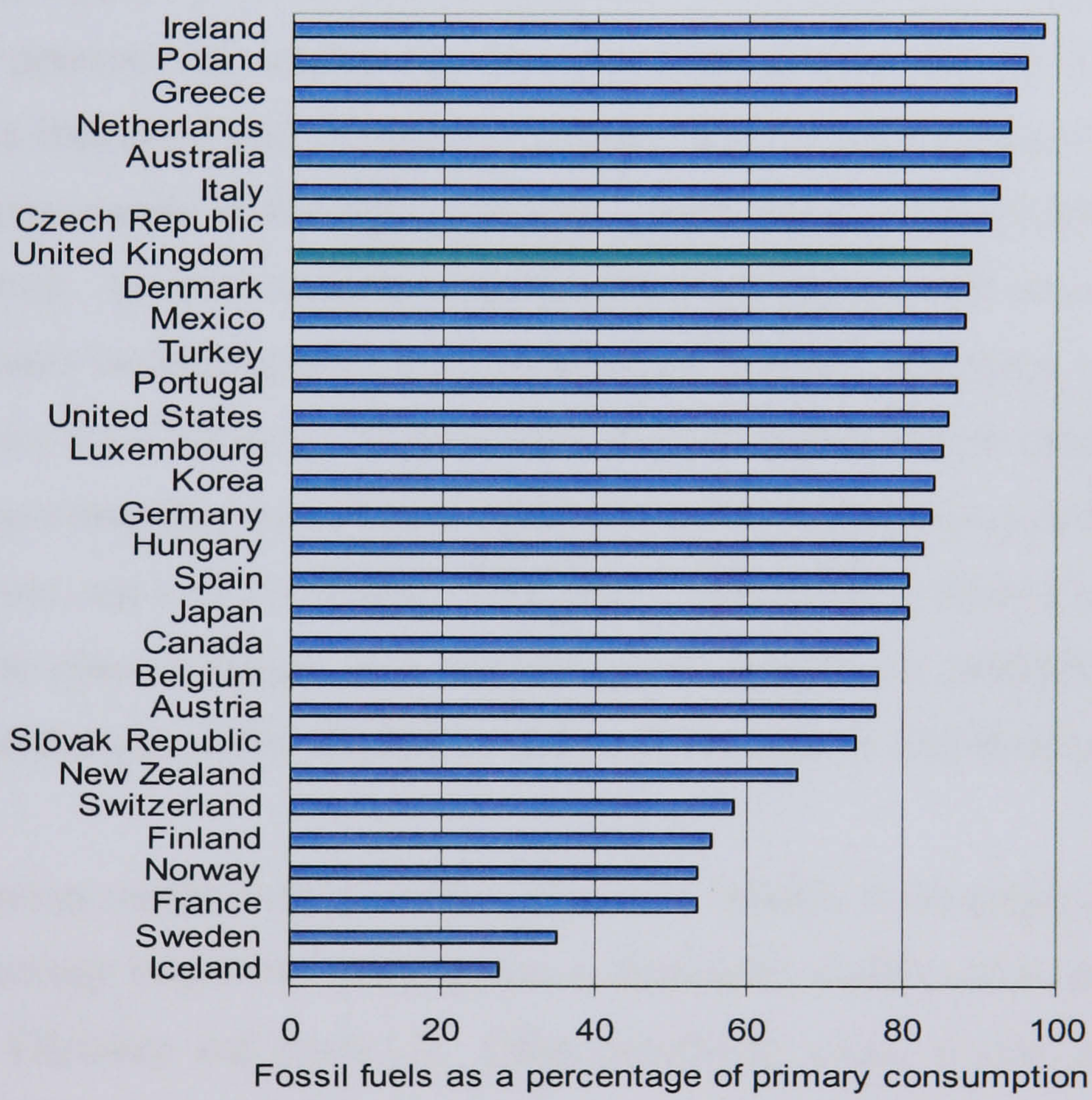

Figure 1.1: Fossil fuel dependency in OECD countries in the year 2000 [1]. Source - International Energy Agency.

In addition to the expected increase in energy use by developed countries, it is also estimated that there are two billion people in the world with no access to electricity, a figure that will fall as those particular countries develop. As the world's demand for energy increases there are a number of problems to be addressed. Firstly, the supply of

coal, oil and gas is destined to become less certain in the foreseeable future. Secondly, and more importantly for the planet itself, is the undeniable effect which the greenhouse gases are having on the atmosphere and the climate. These gases, of which carbon dioxide is the most important, are produced by the combustion of fossil fuels. Tempting though it is in Britain to look forward to the projected increases in temperature, the rises will have potentially devastating consequences. Flooding and increased desertification are already reported to be occurring. However, many governments are slowly awaking to the situation and environmental issues are on the political agenda more than ever.

In view of increasingly pessimistic assessments of man's effect on the planet, it is vital that renewable energy begins to compete more effectively with fossil fuels and take a greater part in supplying the world's energy needs. The reason for their previous failure to seriously penetrate the market has been the high relative cost of the energy they produce. Tax incentives and increased investment in renewable energy are an excellent way of steering people in the right direction, loathe though most governments are to take such action. In order to achieve better market penetration, the positive aspects of renewables must be highlighted. Less reliance on foreign oil imports provides more energy security for a country. There is also great potential for job creation in a new sustainable economy [2]. In addition, many renewable technologies, particularly wind and solar power, are well distributed. With only a limited proportion of energy coming from any one place a failure in a specific region would not produce a significant shortfall in production, unlike the failure of a single nuclear or coal-fired power station.

The global energy output from renewable sources is steadily increasing, as the cost falls and the technology improves. Wind power is reasonably healthy at present, especially in Denmark, Germany and Spain [3]. Other potentially major sources are geothermal energy, hydroelectric power, solar heating, wave power and the burning of biomass and other non-fossil fuels such as landfill gas. Within the discussion of energy production, nuclear power occupies an uneasy central position. There are clear concerns over the safety of power plants and the decommissioning and secure storage of waste, not to mention the finite supply of uranium fuel, around 50 years. However, nuclear power produces virtually no greenhouse gas, making it a suitable short-term solution to the problem of reducing emissions. Indeed nuclear power is the reason why countries such

as France can boast less reliance on fossil fuels than most other countries, see Figure 1.1.

One of the best known methods for producing 'green' energy is the photovoltaic (PV) cell, a device which converts sunlight directly into electricity. The subject of this thesis is the area of thermophotovoltaics (TPV). Here, the illuminating source for the cell is not the sun but heat radiation produced by the burning of a fuel. This offers the possibility of the co-generation of heat and electricity, which would be extremely useful in situations such as remote cabins and aboard boats. Indeed such a device is now commercially available [4]. It has also been suggested that TPV technology could be used to reclaim energy from some of the waste heat energy produced by industry [5].

The project with which this thesis is concerned is a European collaboration, called THE REV, aiming to produce a range extender for FIAT's electric car. It involves a number of European institutions working on the various aspects of a TPV system. At present, the FIAT electric car can travel no more than about 100km before it requires recharging, which itself takes a great deal of time. A TPV system is a novel method of charging the battery whilst the car is in motion. The system, which will fit into the boot of the car, is described in Section 1.3.

This chapter discusses the basic theory of photovoltaics and TPV systems, and also introduces the novel concepts of quantum wells and strain compensation, designed to improve the quality and efficiency of photovoltaic devices.

1.1. Photovoltaics

The physics of the p-n junction is treated in many texts [6, 7]. Only a brief overview of its use in photovoltaics is presented here. As shown in Figure 1.2, the formation of a p-n junction creates a built-in electric field across a depletion region free of carriers.

Any incident photon with less energy than the band-gap energy will fail to excite any carriers across the band-gap and will not be absorbed. A photon with more energy than the band-gap energy will excite an electron into the conduction band, creating a

corresponding hole in the valence band. If this occurs within a region of the cell with a built-in field, the carriers can then drift to the base and emitter regions. Any excess energy possessed by the carriers above that needed for absorption is lost to the cell as they thermalise to the band-edge. The maximum energy an individual carrier pair can provide to the circuit is marked in Figure 1.2 by a voltage V, which is always less than the band-gap energy.

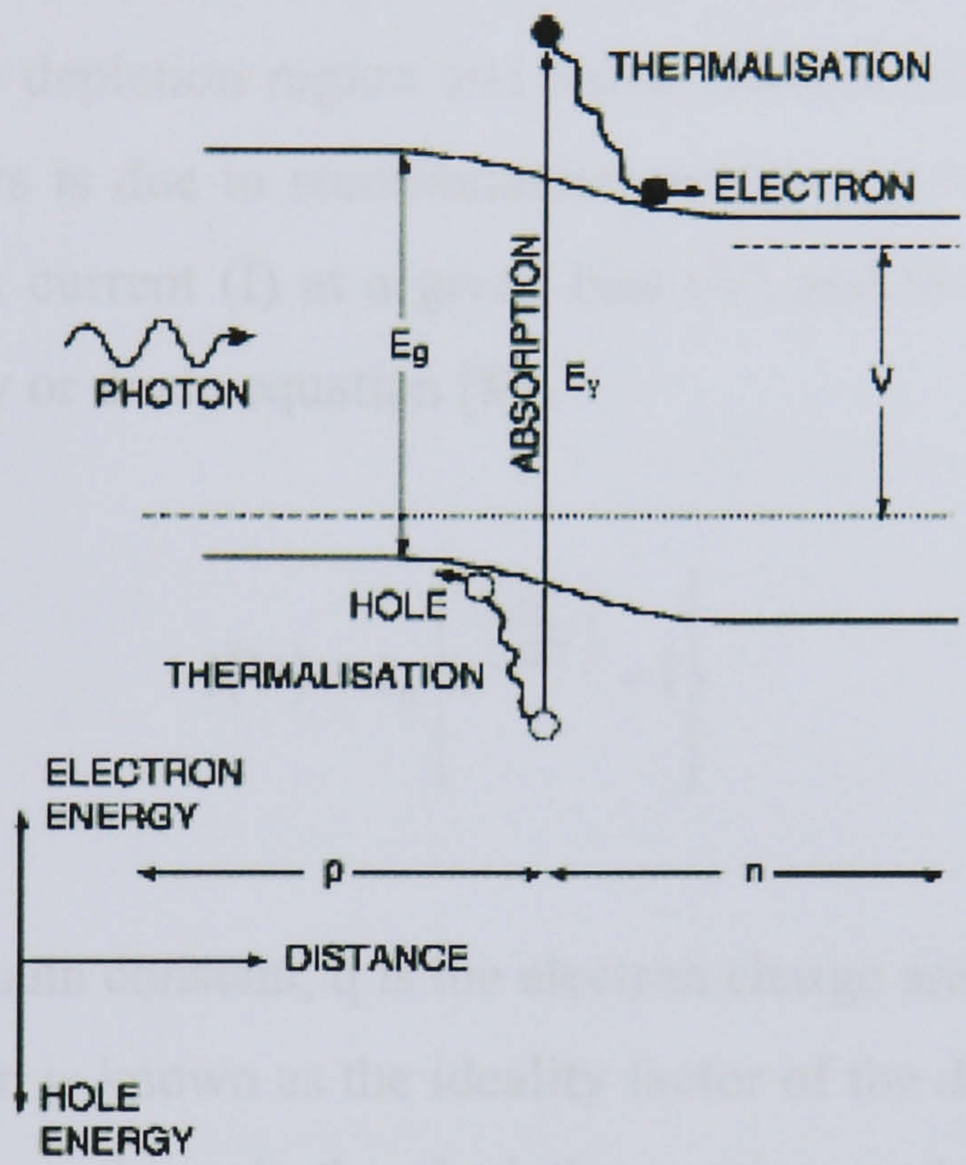

Figure 1.2: A p-n junction in operation, illustrating absorption, thermalisation and collection.

If absorption occurs in the neutral p- or n- region then the majority carrier is already on the side of the active region it needs to be. The other carrier is a minority carrier, and on average is only able to diffuse a certain distance, the diffusion length, before recombining. Therefore, if absorption occurs within one diffusion length of the field-bearing region then there is a favourable probability that the minority carrier will succeed in diffusing to this region and be collected. Given that light must always travel through neutral material before reaching the depletion region there is a high probability that a large proportion will be absorbed where minority carrier diffusion is necessary. It is clear that material quality is important for a number of reasons, minority carrier lifetime and non-radiative recombination centre density amongst them.

1.1.1. Diode Characteristics

At zero bias, the cell is in equilibrium. The Fermi levels in the p- and n-regions are at equal levels and diffusion between the regions is balanced. Also, thermal carrier generation is balanced by recombination. When a bias is applied to the cell in the dark the ideal current-voltage characteristic is simply that of a diode. The diode acts as a barrier to majority carriers. In reverse bias, unless breakdown occurs, this barrier increases and the reverse current remains constant. In positive bias the barrier decreases and carriers enter the depletion region and move towards the minority carrier regions. The current that flows is due to recombination, which can be both radiative and non-radiative. This dark current (I) at a given bias (V) and temperature (T) is generally given by the Shockley or diode equation [8]:

$$I(V) = I_0 \left\{ e^{\left(\frac{qV}{nkT}\right)} - 1 \right\} \tag{1.1}$$

where k is the Boltzmann constant, q is the electron charge and I_0 is called the saturation current. The symbol n is known as the ideality factor of the device. For an ideal diode, where all carriers pass through the depletion region and recombine solely in the minority carrier regions, n=1. This corresponds to an ideal Shockley diode. In a realistic diode the more dominant process in low forward bias is non-radiative recombination through mid band-gap states, so called Shockley-Hall-Read recombination, and for this process $n \approx 2$ [9]. An ideality factor of $n \approx 2$ is indicative of the presence of recombination centres such as trap states. The diode may display characteristics of both idealities, with n=1 dominant at higher biases as a consequence of its exponential growing more quickly.

The diode characteristics of a device may be affected by other factors that can be unrelated to the quality of the p-n junction. Series resistance, which can be introduced by poor contacting to the device, reduces the level of dark current produced by a given bias and hence should be as low as possible. Parallel, or shunt, resistance can offer the current the opportunity of completely bypassing the diode and hence should be as large as possible. A low shunt resistance can be caused by dangling bonds present on the

sides of devices after etching. An illustration of the effects of a high series resistance (20 Ω) and a low shunt resistance (10^5 Ω) on dark current is given in Figure 1.3.

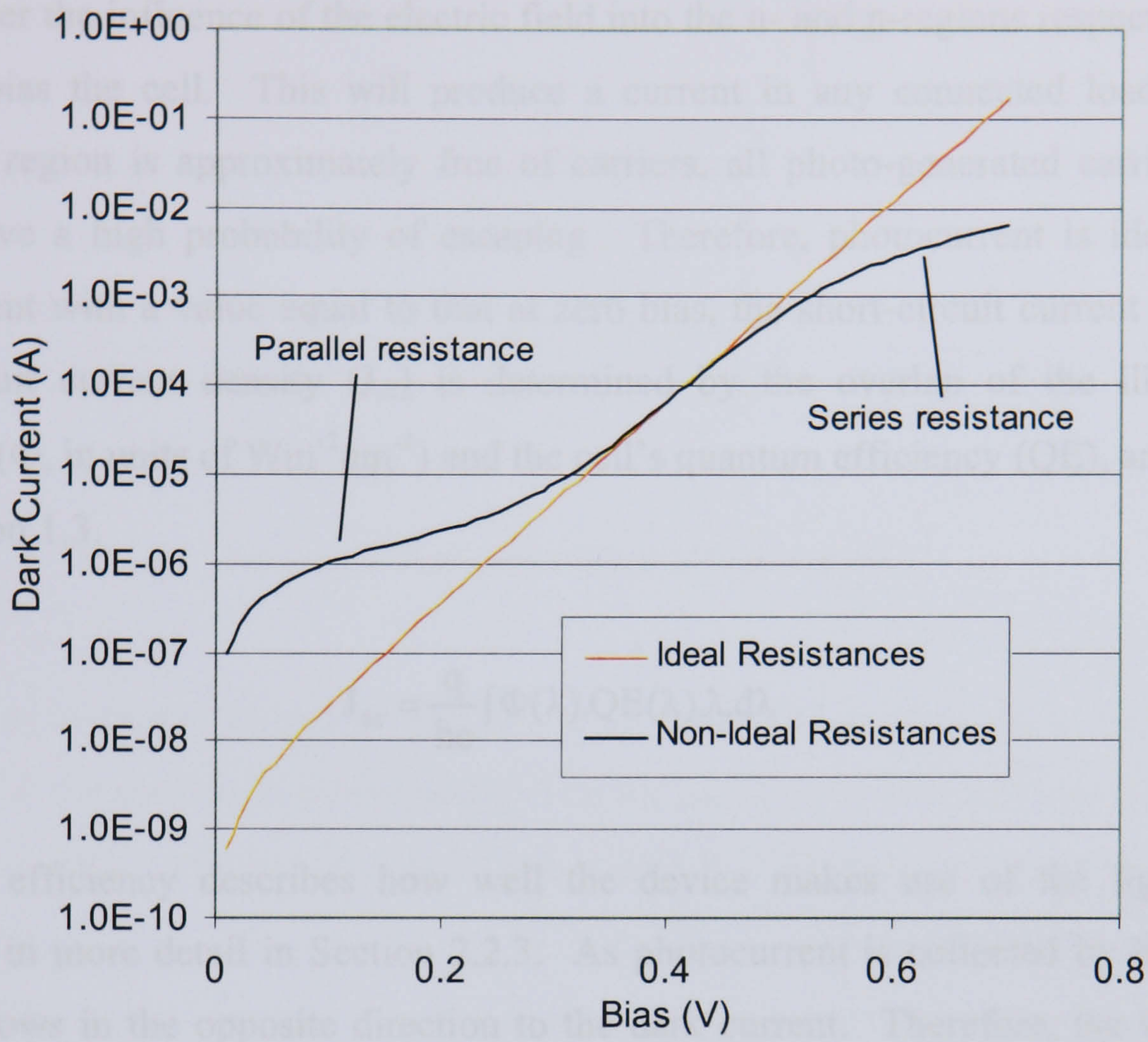

Figure 1.3: Dark current curves illustrating the effects of non-ideal series (20 Ω) and parallel resistances (10^5 Ω) .

Taking all these factors into consideration, including two ideality factors n_1 and n_2, the total dark current I_{tot} can be written as

$$I_{tot} = I_{o_1}\left(e^{\frac{q(V-I_{tot}R_s)}{n_1 kT}} - 1\right) + I_{o_2}\left(e^{\frac{q(V-I_{tot}R_s)}{n_2 kT}} - 1\right) + \frac{V - I_{tot}R_s}{R_p} \qquad (1.2)$$

where R_s and R_p are the series and parallel resistances and I_{o1} and I_{o2} are the saturation currents for each ideality factor. Using this equation, experimental dark currents can be fitted to extract the characteristic parameters.

1.1.2. Photocurrent

When a photon of light is absorbed in the active region the resultant electron and hole move under the influence of the electric field into the n- and p-regions respectively, and forward bias the cell. This will produce a current in any connected load. As the depletion region is approximately free of carriers, all photo-generated carriers in the region have a high probability of escaping. Therefore, photocurrent is ideally bias-independent with a value equal to that at zero bias, the short-circuit current (I_{sc}). The short-circuit current density (J_{sc}) is determined by the overlap of the illuminating spectrum (Φ, in units of $Wm^{-2}nm^{-1}$) and the cell's quantum efficiency (QE), and is given by equation 1.3.

$$J_{sc} = \frac{q}{hc}\int \Phi(\lambda).QE(\lambda).\lambda.d\lambda \tag{1.3}$$

Quantum efficiency describes how well the device makes use of the light and is discussed in more detail in Section 2.2.3. As photocurrent is collected by the electric field, it flows in the opposite direction to the dark current. Therefore, the total light-biased current is given by

$$I(V) = I_d(V) - I_{sc}\,. \tag{1.4}$$

Figure 1.4 shows the I-V characteristic of a cell. It is clear that if the photo-generated current exceeds the dark current then power, as the product IV, can be extracted from the cell.

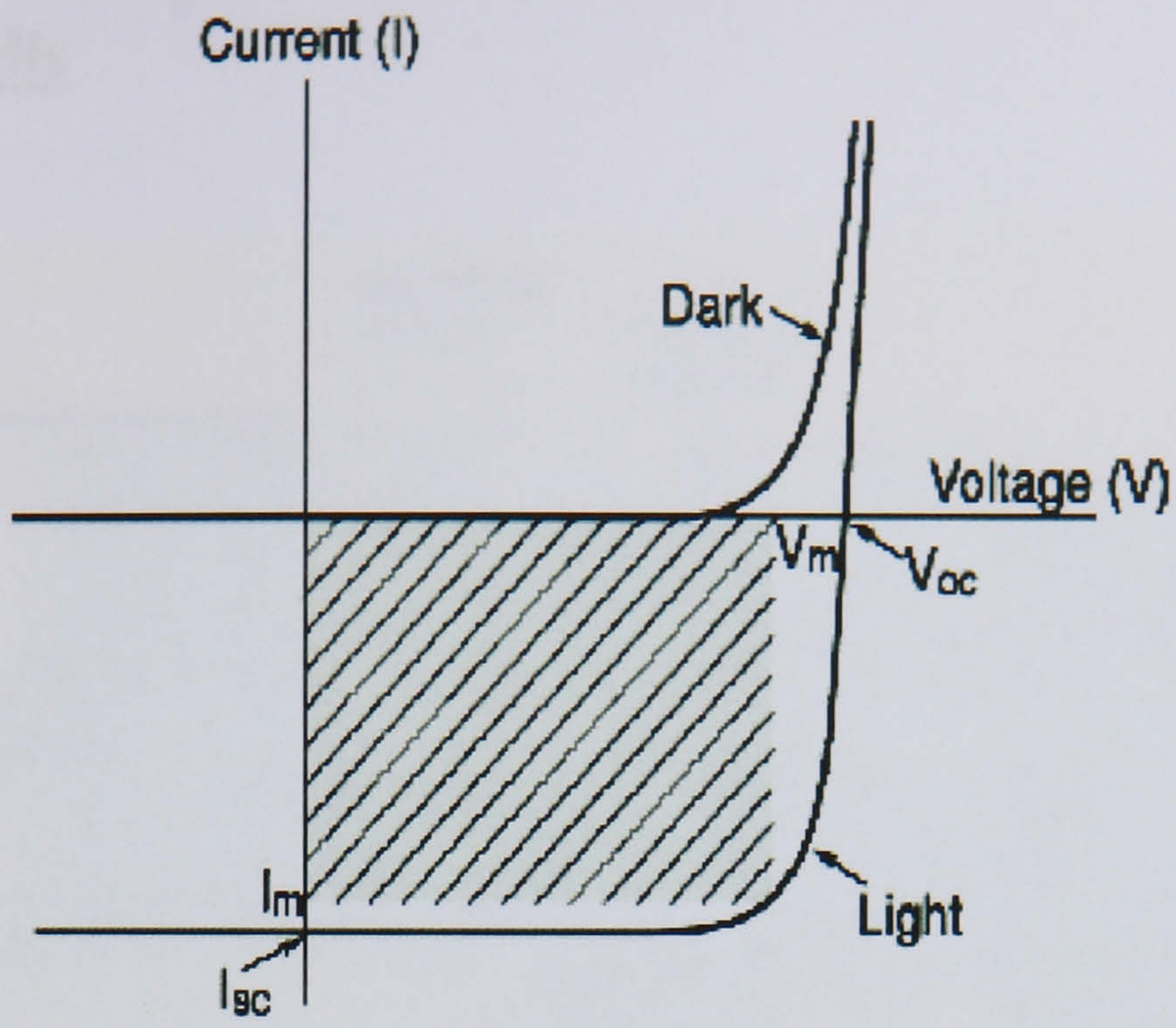

Figure 1.4: Dark and Light I-V characteristics.

The maximum power output of the cell is given by the product of voltage V_m and current I_m at the maximum power point. The fill factor compares this maximum power to that given by the product of open-circuit voltage and short-circuit current. It is given by

$$FF = \frac{V_m I_m}{V_{oc} I_{sc}} \tag{1.5}$$

Therefore, the absolute power conversion efficiency of the cell can be given as

$$Eff = \frac{V_m I_m}{P_{in}} = \frac{FF.V_{oc} I_{sc}}{P_{in}} \tag{1.6}$$

Most spectra, like the solar spectrum, are broad. It is primarily for this reason that cell efficiencies are limited. Photons of below band-gap energies do not contribute and those above only contribute an energy close to that of the band-gap. This is a consequence of the single band-gap nature of the cell. A number of different cell designs have been invented, such as tandem cells [10] and the use of quantum wells, discussed in Section 1.2. In thermophotovoltaics, described in Section 1.3, this problem is approached from the aspect of the spectrum itself.

1.2. Quantum Wells

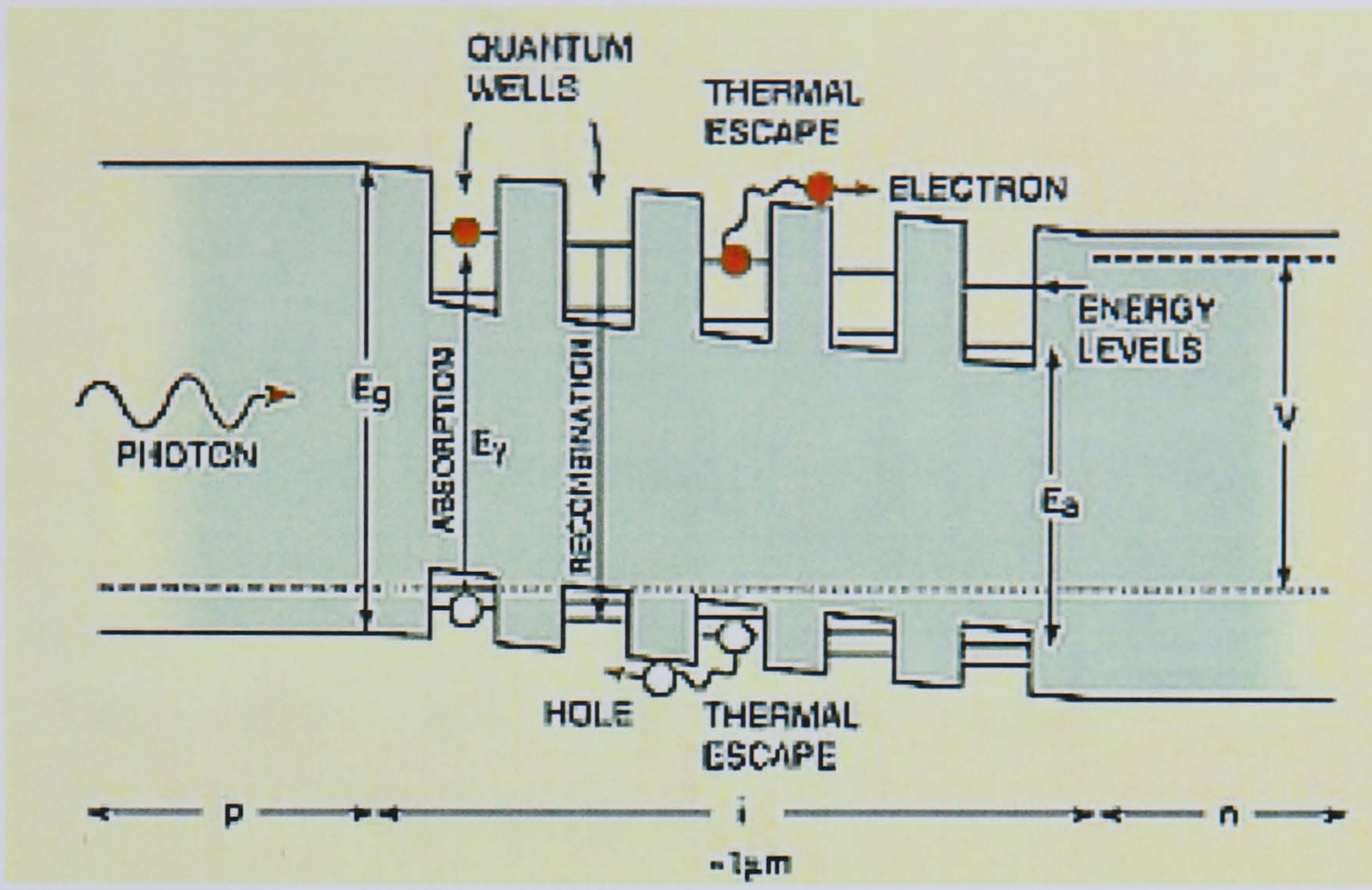

Figure 1.5: Quantum Well Solar Cell.

The quantum well solar cell was proposed in 1990 by Barnham and Duggan [11]. The band-gap diagram of a typical quantum well solar cell is shown in Figure 1.5. Quantum mechanically thin layers of a lower band-gap material are inserted into the intrinsic region of a p-i-n diode. These layers are able to absorb longer wavelength light, which is not absorbed by the rest of the cell. If the carriers can escape from the wells, by thermally assisted escape for example, then they can be collected in the usual manner [12]. Carrier escape from quantum wells in investigated in two samples in Section 4.4.

The absorption of a greater proportion of the illuminating spectrum, and more excited carriers, results in an increase in short-circuit current [8]. The open-circuit voltage of a cell is found somewhere between the band-gaps of the well and barrier materials, but is higher than that expected from the effective band-gap [13], which is found from the absorption edge of the cell. If the loss in open-circuit voltage is less than the increase in short-circuit current, as has been seen, then using quantum wells can improve the efficiency of cells [14]. Figure 1.6 [15] gives a clear example of the extension in the absorption produced by the addition of quantum wells to the cell.

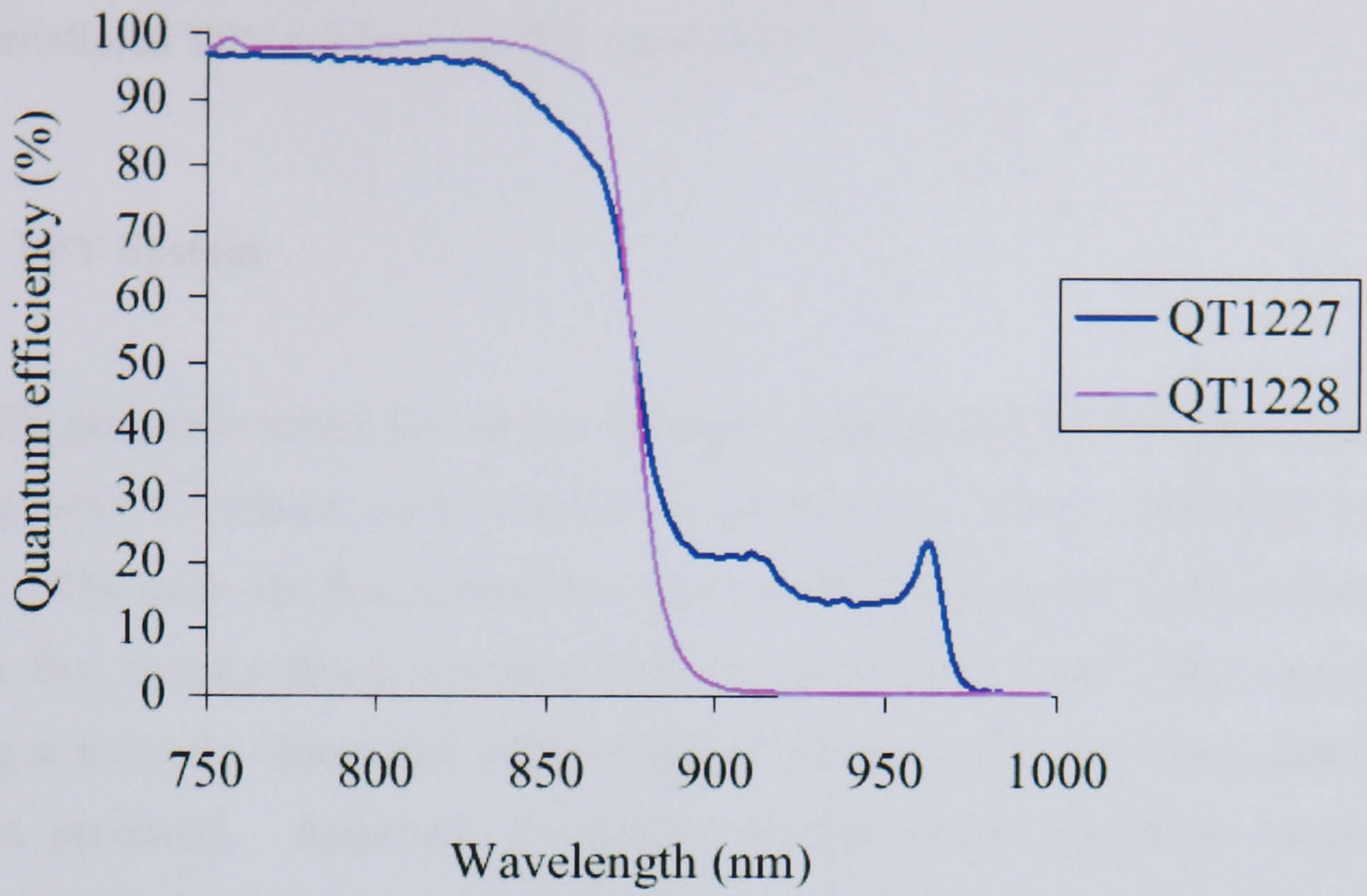

Figure 1.6: Quantum wells in device QT1227 have extended the absorption to longer wavelengths compared to the bulk device QT1228.

Clearly, choosing different materials for the quantum wells will shift the absorption edge of the cell. This ability to effectively 'engineer' the band-gap of a quantum well cell in order to match a particular spectrum is one of the main advantages over bulk cells [16].

1.3. Thermophotovoltaics

The process of converting heat radiation into electricity using PV cells is known as thermophotovoltaics (TPV). The physical principles remain the same as in conventional PV, but for a source we are not constrained to the sun; TPV generally refers to sources at temperatures around 1300-2000K. The second significant difference to solar PV is the proximity of the cells to the source. At distances of as little as a few millimetres the power incident on the cells is much increased, and also the interaction between source and cells cannot be neglected. TPV cells are typically part of a complex system which utilises many more disciplines than just semiconductor physics. For a thorough review of TPV and its system components, the reader is referred to Coutts' paper [17], the

Semiconductor Science and Technology special edition [18] or the proceedings from the five international TPV conferences that have taken place to date [19, 20, 21, 22, 23].

1.3.1. A TPV System

THE REV project is scheduled to run for three years and produce a prototype system operating with a thulium oxide (thulia) based selective emitter, radiating at around 1700nm. The cells for this system are to be strain-compensated multi-quantum well cells. A first demonstration system, employing an erbium oxide (erbia) based emitter radiating at around 1500nm and lattice-matched InGaAs cells, was also scheduled, and has been produced. Appendix A contains all the device structures received and characterised in this thesis, including those structures to be used in the prototype systems. A fuller description of THE REV project can be found in Appendix D.

The left hand part of Figure 1.7 shows the TPV system from Ref. 4. It contains all the basic components of a standard system. On the right of the figure is a drawing of the system which is being produced for THE REV project. A description of the system begins from the inside.

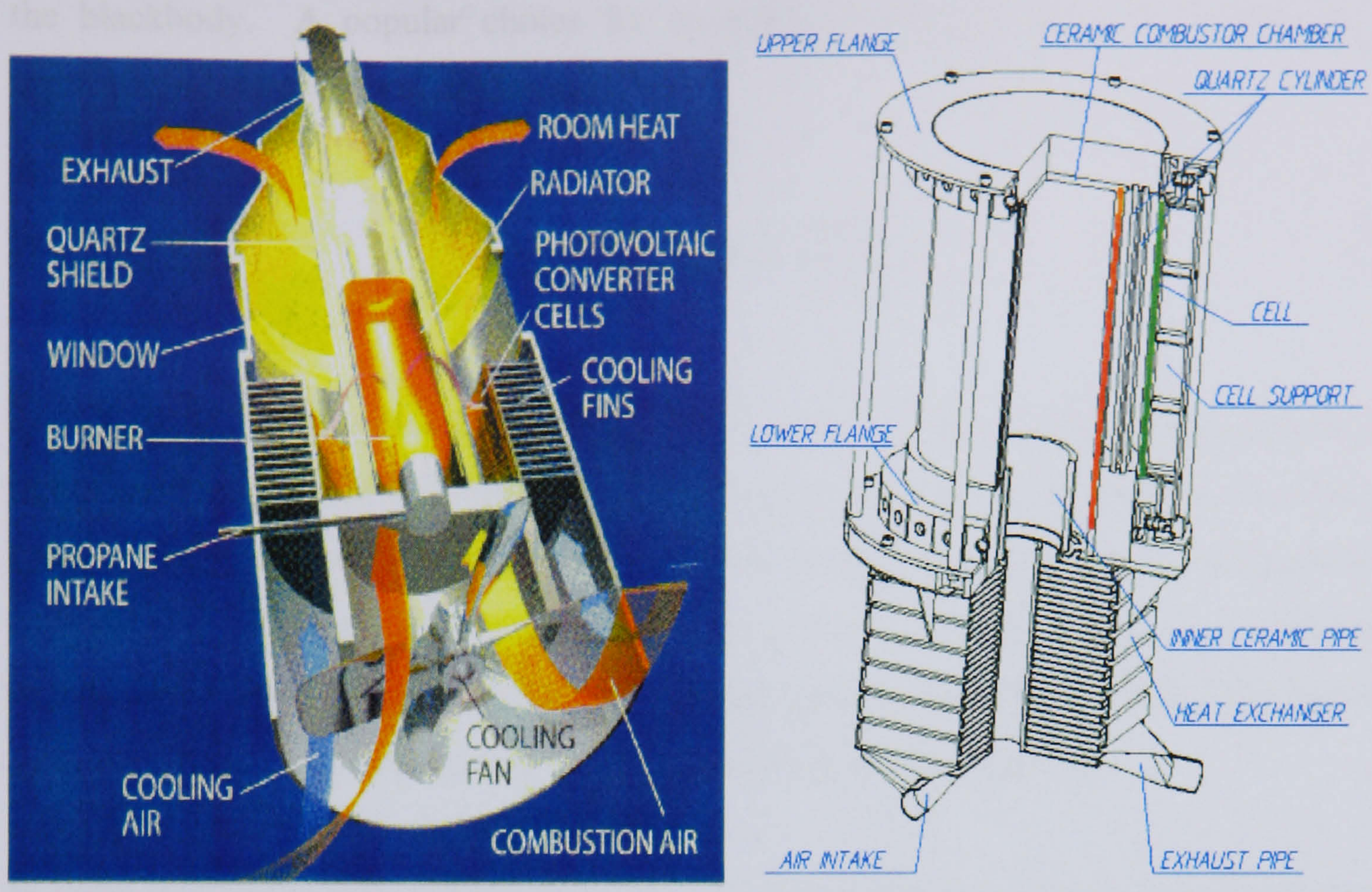

Figure 1.7: A functioning TPV system (left) and a drawing of THE REV system (right). The red layer denotes the selective emitter while the green layer is the photovoltaic cells.

1.3.1.1. Heat Source

A number of methods for providing a heat source exist at present. Stationary systems employing concentrated sunlight [24] or the burning of bio-fuel [25] have been demonstrated. Heat generation using the decay of a radioisotope is another method. The latter is proposed mainly as a space application when too far from the sun to use conventional PV [26]. However, given the mobility, and indeed safety, requirements of a system to be placed inside a car, the heat source for THE REV is provided by the combustion of a conventional fuel, which has been chosen to be diesel. This can also take advantage of existing infrastructure for refuelling.

1.3.1.2. Selective Emitter

The next part of a TPV system is the emitter, a material which absorbs the heat from the source and radiates an incident spectrum upon the cells. The simplest emitter takes the form of a blackbody radiator, which will produce a broad spectrum with a peak at a wavelength (λ_{peak}), given in Equation 1.7 by Wien's law, where T is the temperature of

the blackbody. A popular choice for broadband emitter is silicon carbide, for its mechanical properties and emission.

$$\lambda_{peak}(\mu m) = \frac{2900}{T(K)} \tag{1.7}$$

As discussed earlier, a broad spectrum has a number of disadvantages when employed in conjunction with a single band-gap cell. Firstly, the long wavelength photons cannot be absorbed by the cells. In the worse case these would be absorbed in the substrate and contribute to cell heating. Therefore methods need to be considered of preventing this unwanted absorption. Secondly, the high energy photons which are absorbed by the cell will also contribute to cell heating as they thermalise to the band-edge.

In order to accommodate the requirements of single band-gap material, the ideal emitter illuminates the cells with radiation of energy slightly above the band-gap energy of the cells, while suppressing emission in all other parts of the spectrum: selective emission. The emitters of most interest at present, and those involved in THE REV, are those based on rare-earth elements [27, 28], such as erbium and thulium. When oxidised, the electrons in the unfilled 4f shell, which are responsible for emission and absorption, are strongly localised due to the attraction of the nucleus. Because of this they do not interact with other atoms and they radiate in narrow bands like isolated atoms. The ability of the emitter material to withstand the conditions within a TPV system, whilst simultaneously providing the optimum emission is a critical factor [29]. One choice for selective emitter is ytterbium oxide, which emits around 1.29eV and has been incorporated into a system with photovoltaic cells made of silicon, the least expensive of all the crystalline photovoltaic cell materials [30].

The reason that such low band-gap materials are being used in THE REV project is that one aim of the system is to produce lower nitrogen oxide emissions than an internal combustion engine. One way this can be achieved is by using a lower combustion temperature. As can be seen from Equation 1.7, lowering the temperature increases the wavelength at which the maximum emission can occur. In order to maximise the radiated power a selective emitter is needed whose emission peak coincides with this maximum.

A significant drawback of a selective emitter is that restricting emission to a narrow range can significantly reduce the power density incident on the cells. The trade-off between overall efficiency and power output is central in deciding on a design of TPV system [31].

1.3.1.3. Photovoltaic Cells

For blackbody radiation at 1300-2000°C, the ideal band-gap is as low as 0.5eV. Therefore, the development of low band-gap materials, preferably lattice-matched to available substrates, is essential for TPV applications. Having said this however, one possible cell material for TPV is silicon, as mentioned above. Silicon can be matched to selective emitters based on materials such as ytterbium oxide, but the main motivation is cost reduction. Despite the popularity of a silicon approach, much work is being undertaken on other cell materials.

One of the materials currently benefiting from a large amount of research is GaSb. It has a band-gap of 0.72eV and was originally used as the bottom cell of a solar tandem device [32]. The ability to produce GaSb cells by a zinc diffusion process [33], thus dispensing with epitaxial growth, allows a significant reduction in the cost. GaSb is the cell material used in the only currently available commercial TPV device [4].

The most mature of the relevant material systems is InGaAs, thanks mostly to the work of the optical communications industry at 1.55μm. Grown on InP substrates, the lattice-matched $In_{0.53}Ga_{0.47}As$ has a band-gap of 0.74eV (~1.67μm). In order to reduce the band-gap of the cells it is necessary to use lattice-mismatched compositions. This, however, introduces strain into the structure, which can cause misfit dislocations and deterioration in performance. One approach to this problem has been to use a virtual substrate of the required lattice constant by incorporating a relaxed buffer layer between the substrate and the device, to keep any dislocations away from the active region of the cell [34]. The approach taken in this project has been the use of quantum wells and the strain compensation method, described in Sections 1.2 and 1.4 respectively. Strain compensation is used to achieve lower band-gaps with the well and barrier being lattice-

mismatched materials. The formation of dislocations is avoided by balancing the tensile and compressive strains between layers. Quantum well solar cells also display a smaller reduction in efficiency at higher temperatures than conventional p-n cells [35], extremely favourable for this particular system.

For THE REV system the cells are mounted in arrays of 46 devices connected in series. Figure 1.8 shows a picture of one of these arrays. On the right is a close-up, where the bonding between the individual devices can be seen.

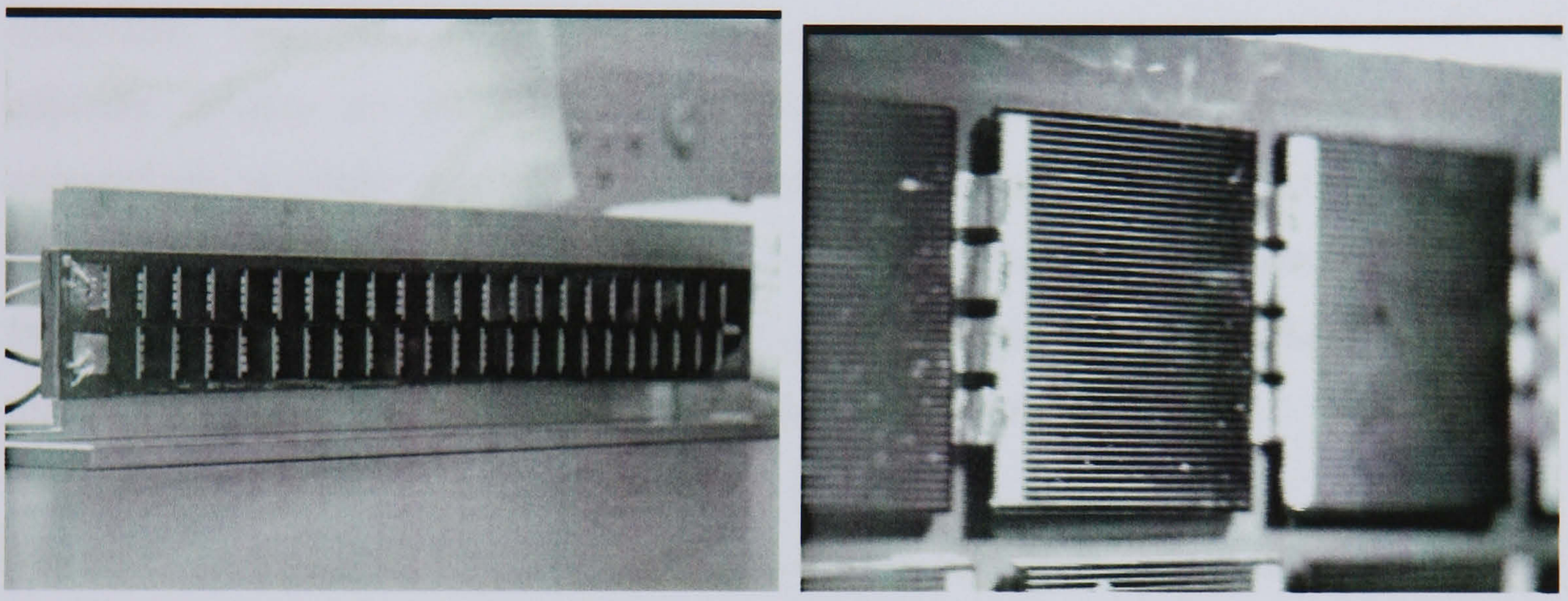

Figure 1.8: Pictures of the arrays produced for THE REV system. The close-up on the right shows the series connections between devices.

1.3.1.4. Other System Considerations

The heat source, emitter and cells form the basis of a TPV system, but additions can be made leading to further improvements. THE REV system includes a heat exchanger to recuperate some of the exhaust heat and pre-heat the incoming fuel mixture. The inclusion of quartz shields between the emitter and the cells can reduce convective heat transfer to the cells and if there are two shields then a vacuum can be formed between them, further reducing this process. Although in THE REV system there will be no vacuum, the quartz does perform a second function. At present, emission from the rare earth selective emitters contains a large amount of energy at longer wavelengths. Quartz begins to absorb at around 4μm and is therefore able to prevent these photons from reaching the cells, although specifically designed filters can also be used. Despite

these measures a certain amount of cell heating is to be expected and for this reason the cells are water cooled from behind.

If the rear contact of the cells can form a suitably reflective surface then this can be used to reflect unabsorbed photons. Returning them to the source can help to maintain the system temperature and increase efficiency, in addition to preventing cell heating caused by their absorption.

A further innovation that can be extremely beneficial to TPV systems is the use of monolithic interconnected modules (MIMs) [36]. In this technique a number of adjacent devices on the same wafer are connected in series with the external connections at either end of the series, rather than the reverse contact being made through the substrate. For this reason an insulating substrate and a lateral conduction layer are needed, along with a more complicated fabrication process, where the contact metal connects the bottom of one cell with the top of the next.

The main advantage of MIMs is that by placing the devices in series rather than parallel the current is reduced. Power loss (P) in a resistance (R) for a given current flow (I) is given by $P=I^2R$. Thus, the reduction in current through the cells reduces power loss. The single wafer also gives better thermal properties than separate devices. The use of an insulating, and therefore less highly doped, substrate also reduces unwanted substrate absorption, thus improving the usefulness of a rear surface reflector for returning low energy photons to the source.

1.3.2. General TPV Considerations

Clearly for THE REV, in its position as an alternative power source for a car, the TPV system is in direct competition with the internal combustion engine. In this respect its main advantages are its silent operation, lack of moving parts and the fact that it can be operated always at its optimum, rather than being dictated by the movement of the vehicle.

For TPV systems in general, there are a number of qualities which can make them attractive as power sources. In addition to those mentioned above, they offer the possibility of co-generation of heat and electricity and they have a high power density.

The fact that a TPV system can be used to supply heat in addition to electricity allows the heat leaving the system to be considered useful, rather than a loss. For this purpose co-generation TPV systems can claim to be highly efficient. Calculating the fuel-to-electricity efficiency of a system is far more complicated. Each distinct section of the system (burner, emitter, cells) contributes an efficiency of less than unity, and these combine to give a lower overall efficiency. Studies on a GaSb based system have predicted a thermodynamic limit of 60.5%, with system efficiencies of around 16% shown to be realistic targets given the required research effort [37]. A significant difference between TPV and conventional photovoltaics is that if unabsorbed photons can be reflected back to the source, then they are not considered to be lost. In the ideal system, all below band-gap photons would return to the emitter, helping to maintain its temperature. In this situation, the only way that the emitter would lose temperature is by radiating above band-gap photons, which can then produce electricity.

1.4. Strain Compensation

The aim of THE REV project is to produce a TPV system employing strain-compensated quantum wells cells which allow matching to emitters for which there are no materials of appropriate band-gaps that are lattice-matched to existing substrates. This section describes the technique of strain compensation and how it can be used in conjunction with quantum wells.

Whenever quantum wells are inserted into the i-region of a p-i-n cell they must necessarily, in order to have a smaller band-gap, be a different material. Unless the material system of interest allows, the well material will possess a different lattice constant, and this introduces strain into the system.

1.4.1. The Problem of Strain

A thin layer of lattice-mismatched material can be grown pseudomorphically with the in-plane lattice constant of the substrate, but only until a certain amount of strain energy has built up. At this point it becomes more energetically favourable for the epilayer to begin to relax back to its natural lattice constant. This introduces misfit dislocations into the structure, non-radiative recombination centres potentially fatal to a photovoltaic cell, particularly when in the active region [38]. As an illustration, Figure 1.9 is taken from Ref. 38 and shows the effect of increasing strain on the dark current of a device. The devices contain varying well numbers and compositions, with the excess strain shown on the x-axis. Dark current density at a bias of 0.5V is shown on the y-axis.

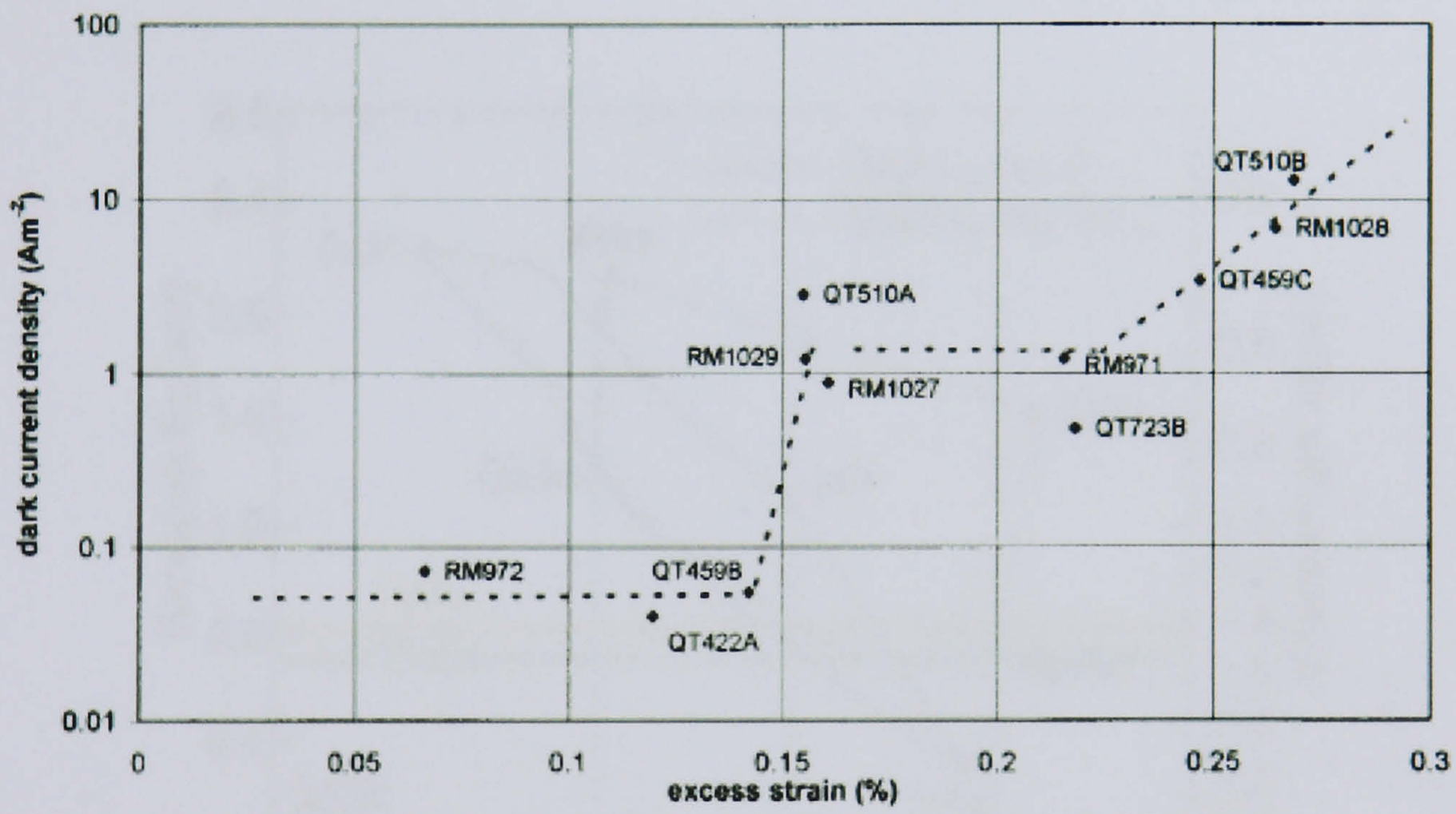

Figure 1.9: Dark current density at 0.5V of a series of devices with differing strains, taken from Ref. 38.

Matthews and Blakeslee originally calculated the critical thickness for relaxation to be that thickness at which the strain energy is sufficient to generate dislocations in the epitaxial layers [39]. Although each individual quantum well may itself be thin enough not to relax during growth, for each well that is grown the overall stress within the structure increases. Again, once a certain limit is reached, relaxation will occur. This places a limit on the thickness of the structure and hence on the number of wells which can be incorporated. For example, inserting $In_xGa_{1-x}As$ quantum wells into a GaAs cell

is desirable for use in tandems cells in order to increase the current produced by the bottom cell [40]. However, InGaAs is not lattice-matched to GaAs, therefore only a finite number of wells can be incorporated before the strain results in the collapse of the structure.

With regards to THE REV, Figure 1.10 shows a chart of band-gap against lattice parameter. The peak emission energies of the intended selective emitters erbia and thulia are also displayed. Clearly, the erbia is of a suitable wavelength for lattice-matched InGaAs. However, using the InGaAsP system, the thulia requires the use of lattice-mismatched materials. As discussed above, a quantum well cell with mismatched InGaAs would be limited by the number of wells that could be inserted before relaxation occurred.

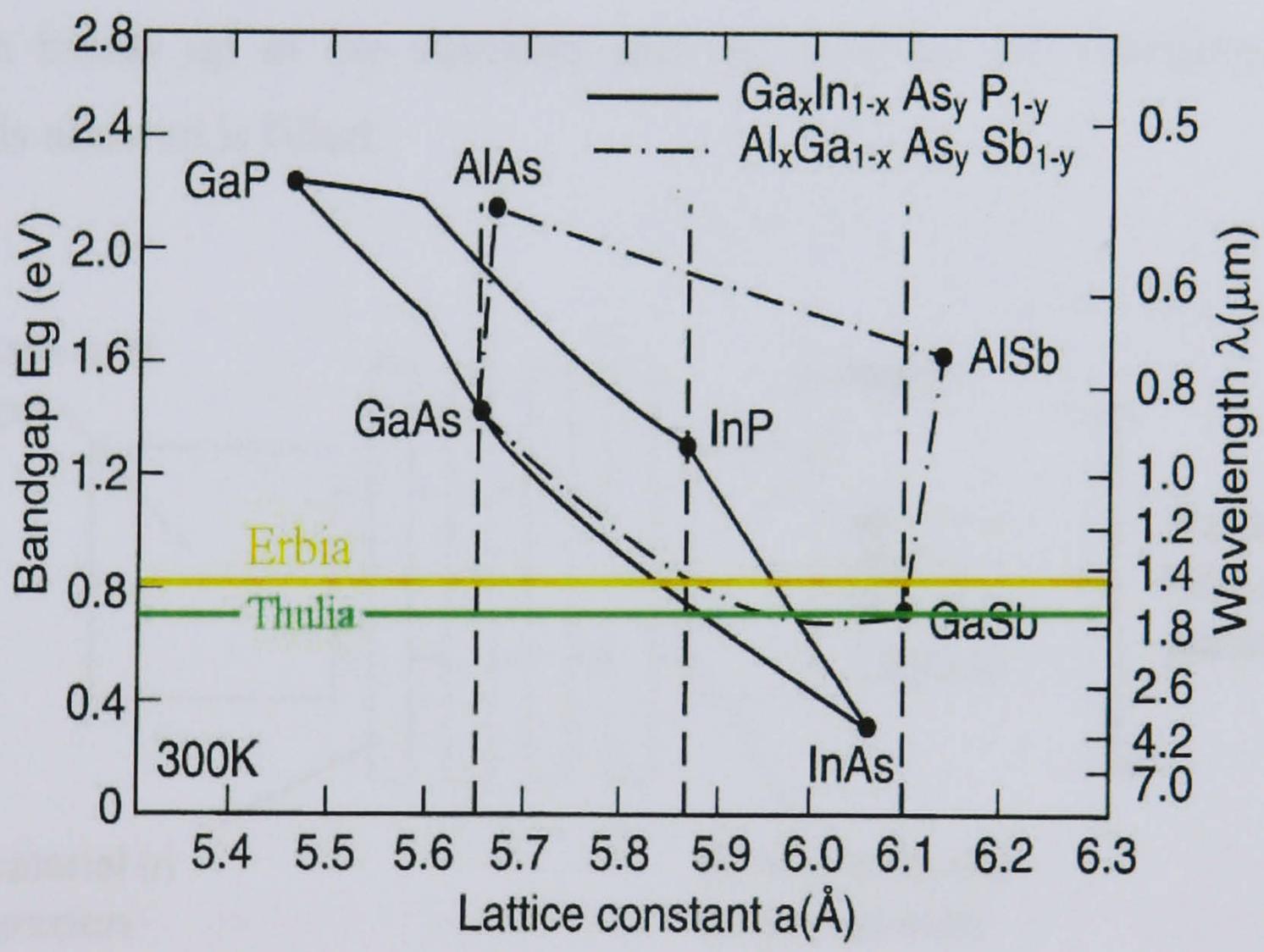

Figure 1.10: Band-gap vs lattice parameter for the InGaAsP material system. Superimposed are the expected peak emission wavelengths for the selective emitters erbia and thulia.

1.4.2. Strain compensation

In order to resolve these two situations, the method of strain compensation is employed, where not only are the wells a different material to the bulk, but so are the barriers. If the wells have a natural lattice parameter larger than that of the substrate then the barriers have one that is smaller. Whichever strain, compressive or tensile, the wells are experiencing as they deform to the substrate lattice parameter, the barriers are experiencing the opposite, see Figure 1.11. The precise compositions of well and barrier are chosen such that the two strains 'compensate' each other and the stress at the interfaces between the well/barrier periods is reduced to zero. In this way minimal overall strain builds up in the structure and the limit on the maximum number of quantum wells allowed is lifted.

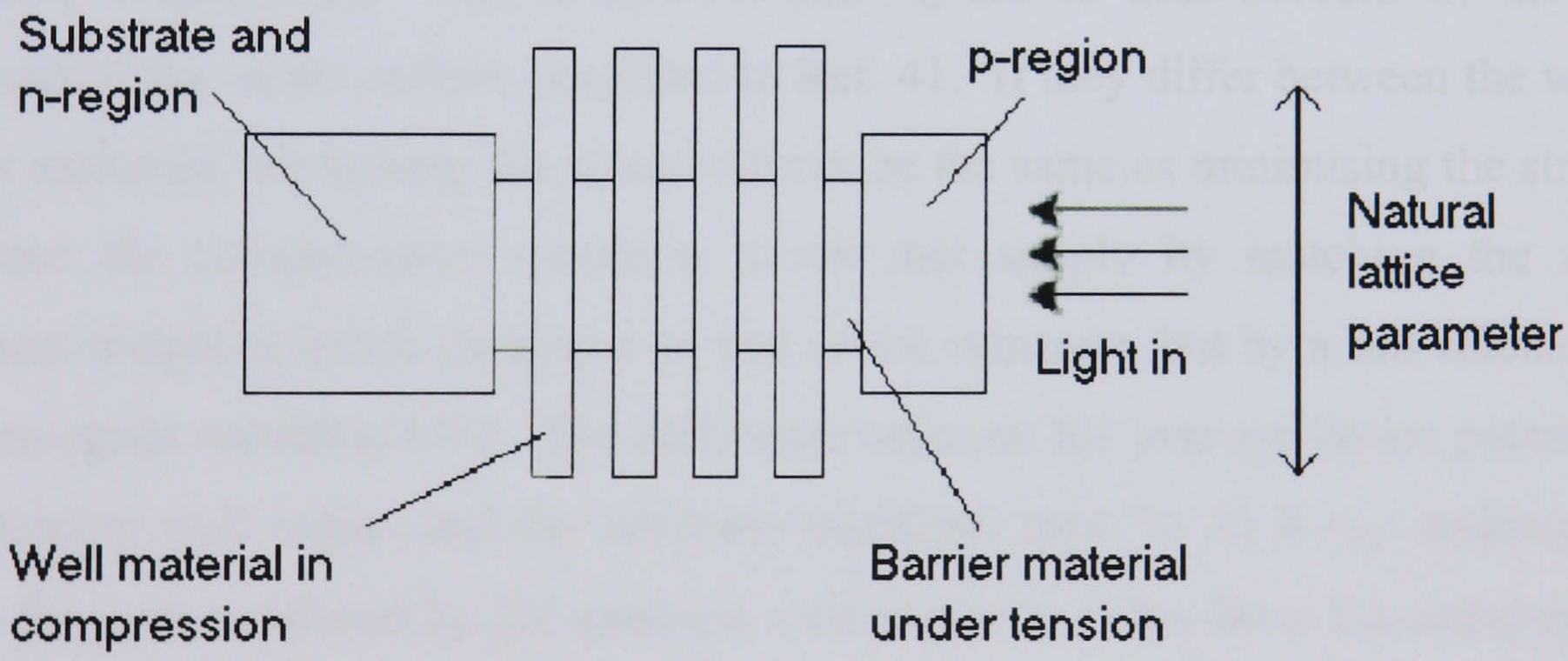

Figure 1.11: A schematic diagram of the materials involved in a strain-compensated structure. The quantum wells have a natural lattice parameter larger than that of the substrate. Therefore, the barriers have a smaller natural lattice parameter to 'compensate' the strain. It must be remembered that in the actual structure all the layers possess the same lattice parameter as the substrate. Due to compression in the direction parallel to the substrate, the lattice parameter of the well normal to the substrate will increased compared to its natural value, and vice versa for the barrier.

A quantum well cell is in effect an ideal partner for the application of strain compensation in that the well/barrier structure is able to balance a large amount of strain in small portions, as opposed to two bulk layers, which could in theory be strain-compensated but where the first layer would collapse long before the compensating layer could be grown.

In simple mathematical terms, successful strain compensation is achieved when the strain-thickness product for the whole structure is zero [41]. The expressions to be satisfied are

$$A_1 \varepsilon_{well} t_{well} + A_2 \varepsilon_{barrier} t_{barrier} = 0 \tag{1.8}$$

$$\varepsilon_{layer} = \frac{\left(a_{layer} - a_{substrate}\right)}{a_{layer}} \tag{1.9}$$

where ε_i denotes the strain of layer i, and t_i and a_i denote the layer's thickness and lattice parameter respectively. The factors A_1 and A_2 are to take account of the elastic constants of the layers and are described in Ref. 41. If they differ between the well and barrier materials minimising the strain will not be the same as minimising the stress. In this case the compensation condition is not met simply by matching the average thickness-weighted lattice parameter to that of the substrate, but by a full calculation of the zero-strain condition [41]. The difference between the average lattice parameter of the quantum well region and the substrate manifests itself in an X-ray rocking curve, where the peak produced by the quantum well region is offset from the substrate peak. This characterisation technique can then give an indication of the success of the strain compensation.

In general, and always for THE REV, the quantum well region begins and ends with a half-barrier. This ensures that the outer quantum wells are still confined by barrier material, without inserting an additional barrier into the structure. Providing that each individual layer does not exceed its own critical thickness as it is grown, each cycle of half-barrier, well and half-barrier contributes zero strain to the structure. The situation

is aided somewhat by the fact that the Matthews-Blakeslee limit for the maximum allowed thickness of a strained layer is considered a lower limit.

1.5. References

[1] UK Energy Sector Indicators 2002, Department of Trade and Industry.

[2] M Renner, Energy Alternatives and Jobs, Renewable Energy World, James and James Ltd, Nov-Dec 2000, pp.26-32.

[3] P Gipe, Wind Booms Worldwide, Renewable Energy World, James and James Ltd, Jul-Aug 2000, pp.133-149.

[4] L Fraas et al., Commercial GaSb cell and Circuit Development for the Midnight Sun® TPV Stove, 4th NREL Conf. Thermophotovoltaic Generation of Electricity, Denver CO, pp.480-487, 1998.

[5] T. Bauer et al., The Potential for Thermophotovoltaic Heat Recovery for the Glass Industry. In Coutts et al [23], pp.101-110. Rome, Italy, September 2002.

[6] S M Sze, Physics of Semiconductor Devices, 2nd Edition, Wiley Interscience, 1981.

[7] H M Rosenberg, The Solid State, 3rd Edition, Oxford Science Publications, 1992.

[8] W Shockley, The theory of p-n junctions in semiconductors and p-n junction transistors, *Bell Syst. Tech. J.*, **28**, p435, 1949.

[9] W Shockley and W T Read Jr., Statistics of recombination of holes and electrons., *Phys Rev.*, **87**, pp835-842, 1952; R N Hall, Germanium rectifier characteristics, *Phys. Rev.*, **83**, p228, 1951.

[10] N J Ekins-Daukes et al., Strained and Strain-Balanced Quantum Well devices for High Efficiency Tandem Solar Cells. *Solar Energy Materials and Solar Cells*, **68**, pp.71-87, 2001.

[11] K W J Barnham and G Duggan, A new approach to high-efficiency multi-band-gap solar cells. *J. Appl. Phys.* **67**, pp.3490-3493, 1990.

[12] A Zachariou et al., A Carrier Escape Study from InP/InGaAs Single Quantum Well Solar Cells. *J. Appl. Phys.* **83**(2), pp.877-881, 1998.

[13] Keith Barnham et al., Voltage enhancement in quantum well solar cells. *J. Appl. Phys.* **80**, pp.1201-1206, 1996.

[14] Keith Barnham et al., Quantum Well Solar Cells. *Appl. Surface Science*, 113/114, pp.722-733, 1997.

[15] D B Bushnell, PhD Thesis, Imperial College of Science, Technology and Medicine, 2000.

[16] J P Connolly and C Rohr, Quantum Well Cells for Thermophotovoltaics. In Barnham et al [18], pp.216-220, 2003.

[17] T J Coutts, A review of progress in thermophotovoltaic generation of electricity. *Renewable and Sustainable Energy Review,* **3**, p80, 1999.

[18] Keith Barnham, James Connolly and Carsten Rohr, editors. *Semiconductor Science and Technology, Special Issue on Thermophotovoltaics*, vol. 18, no. 5. Institute of Physics Publishing, Bristol, UK, May 2003.

[19] Timothy J. Coutts and John P. Benner, editors. *The First NREL Conference on Thermophotovoltaic Generation of Electricity*, vol. 321 of *AIP Conference Proceedings*. American Institute of Physics, Woodbury, New York, 1995. Copper Mountain, Colorado, USA, July 1994.

[20] John P. Benner, Timothy J. Coutts and David S. Ginley, editors. *The Second NREL conference on Thermophotovoltaic Generation of Electricity*, vol. 358 of *AIP Conference Proceedings*. American Institute of Physics, Woodbury, New York, 1996. Colorado Springs, Colorado, USA, July 1995.

[21] Timothy J. Coutts, Carole S. Allman and John P. Benner, editors. *Thermophotovoltaic Generation of Electricity: Third NREL Conference*, vol. 401 of *AIP Conference Proceedings*. American Institute of Physics, Woodbury, New York, 1997. Colorado Springs, Colorado, USA, May 1997.

[22] Timothy J. Coutts, John P. Benner and Carole S. Allman, editors. *Thermophotovoltaic Generation of Electricity: Fourth NREL Conference*, vol. 460 of *AIP Conference Proceedings*. American Institute of Physics, Woodbury, New York, 1999. Denver, Colorado, USA, October 1998.

[23] Timothy J. Coutts, Guido Guazzoni and Joachim Luther, editors. *Thermophotovoltaic Generation of Electricity: Fifth Conference on Thermophotovoltaic Generation of Electricity*, vol. 653 of *AIP Conference*

Proceedings. American Institute of Physics, Melville, New York, 2003. Rome, Italy, September 2002.

[24] Kenneth W. Stone et al., Testing and Modelling of a Solar Thermophotovoltaic Power System. In Benner et al [20], pp.199-209. Colorado Springs, Colorado, USA, July 1995.

[25] Lars Broman and Jorgen Marks, Co-generation of Electricity and Heat from Combustion of Wood Powder Utilizing Thermophotovoltaic Conversion. In Coutts et al [19], pp.133-138. Copper Mountain, Colorado, USA, July 1994.

[26] A. Schock et al., Small Radioisotope Thermophotovoltaic (RTPV) Generators. In Benner et al [20], pp.81-97. Colorado Springs, Colorado, USA, July 1995.

[27] Robert E. Nelson, Thermophotovoltaic Emitter Development. In Coutts et al [19], pp.80-96, Copper Mountain, Colorado, USA, July 1994.

[28] D. Diso et al., Selective Emitters for High Efficiency TPV Conversion: Material Preparation and Characterisation. In Coutts et al [23], pp.132-141. Rome, Italy, September 2002.

[29] A Licciulli et al., The challenge of high-performance selective emitters for thermophotovoltaic applications. In Barnham et al. [18], pp174-183, 2003.

[30] B Bitnar et al., A TPV system with silicon photocells and a selective emitter. *Proc. 28th IEEE PVSC,* Anchorage, USA, pp.1218-1221, 2000.

[31] P F Baldesaro et al., Thermodynamic analysis of thermophotovoltaic efficiency and power density tradeoffs. *J. Appl. Phys.*, **89**, pp.3319-3327, 2001.

[32] L M Fraas et al., GaSb booster cells for over 30% efficient solar-cell stacks. *J. Appl. Phys.* **66**, (8), pp.3866-3870, 1989.

[33] A W Bett and O V Sulima, GaSb Photovoltaic Cells for Applications in TPV Generators. In Barnham et al [18], pp.184-190, 2003.

[34] Susan L Murray et al., MOCVD growth of lattice-matched and mismatched InGaAs materials for thermophotovoltaic energy conversion. In Barnham [18], pp.202-208, 2003.

[35] P Griffin et al., The Application of Quantum Well Solar Cells to Thermophotovoltaics. *Solar Energy Materials and Solar Cells*, **50**, pp.213-219, 1998.

[36] D Wilt et al., Monolithic Interconnected Modules (MIMs) for Thermophotovoltaic Energy Conversion. In Barnham et al [18], pp.209-215, 2003.

[37] Matthias Zenker et al., Efficiency and Power Density Potential of Combustion-Driven Thermophotovoltaic Systems using GaSb Photovoltaic Cells. *IEEE T. Electron Dev.* **48**, (2), pp.367-376, 2001.

[38] P R Griffin et al., Effect of Strain Relaxation on Forward Bias Dark Currents in GaAs/InGaAs Multi-Quantum Well p-i-n Diodes. *J. Appl. Phys.*, **80**, p5815, 1996.

[39] J W Matthews and A E Blakeslee, Defects in epitaxial multilayers, Part I. Misfit dislocations, *J. Crystal Growth*, **27,** 1974.

[40] D B Bushnell et al., GaAsP/InGaAs Strain-Balanced Quantum Well Solar Cells. *Proc. 16th European PV Solar Energy Conf.,* Glasgow, 2000.

[41] N J Ekins-Daukes et al., Strain-Balanced Criteria for Multiple Quantum Well Structures and Its Signature in X-ray Rocking Curves. *Crystal Growth and Design*, **2**, (4), pp.287-292, 2002.

2. Experimental Methods

The journey of a wafer from leaving the growth chamber to its final status as a fully characterised photovoltaic device is presented in this chapter. Section 2.1 discusses the source of the wafers and the processing required to convert them into functioning devices. In Section 2.2 the tests performed on these devices are described. These characterisation tools assess the quality of the material and the processing and also provide insights into the physics behind the behaviour. They include measuring the current-voltage characteristics in the dark and under illumination, bias and wavelength dependent photocurrent and the reflectivity. Measurement techniques used within the project but outside Imperial are also briefly discussed.

2.1. Origin and Production of Samples

The devices investigated in this thesis came from two sources. The majority were grown as part of THE REV project at IQE, Cardiff, UK and were processed at the National Microelectronics Research Centre (NMRC), Cork, Republic of Ireland. These devices were given names with the prefix E. The remaining devices were both grown and processed at the EPSRC National Centre for III-V Technologies at the University of Sheffield, UK and have the naming prefix MR. All were grown by Metal-Organic Vapour Phase Epitaxy (MOVPE) on InP substrates. As expected, the processing steps used by the two institutions are essentially identical. An overview of the processing involved is given in section 2.1.1.

When complicated and expensive structures are grown the main purpose for characterising devices is to investigate the inherent material properties. The processing itself should not be under examination and generally is not, given that it is well established and much utilised. Devices referred to from here onwards as small area devices, which includes all devices from Sheffield, were processed as 1mm diameter mesa diodes with 600μm optical windows, then mounted on TO5 headers, as shown in Figure 2.1.

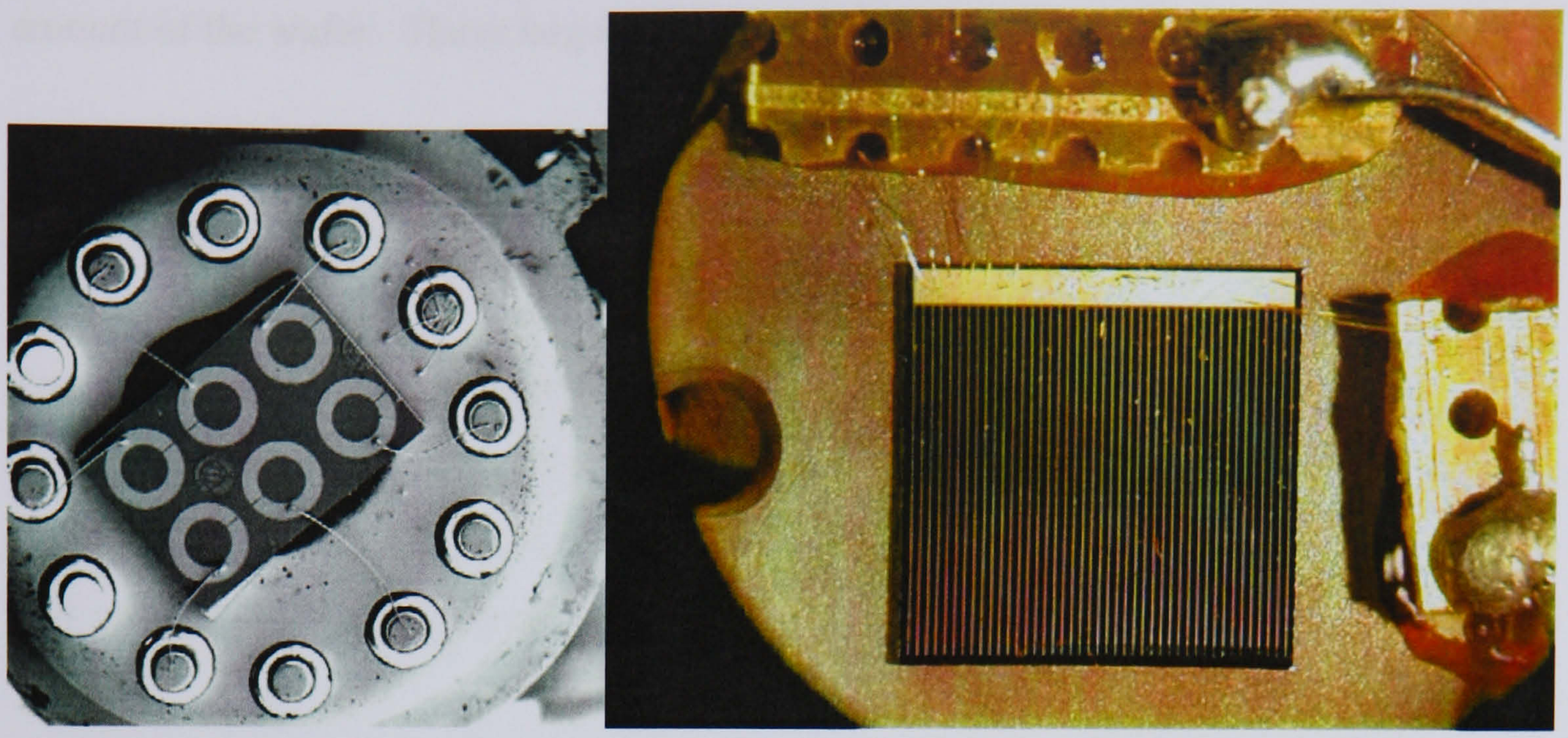

Figure 2.1: Plan views of six 1mm mesa devices mounted on a TO5 header (left) and a 1cm device mounted on a copper disc (right). For the 1cm device the rear contact is the copper disc itself. For the 1mm devices the rear contact is the base of the header, which is bonded to the pin next to the tab, in the top right of the figure.

In these small area devices, the amount of device material that is covered by the metal contact, the shading factor, is 59.6%. Although clearly not optimised for application performance this is important for testing. The high level of metallisation is present in order to reduce any series resistance that may be caused by a poor contact. This removes it as a potentially dominant effect, allowing purely material effects to be more visible. The optical window that this device provides is more than sufficient to allow full optical characterisation to be undertaken. The contact grid pattern, and hence the level of metallisation, can be optimised later for particular applications, while the high device metallisation in test structures can be corrected for when predicting full device performance.

A number of devices of IQE material were also processed into 5mm and 1cm (edge length will be given, not device area) square devices. These devices possess a finger design of a busbar with protruding fingers, which become thinner away from the busbar, as in Figure 2.1. For characterisation purposes, these devices can be mounted onto copper blocks and bonded to a piece of gold coated stripboard. This large area design is the contact design used for the first part of THE REV. Devices of this size not only

require less metallisation, 15.7% for 1cm devices, but can also make use of a larger amount of the wafer. These larger devices will be referred to as 'large area' devices.

2.1.1. Device Processing

The device processing performed by NMRC and Sheffield is essentially the same and as processing does not form a significant part of this thesis the differences will not be highlighted. Below is a brief summary of the major steps involved in converting the bare as-grown wafer into devices.

Step 1 – Back contact preparation:

The rear contact metals, typically germanium and then gold, are evaporated onto the substrate side of the wafer. The contact is then annealed to diffuse the germanium into the InP and create an ohmic contact. If any unwanted growth has occurred on the rear side of the wafer, this can be removed by lapping prior to evaporation.

Step 2 – Front contact preparation:

Photoresist is applied to the front surface and exposed using the contact mask (this will expose the areas intended for the contact metal). Developing then removes the photoresist from the exposed areas and contact metal is evaporated onto the wafer. The remaining photoresist is removed, leaving only contact metal on the front surface.

Step 3 – Contact/cap layer removal and anti-reflection coating:

The front surface is coated again in photoresist and is now exposed using the optical window mask (designed to expose everywhere on the device where the light will enter). After developing, the front contact layer is etched away in the optical window, using a selective etch that will not continue to etch into the emitter layer. At this point, if required, an anti-reflection coat is deposited over the window. Remaining photoresist is removed.

Step 4 – Mesa definition:

Photoresist is again applied to the front surface. This is exposed using the mesa mask (to expose the area between neighbouring devices) and developed. The

material around the individual mesas is then etched away to isolate the devices from one another. Photoresist is removed.

Step 5 – Device mounting:

The wafers are cleaved or sawn. In the case of small area devices the wafer is divided into pieces small enough to be mounted on TO5 headers and bonded to different pins. In the case of large area devices either the wafer itself is delivered, or it is first mounted onto a piece of copper, to which contacts can be applied, see Figure 2.1.

The procedure for processing InP devices has been largely borrowed from the processing of GaAs devices. A detailed description of GaAs processing can be found in Ref. 1, whilst the work carried out at Imperial College is described in Ref. 2. Full devices were processed by the author using remaining pieces of wafers E1057 and MR1091, see Sections 4.1.4 and 5.3.2 respectively.

2.2. Characterisation Methods

This section describes the methods used to characterise devices and discusses the importance of each experiment. Knowledge of the quality and performance of devices is important not only in deciding on the worth of an individual structure but also in that the results can be used to predict the performance of other structures as an aid to future designs using the model SOL, designed at Imperial College [3], see Appendix C.

2.2.1. Current-Voltage (I-V) characteristics in the dark

The measurement of the dark current gives a simple initial indication of the quality of the device material and the processing. A Keithley 238 Source-Measure Unit (SMU) records the current whilst sweeping the voltage. For constant temperature measurements the device is mounted on a Peltier plate with a temperature controller [4]. All dark currents are measured at room temperature (25°C) unless otherwise stated.

As described in Section 1.1.1, a dark current may be broken down into regions of shunt resistance, series resistance and a number of regions with different ideality factors. Fitting these parameters can give information about how successful the structure is or whether areas of growth or processing require changing. For example, a large series resistance may indicate that the contacting needs improvement.

The presence of an anti-reflection coating over the optical window should not per se significantly affect the dark current. However, when mesas are etched in order to separate the individual devices, the edges of the mesas may contain dangling bonds. These surfaces can then act as recombination centres for carriers within the device and cause an increase in dark current. When the AR coating is applied it can also coat the edges of the devices. In this way, the coating can occupy these loose bonds and remove them as potential recombination sites. Hence, if there is a high level of surface recombination then an AR coat may be expected to reduce this effect. However, the choice to add an AR coat for this reason must be weighed against any possible effects of the additional step in the production process.

In order that further resistances are not introduced by the measurement leads, I-Vs can be taken using a four-point measurement. As Figure 2.2 illustrates, a two-point measurement involves passing a known current through the system, which includes the device, and measuring the voltage required to do this. Unfortunately, the voltage recorded will also include the voltage required to push the current through the cables and the contacts and as such will be greater than the actual voltage across the device. In an I-V measurement this resistance would manifest itself as additional series resistance, preventing accurate high current measurements in large area devices.

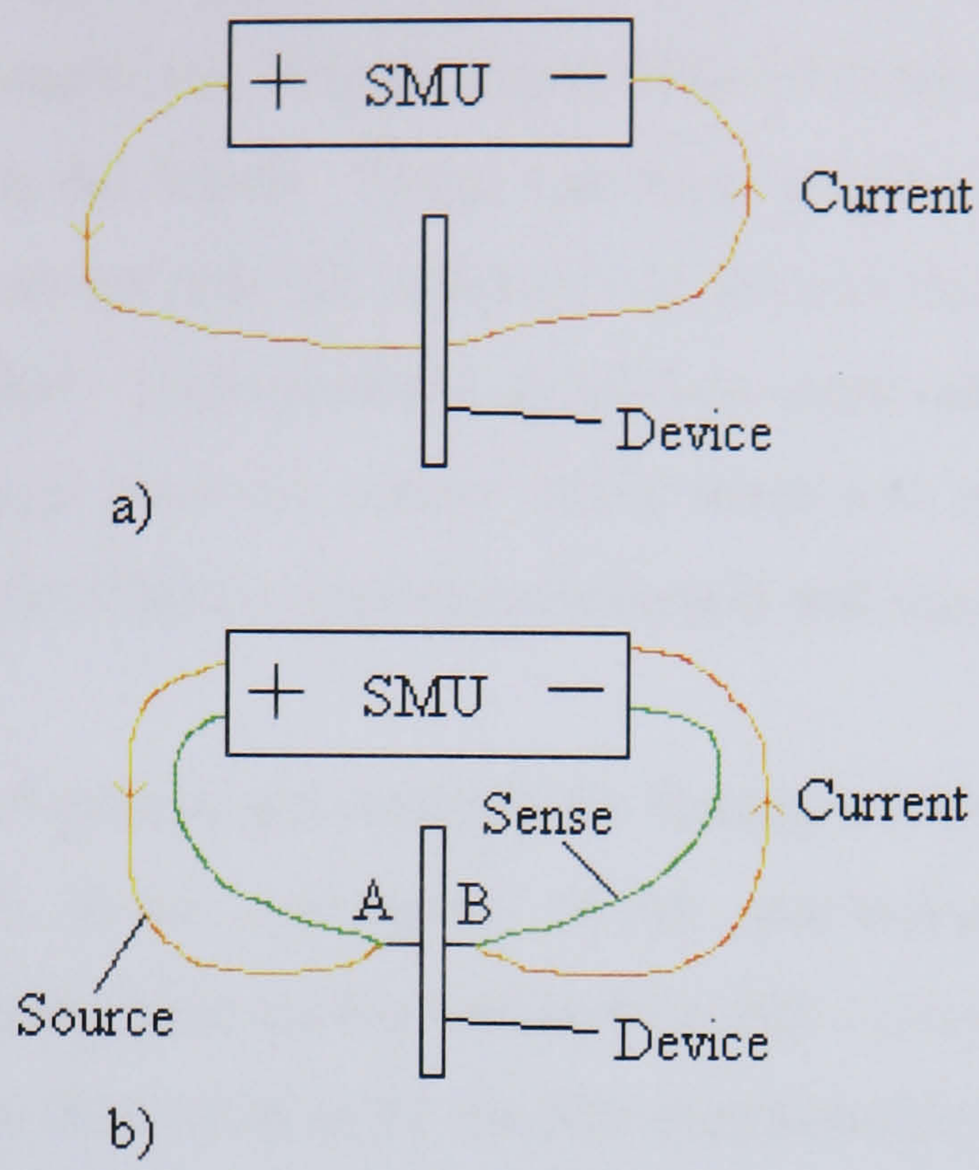

Figure 2.2: Schematic depictions of a) two-point, and b) four-point measurements using a source-measure unit (SMU). By sensing the voltage between points A and B with the high impendance voltmeter facility on the SMU the resistance of the cables is not measured. However, by joining the circuits at points A and B any resistances between these points and the device would still be detected. In the lower diagram, the points A and B represent two each of the 'four' points.

In a four-point measurement, Figure 2.2 also, there are two circuits connected to each of the device contacts. As before, the required current is generated in one of the circuits, the 'source'. The second 'sense' circuit is then used to measure the voltage across the device. As the voltmeter is high impedance, negligible current flows through the 'sense' circuit, and a more accurate device voltage can be recorded. To maximise the effectiveness of the four-point method the joining points of the two circuits (Points A and B) must occur as close to the device as possible. In the case of small area devices, as seen in Figure 2.1, the top contact of each device is bonded to one pin only. Likewise the base of the TO5 header (the bottom contact) is also bonded to only one pin. The pins themselves are the closest that the four-point contacts can be to the device. This can be improved by bonding each device and the header base to two pins each. However, this method is not generally used, as it would mean only five of the six devices could be contacted.

BIBL. LONDIN. UNIV.

In the case of the large area devices, as Figure 2.1 shows, the top contacts are bonded to pieces of gold-coated stripboard. It is simple to bond each top contact to two different, unconnected 'strips' on the board. These can then be used for 'source' and 'sense' contacts. This eliminates not only the resistance of the wire bonds but also the soldered wire contact on the board. Unfortunately, a full four-point measurement can reach no closer to the rear contact than the copper block itself and so any resistance due to attaching the device to the copper cannot be eliminated and must be assumed to be low.

When a large number of devices are available for testing, the spread of the dark currents can give an indication of the consistency of the processing with the best devices expected to cluster, usually with the lowest level of dark current. The devices with the lowest dark currents are then taken to be the best representations of the material quality and it is these devices which are characterised further.

2.2.2. Current-Voltage (I-V) characteristics under illumination

The simplest measure of I-V under illumination is performed using the dark I-V experimental set-up and a tungsten halogen lamp in an Oriel fibre illuminator. This has a stabilised DC power supply and the lamp gives an output approximating a 3200K blackbody spectrum. The light reaches the device via a fibre lead which alters the spectrum such that it becomes more like a 3000K blackbody. The fibre terminates with a defocusing lens to give more uniform illumination across the device.

In order to illuminate the device with spectra of the kind expected from selective emitters, a filter can be placed at the exit of the lamp unit. The addition of one of the filters results in illumination in narrow wavelength ranges about 1500nm or 1700nm, the expected peaks from erbia and thulia emitters respectively.

A light I-V measurement can give the clearest picture of the performance of devices, as it is effectively examining the device in its intended environment, or as close as is possible in a laboratory. However, the idealised filtered spectra available with the above set-up can only be an approximation of those expected from the possible emitters in the final TPV generator. In particular, placing a selective filter in the beam severely

reduces the power density arriving at the device. The light I-Vs produced by this set-up may not indicate the properties of the devices at the high illumination intensities expected, but they can still be useful as a tool for comparing structures, and are used as such in this thesis.

A further investigation of high intensity light I-V of the most important devices is conducted using a separate set-up. Here, the intention is not to simulate the exact spectrum of an emitter, but only to recreate the current levels that are expected to be generated within the device in the working TPV system. This will then examine the device's ability to cope with the large current flows for which the system is designed. At these intensities, where device cooling will be necessary, all experiments take place with the device mounted on a temperature controlled stage.

For high intensity light I-Vs, the illumination source is a 150W tungsten halogen lamp with a dichroic mirror lens. Given the amount of cooling that would be required by the temperature stage if the tungsten bulb were providing constant illumination, this experiment is shuttered. In order to coordinate the operation of the shutter with biasing and sensing the sample a new series of electronics was built by the author. A computer programme was also written to control the whole experiment. A detailed description is given in Appendix B.

2.2.3. Quantum Efficiency

External quantum efficiency (EQE) at a particular wavelength is defined as the number of successfully collected carrier pairs produced by the device, as a percentage of the number of photons of that wavelength incident upon it. Unless a distinction is needed, this will hereafter be known simply as quantum efficiency (QE)*. The experimental set-up for this measurement is shown in Figure 2.3. The light source is a 100W tungsten lamp with a Bentham 505 current-stabilised filament lamp power supply. This light is chopped and passes through a Bentham M300 monochromator. At the exit of the

* Internal quantum efficiency is the number of collected carrier pairs as a percentage of number of photons which enter the cell, thus discounting those reflected at the front surface.

monochromator is a 200μm pinhole, small enough that the image projected onto a small area device fits fully into its optical window. After then passing through a pair of achromatic lenses, the light reaches the device, producing a photocurrent. This signal is detected by a Stanford SR510 lock-in amplifier via a series of electronics, designed to allow measurements to be made with the device in forward bias [2]. The device bias may be supplied either by the lock-in amplifier or manually through the measurement electronics. The achromatic lenses, the beam-splitter (see Section 2.2.5), and the stage on which the device is mounted all sit on a rail which is aligned with the exit of the monochromator.

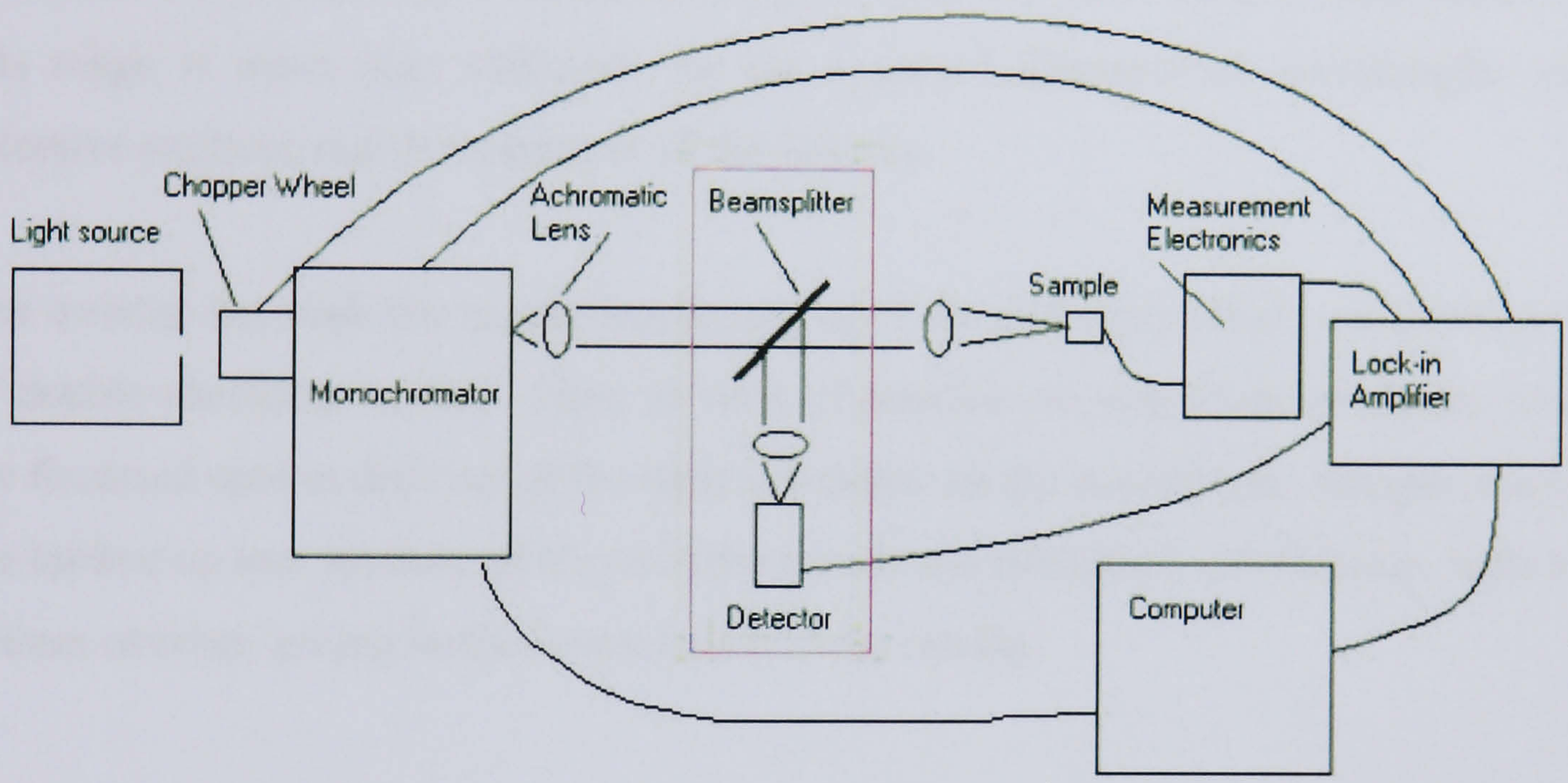

Figure 2.3: Quantum efficiency set-up. The purple box indicates extra equipment used only for reflectivity measurements, see Section 2.2.5.

The reason for chopping the light, other than to reduce noise and the influence of background light, is to eliminate the d.c. dark current element which would be present in non-zero bias measurements. This allows the photocurrent only to be measured. Unless otherwise stated, quantum efficiencies are taken at zero bias. The quantum efficiency of the device is found by comparing its photocurrent with that of a calibrated detector cell, of known quantum efficiency (QE_{cal}). The time between the measurements of device and detector should be as small as possible to reduce the effect of changes in the output of the lamp. Having measured a photocurrent from both the device (I_{device}) and the calibrated cell (I_{cal}), the quantum efficiency of the device is

$$QE_{device} = \frac{QE_{cal} I_{device}}{I_{cal}}. \tag{2.1}$$

Given the large range over which devices are measured (400-2100nm), there are two such experimental set-ups, identical apart from different gratings in the monochromators and different detectors covering a number of wavelength ranges. One set-up measures from 400-1100nm using a silicon detector (Newport 818-SL). The second set-up uses an InGaAs detector for 900-1700nm and an extended InGaAs detector (Hamamatsu G5853-01) for 1100-2400nm. The output of the second system decreases beyond around 2100nm, placing an effective limit on the measurement, but this range is more than sufficient for the expected illumination wavelengths of the selective emitters and the responses of the devices.

The overlap between the measurement ranges of the detectors offers a convenient way of double-checking results. Also, in view of possible misalignment problems causing the focussed spot to drift out of the optical window as the wavelength changes, the scans are broken up into sections of about 300nm, each one optimised individually, with about 100nm overlap, giving further consistency to the results.

2.2.4. Monochromatic I-V

Monochromatic I-V is performed using the same experimental set-up as quantum efficiency, and here the bias dependence of the photocurrent is measured at a fixed wavelength. Although the word 'monochromatic' refers to the form of the illumination, the name is slightly can be slightly misleading in that this is not a d.c. measurement like all the previous I-V measurements described.

Monochromatic I-V is an indication of how successfully the photo-generated carriers are collected by the electric field. In an ideal p-i-n junction, the electric field is constant across the undoped i-region. When the device is in forward bias, as would be the case under operating conditions, the electric field drops uniformly across the i-region and at a certain bias it reaches zero across the whole region. However, if there is substantial

background doping in the i-region this will cause variations in the electric field. In this case, when forward bias is applied, the electric field again drops uniformly but it reaches zero in parts of the region at a smaller bias. Without the field, carriers cannot be separated and may recombine and be lost. The effect of i-region doping on carrier collection can be seen in Figure 2.4.

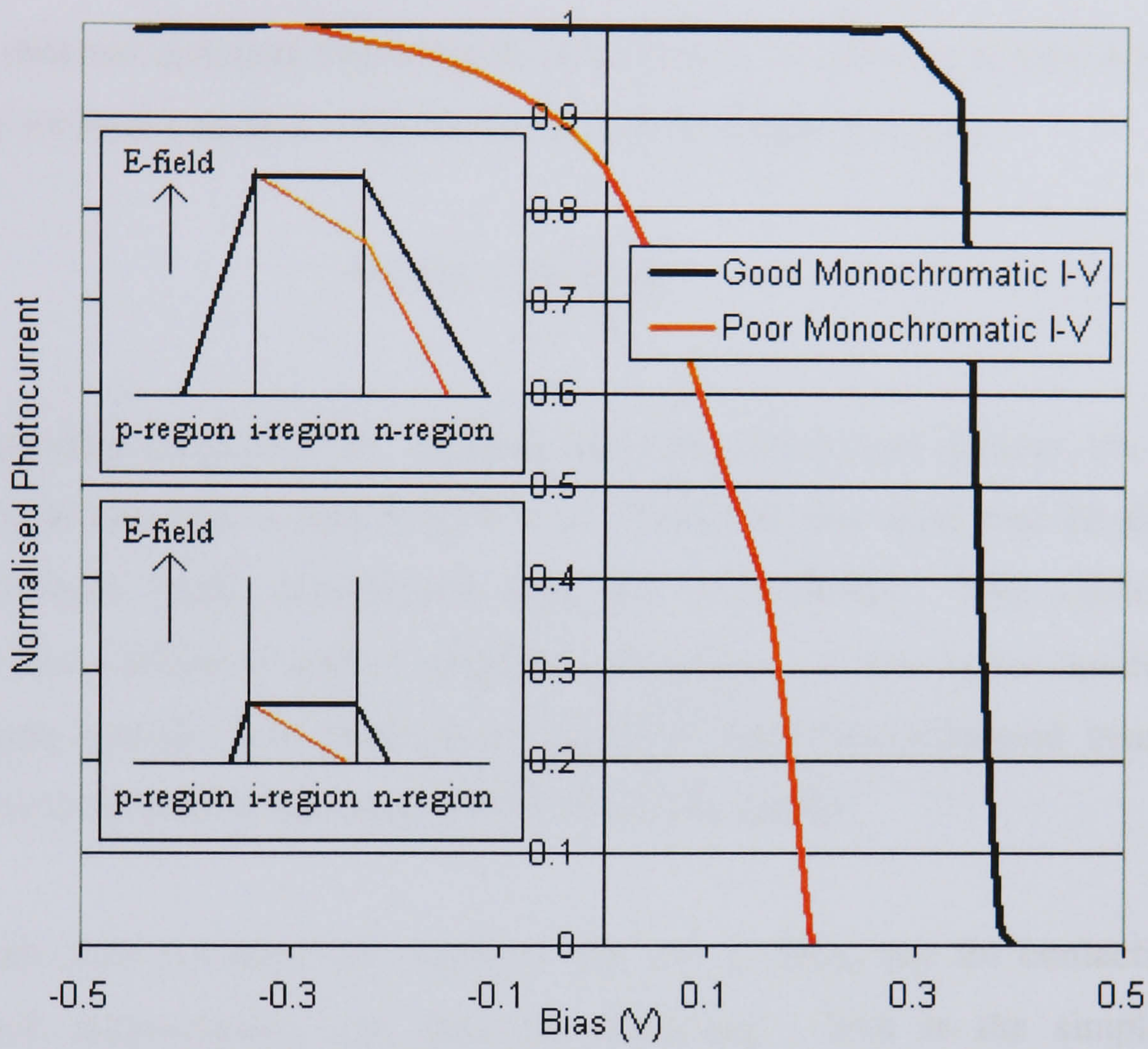

Figure 2.4: Illustration of the effect of background doping on monochromatic I-V. The upper of the electric field profiles shown inset refers to a point in reverse bias around –0.5V. The lower inset shows the electric fields at around –0.2V bias. Now, the poor structure has zero electric field in part of the i-region, with the result that fewer carriers are collected.

2.2.5. Reflectivity and Transmission

A reflectivity measurement gives the best indication of the quality of anti-reflection (AR) coatings and is important in modelling the quantum efficiencies of devices [3]. It can also be used to assess the extent of photon re-circulation, which is important for TPV applications. Reflectivity is also performed on the same equipment as quantum efficiency, see Figure 2.3, where the highlighted purple area is now included. A beam-

splitter is placed between the two collimating lenses. The transmitted signal reflects off the device and then off the beam-splitter to the detector at the side. The measurement is then repeated but with the device replaced by a mirror of known reflectivity. The reflectivity of the device is then given by the device-to-mirror detector signal ratio multiplied by the mirror's known reflectivity.

Once the external quantum efficiency (External) and the reflectivity (R) of a device are known the internal quantum efficiency (Internal) is simply given by

$$\text{Internal} = \frac{\text{External}}{(1-R)}. \tag{2.2}$$

When measuring the reflectivity of pieces of wafer, rather than devices, the beam does not need to be focussed to such a small area. Therefore, the wafer may be placed in the collimated beam itself, immediately after the beam-splitter. This method is valid providing the calibrated mirror is placed likewise. If the beam incident on the measurement sample does need to be narrower than the collimated beam then an aperture can be placed in the beam, before the beam-splitter.

If the wafer does not have any metal on the rear surface, say for contacting, then a transmission measurement may also be conducted. This is the simplest of the experiments performed on the quantum efficiency set-up. The detector is placed after the achromatic lenses, collecting the focussed light, and two scans are made: one with the wafer in the collimated beam and one without. Again, the collimating beam may be narrowed if necessary.

2.2.6. Modelling of Reflectivity, Transmission and Absorption

In a number of places within this thesis, properties of the wafer such as reflectivity, transmission and absorption have been modelled. This modelling was performed either for comparison with experimental data, or in order to extract the value for a property that was not directly measurable. For example, for a number of device structures the reflectivity of the rear contact is calculated.

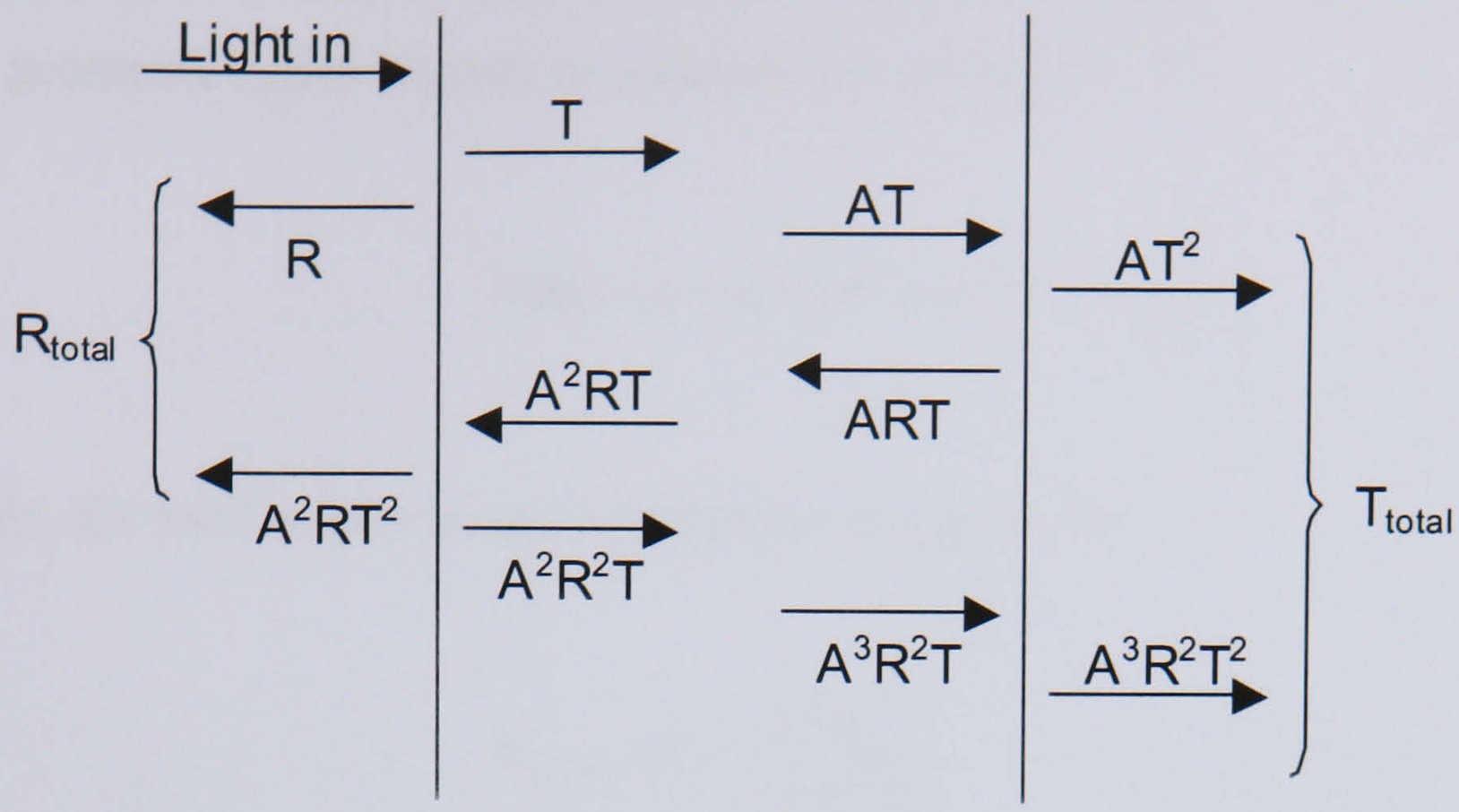

Figure 2.5: Schematic diagram of the infinite pass model, using a single material. Different reflected components sum to give the total reflectivity (R_{total}) and transmission (T_{total}), or the total absorption.

To model the devices, an infinite pass model is used where the material is treated as a uniform sheet of one or two absorbing regions, bounded by smooth parallel surfaces. No internal boundaries are considered and so reflections occur only at the front and rear surfaces of the wafer. The technique is shown in Figure 2.5, which illustrates the individual components that add up to parameters such as total reflectivity. The factor A denotes the fractional intensity that remains after a single pass through the absorbing region. The formula relating the absorption coefficient (α) to the distance travelled through the material (x) is

$$I(x) = I(0)e^{-\alpha x}, \tag{2.3}$$

where I(0) is the initial intensity. Therefore, the factor A relates to the absorption coefficient by the equation

$$A = \frac{I(x)}{I(0)} = e^{-\alpha x}. \tag{2.4}$$

As is shown in Figure 2.5, the total reflectivity and transmission of the sample are comprised of an infinite number of contributions. With the exception of the first

reflection (R), both sets of elements form a geometric series. The total sum of an infinite geometric series is given in equation 2.5, provided $r < 1$.

$$\text{Total} = a + ar + ar^2 + ar^3 + \ldots = \frac{a}{1-r} \tag{2.5}$$

Therefore, the total reflection and transmission are given by

$$R_{total} = R + \frac{A^2RT^2}{1-A^2R^2} \tag{2.6}$$

$$T_{total} = \frac{AT^2}{1-A^2R^2} \tag{2.7}$$

Figure 2.5 only shows one absorbing region. The addition of more requires the factor A to be the product of the individual factors from all absorbing regions and may also result in the reflections at the surfaces being different.

The front surface is usually to air, while the rear surface can be bounded to air in the case of a wafer, or a metal with a certain reflectivity in the case of processed devices. One of the absorbing regions is the InP substrate, the absorption of which has been measured and is discussed in Section 5.2.3. The active region, for quantum well samples this is the well region, is the second absorbing region. The total absorption in this region can be taken to be the measured quantum efficiency of the device, which assumes, generally reasonably, that all photo-generated carriers escape and are collected. Additional absorbing regions can also be considered as required. The reflections at surfaces bounded to air can be calculated from refractive index data of the outer materials. The total reflection and transmission can be measured experimentally. Any unknown parameters that are needed can then be deduced using this model and the available experimental data.

As a further validation of the author's model, many of the samples fitted as described above are also fitted with the modelling programme SOL developed at Imperial College [3], which produces quantum efficiencies of structures.

2.2.7. X-ray diffraction analysis

X-ray diffraction utilises Bragg's law of diffraction to highlight periodicity within a structure. For a series of planes, a distance d apart, the governing equation is

$$n\lambda = 2d\sin\theta \tag{2.8}$$

where λ is the wavelength of the light, θ is the incident angle and n is the order. Reciprocal space mapping utilises this equation to produce the reciprocal lattice of the material. The map is produced around a reciprocal lattice point of the substrate. Additional structure observed around this point is due to the structure of the layers that have been grown. For cubic lattices, reciprocal directions are the same as real directions, hence the reciprocal points give information about the directions in which the structure exhibits periodic structure. The arrangement of structure in a reciprocal space map can give an indication of how successfully a quantum well region has been grown.

2.2.8. Further measurement techniques

A number of characterisation techniques used during the course of the project, some of which are presented here, were produced outside Imperial. Table 2.1 gives a brief description of these techniques, their purposes and a rough measure of their accuracy.

Name of Technique	Acronym	Main use(s)	Destru ctive?	Resolution
X-ray Diffraction	XRD	Determination of the quality of strain-balancing and of layer thickness and composition	N	Better than a few arcsec over a scan of more than 10000 arcsec.
Transmission Electron Microscopy	TEM	Determination of layer thickness and quality (dislocations etc.)	Y	10nm
Electron Beam Induced Current	EBIC	Determination of surface dislocation density	Y	to 0.1μm
Photo-luminescence	PL	Determination of absorption edges within structure	N	Arbitrary intensity units, 1nm wavelength resolution
Cathodo-luminescence	CL	As PL	N	As PL
Atomic Force Microscopy	AFM	Determination of surface smoothness	N	0.5μm lateral, 10nm depth

Table 2.1: Summary of THE REV characterisation techniques performed outside Imperial.

2.3. References

[1] R E Williams, Modern GaAs device processing, Artech House, Boston, 1990.

[2] D B B Bushnell, Optimisation of strain-compensated multi-quantum well solar cells, PhD Thesis, Imperial College London, 2002.

[3] J P Connolly et al., Modelling Multi Quantum Well Solar Cell Efficiency. *Proc. 17th European Solar PV Energy Conf.* Munich, Germany, 2001.

[4] Ian Mark Ballard, Temperature Dependence of Quantum Well Solar Cells, Master's thesis, Imperial College of Science, Technology and Medicine, 1995.

3. Results on Lattice-Matched Structures

The aim of the first half of THE REV project was to produce a system containing TPV cells matched to an erbia emitter with a peak emission at 1500nm. For this purpose $In_{0.53}GaAs$ lattice-matched to InP is suitable. This chapter presents characterisation results from all the lattice-matched structures received, in roughly chronological order. Device structures are given in Appendix 1. All the devices discussed in this chapter were based on lattice-matched InGaAs and possessed a band-edge of around 1660nm. This chapter begins by discussing the initial characterisation performed on all of the devices: dark current, quantum efficiency and reflectivity, with comparisons between the structures. The final section describes high intensity light I-V measurements of selected structures.

3.1. Initial Characterisation

3.1.1. Wafers E004 and E006

The first structure received was an InGaAs p-n device based on an existing design and including a lateral conduction layer [1]. The absorption edge of lattice-matched InGaAs at 1660nm makes an InGaAs p-n structure a good starting point from which to develop a structure matched to erbia emission around 1500nm. Devices from two wafers of this structure were received: E004 with an n-type substrate and E006 with a semi-insulating (SI) substrate. Of E004, four small area devices (all non-AR coated) and two 5mm x 5mm devices (one AR coated) were received. For E006, only small area devices were received, of which approximately half were AR coated (optimised at 1550nm. See section 5.4 for the theory of AR coats.). As a reminder, these small area cells were used only for testing device and material quality, whereas the TPV system itself includes 1cm x 1cm large area devices.

The dark current densities of the best devices from the two received wafers, and the two large area devices, are shown in Figure 3.1. There are insufficient E004 devices to make quantitative statements about the spread in dark currents, but one of the devices

has a much lower dark current than the others, indicating a level which is achievable in the best samples. This device was well fitted with ideality factors of n=2 at low biases and n=1 at higher biases, as shown in Table 3.1. The results of fitting the lowest E006 dark current is also given.

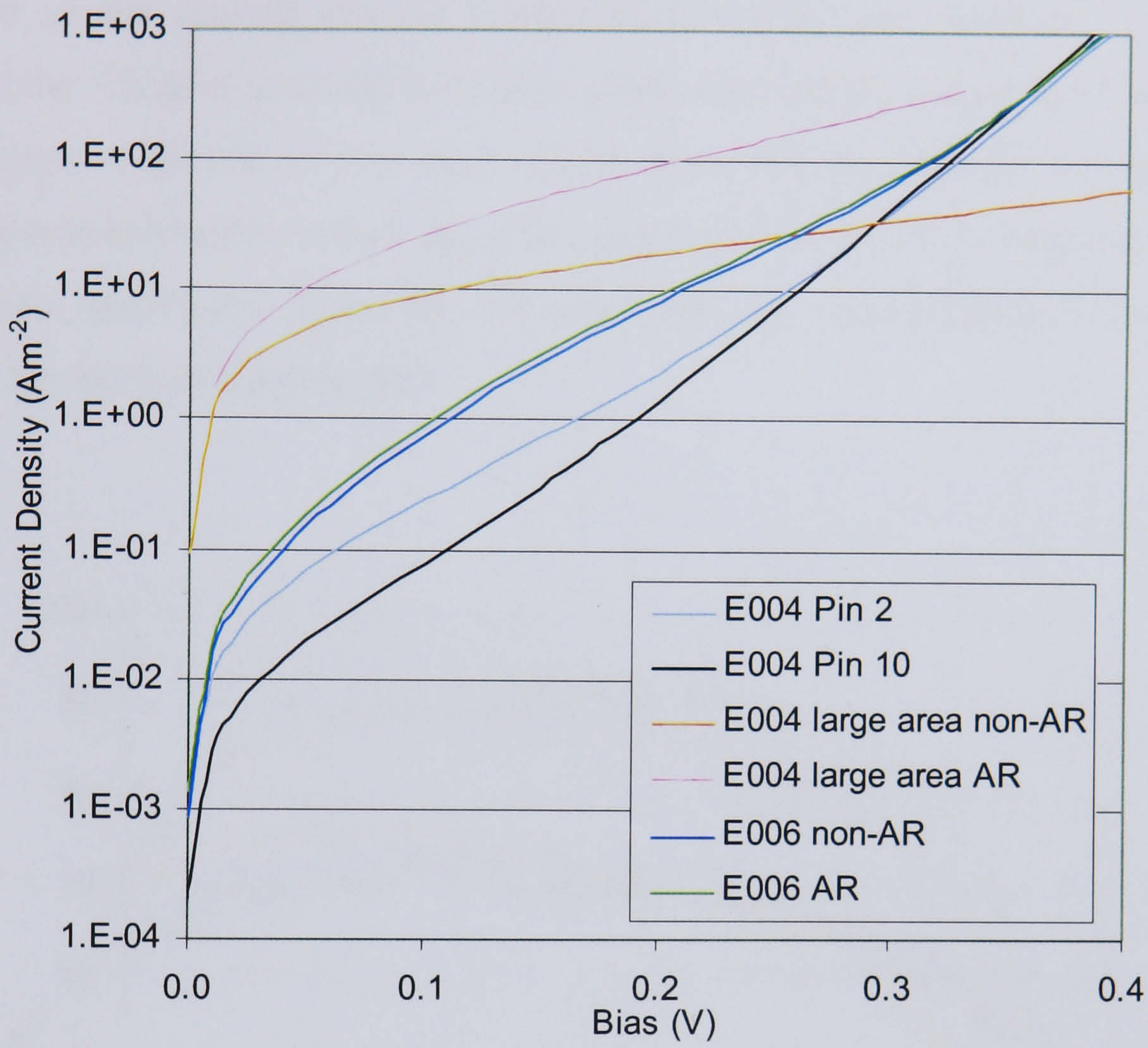

Figure 3.1: Dark current densities of wafers E004 and E006.

Device	Ideality n_1	Saturation current J_{o1} (Am^{-2})	Ideality n_2	Saturation current J_{o2} (Am^{-2})	Series resistance R_s (Ω)	Parallel resistance R_p (Ω)
E004 Pin 10	1	2.75E-4	2	1.16E-2	1.90	1.26E+17
E006 non-AR	1	1.97E-4	2	2.56E-1	0.18	4.21E+20

Table 3.1: Results of fitting the best E004 and E006 small area non-AR dark currents.

The dark currents from the two large area devices could not be fitted using sensible values for n, indicating significant non-ideal behaviour. However, one of these devices was examined by Electron Beam Induced Current (EBIC) at MASPEC in Italy and the material quality was found to be free of dislocations, which suggests that problems exist with large area processing. E006 dark currents showed a large spread, but the best

devices were only at a slightly higher level than the best from E004, demonstrating that, as expected, the use of a SI substrate in place of an n-type substrate does not significantly affect performance.

For E006 there is little difference in dark current between AR and non-AR samples; the application of the coating has not compromised device performance. Lower dark currents in the AR devices could have been evidence of surface passivation, but the lack of a reduction in the AR devices may simply mean that the surfaces are not acting as significant recombination centres and that passivation is not an important requirement. Alternatively, passivation from the AR coat may be compensating for an increase caused by the extra processing step.

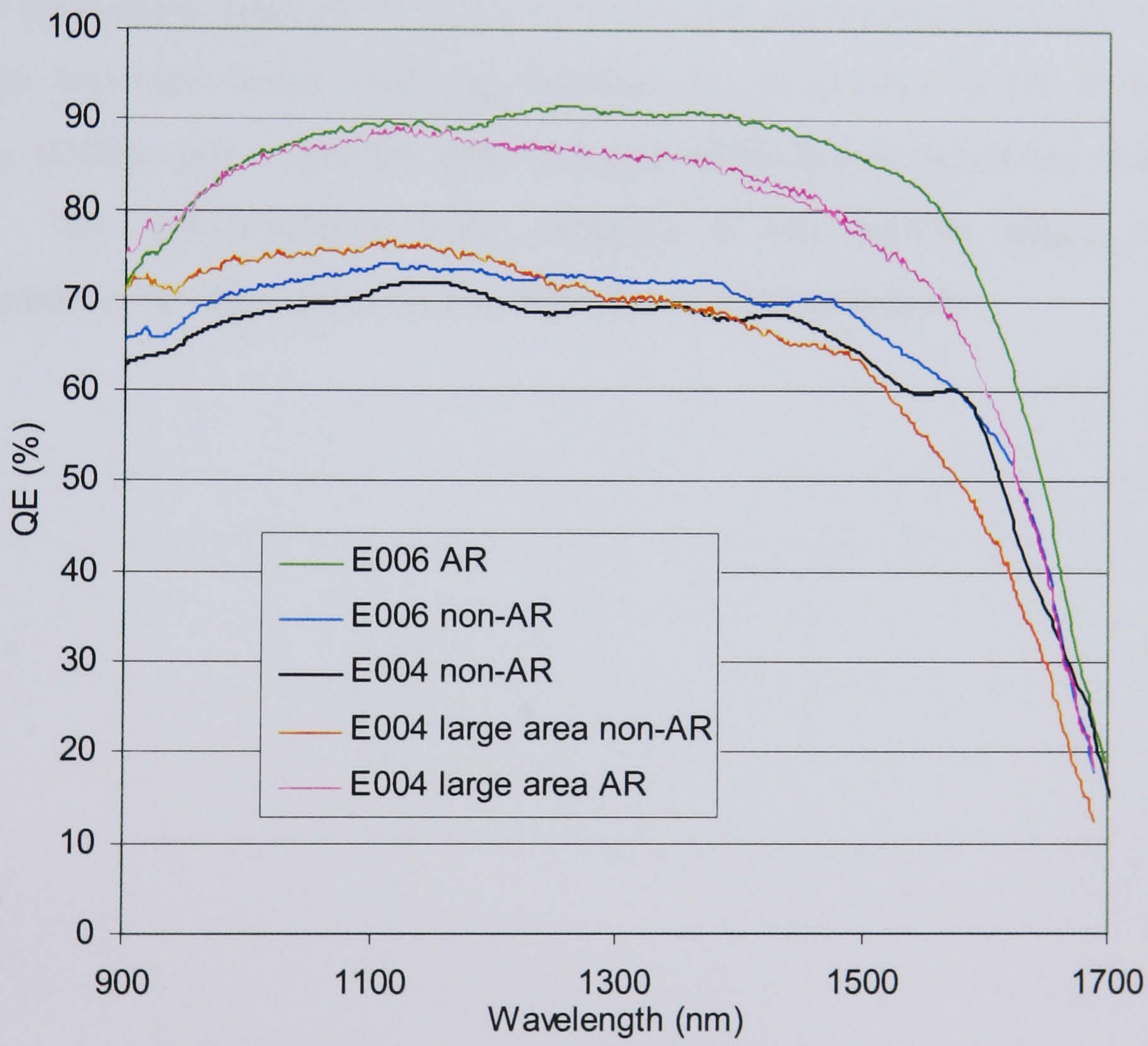

Figure 3.2: Quantum efficiencies of wafers E004 and E006 AR and non-AR samples.

The quantum efficiencies of wafers E004 and E006 AR and non-AR devices are shown in Figure 3.2. The results from the two wafers are very similar, with the AR coat clearly improving the response beyond 1000nm by almost 30%.

Figure 3.3 presents the reflectivity of E004 non-AR and E006 AR and non-AR devices, again showing how effective the coating is at reducing front surface reflective losses between 900-1700nm. An important feature of Figure 3.3 is that the reflectivity of E004 rises beyond the band-gap of InGaAs, at 1660nm. Included in the figure is the reflectivity of an air/InP interface, which is present at the front surface of the devices. This reflectivity is around 30% and above the band-gap the reflectivities of the non-AR samples are clearly dictated by this. However, at longer wavelengths when the absorption begins to decrease, the reflectivity of E004 shows that a proportion of the light is re-emerging from the device. There must therefore be a mirroring effect occurring at the rear contact, which was unexpected having not been observed on previous TPV devices grown and processed in Sheffield [2]. A rear surface reflector is important in TPV, as a second pass will allow more of the light to be absorbed. It will also allow unabsorbed photons to return to the source, increasing the overall efficiency. The reason why this below band-gap increase is not present in the E006 non-AR samples is unclear given that the only nominal difference between the wafers is the substrate. The semi-insulating E006 substrate is less heavily doped, and so its absorption would be expected to be less than that of E004 substrate.

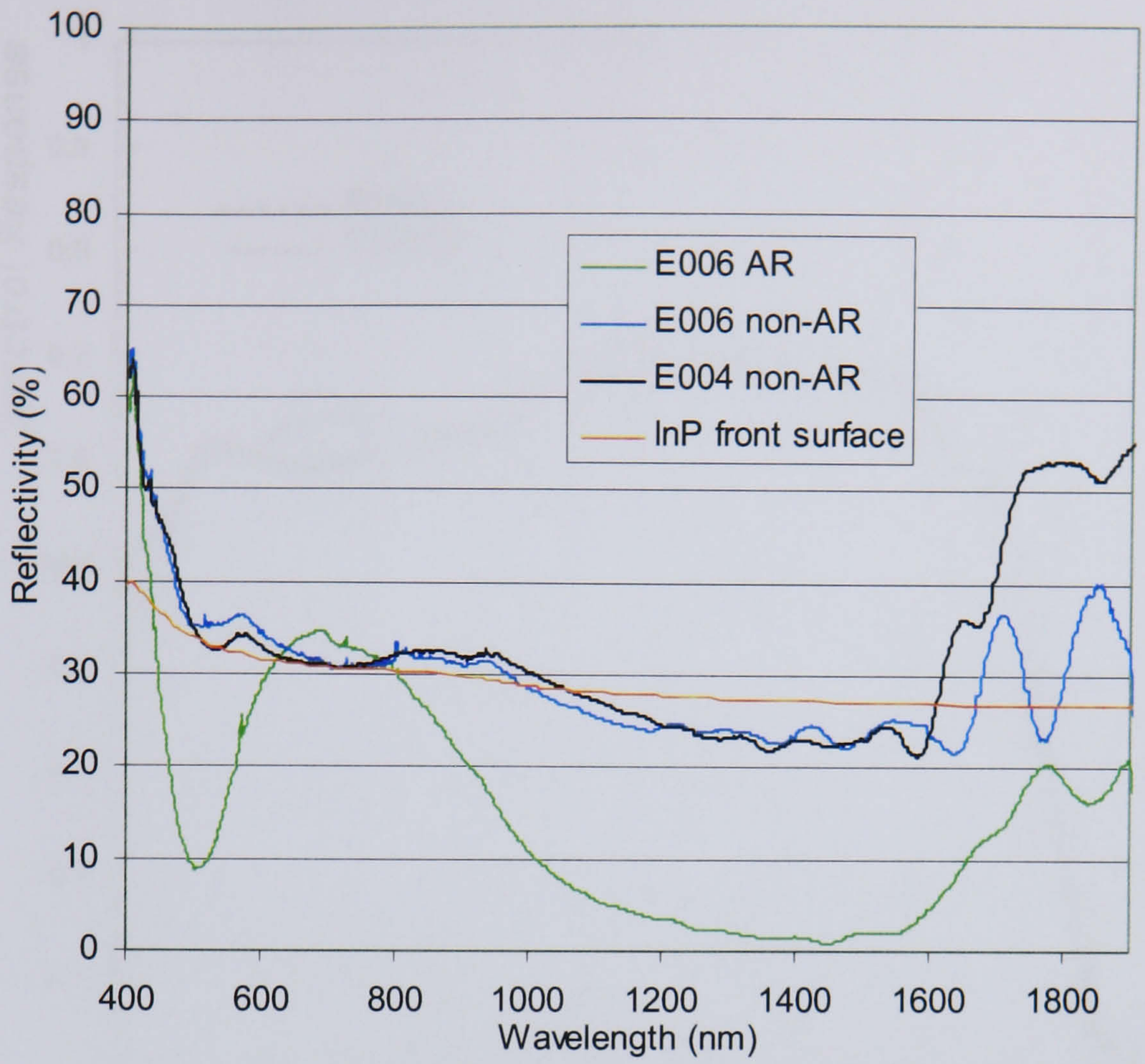

Figure 3.3: Reflectivities of wafers E004 and E006 AR and non-AR samples. The expected reflectivity from the InP front surface is included for reference. E004 AR is not present, as the device had been sent to Italy for further characterisation.

The magnitude of this rear surface reflection in E004 can be estimated using the author's model, as described in Section 2.2.6. Above the band-gap of the lattice-matched InGaAs the absorption is too great to model the reflection, but it can be found using a wavelength beyond the band-gap, 1800nm. The model uses an InP front surface and no absorption other than below band-gap absorption in the InP, which is discussed in Section 5.2.3. The measured total reflectivity of 53% can be obtained when the model includes a rear surface reflection of 45%. This result can also be duplicated using the modelling programme SOL [3]. Figure 3.4 shows a modelled quantum efficiency of the structure E004, compared to the experimental result. A rear surface reflection of 45%, found by the author's model, can produce a result that is consistent with the experimental data. An enhancement of quantum efficiency and reflectivity caused by the presence of a rear surface reflector is important as it will be found in a number of structures within this thesis.

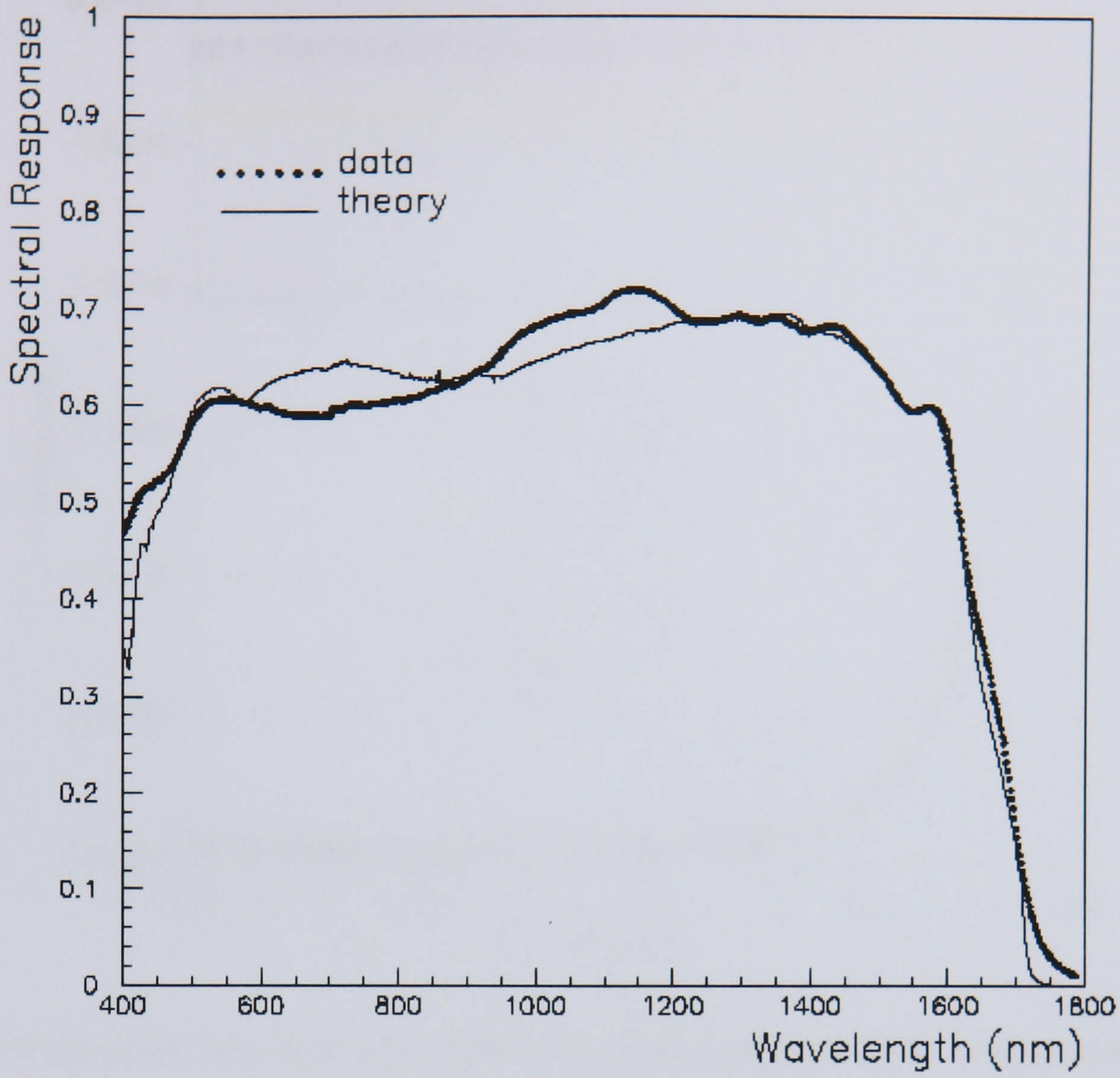

Figure 3.4: E004 quantum efficiency modelled with the programme SOL. A rear surface reflection of 45% and good minority carrier transport can produce a modelled quantum efficiency that is consistent with the experimental quantum efficiency.

Light I-V measurements under erbia-like illumination were taken from E004. Figure 3.5 shows a number of such measurements, with varying intensity. As is to be expected from good light I-Vs, the fill factor increases with the intensity. Using the parameters fitted from the dark current, the form of the light I-V has been predicted for the highest measured short-circuit current. This is also shown in Figure 3.5. The closeness of the prediction indicates that the light I-V can indeed be predicted directly from the dark current at these intensities; this is known as additivity. The success of additivity will be tested further in this thesis, both for different structures and at high intensity illumination.

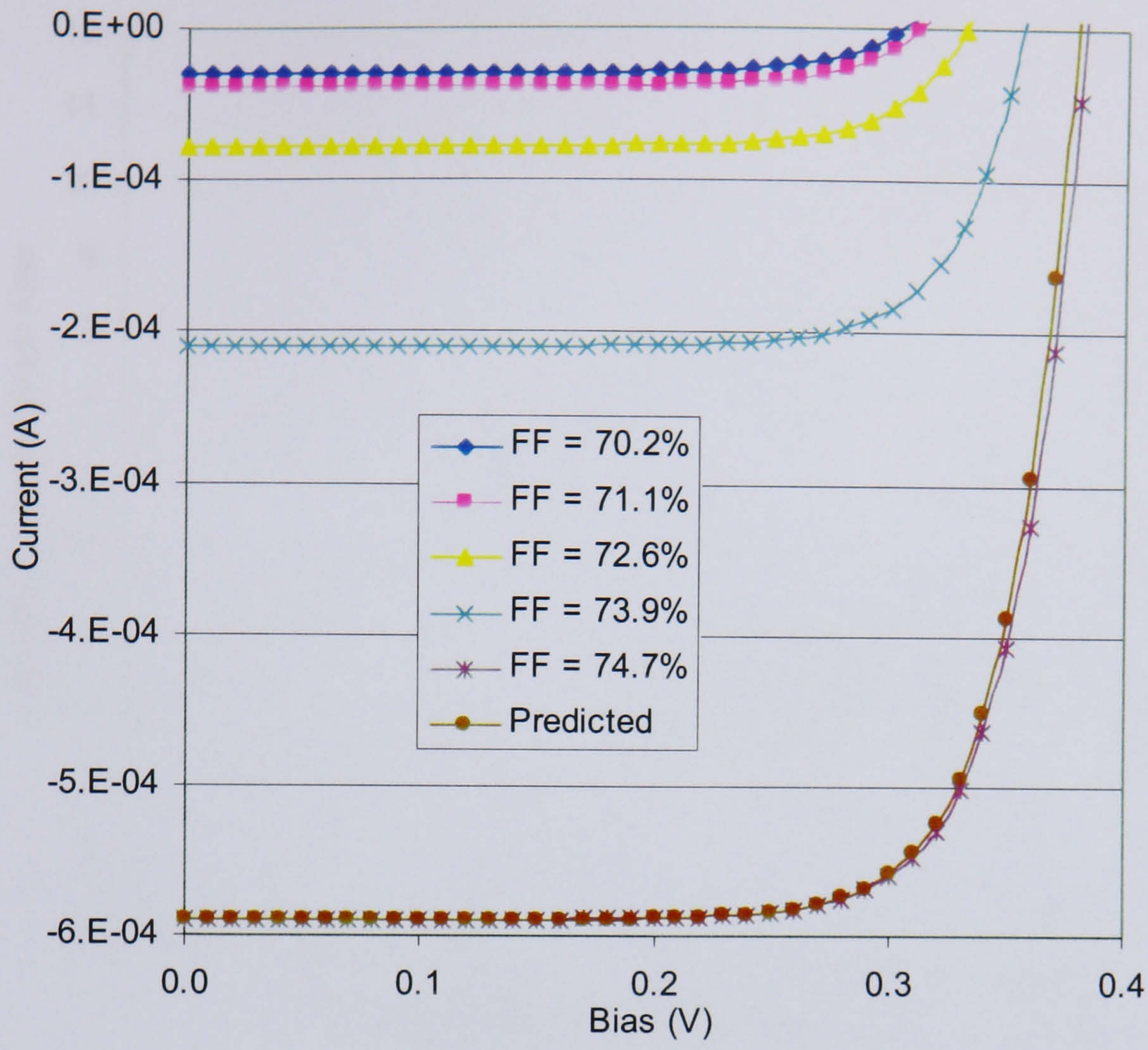

Figure 3.5: Varying intensity light I-Vs of E004 under erbia-like illumination, with their fill factors. Also included is a light I-V predicted for the highest short-circuit current, using the fitted dark current.

Using a measured erbia emitter spectrum and measured quantum efficiency, the short-circuit current at a given incident power density can be calculated (see Equation 1.3). For each light I-V the measured short-circuit can be assumed to be proportional to the power density falling on the device. Therefore, a plot of efficiency against power density can be produced. Shown in Figure 3.6, the data from the five measured light I-Vs can be used to predict efficiencies at higher intensities. The left hand axis gives the measured efficiency of the small area devices. Allowing for the metallisation of these devices being 59.6%, and for large area devices around 15.7%, roughly a third of that for small area devices, predicted efficiencies for large area devices are also shown.

From Figure 3.6, it is predicted that cell efficiencies above 30% can be produced for power densities above $30kWm^{-2}$, provided that series resistance can be minimised for these high current levels.

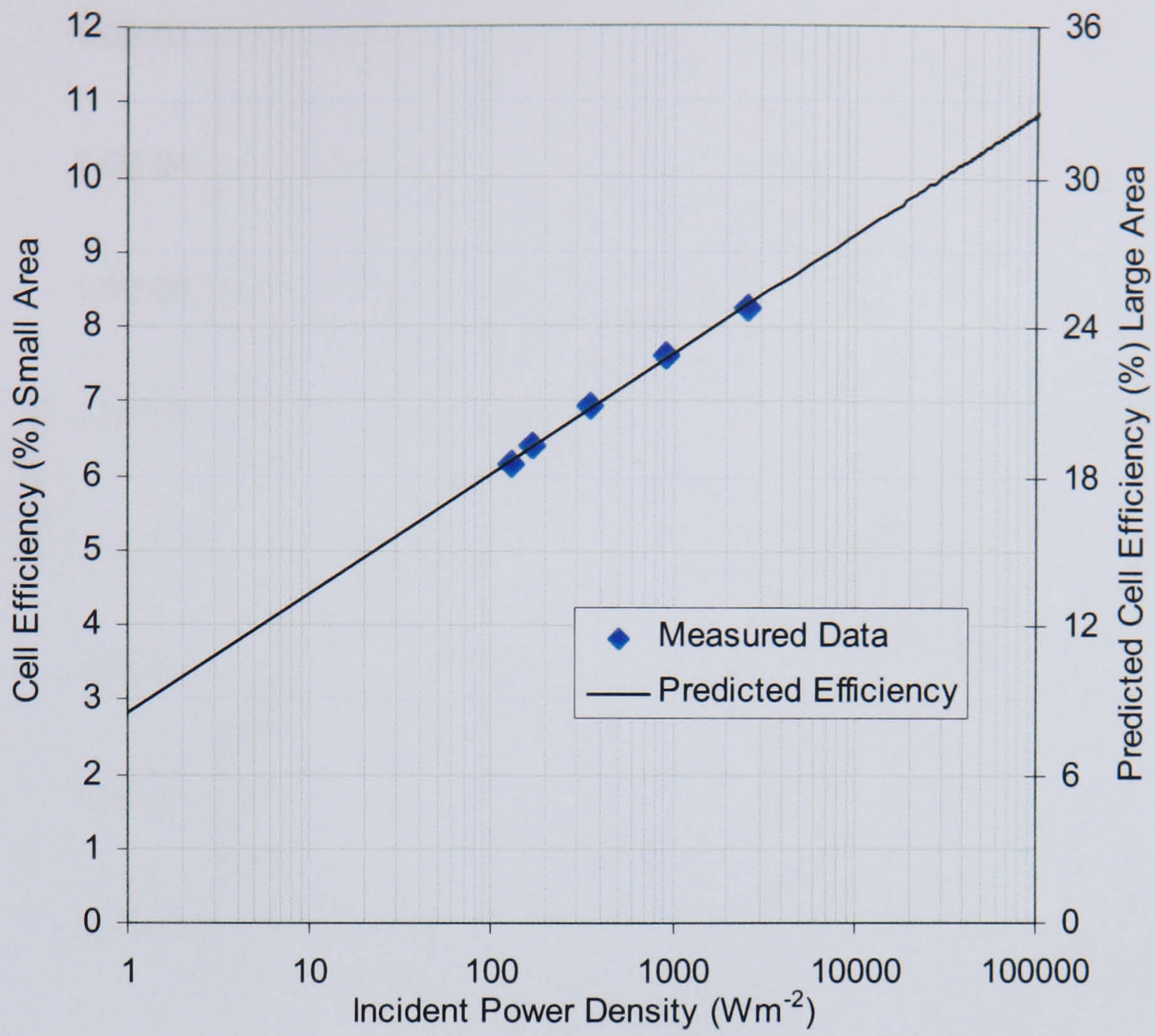

Figure 3.6: Efficiency of E004 at varying incident power densities. The left-hand axis is measured efficiency of small area devices. The right-hand axis gives a predicted efficiency for large area devices, which have around three times less metal coverage.

3.1.2. Wafers E005 and E007

Wafers E005 and E007 were identical in structure to E004 and E006 except for the inclusion of a quaternary etch-stop layer, intended as an aid to top-contacting, which is required when using an SI substrate. E007 and E005 had n-type and SI substrates respectively. Small area devices only were produced from this structure, all of which were without an AR coating. Many E005 devices were received and these show a large spread in dark currents, whereas only four E007 devices were received. Figure 3.7 shows the lowest dark currents of the two wafers compared to the best device from E004.

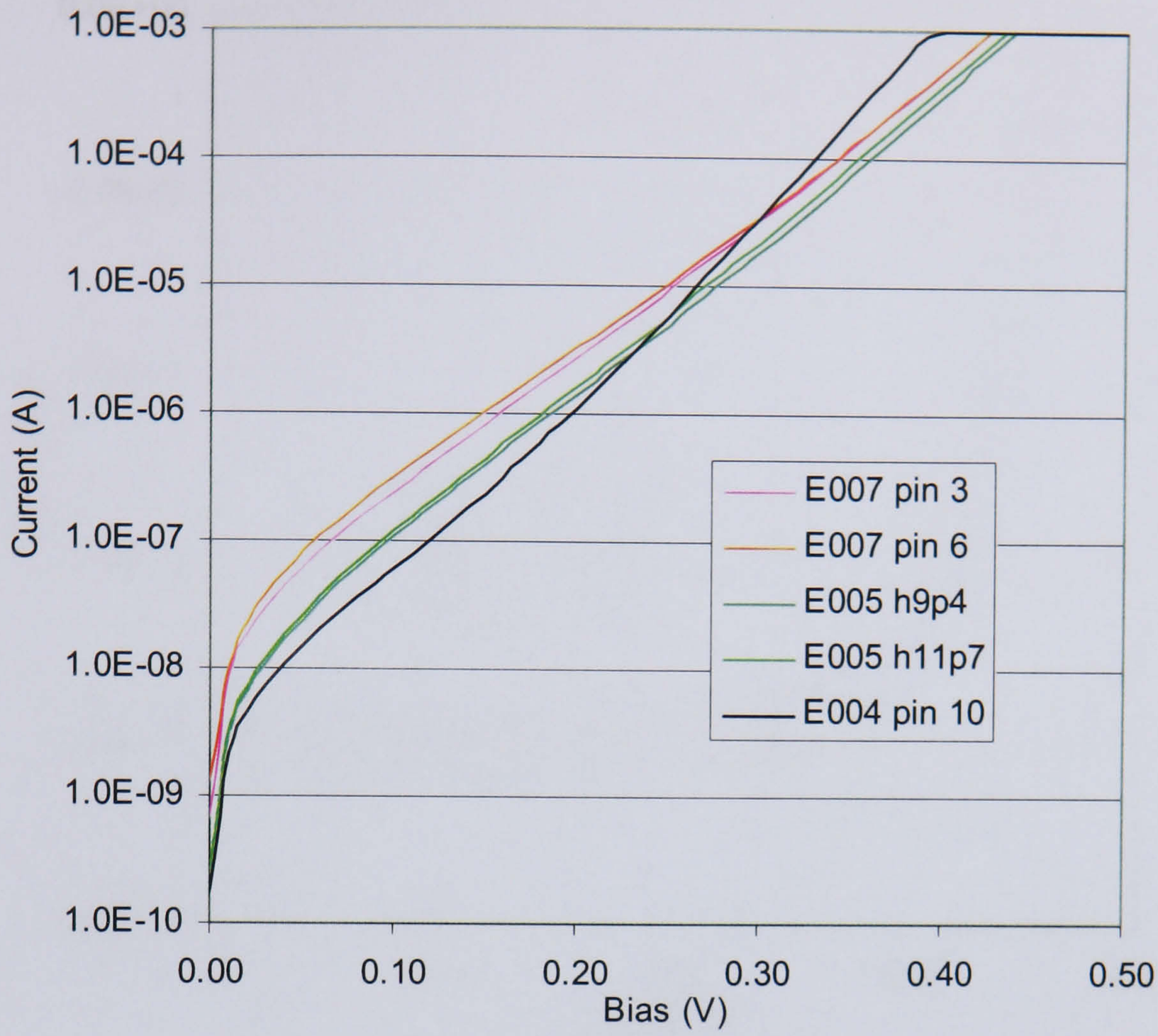

Figure 3.7: Dark currents of wafers E005 and E007 compared to E004.

The light I-Vs taken under 3000K blackbody illumination of the best devices from each wafer are shown in Figure 3.8. For comparison, also shown is the result taken under the same spectrum from E004, with a similar short-circuit current. That the dark currents and the light I-Vs are of similar shape and level shows the inclusion of the quaternary layer has not affected the device performance significantly. This is also confirmed by the quantum efficiency, which was measured and found to be the same as E004.

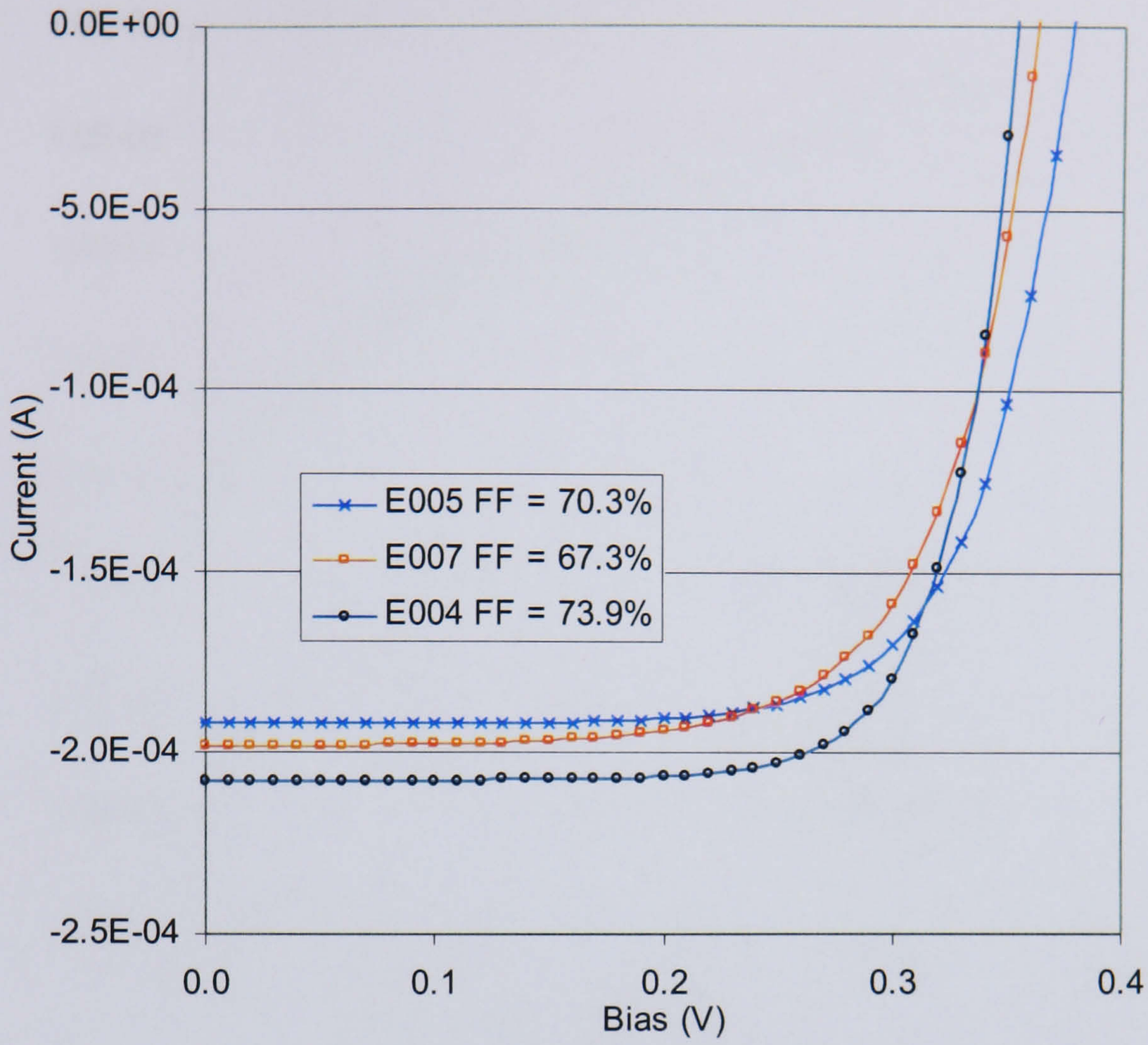

Figure 3.8: Light I-Vs of E005 and E007 devices under 3000K blackbody illumination.

3.1.3. Wafer E008

Wafer E008 was designed to investigate p-i-n structures. The p- and n- regions were a lattice matched composition of quaternary InGaAsP rather than InGaAs as in the previous structures. This was in order to reduce the dark current with higher band-gap materials but to continue to use InP as a higher band-gap window layer. In order to avoid zinc diffusion and maintain a low level of background doping in the i-region a quaternary buffer layer was added between the p- and i- regions. For this structure, only n-doped substrate was used.

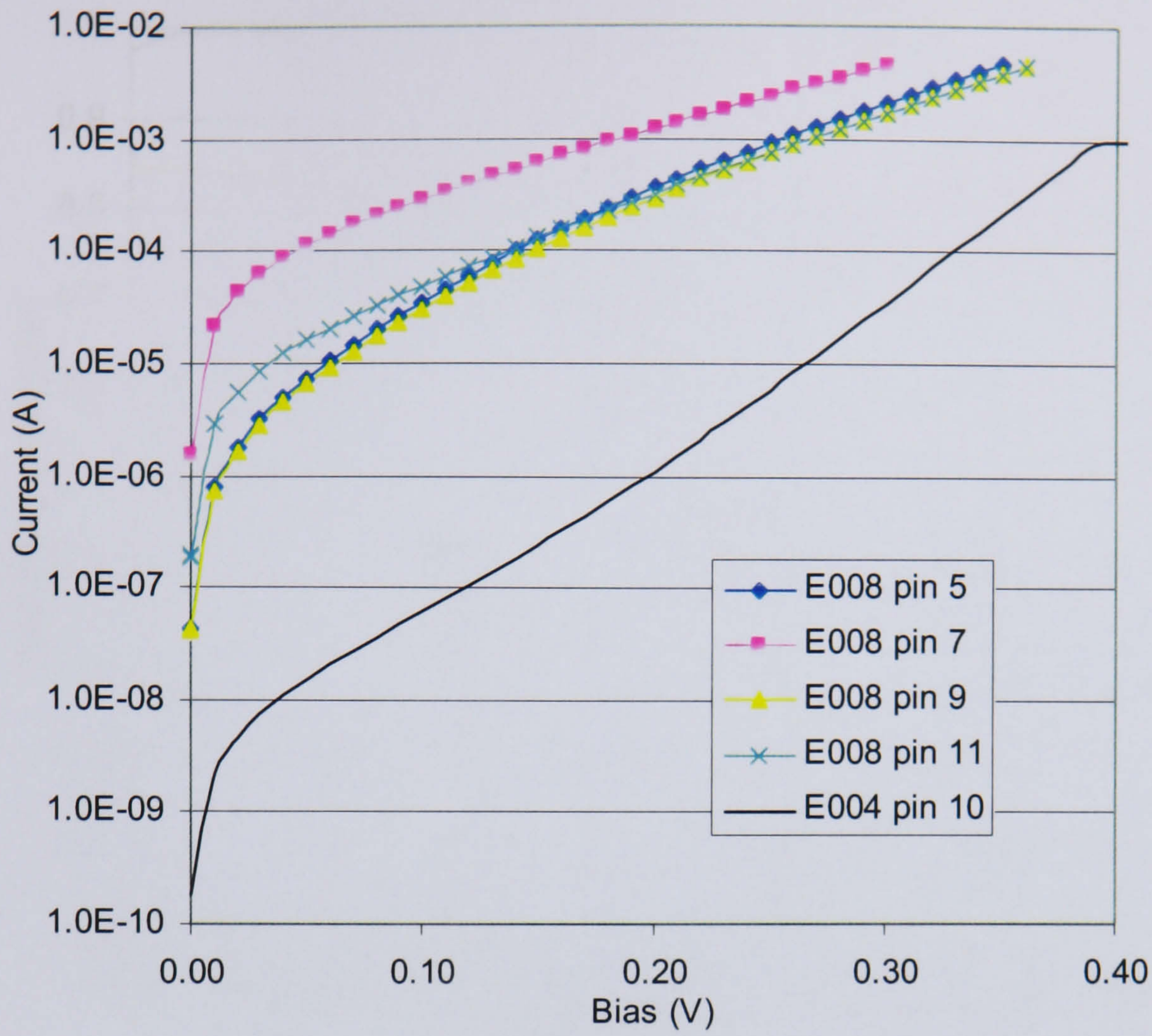

Figure 3.9: E008 dark currents compared to E004.

Again, only four devices were received but, as Figure 3.9 shows, the lowest dark current from E008 is much higher than that of E004, indicating a drastic decrease in device quality. Figure 3.10 compares the monochromatic I-Vs of E008 and E004 at 1200nm. The decrease in current indicates that the electric field across the active region is failing as the device moves into forward bias, leading to a severe reduction in collection efficiency. This apparent background doping in the i-region and the high level of dark current could be connected to the presence of thick quaternary layers, which is the main difference between this and previous structures.

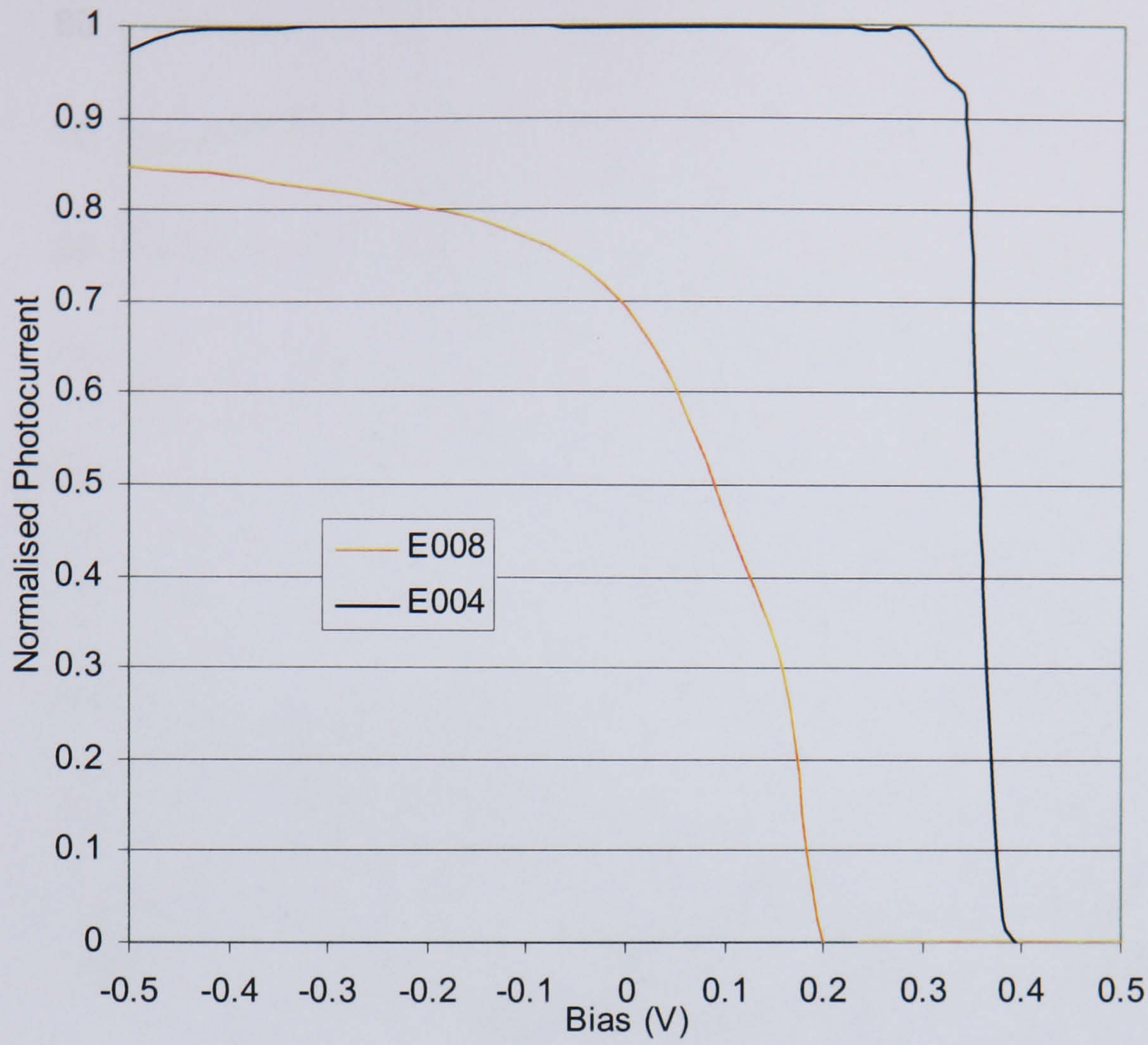

Figure 3.10: Monochromatic I-V of E008 at 1200nm. Compared to E004 there is poor carrier collection indicative of a failure to maintain the electric field in the active region.

The effect of poor carrier collection in E008 is well illustrated in Figure 3.11 where the quantum efficiency is measured at various applied biases. As described in Section 1.1.2, photovoltaic devices operate in forward bias and it is apparent that the performance of E008 would be seriously affected by such a poor response.

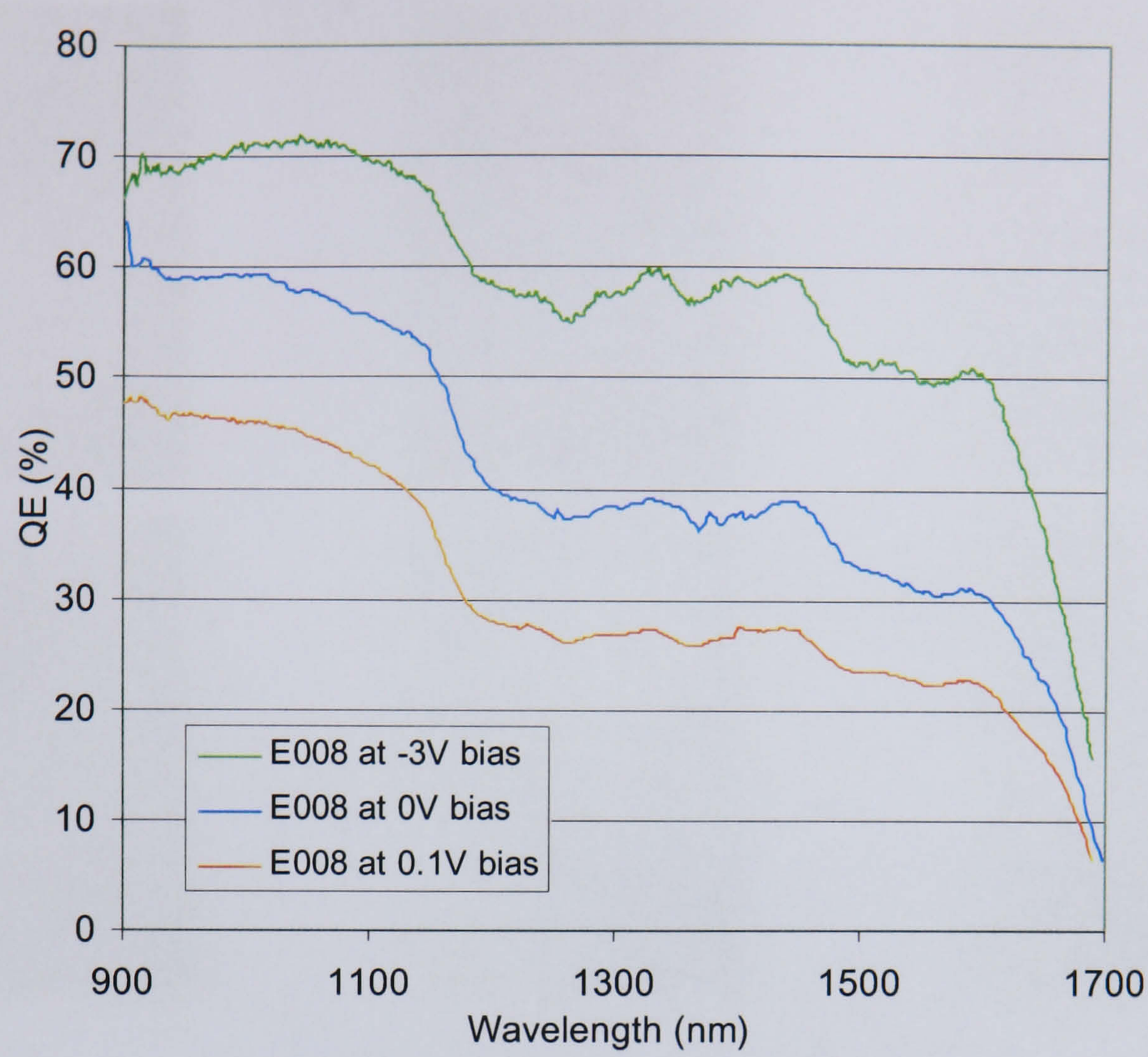

Figure 3.11: E008 quantum efficiencies at varying applied biases.

In conjunction with the devices processed for Imperial, NMRC also processed and measured a number of other small area E008 devices. As is described in Ref. 4, they also found dark currents to be much higher than E004. To investigate this, they then etched away the top InGaAs and InP layers in order to perform photoluminescence (PL) on the quaternary junction. They found an intense luminescence peak suggestive of good quality material, but during etching of the next few layers they observed what was described as a 'milky' layer. This was investigated further by etching slowly. Figure 3.12 is taken from Ref. 4 and describes what was seen during etching. This experiment was not performed on any other sample to compare quaternary layers, but the layers seen here certainly indicate less than ideal growth, which could be the cause of the poor I-V characteristics.

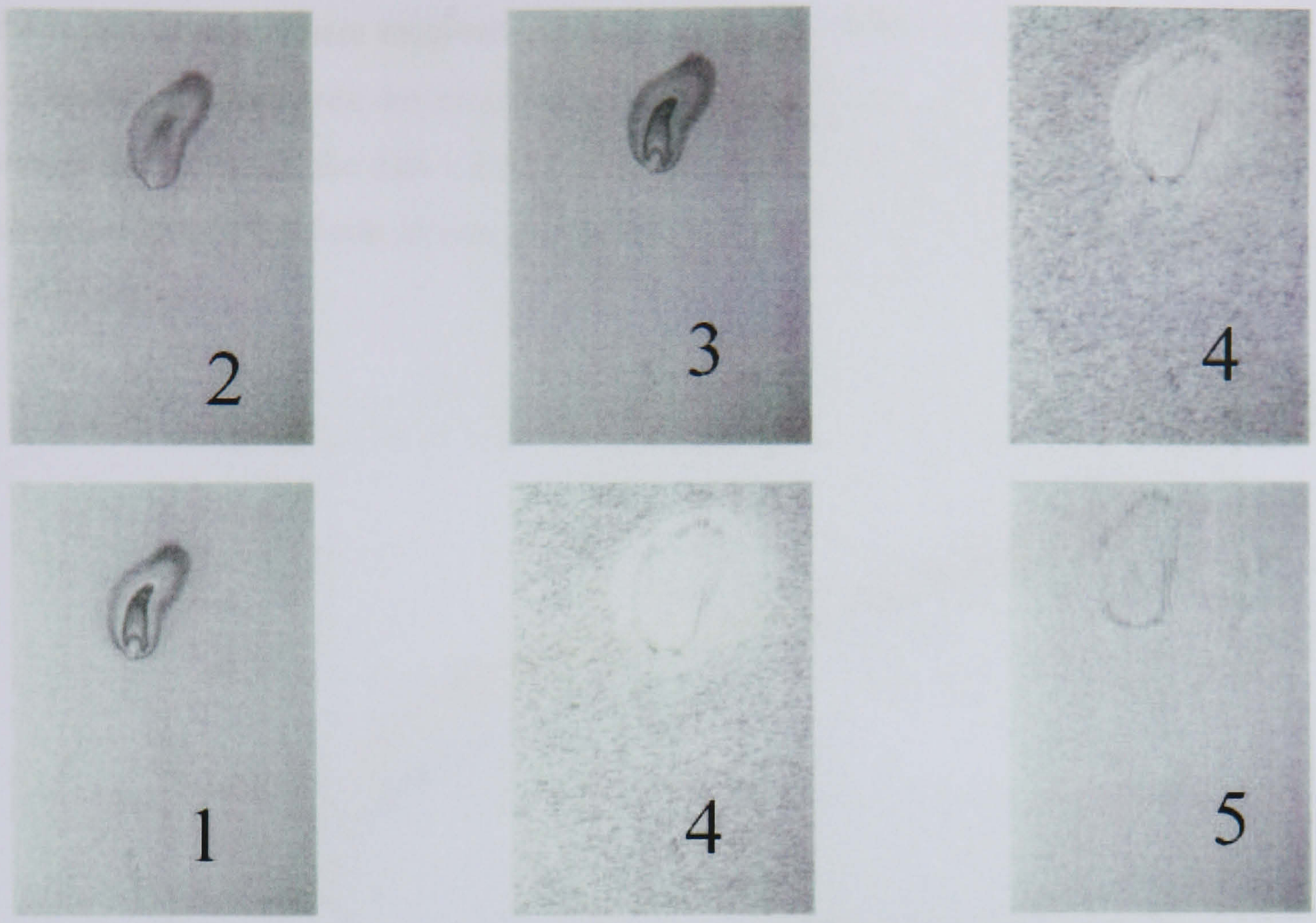

The key is as follows:
1: Surface as grown. A large defect is shown to facilitate focussing
2: Surface after removal of InGaAs (layer 8)
3: Surface after removal of InP (layer 7)
4: Surface on appearance of 'milky' layer. The surface was etched in 3:1:1 as above which is selective for InGaAsP, InGaAsP over InP. The etch rate of 1.1um InGaAsP is approximately 2.5nm/s. Using step heigh measurements the appearance of this layer corresponds to the interface between layer 4 and 5.
5: Surface after continued etching in 3:1:1. It takes 20-30 seconds to penetrate the milky layer following which a high quality surface is obtained.

Figure 3.12: Etch study of wafer E008 conducted by NMRC with explanations of each picture, taken from Ref. 4.

3.1.4. Wafer E014

E014 was based on the successful E004, with a few changes. The p-region doping was reduced in order to lower unwanted sub-band-gap free-carrier absorption in the p-region. The width of the n-region was increased in an attempt to increase absorption in the range of the erbia emitter. Also, the InGaAs lateral conduction layer was removed. This conduction layer is only necessary when using the MIMs technique, but it had been decided that the technique would not be used for the 18-month deliverable. Devices

from this structure were received in three separate batches. The first batch consisted of a number of small area devices, and a 5mm device mounted on a TO5 header. There was some spread in the dark current densities of the small area devices but those of the two best and of the 5mm device are shown in Figure 3.13. Also displayed is E004 for comparison.

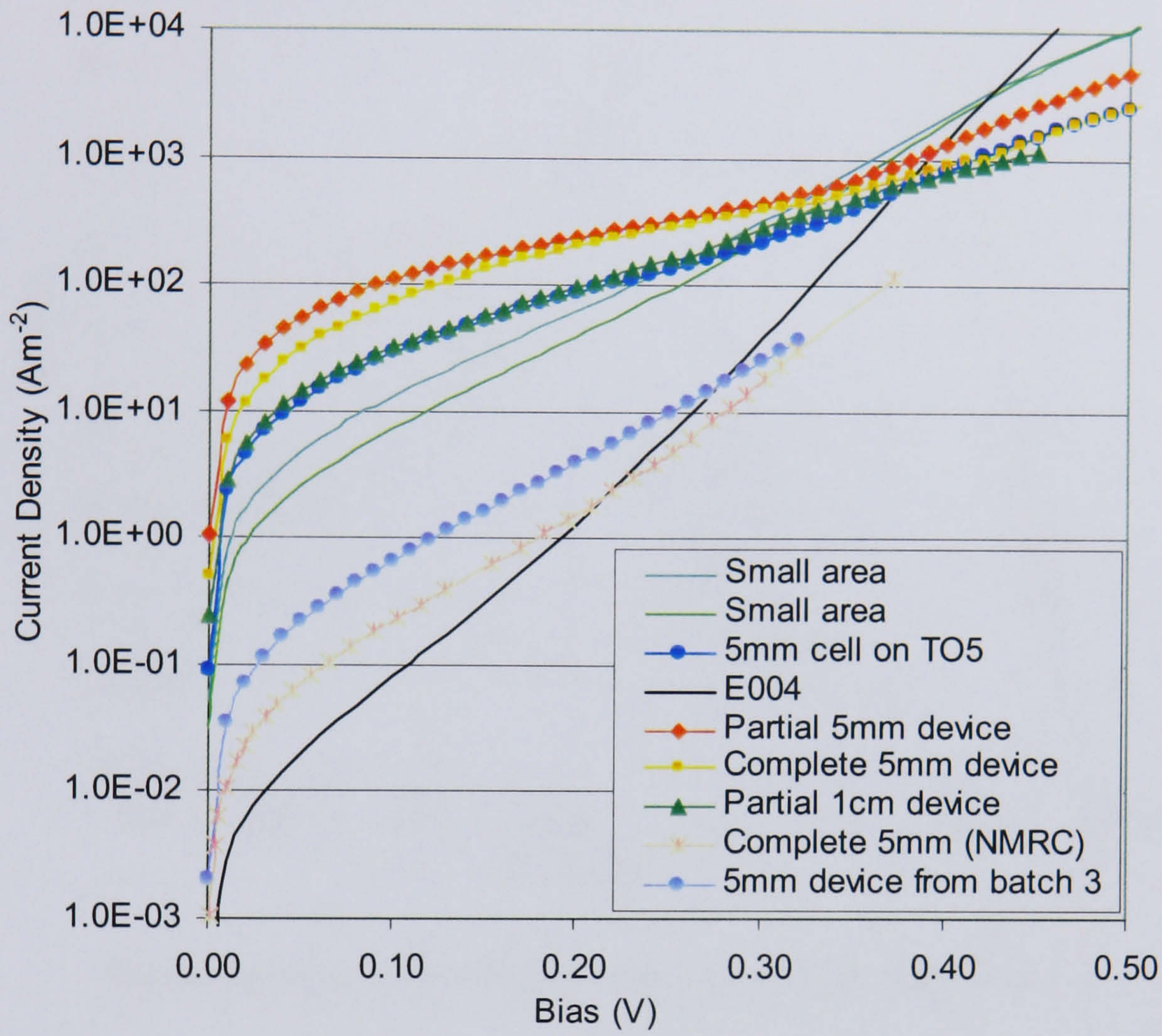

Figure 3.13: E014 dark current densities.

The second batch received was a single piece of wafer containing a complete 5mm device, a partial 5mm device and a partial 10mm device. The dark currents of all three devices were measured by probing and the results are also shown, along with a measurement of the complete 5mm performed by NMRC prior to delivery. Although the measuring techniques at Imperial and NMRC may vary, the results appear to indicate a worrying deterioration in the dark current between the measurements, over a timescale of only a few weeks.

The third batch was two separate pieces of wafer, each containing a 5mm device. These devices were measured on arrival and again after 24 hours. Although the initial results

were promising (purple circles in Figure 3.13), again later deterioration in dark current was evident. This is likely to be strongly linked with a problem experienced with the adhesion of the rear contact metal.

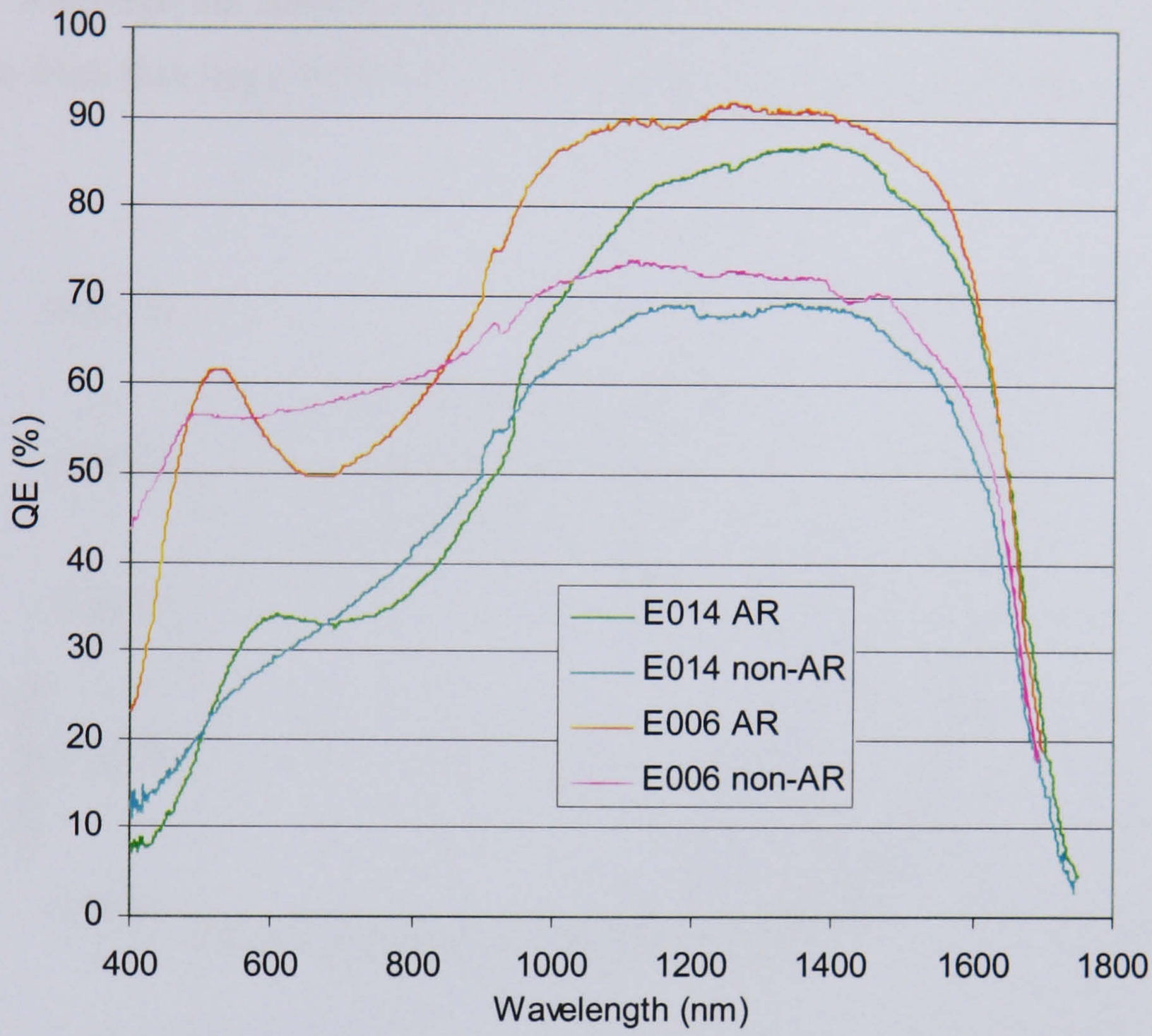

Figure 3.14: Quantum efficiency comparison of E014 and E006.

Figure 3.14 compares the AR and non-AR quantum efficiencies of E014 with those of E006. The short wavelength response from the first structure has been degraded. A reduced doping density results in a higher minority carrier diffusion length, which would be expected to increase the response in the region. Fortunately, in TPV and particularly THE REV, the shorter wavelength performance of the device is less important as the majority of the emission is at longer wavelengths (see the measured erbia spectrum in Figure 3.24). Also, the response at longer wavelengths is comparable to that of the initial structure but is no higher, which suggests that the thicker n-region has not contributed an increase in photocurrent. The reflectivities of E014 devices are shown in Figure 3.19. The E014 AR coat appears to be a little thicker than in E006, given that the minimum is at a longer wavelength, but otherwise the reflectivities are comparable, which suggests that the loss in response is due to material problems.

The apparent problems in this wafer have also extended to poor light I-V performance. Two 3000K light I-V measurements from E014 small area devices are shown in Figure 3.15, alongside an E004 measurement. The fill factors are greatly reduced in this structure. Although not shown, one of the 5mm devices was also measured. The light I-V results from this larger area device was of much poorer quality than the small area devices.

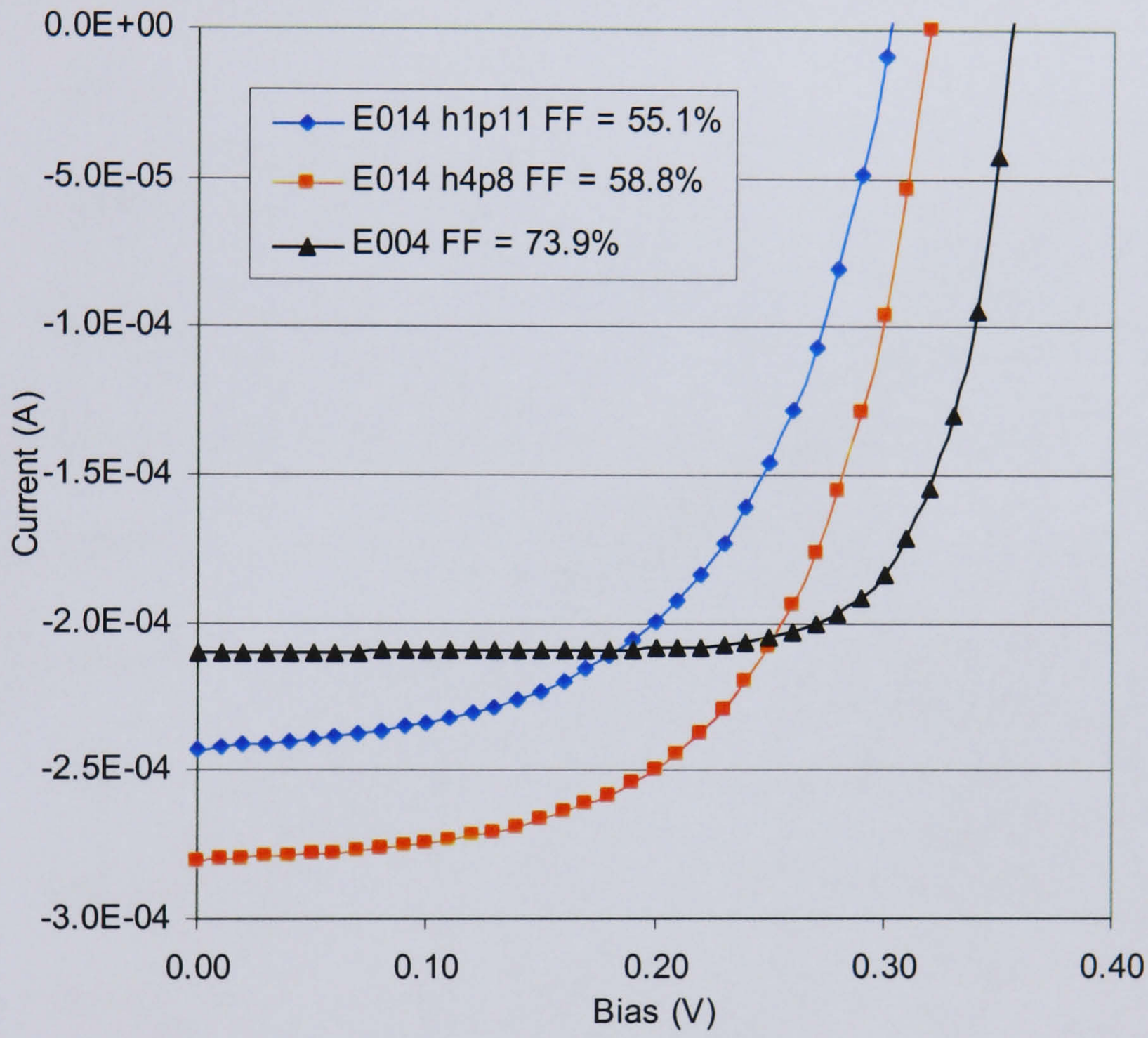

Figure 3.15: 3000K blackbody light I-Vs of E014 small area devices. The fill factors are much lower than from E004.

3.1.5. Wafer E015

E015 was designed in light of the loss of performance seen in E014; the p doping was returned to the higher level of E008 and the cap layer thickness was increased three-fold. The cap layer was thickened in an attempt to provide better contacting and reduce the associated series resistance. The first samples received were small area, mostly AR

coated. Secondly, there were two 1cm devices, mounted on copper blocks, one of which was AR coated. It was necessary to bond these devices as described for large area devices in Section 2.1. Finally, there were two 5mm devices on one piece of wafer. This also required mounting on copper and bonding. The lowest dark currents from the small area, 5mm and 1cm devices are shown in Figure 3.16, along with E004 for comparison. The results of fitting the small area and 1cm devices are also shown in Figure 3.16, with the values given in Table 3.2. For both devices, the ideality factors were fixed at n=1 and n=2.

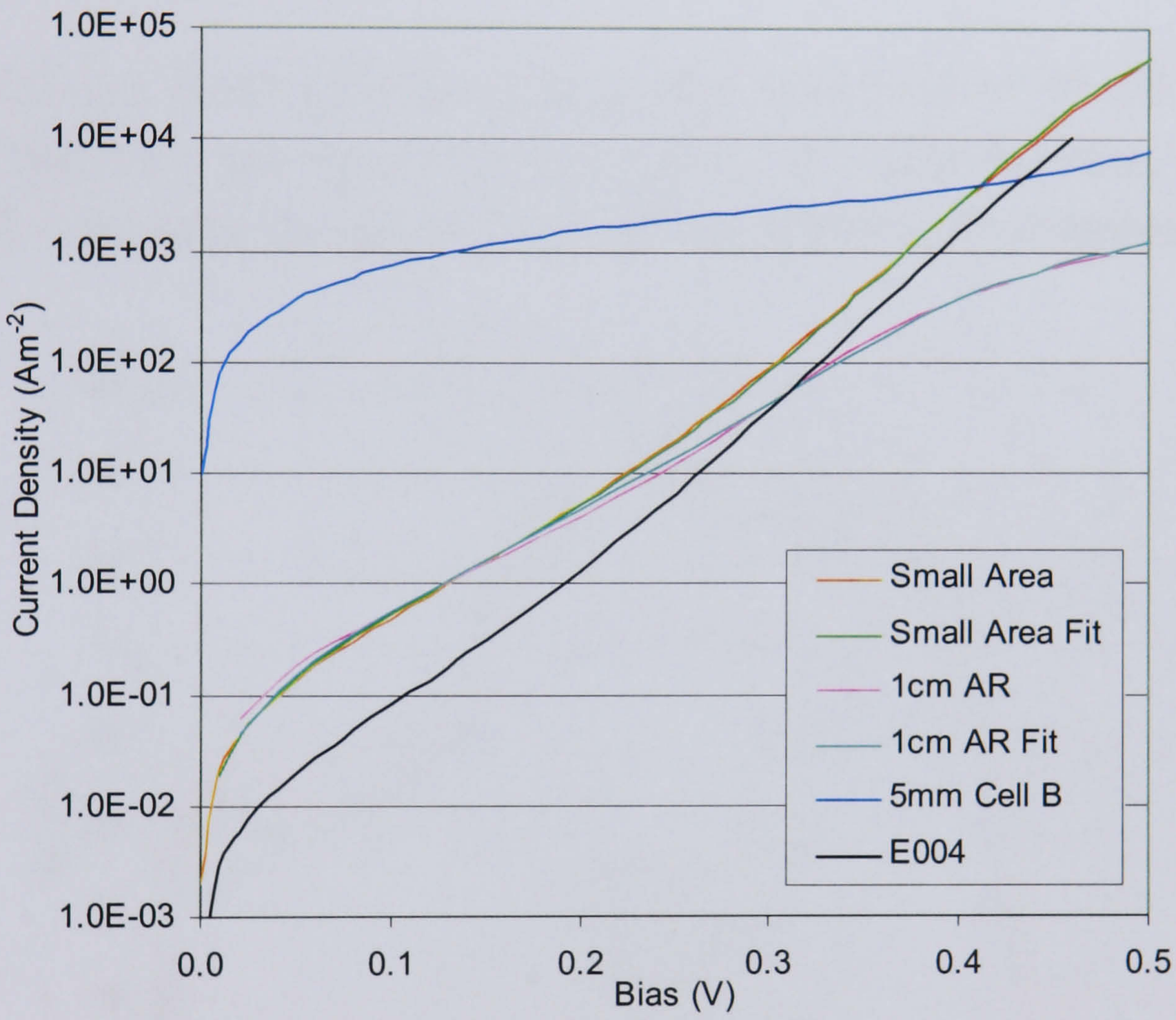

Figure 3.16: Dark currents of all the sizes of E015 devices, compared to E004.

Device	Ideality n_1	Saturation current J_{o1} (Am^{-2})	Ideality n_2	Saturation current J_{o2} (Am^{-2})	Series resistance R_s (Ω)	Parallel resistance R_p (Ω)
Small area (red line)	1	5.10E-4	2	8.53E-2	0.54	1E+30
1cm AR (pink line)	1	2.25E-4	2	0.72E-1	0.96	7.68E+3

Table 3.2: Results of fitted dark currents of E015 devices from Figure 3.16.

There was little spread in the small area dark currents. The lowest level is slightly higher than the best device of E004. The extracted series resistances when compared with 1.90Ω from E004 in Table 3.1 suggest that the thicker cap is working and that series resistance problems at high intensities can be reduced. The 1cm devices appear to be suffering from problems with parallel resistance, possibly connected with the mesa etching of large area devices. This problem is also clear in the case of the 5mm devices. However, the parallel resistance of the AR 1cm device is appreciably lower than the non-AR device, suggesting that there may have been some passivation of the mesa edges and a reduction in recombination there.

Figure 3.17 is a comparison between the quantum efficiencies of AR and non-AR samples from E015 and those of the wafer E006. The results are almost as good, especially at the shorter wavelengths where E014 had suffered a loss of response.

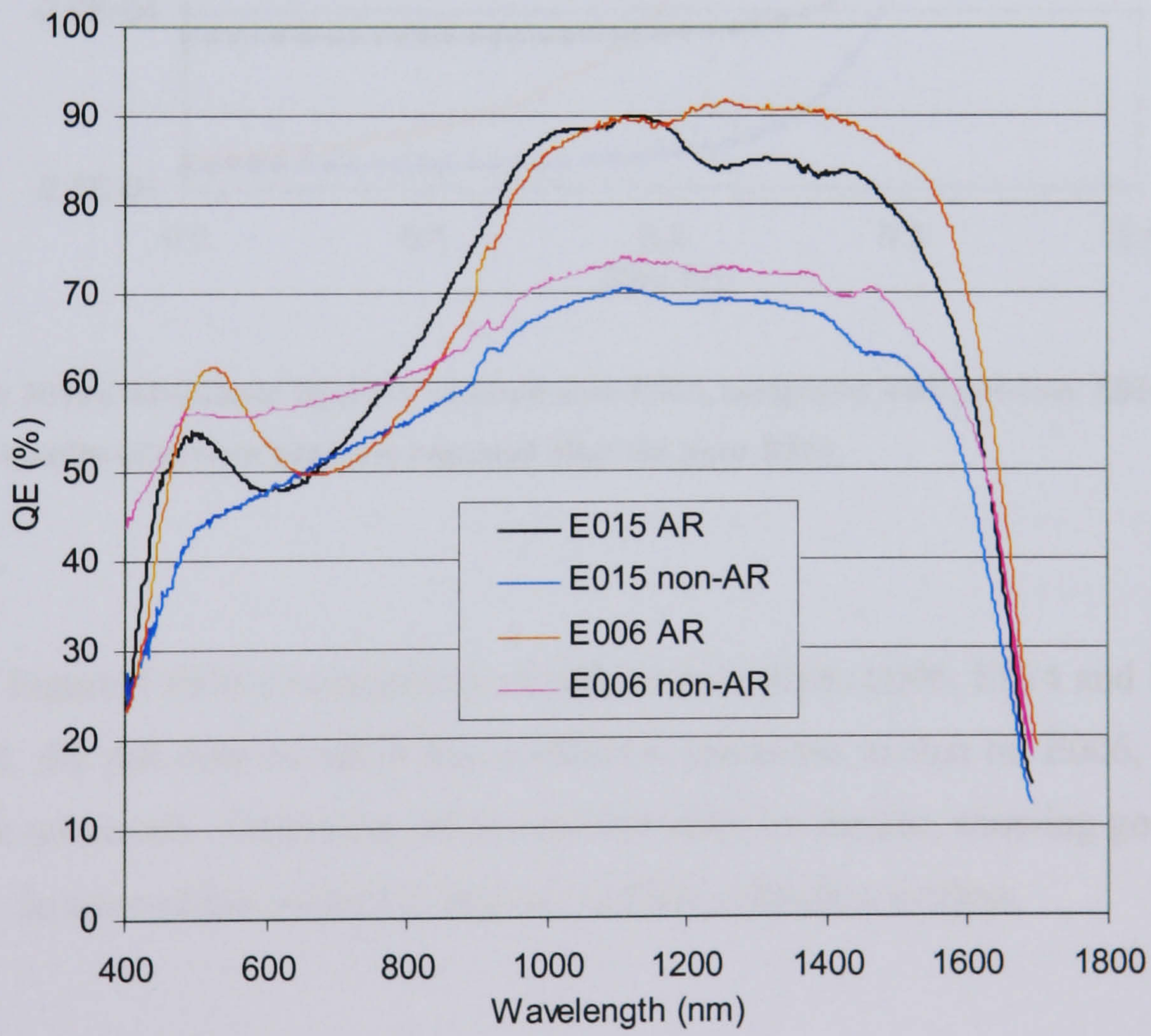

Figure 3.17: Quantum efficiency comparison of E015 with E006, the original structure.

The recovery in E015 performance compared to the E014 structure is also shown in the light I-V measurement. Figure 3.18 displays 3000K blackbody light I-Vs from E015,

E014 and E004, and it can be seen that the good characteristics, including fill factor have been regained.

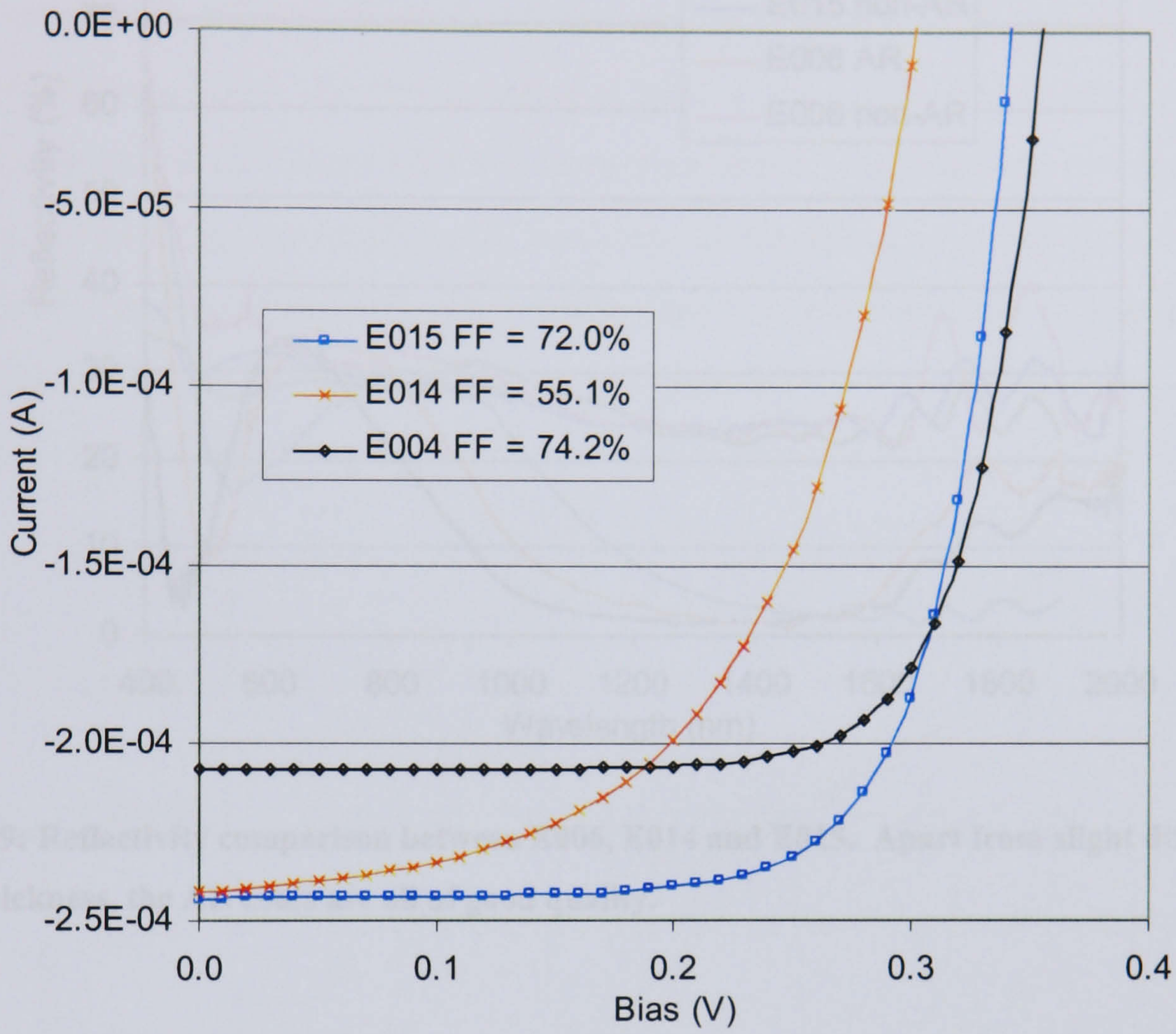

Figure 3.18: 3000K blackbody light I-V of small area E015, compared with previous E014 and E004. The quality of devices has been regained after the poor E014.

Shown in Figure 3.19 is a comparison of reflectivities from E006, E014 and E015. As with E014, the AR coat on E015 has a different thickness to that on E006, causing a shift in the minimum. Otherwise, all the reflectivities are similar, showing good quality AR coats. In none of the devices is any rear surface reflection evident.

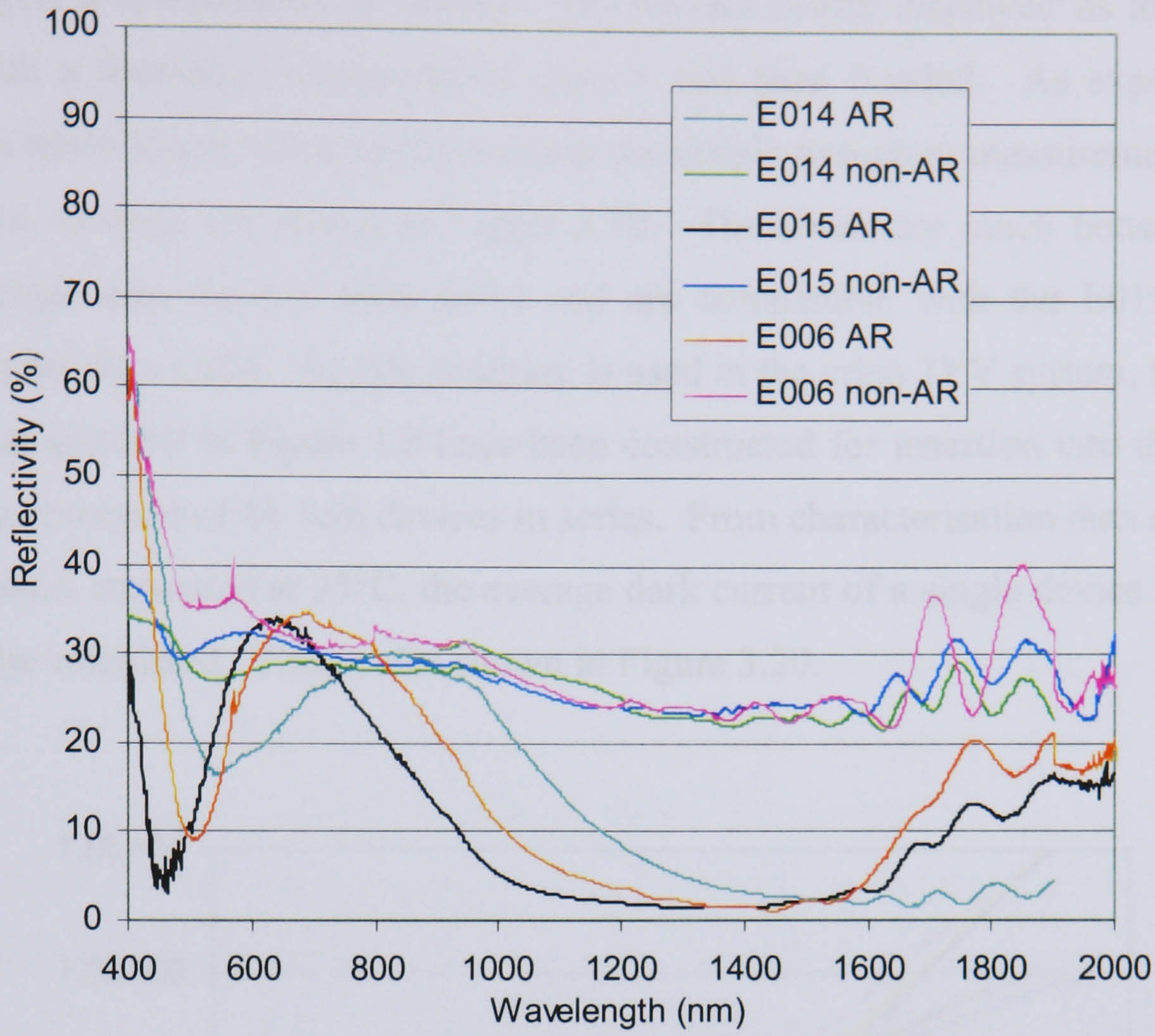

Figure 3.19: Reflectivity comparison between E006, E014 and E015. Apart from slight differences in layer thickness, the AR coats are all of good quality.

3.1.6. Wafer E042

Wafer E042 is the structure which was decided upon for the 18-month erbia-based demonstrator system. In view of the lack of notable success of the previous structures to improve upon the characteristics of E004, this structure is a 'near repeat' of E004. The only differences were the thicker top contact layer and the removal of the lateral conduction layer. All E042 devices were processed by RWE in Germany. The only devices received of this structure were two 1cm devices, mounted on copper discs. Measurements could be obtained from these devices either by probing or by bonding using the gold plated stripboard described in Section 2.1.

The lowest dark current achieved with the first device was the initial two-point probed measurement. This level of dark current could not be replicated with further measurements, even with four-point measurements once the device was bonded, which

could suggest a deterioration in quality. The second device displayed its lowest dark current with a four-point measurement once it had been bonded. As expected, this produced a much lower series resistance than the simple two-point measurement. These lowest dark currents are shown in Figure 3.20. The levels are much better than the previous large area devices from E014 and are comparable with the E015 devices, slightly higher than E004. As this structure is used in the erbia TPV system, two arrays such as that pictured in Figure 1.8 have been constructed for insertion into the system. Each array consisted of 46 1cm devices in series. From characterisation data of the first array received, measured at 35°C, the average dark current of a single device within the array can be calculated. This is also shown in Figure 3.20.

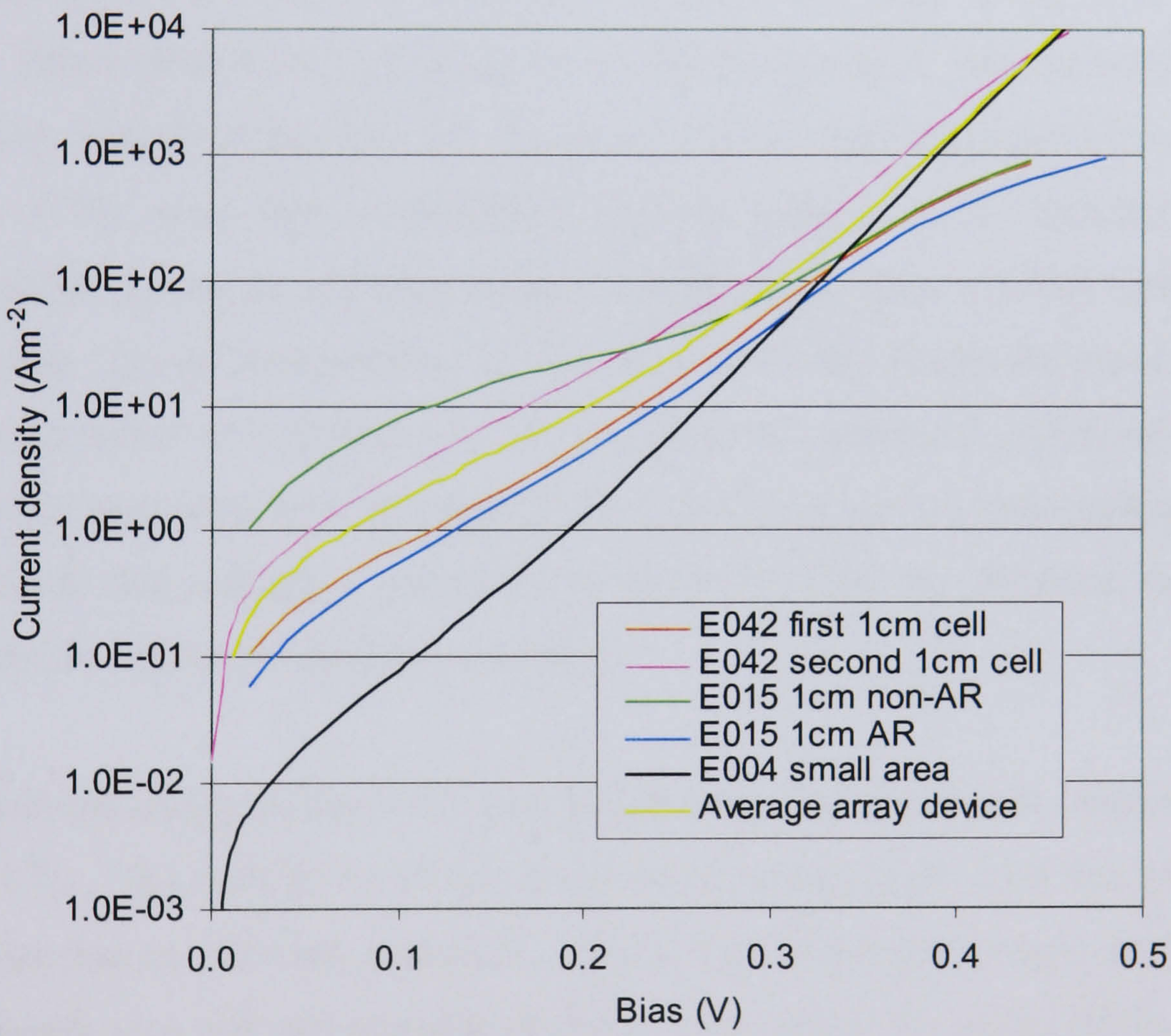

Figure 3.20: Dark currents of E042 large area devices, compared to E004 and E015. The average dark current of a single 1cm device from within the final system array is also shown.

The results of fitting the dark currents of the two E042 1cm devices and the average array device are shown in Table 3.3.

Device	Ideality n_1	Saturation current Jo_1 (Am^{-2})	Ideality n_2	Saturation current Jo_2 (Am^{-2})	Series resistance R_s (Ω)	Parallel resistance R_p (Ω)
First device	1	3.38E-4	2	7.88E-2	0.76	3270
Second device	1	3.45E-4	2	3.02E-1	0.02	997
Average system device	1	1.17E-4	2	1.06E-1	0.003	2040

Table 3.3: Results of fitting E042 1cm device dark currents and the average array device.

The saturation current levels of the two 1cm devices are comparable, as are the parallel resistances. However, the series resistance achieved in the array devices appears to be much lower than that in the test devices. At the current levels expected in the system (>1Acm^{-2}), the series resistances measured in the test devices are far too high to be practical. This will also have a bearing on the quality of results that can be achieved at high intensity with these test devices. However, for system performance it is the series resistance of the array that is important, and this appears to be satisfactorily low. Clearly, current travels by different routes through the devices for dark and light I-V measurements. It is to be hoped that the low array series resistance detected by the dark current measurement is indicative of a low overall series resistance within the array. As all the devices measured were processed in the same way, by the same processors, it is highly unlikely that changes in resistivity of the devices due to variations in geometry can explain the differences in series resistance.

The quantum efficiency of the E042 1cm device with the lowest dark current is shown in Figure 3.21. The reflectivity of the device is given in Figure 3.19, the low level of which shows that an AR coat is present. Also shown in the two graphs are the results for E006 small area AR and non-AR devices. The reason for using E006 instead of E004 is that no small area AR coated E004 devices were received, and E006 performed well enough against E004 to be used as the comparison structure.

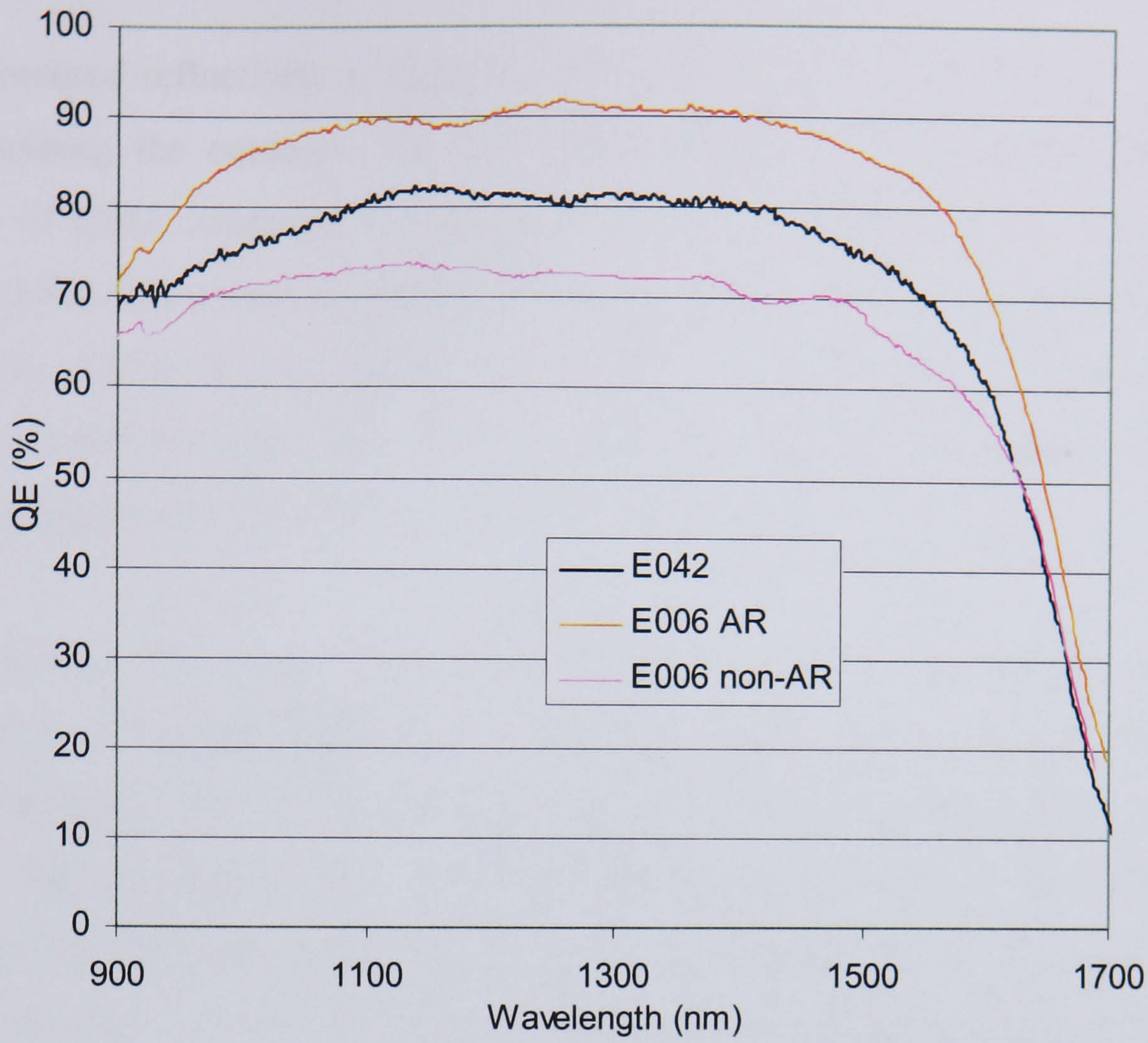

Figure 3.21: E042 quantum efficiency compared with E006. The E042 line lies between the AR and non-AR devices from E006.

The response of E042 lies between those of the AR and non-AR devices from E006. Knowing E042 to be AR coated, this could suggest that the response of the device is as good as E006, but for a proportion of light that is striking the contact fingers and being reflected. The grid finger pattern is shown in Figure 2.1. The reflectivity can be used to investigate this possibility.

The most positive aspect of the reflectivity is that it rises after 1600nm, suggesting the presence of a rear surface mirroring effect as was seen in E004. Also, ignoring that rise at longer wavelengths, the reflectivity has the appearance of a double layer AR coat instead of the single layer coat used previously. The normal AR coat of RWE, who are responsible for processing the devices for the final prototype system, is TiO_2 and Al_2O_3. Therefore a double layer AR coat of these materials on an InP substrate was modelled and is shown on Figure 3.22. The measured reflectivity was most accurately matched when the quarter wavelength thicknesses of the layers were 1200nm. This modelling of AR coats is discussed in more detail in Section 5.4.

As the measured reflectivity is higher than that modelled, the possibility remains that light is striking the contacts. If it is then assumed that the shortfall in quantum efficiency of E042 compared to E006 AR is due to reflection off the contact fingers then, taking the data points at 1400nm in Figure 3.21, the fingers must be blocking 11% of the beam. However, the high reflectivity of the contact metal would be expected to reflect the majority of that 11%, whereas the total reflectivity at 1400nm is less than 6%. This suggests that the material itself cannot be ruled out as a cause.

The reflectivity of the rear contact can be calculated using the model discussed in Section 2.2.6. If it is assumed that 11% of light is striking the contact fingers then the high reflectivity of that metal will result in around 9% of absolute reflectivity. The remaining 89% of light strikes the front surface of the device. At 1800nm, it is considered that the front surface has the reflectivity shown as the blue line in Figure 3.22 and that there is only absorption in the substrate. Using the author's model, the rear surface reflectivity needed to produce the actual measured reflectivity is 60%. This is different from the figure of 45% found for E004, but as the exact reason for the presence, or absence, of this reflection is unclear it should be sufficient to remark that the reflection itself, when it has appeared, has been extremely beneficial to the performance of those particular devices. It is agreed by both the author's model and SOL that a hitherto absent rear surface reflection is present in a number of THE REV devices, with values of 45-60% being agreed upon for its magnitude.

It must be noted however, that in no other structure where both small and large area devices were received was a discrepancy of this magnitude found between the quantum efficiencies of the different sized devices, for example see E016 in Figure 4.9. It would therefore be unwise to rule out material as the cause, particularly as no small area devices were provided for comparison.

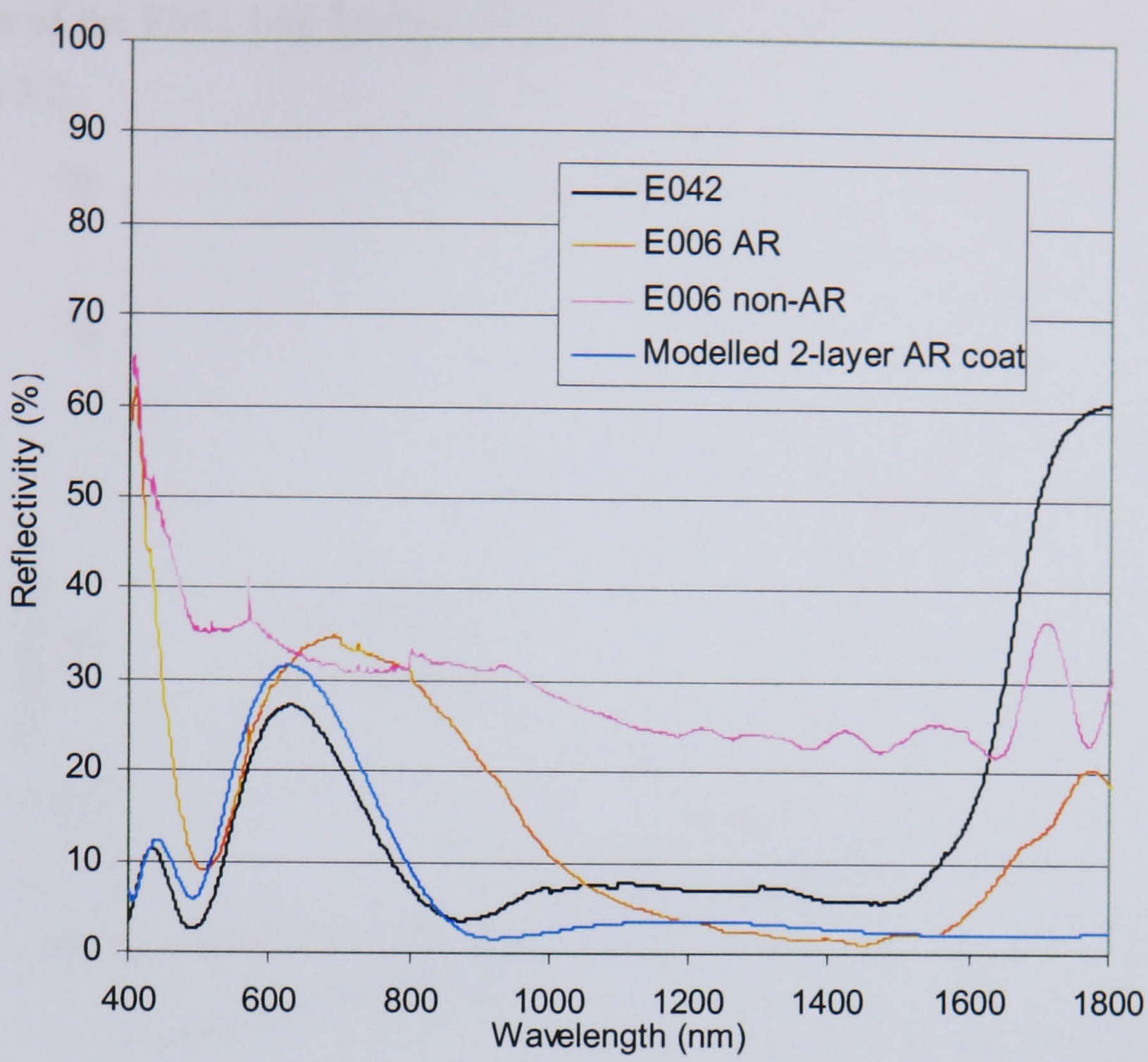

Figure 3.22: Reflectivity comparison of E042 and E006 devices. Also included is a modelled two layer AR coat of TiO_2 and Al_2O_3 optimised at 1200nm.

Light I-V measurements have been performed on the two system arrays. The temperature of the devices was 40°C and they were illuminated, as for the completed system, by the erbia selective emitter, which was heated by fuel combustion. The emission spectrum of this selective emitter is shown in Figure 3.24. By integrating the spectrum with the E042 quantum efficiency, as is described in Section 3.2, the short-circuit current in the 1cm device system array is expected to be 0.88A. The results are shown in Figure 3.23, where the measured short-circuit current is much less than expected. Although the selective emitter is expected to have an operational temperature of 1600°C, due to technical problems during the measurement it could only be heated to 1025°C. This can explain the low current levels obtained in the arrays and the low resultant power outputs. The curves for both arrays are sloping around the short-circuit current point, suggesting that resistive problems may have been encountered, but this should be investigated more thoroughly at higher intensity illumination once the system is fully operational.

Light I-Vs of the E042 1cm devices were taken under high intensity and are discussed in Section 3.2.

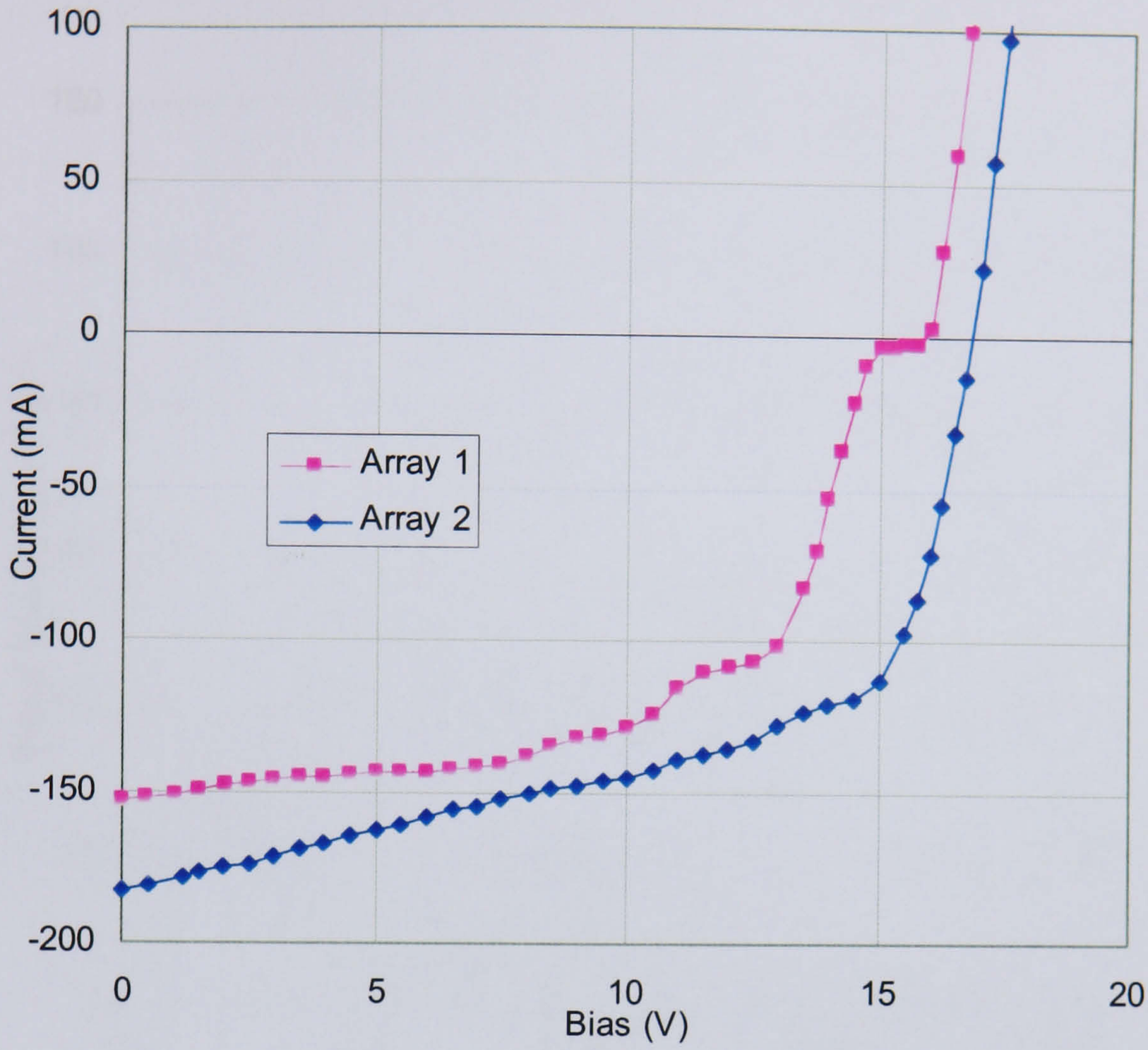

Figure 3.23: Light I-V measurements of the two TPV system arrays. Illumination is provided by the erbia selective emitter at 1025°C. The cell temperature was 40°C.

3.2. Light I-V comparisons

Although the shape of the spectrum radiated by the erbia emitter cannot be accurately reproduced, as was discussed initially in Section 2.2.2, the intensity can to some extent be simulated. The erbia spectrum on which this section is based is shown in Figure 3.24. It was measured at a temperature of 1441°C at the University of Lecce in Italy [5]. The power density of this spectrum is 32kWm^{-2}. However, this spectrum was measured at the surface of the emitter and the intensity will have reduced upon reaching the surface of the cells. The geometry of the system dictates that the power density at the surface of the cells will be 13.8kWm^{-2}. However, it is proposed that light funnels

are included in the system, intended to increase the intensity of illumination by a factor of two [6]. For the purposes of comparison, the spectrum below will be used.

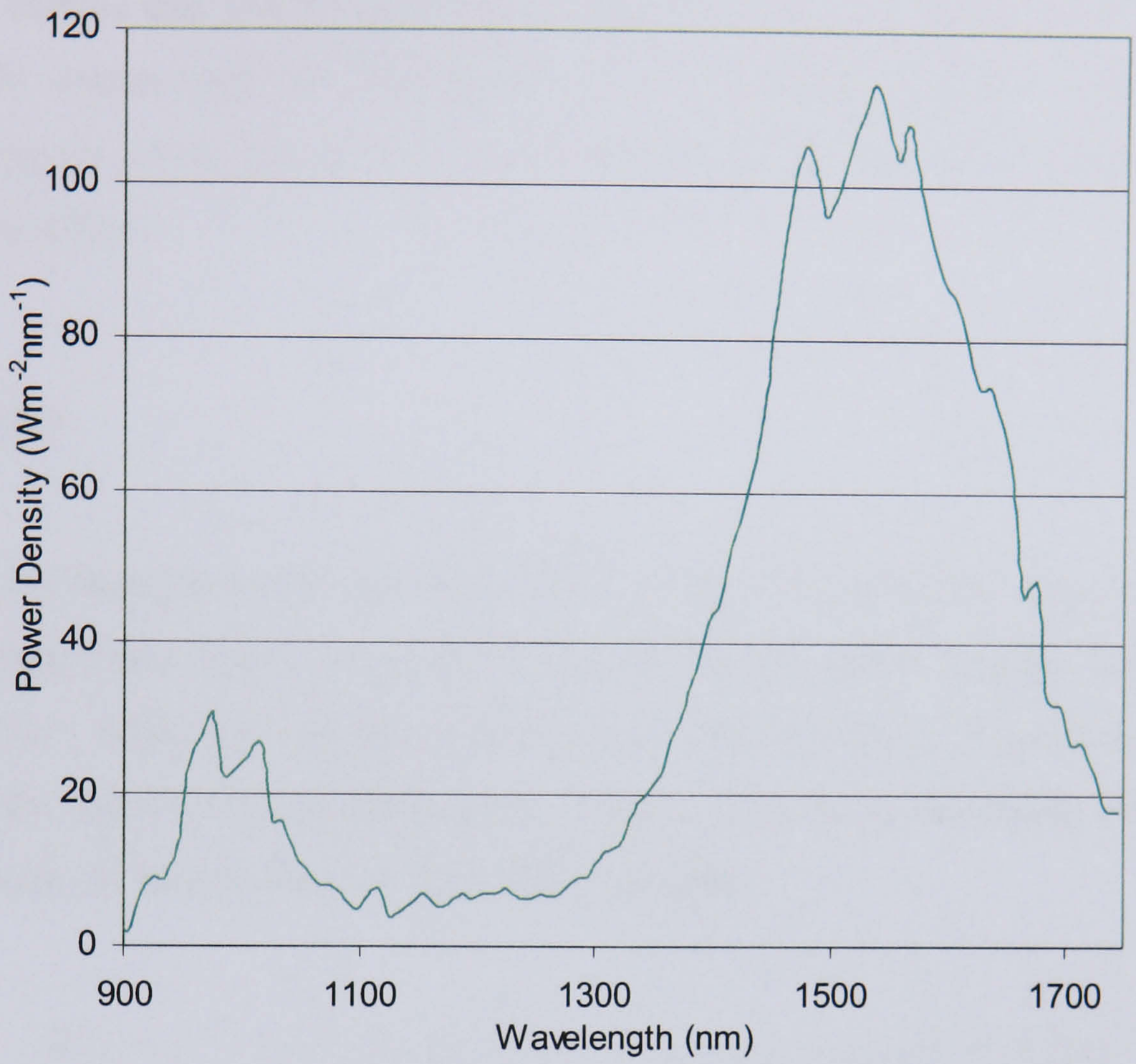

Figure 3.24: Measured erbia emission spectrum.

By integrating this spectrum with quantum efficiency, as is given in Equation 1.3, and taking account of the amount of metal shading, the short-circuit current expected in any given device can be calculated. Therefore, the actual short-circuit current produced will give a measure of the incident power on the device and the maximum output power will then give the efficiency of the device at that power density.

Using a 150W tungsten bulb on a movable stage, a range of intensities were achieved by adjusting the distance to the devices. In this section, a number of light I-V measurements are presented from wafers E004, E006 (AR-coated) and E042. As wafer E004 was the best lattice-matched structure, its performance can give an indication of the efficiencies that are achievable in this system. E004 devices were not AR-coated and for this reason AR-coated E006 is also measured. As the two wafers are structurally identical, a direct comparison should be justified. The emitter spectrum

would produce a short-circuit current in a 1mm device of around 6mA in E004, or 8mA in the AR-coated E006. It must be remembered that the small area devices possess a metal coverage of around 59.6%, which drastically reduces the light that can enter and hence the current that can be generated. E042 is the actual material used for the erbia based TPV system and its performance is of the most interest. The amount of metallisation on a 1cm device is 15.7% and the short-circuit current expected from this spectrum is 0.88A.

3.2.1. Results

Assuming no resistive losses, the short-circuit current measured for each device in each separate experiment can be assumed proportional to the power density that is incident on the device. Efficiency can be calculated from the maximum IV product point in the light I-V plot and the total incident power. Figure 3.25 shows the results obtained from measurements of devices from wafers E004 and E006.

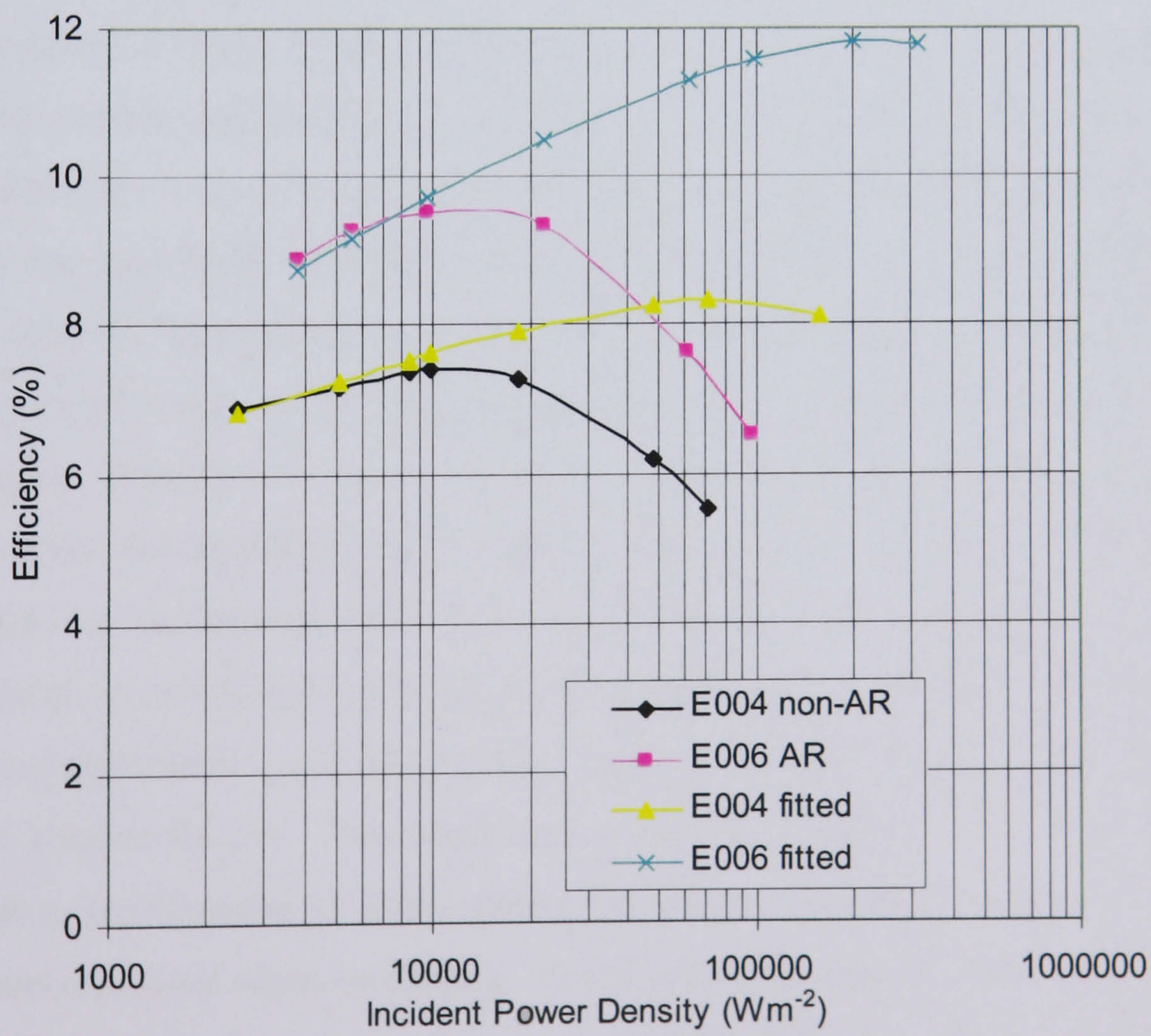

Figure 3.25: Light I-V measurement results under varying incident power density for E004 (non-AR) and E006 (AR), plus results modelled from the fitted dark currents of the two devices.

There are a number of points to note about these results:

1. The level of E006 is higher than that of E004, again demonstrating the effect of an AR coat on the performance of a structure.

2. The experimental efficiencies increase initially with intensity, before falling again. The initial rise is due to the shape of a light I-V curve. As photocurrent increases, the dark current curve is effectively pulled further down, as shown in Figure 1.4. This increases the fill factor and hence the efficiency. However, once substantial current is flowing, the series resistance of the device begins to drop significant voltage and this then brings the total efficiency down. Series resistance is intimately linked to the pattern of the top contact, and so this is a factor that must be optimised for a particular application. Clearly, the 1mm ring contact is not ideal for high intensities, as carriers generated in the centre must travel up to 300μm to reach the contact.

3. Also shown in Figure 3.25 are efficiency results from light I-V curves that were modelled using the experimental dark current. This involves using all the fitted dark current parameters and the same short-circuit currents as those that were measured. It is clear, for both E004 and E006, that the ideal peaks in efficiency are not only higher than those measured but also occur at higher intensities. The conclusion from this is that 'additivity', ie. the assumption that light I-Vs can be generated using solely the dark current and the photocurrent, is not valid at higher intensities in these devices. One reason for the large discrepancy between the modelled and the actual intensities at which the efficiencies peak could be the different paths taken by the current in the dark and the light. Dark current travels directly through the structure from top to bottom, whereas photo-generated carriers will always have to travel laterally across the device to reach the contact fingers. Any additional spreading resistance caused by this longer path is undetectable in dark currents and so the overall series resistance could be underestimated when modelling. As an illustration using E004, in order for the model (yellow curve) to recreate the highest measured (black curve) intensity data point (5.5% at around $70kWm^{-2}$) it is necessary to increase the series

resistance from its fitted value of 1.9Ω to around 13Ω. Although this appears to be extremely high, it does indicate that there is additional resistance present when light I-Vs are measured.

Short-circuit current is defined as the current that flows under illumination at zero applied bias, when both sides of the device are shorted together. When the light I-V curve is flat around zero bias, as is the case for E004 and E006, it is a valid assumption that the short-circuit current is equal to the generated photocurrent, because it is all extracted at zero bias. However, when there is parallel resistance within a device, the shape of a light I-V curve can be altered to such an extent that the short-circuit current can no longer be assumed equal to the generated photocurrent. The effect of parasitic resistance on the shape of a light I-V is illustrated in Figure 3.26, which shows some of the light I-Vs of E042 measured for this section. The amount of photocurrent being fed into the external circuit has begun to dramatically decrease even before zero bias is reached. The pink curve shows the light I-V that would be expected at the highest intensity, using the characteristics fitted from the dark current alone. It shows that the series resistances detected in the dark current cannot be responsible for the poor light I-Vs.

Because the light I-V curves of E042 are poor, it is not possible to extract the true photocurrent, the actual light intensity on the device or the true efficiency of the device. Nor is it possible to measure the device in reverse bias, to attempt to discover whether the photocurrent will saturate. This is because the devices have a low breakdown voltage, which again is consistent with a low parallel resistance. In order to display the experimental data for E042 in the same form as Figure 3.25, the short-circuit current has been taken to be the photocurrent. This vastly underestimates the light intensity and likewise overestimates the efficiency, making comparison with the small area devices impossible, but it does at least give an impression of how the large area devices are limited by series and parallel resistances.

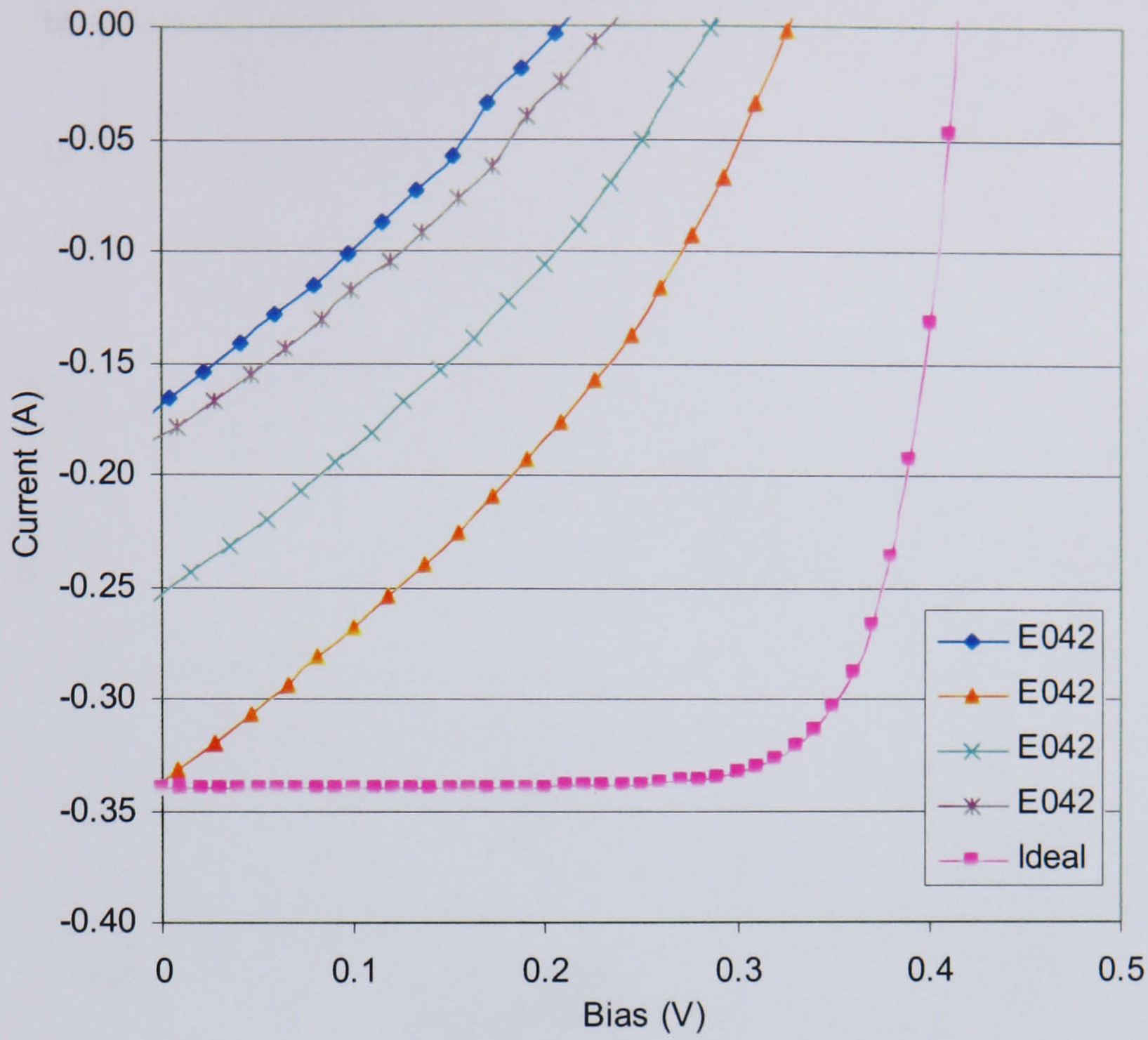

Figure 3.26: E042 high intensity light I-Vs. One of the curves is compared to a more ideal light I-V with the same short-circuit current.

A graph of efficiency against incident intensity for E042 is shown in Figure 3.27. Due to the difficulty in estimating the true light intensity both efficiency and intensity are shown in arbitrary units. Also included in the graph is the fill factor for each of the separate measurements, in absolute percent.

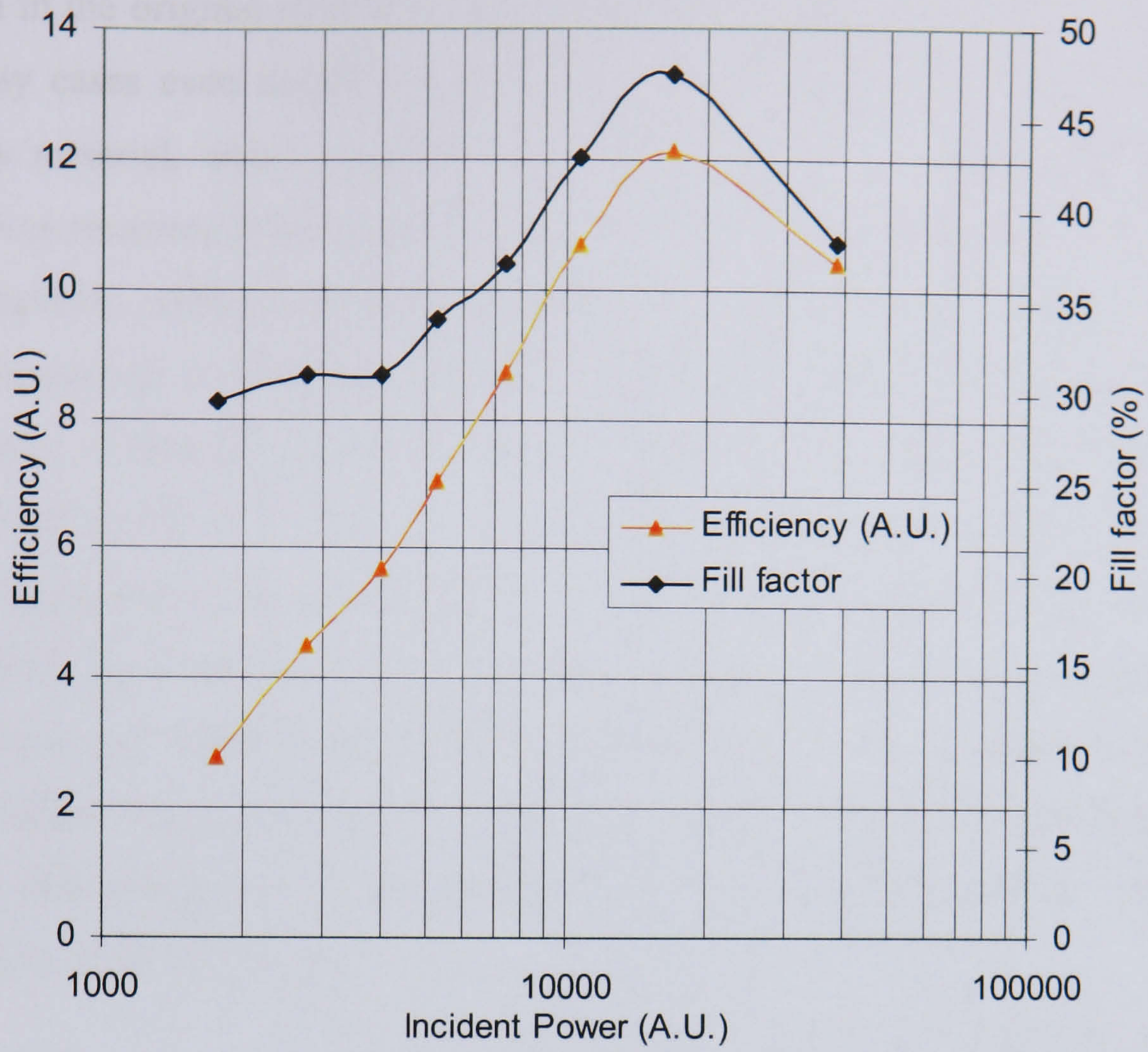

Figure 3.27: Efficiency and fill factors of E042 1cm device at varying light intensities. Both efficiency and intensity are shown in arbitrary units as the absolute intensity cannot be calculated.

As for E004 and E006, Figure 3.27 clearly shows the negative effect that series and spreading resistances can have on the high intensity performance of devices. As the exact intensity is unknown for the 1cm E042 device a direct comparison with the small area devices is not possible. However, the large area grid pattern will still be used in the TPV system, because the finger-like pattern ensures that no carriers need to travel very far before reaching a metal contact. Compared to the small area device's ring contact, this should offer lower overall series resistance and allow the peak of efficiency to occur at higher intensities.

3.3. Conclusions

Each of the lattice-matched structures received during the course of this project has been characterised, both electrically and optically. The most promising characteristics

were seen in the original structure, with subsequent structures failing to improve upon, or in many cases even match, this performance. Problems were suspected with the quaternary material, which was seen in an NMRC study to be non-ideal, and so this material was removed from later structures. A rear surface reflection was detected in the best devices, although present unintentionally, which would allow a second pass through the devices to increase absorption, and also allow unabsorbed photons to return to the source. Using the author's model, the magnitude of this reflection in the initial structure was found to be 45%. A modelled quantum efficiency that was consistent with the experimental data could also be obtained with the model SOL, when a 45% rear reflection was included. This reflection was also found in a later structure, where the magnitude was found by the author's model to be 60%. The difference between this value in different structures is not surprising given that the reflection does not even appear in the majority of the structures and may be attributable to variations in processing or wafer quality.

In those early structures for which large area devices were delivered, there appeared to be problems concerned with the processing. Dark current densities were much higher than in the small area devices, with some appearing to have considerable non-diode characteristics. A small number of later devices achieved good dark current levels, but none of the large area devices displayed satisfactory performance under high intensity illumination.

Through high intensity illumination measurements, a number of observations can be made. The level of illumination, and hence the amount of current, that a device can pass efficiently can be dictated by the series, spreading and parallel resistances. The 1mm ring contact for the small area test devices is unsuitable for such high illumination, as carriers may have to travel relatively large distances to reach the contact metal. By optimising the distance current travels to reach the metal contacts, the finger pattern of the large area devices has greater potential for high intensities. However, in order to determine the ideal contact pattern, a thorough process of optimisation is required.

Experimental results have been received for the devices which have been processed into arrays of 46 devices and are being used in the erbia based TPV system. The dark currents of the arrays showed very little series resistance, which is extremely important

at the high current levels expected within the system. This is expected to be a lower limit to the total series resistance given that the current must travel a different, longer path through the structure when it is created by light rather than in the dark. Light I-Vs from the system arrays have also been received. The low power output measured can be attributed to the selective emitter being at a lower than optimum temperature. Once the system is fully operational, a more accurate examination of the series resistance and overall performance will be possible.

3.4. References

[1] David M Wilt et al., Electrical and Optical Performance Characteristics of 0.74eV p/n InGaAs Monolithic Interconnected Modules. In Coutts et al [Ref. 21 in Chapter 1], pp.237-247. Colorado Springs, Colorado, USA, May 1997.

[2] C Rohr, InGaAsP Quantum Well Cells for Thermophotovoltaic Applications, PhD Thesis, Imperial College of Science, Technology and Medicine, 2000.

[3] J P Connolly et al., Modelling Multi Quantum Well Solar Cell Efficiency. *Proc. 17th European Solar PV Energy Conf.* Munich, Germany, 2001.

[4] Brian Corbett and Carmel Kelleher, Internal Report, Oct 2000.

[5] D Diso, Private Communication.

[6] Salvatore Melcarne and Massimo Mazzer, Internal Report, Aug 2001.

4. Results on Strain-Compensated Structures

The primary aim of THE REV project is to produce a system that operates with low temperature selective emitters, needing low band-gap, lattice-mismatched materials. Quantum well cells enable this long wavelength absorption to be achieved and in this chapter the characterisation results of all such quantum well structures are presented. Quantum well structures were received from both IQE and Sheffield and these are treated in separate sections. Within each section, structures are discussed chronologically. The stated absorption edge for each structure corresponds to the point where the quantum efficiency is half that of the exciton peak. Section 4.3 describes light I-V measurements carried out on a number of the structures to examine their response to the high intensities expected of a TPV system. Section 4.4 contains a study of quantum well carrier escape on some of the structures. The chapter concludes with a summary of the results of strain-compensating quantum wells, comparing the expected band-edges with those measured. Sample structures are given in Appendix 1. A succinct account of the work on strain-compensated structures for thulia emission can be found in Ref. 1.

4.1. IQE grown structures

4.1.1. Wafers E010 and E011 – Absorption edge: 1830nm

Wafers E010 and E011 were quantum well structures attempting to extend absorption towards 2μm, and hence a high amount of strain was involved. The precise compositions of the InGaAs wells and the barriers are unknown. The dark currents of the small area devices, on n-type substrate, E010, were well bunched but the level was many orders of magnitude higher than E004, the lattice-matched bulk InGaAs p-n device. Other indications that the structure was not good were poor light I-V and quantum efficiency. Devices on SI substrates, E011, displayed a level of dark current similar to the n-type substrate and no further measurements were performed.

4.1.2. Wafers E012 and E013 – Absorption edge: 1800nm

The structure of wafers E012 and E013 is an Imperial College design based on a previously successful quantum well device MR1288 grown in Sheffield [2]. However, this structure has quaternary p- and n- regions. This enables the inclusion of higher band-gap InP window layers, whilst simultaneously reducing dark current compared to equivalent lattice-matched InGaAs layers. Wafers E012 and E013 were grown on n-type and SI substrates respectively and all devices were small area. Many E012 devices were received, but there were only four from E013. Dark currents of the two best devices from each wafer are shown in Figure 4.1 and compared with MR1288 and E004. There was considerable spread between devices from both wafers, but there are two excellent E012 devices comparable to MR1288, both of which were well fitted with an ideality factor of n=1.4. These devices were singled out for further examination.

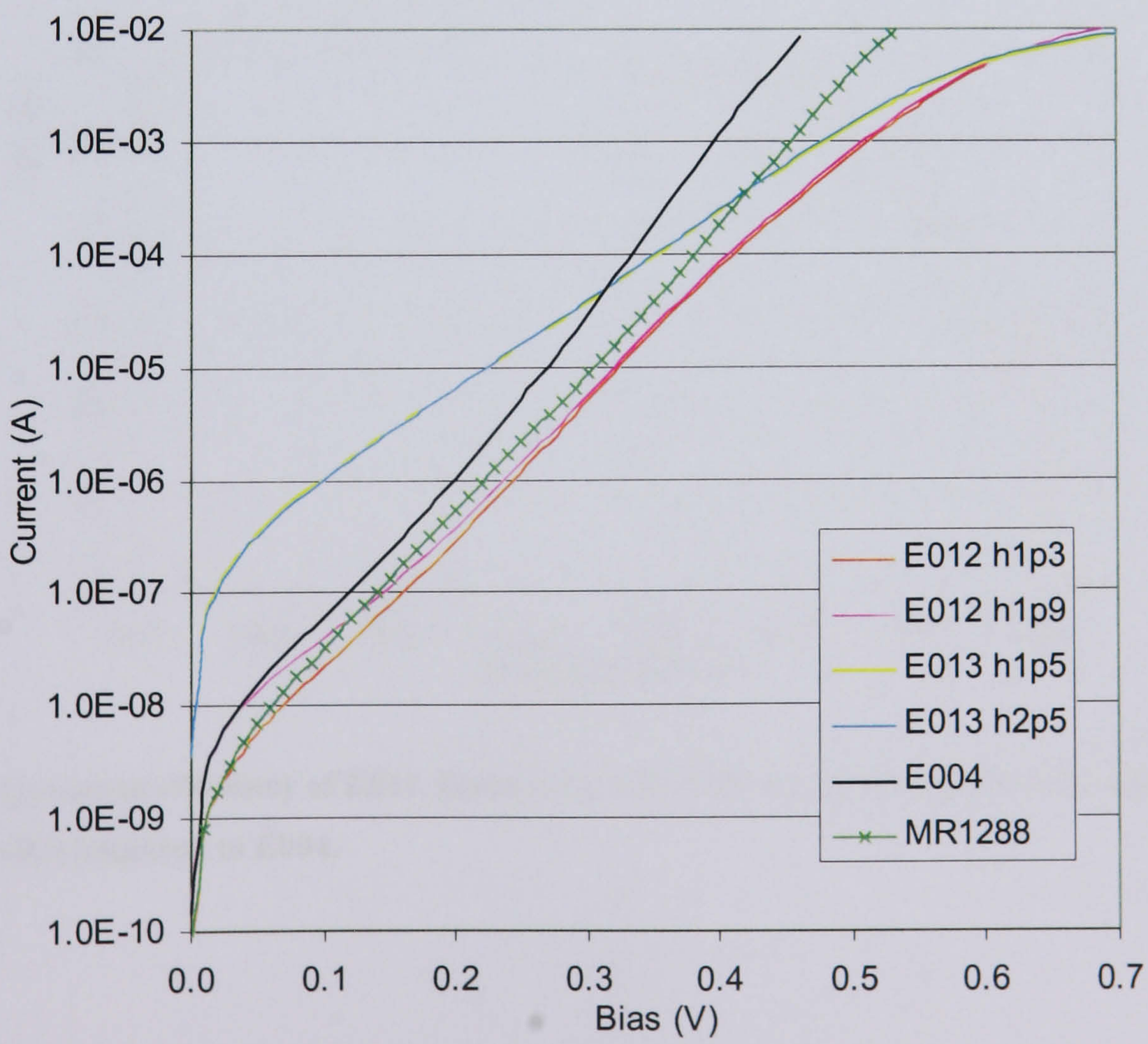

Figure 4.1: Dark currents of E012, E013 and the previous sample MR1288 compared to E004.

The most positive aspect of the structure is the quantum efficiency, shown in Figure 4.2. In comparison to the lattice-matched E004 the response has been extended by approximately 160nm. Referring back to Figure 4.1, this extension in quantum efficiency has been achieved in conjunction with a reduction in dark current. This is a clear indication of the usefulness of quantum wells to this application where lower band-gaps are required but where strain relaxation must be avoided. Another positive aspect of the device is the reflectivity, shown in Figure 4.3. As with E004, the reflection from the front surface (InP) alone cannot account for all the reflected signal received beyond the band-edge. Again, there is a rear surface mirroring effect taking place.

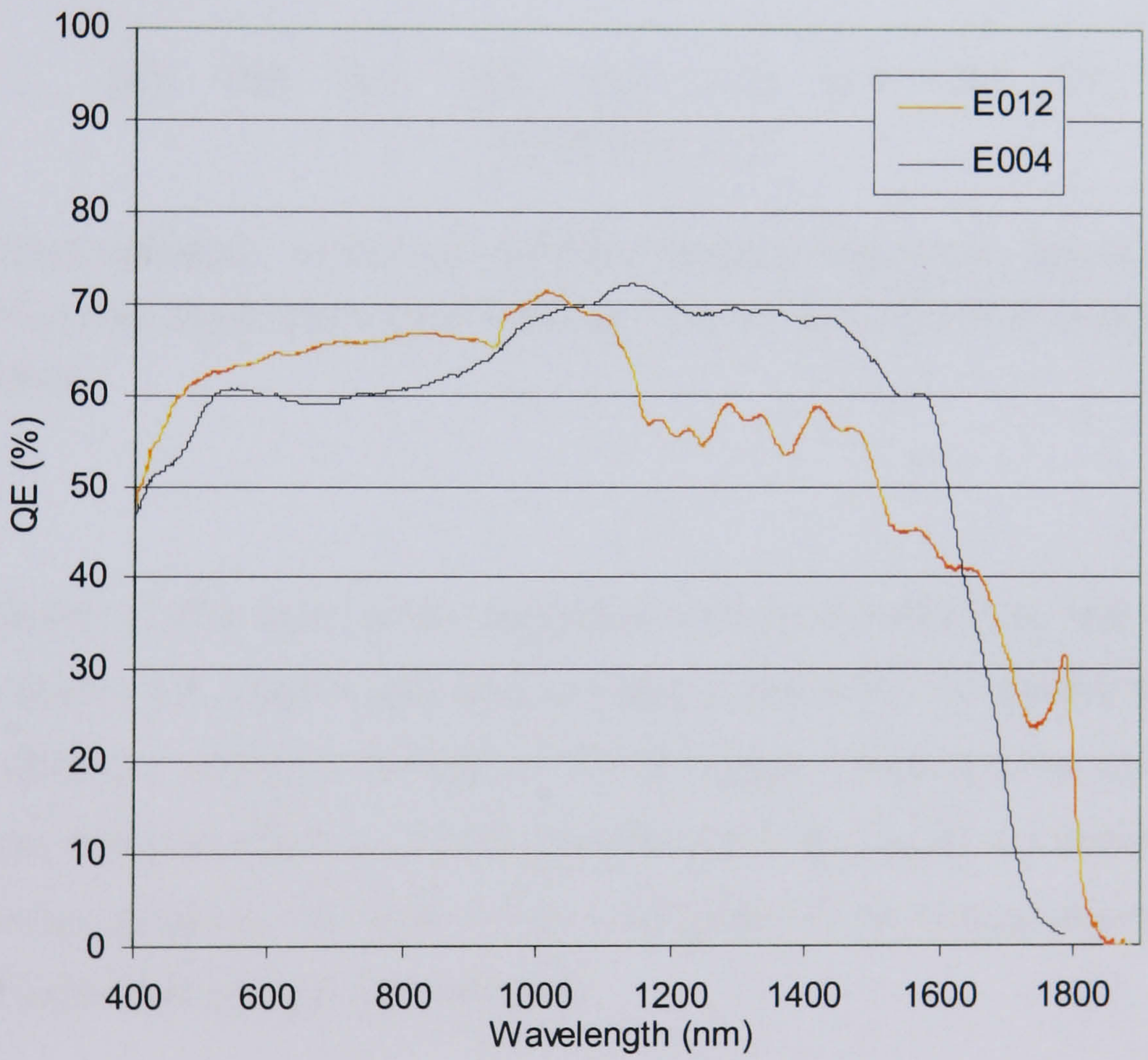

Figure 4.2: Quantum efficiency of E012, illustrating the extension in absorption achieved by the quantum wells compared to E004.

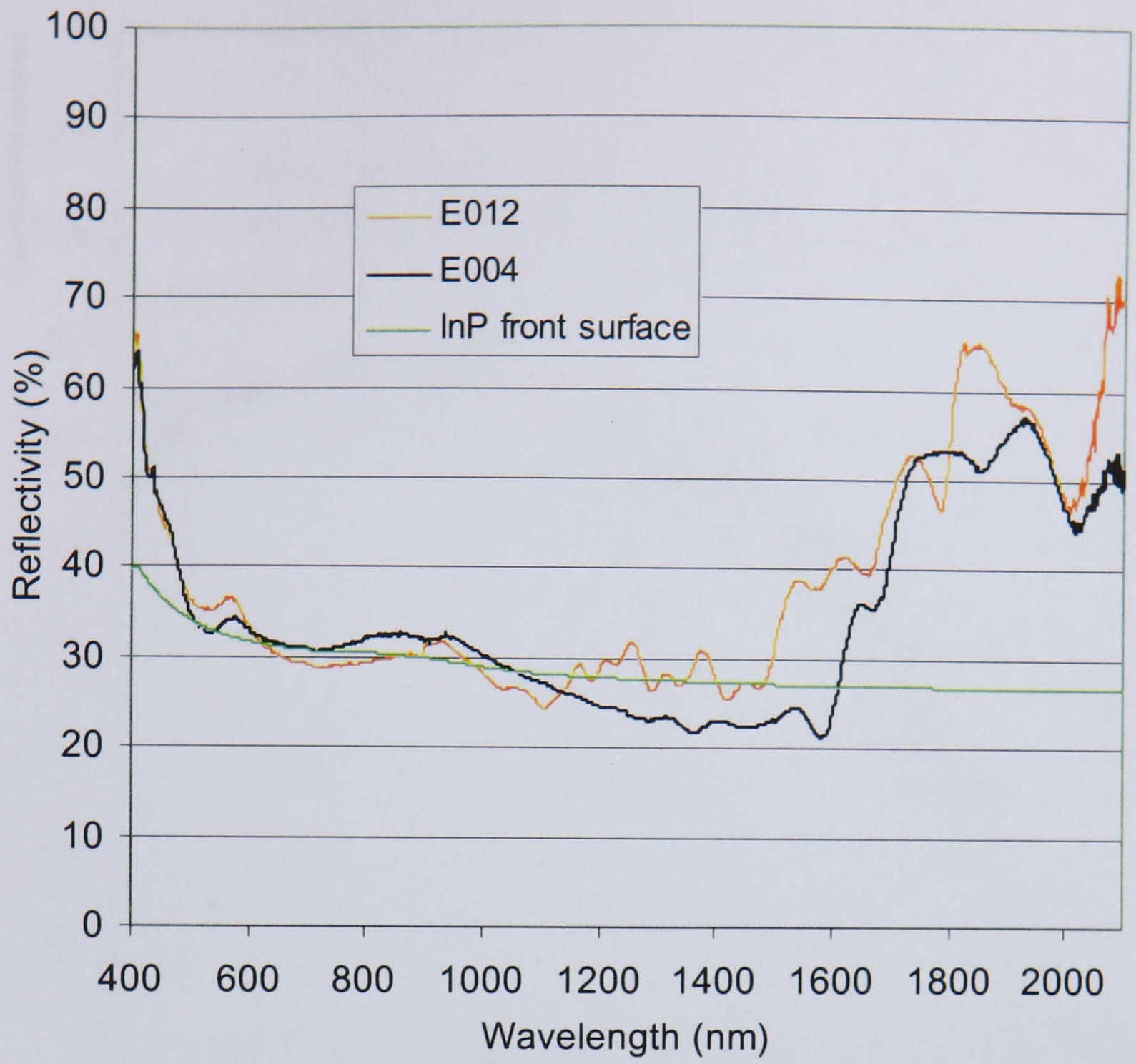

Figure 4.3: E012 reflectivity. As was seen with E004, beyond the absorption edge the reflectivity rises above that from purely front surface reflection. This can be attributed to a rear surface mirroring effect.

The magnitude of this rear surface reflection can be estimated by the model SOL. Shown in Figure 4.4, when a rear surface reflection of 65% is included the modelled quantum efficiency increases beyond the InP band-gap. Although the structure of the experimental quantum efficiency is not reproduced by the model, a consequence of the internal device structure, the level of the continuum, at an energy above that of the exciton, is well matched with this reflection.

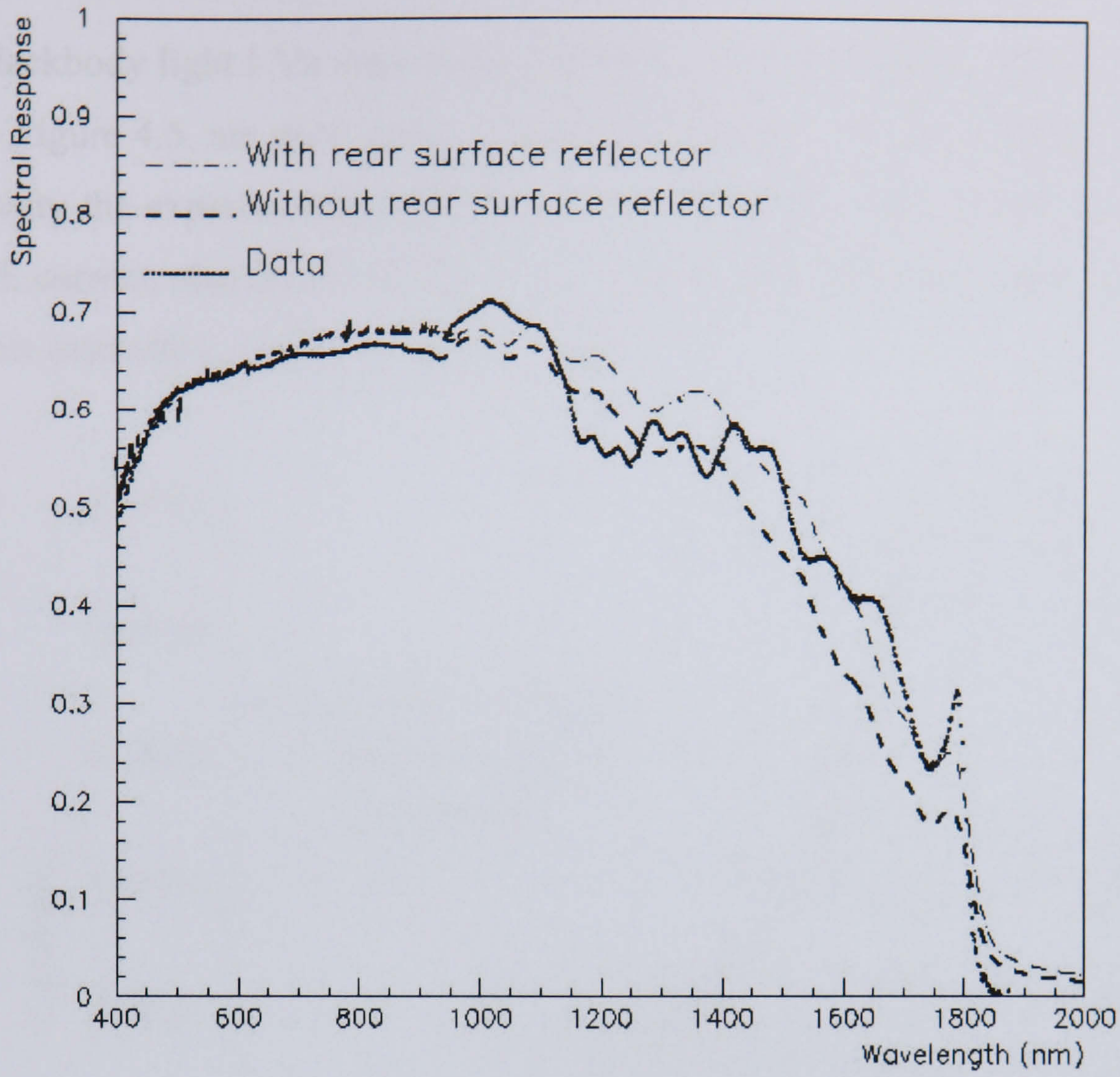

Figure 4.4: E012 quantum efficiency modelled with the programme SOL. A rear surface reflection of 65% increases the quantum efficiency such that the continuum level, at energies above the exciton, matches the experimental data.

The value of the rear surface reflection determined by SOL can also be found using the author's model described in Section 2.2.6. By measuring the total reflectivity and taking the quantum efficiency to be the total absorption of the well region, the only unknowns left are the absorptivity of the well region and the reflectivity of the rear contact. By choosing the wavelength at the peak of the exciton (1786nm, see Figure 4.2) the value for the rear surface mirror is found to be 65%. This figure is also obtained when a wavelength beyond the absorption edge is chosen. Strong agreement between the two models is again demonstrated, showing that this rear surface reflection has a significant effect on the performance of the device.

It is a noteworthy prediction of the author's model that if any devices from E012 had been given an AR coat, the quantum efficiency could have been increased to such a level where the exciton reached 36%.

3000K blackbody light I-Vs were measured on the two best E012 devices. The results, shown in Figure 4.5, are quite poor, producing fill factors of around 45%. Even at this low intensity the experimental light I-Vs are much worse than the prediction from the fitted dark current, also shown in Figure 4.5. This suggests that for these devices, even at such low intensities, additivity does not hold.

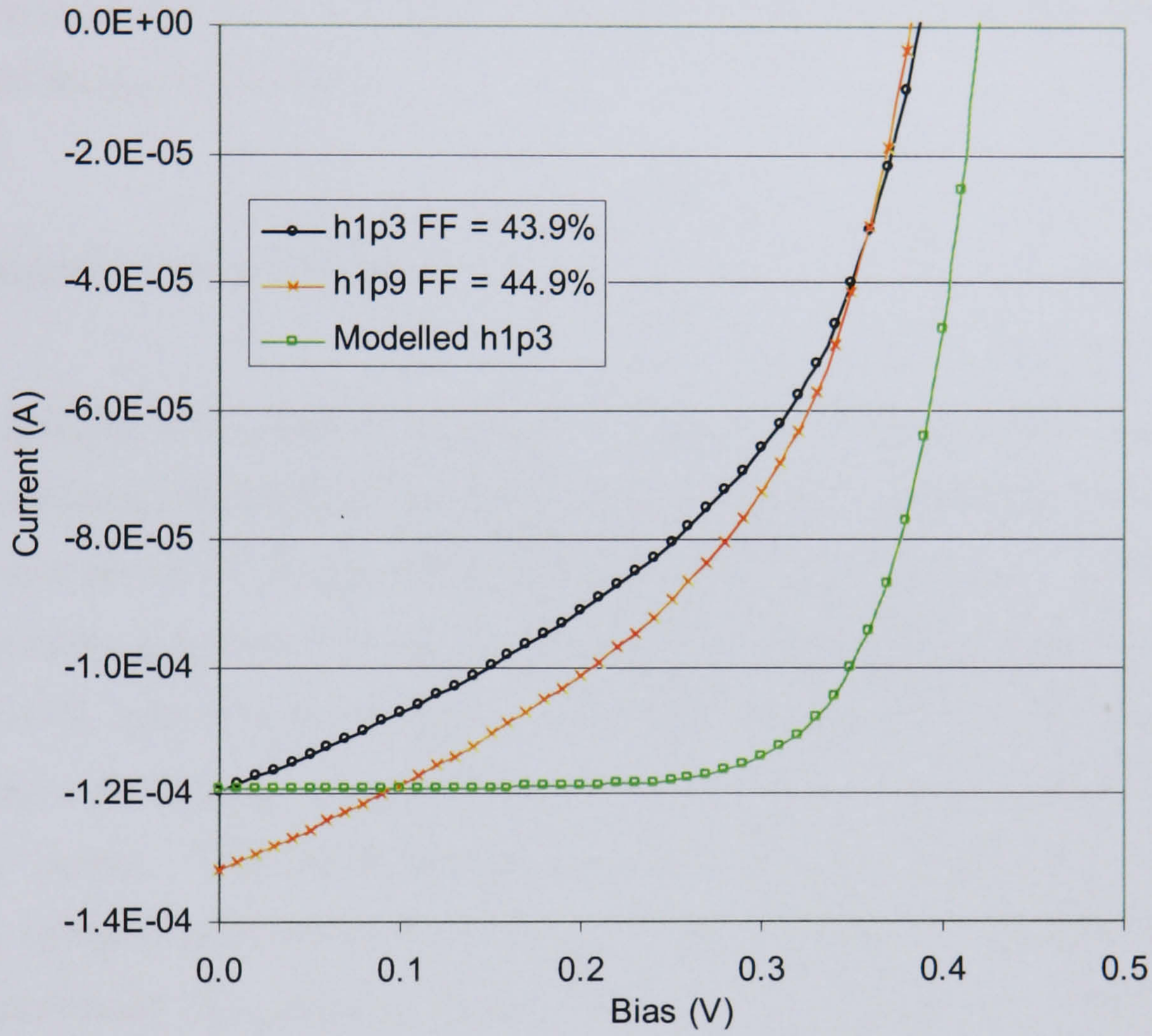

Figure 4.5: 3000K blackbody light I-Vs of E012 devices. The fitted light I-V shows the devices performing much worse than predicted.

The monochromatic I-V of these two devices show that the electric field is being reasonably well maintained across the i-region, suggesting that the i-region doping is unlikely to be responsible for the poor light I-V. One reason could be the quaternary layer, which was given as a possible reason for the poor performance of E008 (see Section 3.1.3).

In spite of the very encouraging results of characterisation of the best devices from this wafer, E012 is not included as one of the high intensity light I-V measurements in

Section 4.3. The first reason is that the light I-Vs of the two best samples were similar to those of E042 in Figure 3.26, in that the short-circuit current could not be taken as the photocurrent. Because of this, the efficiency could not be calculated and comparison with other samples would not be possible. The second, and more worrying reason is that all the samples exhibited signs of deterioration. After only a short period of characterisation, which did not include any high intensity light I-V measurements, the dark currents of the two best devices rose significantly. From these samples, sensible high intensity results could not then be obtained. Also, other measured E012 devices deteriorated during measurements.

4.1.2.1. Material Characterisation

Analysis of E010, E011, E012 and E013 by Transmission Electron Microscope (TEM) and Electron Beam Induced Current (EBIC), by collaborators at IMEM-CNR in Parma, Italy, has revealed that there are significant defects within the structures, extending from the middle of the quantum well region to the surface. The density of these defects was lowest in E012, which could explain why the TEM image of this wafer in Figure 4.6 does not show this feature. Instead, there is visible compositional variation within the quaternary layers. This could be due to some degree of segregation of the four quaternary components at the high temperatures during growth. A non-ideal quaternary layer has previously been detected in the wafer E008 (see Section 3.1.3) and thus could once more be compromising the structure. Test structures of the E012 quantum wells produced prior to full wafer growth were good, which suggests that the problem does not lie with the strain compensation.

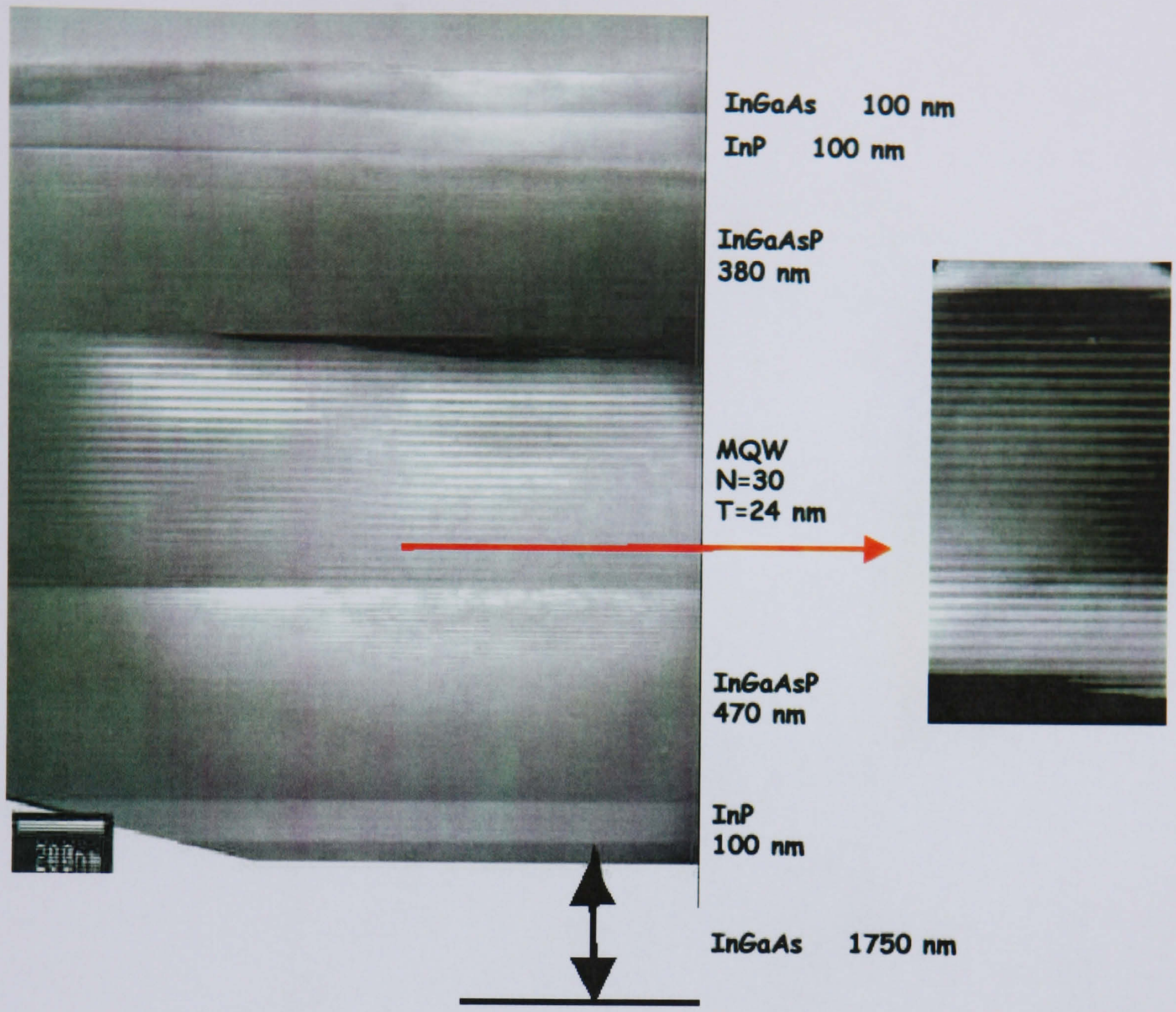

Figure 4.6: Cross-sectional TEM of E012 taken by collaborators in Parma, Italy. The quantum wells in this region do not appear to have relaxed, but there is clear compositional modulation within the quaternary layer.

The clear image of the quantum well region allows the thickness of the layers to measured and coupled with the measured absorption edge to estimate the composition of the quantum wells. This comparison with the nominal values is carried out in Section 4.5.

Although a cross-sectional TEM image only examines a very small area of the wafer, this TEM image suggests that there are areas of the wafer with a good quality of quantum wells. Variations in quality across the wafer are likely to be responsible for the spread in dark currents that was seen, with the best two devices having been taken from a more defect free region of the wafer.

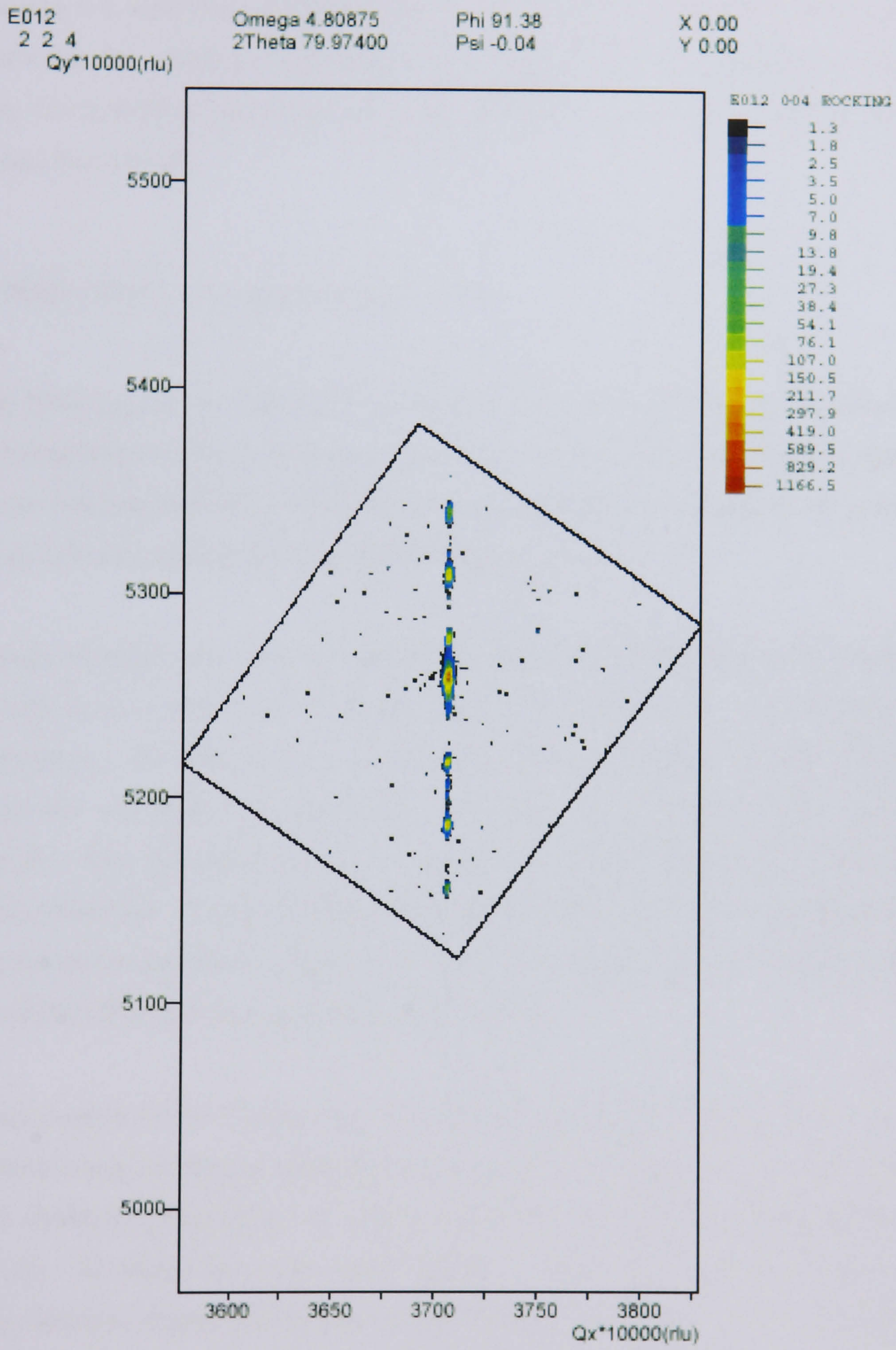

Figure 4.7: Reciprocal space map of wafer E012 about the point [2 2 4]. The lack of lateral features indicates high quality quantum wells.

X-ray diffraction analysis, as described in Section 2.2.7, has also been performed on wafer E012. A reciprocal space map measured around the reciprocal lattice point [2 2 4] is shown in Figure 4.7. The vertical direction in the figure is normal to the wafer surface and it is clear that wafer E012 possesses periodicity only in that direction. This indicates that the quantum wells are of high quality and have not relaxed. Had they relaxed, the reciprocal space map would be expected to indicate structure in directions other than the vertical.

4.1.3. Wafer E016 – Absorption edge: 1750nm

Taking E012 as a basis, the barrier composition was adjusted slightly to improve the strain compensation taking the elastic constants into account [3]. The lateral conduction layer was removed and also, due to the suspected problems connected to the quaternary material, this was replaced in the p- and n- regions with InP.

One piece of wafer was received which contained one 1cm device and a number of small area devices, only some of which could be contacted to by wire-bonding due to their positions. The dark currents of the large area device and the lowest of the small area devices are shown in Figure 4.8. A number of the small area devices are comparable with the previous E012, but the 1cm device is clearly suffering from parallel conduction. A measurement of one of the small area devices made at NMRC during the processing again indicates that a degree of degradation has occurred, albeit to a lesser extent than previous structures such as E014.

The dark current of the 1cm device can be fitted with ideality factors of n=1 and n=2, albeit with a large series resistance and low parallel resistance. However, the small area devices cannot be fitted likewise. At low biases the dark current has an ideality factor of n=1.25. At higher biases the curve begins to turn over. However this cannot be fitted by series resistance but with an ideality factor of n=2, with the n=1.25 component seemingly inactive. Although the biases in Figure 4.8 are much too low for this to occur, one process which can produce n=2 at high biases is high injection. This is when the injected minority carrier concentration equals the majority carrier concentration.

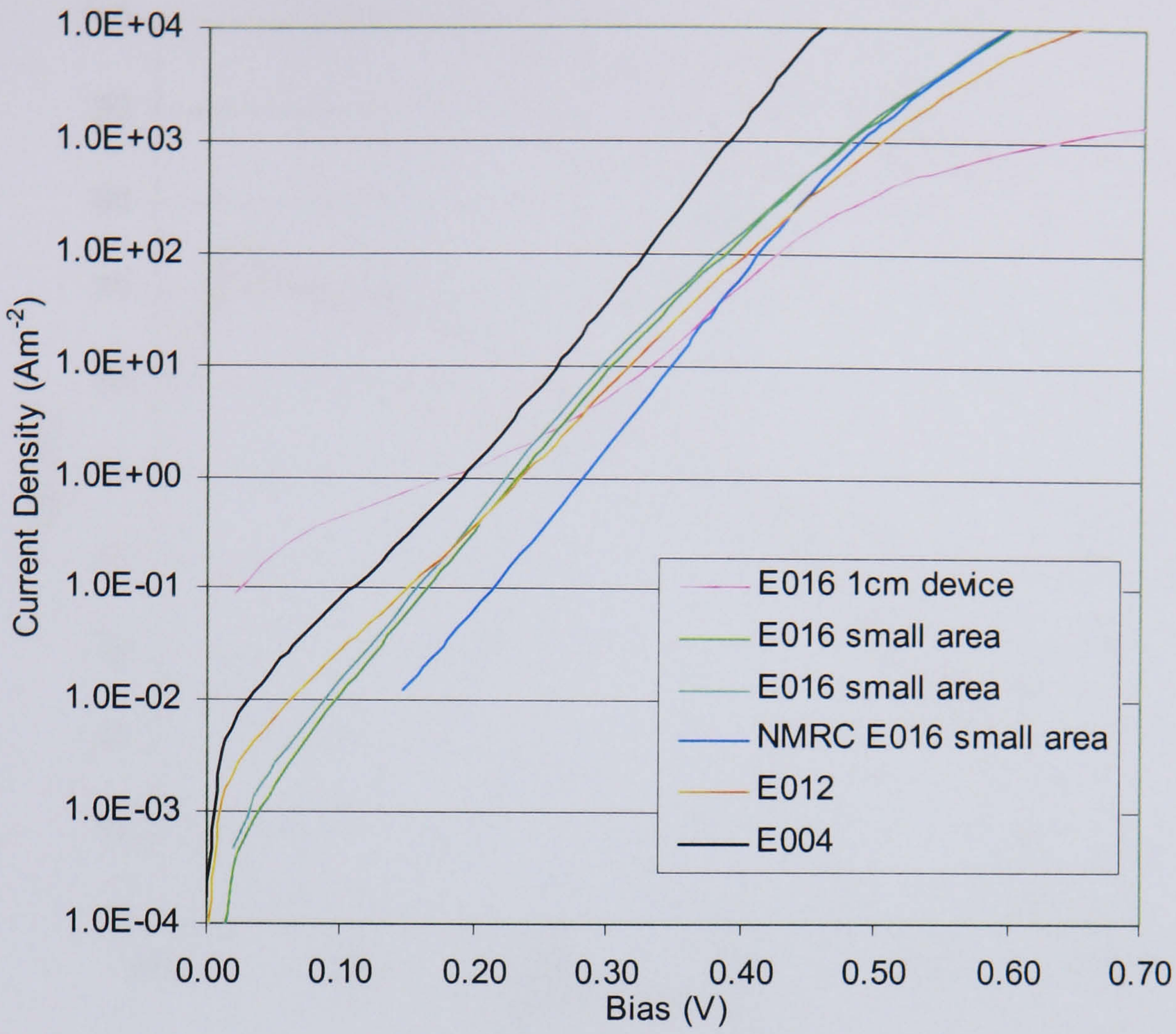

Figure 4.8: Dark currents of E016 devices compared with E004, E012 and a small area device from E016 measured at NMRC prior to delivery.

Despite positive dark currents from the small area devices the quantum efficiencies show that the performance of E012 has not been repeated so successfully. As Figure 4.9 shows the absorption edge is around 50nm short of that in E012, despite an almost identical nominal quantum well region. This unexpected result is discussed in Section 4.5.

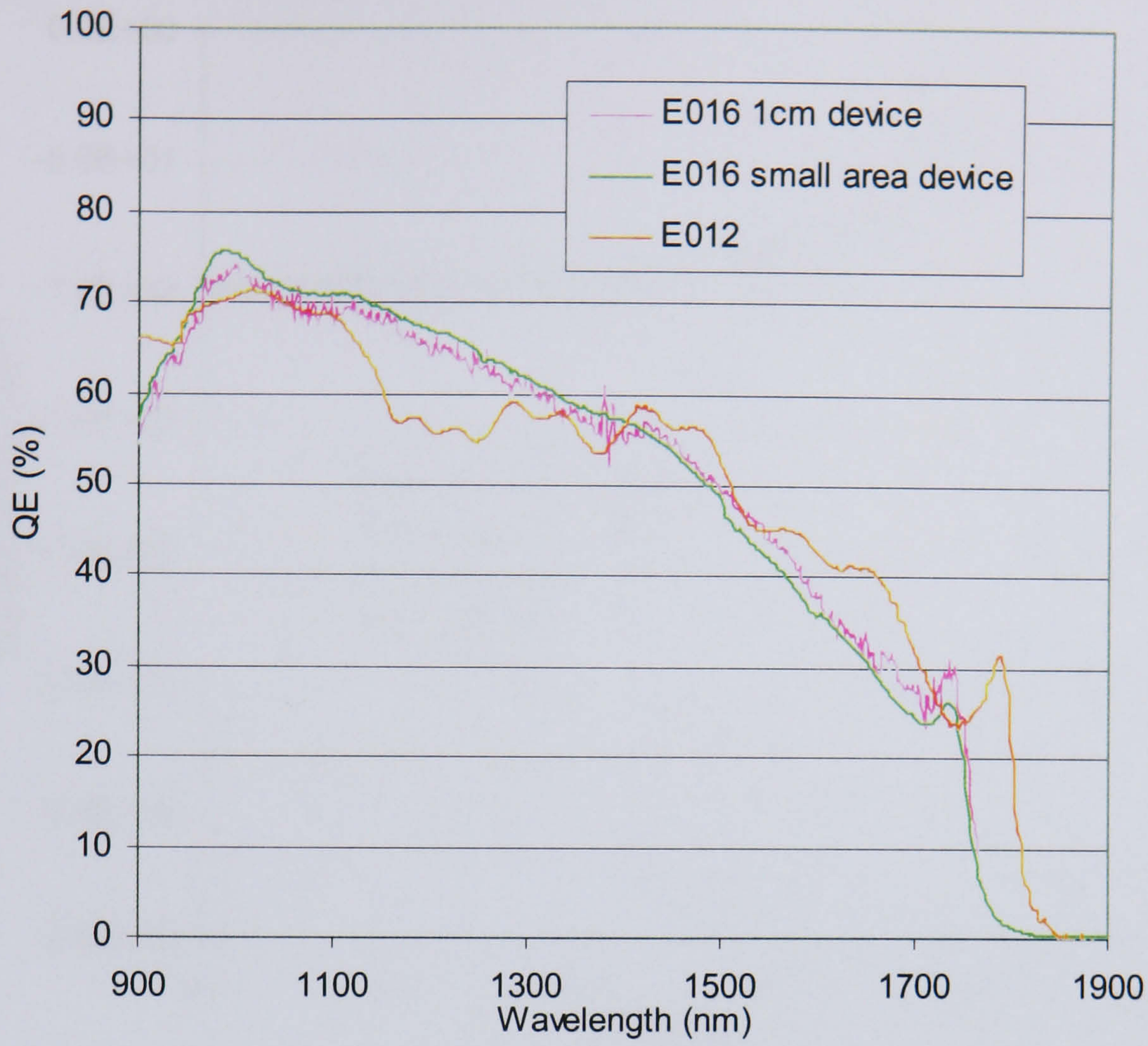

Figure 4.9: E016 quantum efficiencies. Despite an almost identical nominal quantum well region the absorption falls short of E012 by about 50nm.

The 3000K blackbody light I-Vs of E016 devices are given in Figure 4.10. The performances of the small area devices are much better than E012. The 1cm device was slightly worse than the small area devices but was still much better than the E012 devices. Using the fitted dark current and the measured short-circuit current of the large area device, a light I-V was modelled and this is also shown in Figure 4.10. The measured signal begins to decrease before the model, indicating that in this device, the light I-V cannot be predicted from the dark current alone. As the dark currents of the small area devices could not be fitted it was not possible to predict any light I-Vs.

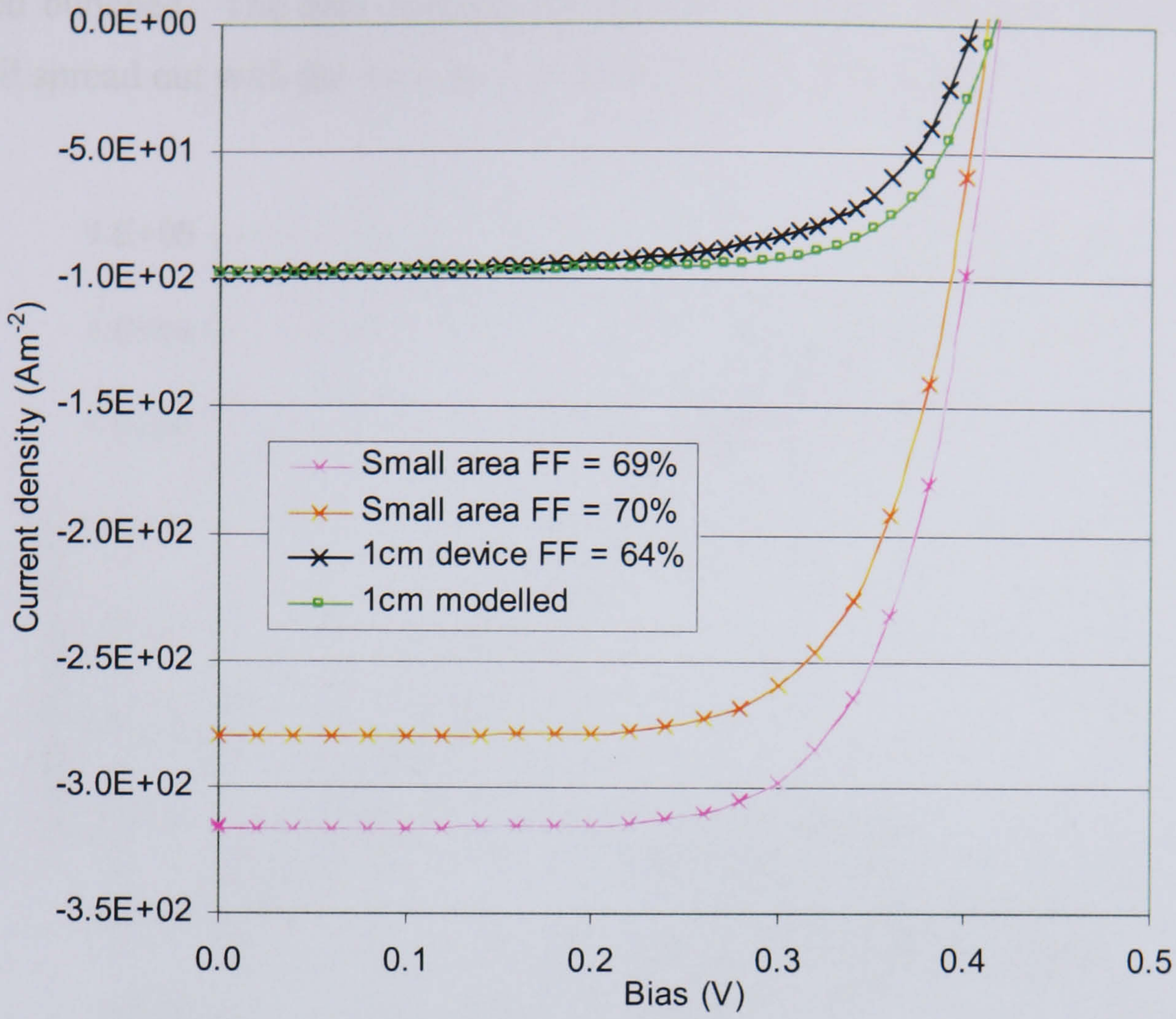

Figure 4.10: 3000K blackbody light I-Vs of E016 devices. Also shown is a modelled light I-V of the 1cm device.

4.1.4. Wafers E1054, E1055 and E1057 – Absorption edges 1900-1940nm

These three structures consist of InP p- and n- regions with InGaAs barriers and wells. The only nominal change between the structures is the barrier thickness, in an effort to determine the optimal thickness for the best strain compensation. From E1054 and E1055 only small area devices were received. Two near identical pieces of E1057 wafer were received, each with a 1cm device and a number of small area devices. A piece of wafer E1057 was also received and this was processed by the author into 1mm mesa devices.

A selection of the better dark currents from the three wafers is shown in Figure 4.11. There was a spread in the quality of the E1055 devices but the E1054 dark currents were

quite well bunched. The dark currents of the received small area devices from E1057 were well spread out with the 1cm devices amongst the lower levels.

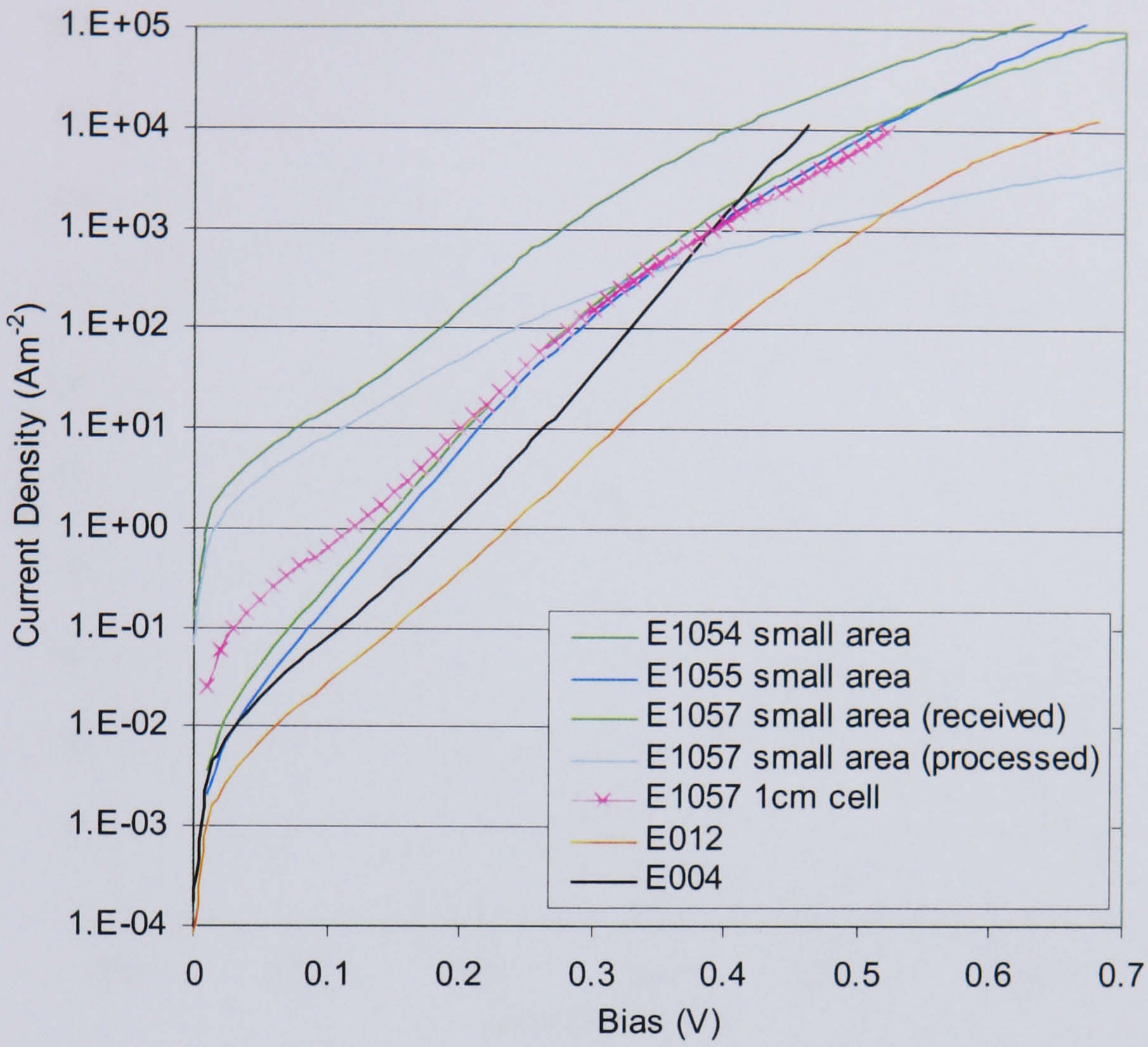

Figure 4.11: Dark currents of E1054, E1055 and E1057 devices compared to E012 and E004.

None of the devices have achieved dark currents as low as the original strain-compensated structure E012, which is expected as the absorption is to longer wavelengths, although encouragingly one of the large area E1057 devices has achieved a level comparable with the E1057 small area devices. The most noticeable aspect of the characteristics, which is particularly evident in E1055, is a similar form of dark current to the E016 small area devices. At lower biases the dark current fits with an ideality factor around n=1, but the high bias section is fitted with an ideality factor around n=2, rather than series resistance.

The only nominal difference between the three structures is the barrier width. Given that barriers of such thickness are sufficient to isolate the quantum wells from each other in terms of quantum interference, and should not therefore affect the electrical properties, the quantum efficiency is not expected to differ between the three structures.

However, as Figure 4.12 shows, the quantum efficiencies of the three samples are noticeably different.

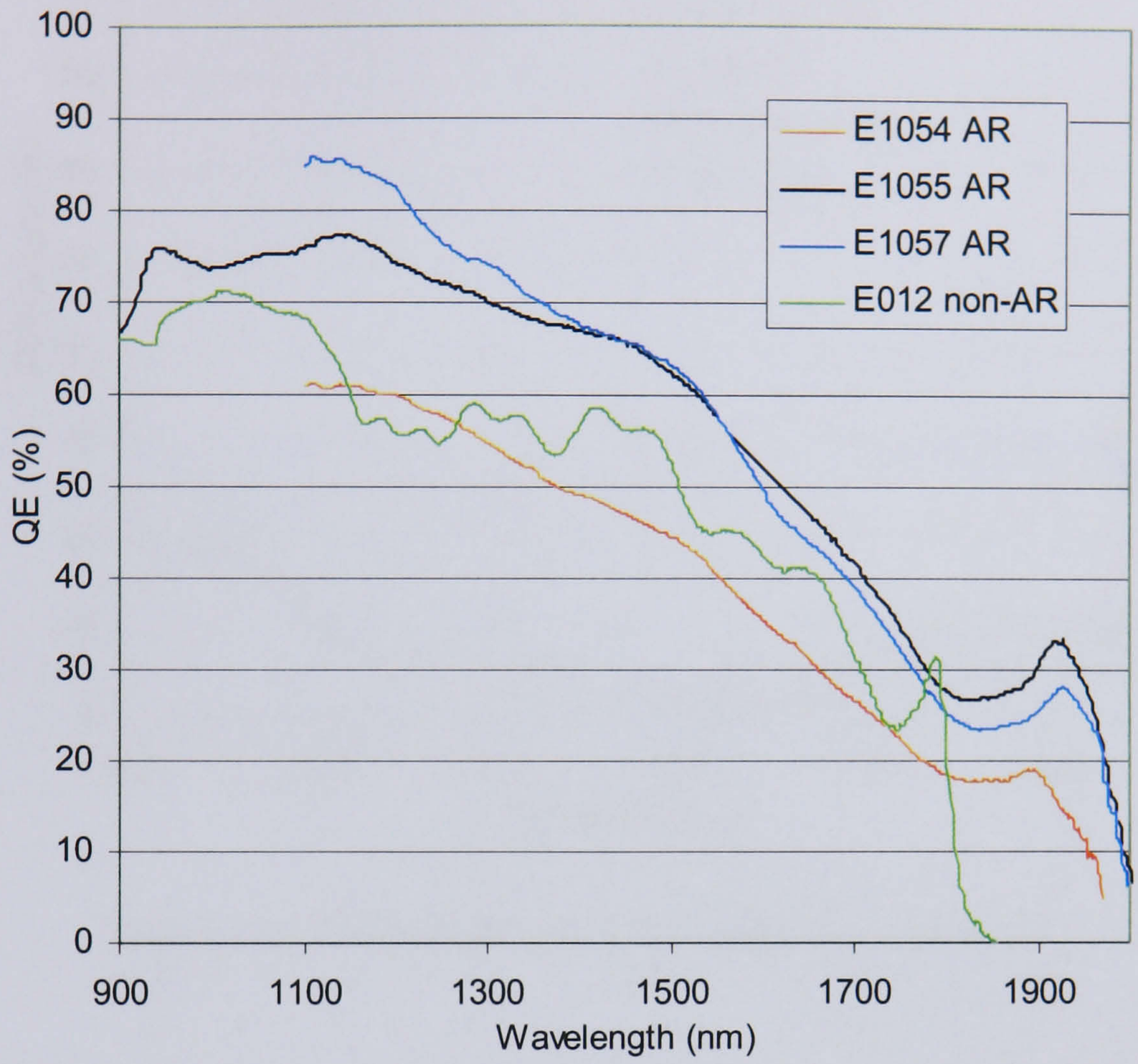

Figure 4.12: Quantum efficiency comparison between E1054, E1055, E1057 and E012.

The levels of the quantum efficiencies can be related to the material qualities. For example, E1054 has the lowest level, and also the highest dark currents, see Figure 4.11. The differences in the positions of the excitons is explicable by differing quantum well thicknesses, which could be expected between three distinct structures grown separately. There is also evidence of multiple excitonic features in all three structures, and this is discussed in Section 4.5.

The reflectivities shown in Figure 4.13 present similar results for the three structures, demonstrating that it is not the AR coating which is causing the great variation in quantum efficiency. They also show that the rear surface reflector evident in E004 and E012 has not been successfully reproduced in this series.

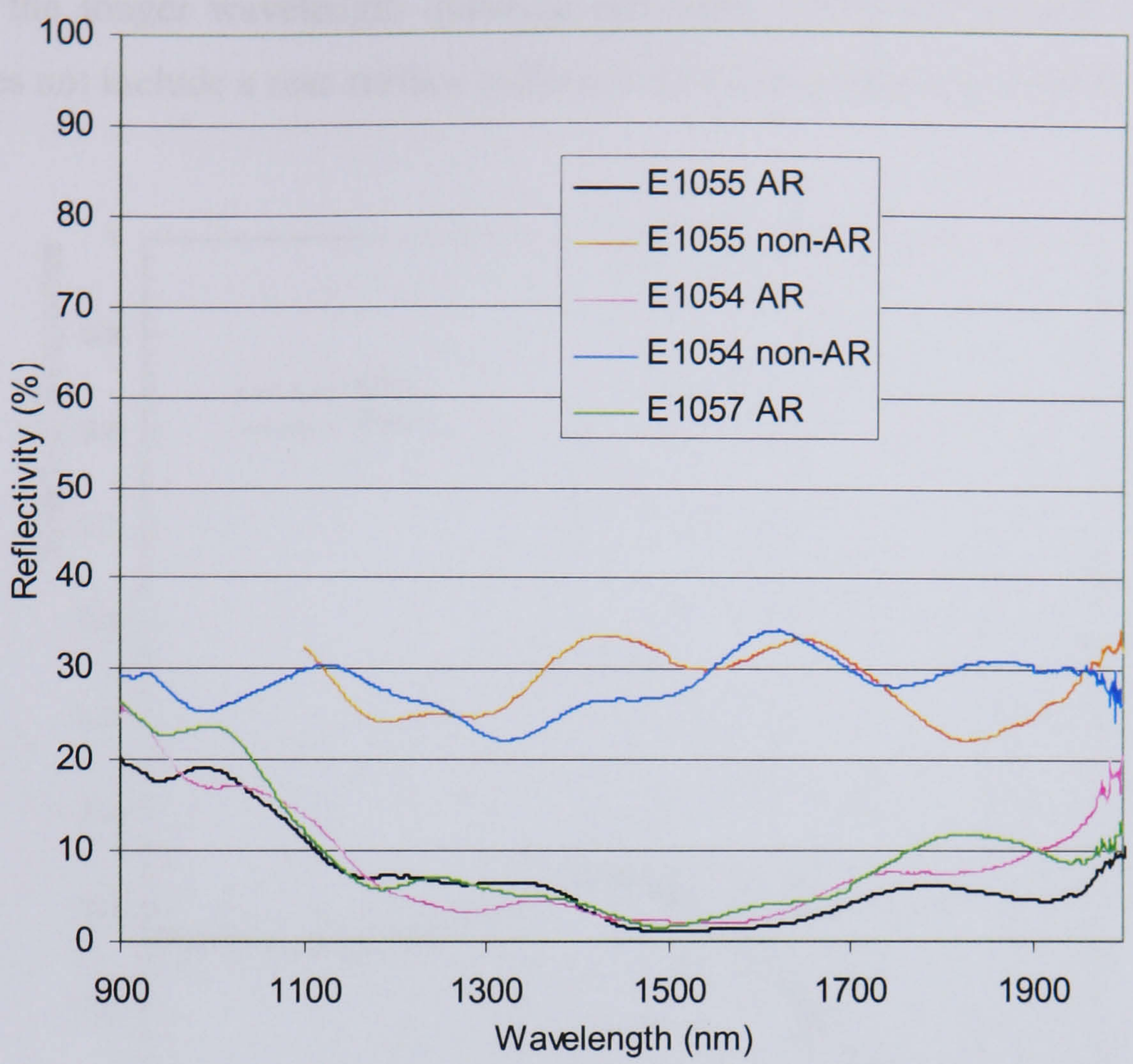

Figure 4.13: E1054, E1055 and E1057 reflectivity comparison.

Selected as the best structure of the three, the performance of E1055 can be understood by modelling its exciton peak as was carried out for E012 in Section 4.1.2. For the non-AR E012 device a 65% reflecting mirror was fitted for the back of the device. The first step to simulating the E1055 AR device is to set this reflectivity to zero. The lack of rear reflector appears justified by the reflectivity shown in Figure 4.13. Secondly, the absorption in the quantum well region is increased by 33%, as the number of wells is increased from 30 to 40. Finally, the front surface reflectivity is reduced to 4%, to simulate an AR coat. As a result the quantum efficiency at the exciton becomes 32%, which is approximately the level of the E1055 AR device. Although not shown in the figure, the non-AR quantum efficiency of E1055 is also accurately predicted in this way. Altogether, this is evidence that the material quality of E1055 is comparable to E012. It does however also highlight the increase in response with the addition of the rear reflector as in E012, and how important the achievement of a good reflector is.

Where the lack of a rear surface reflection in E1055 is concerned, there is again agreement between the author's model and the model SOL. Figure 4.14 shows the SOL

model of the longer wavelength quantum efficiency of the AR coated E1055. The model does not include a rear surface reflection and this produces a good fit.

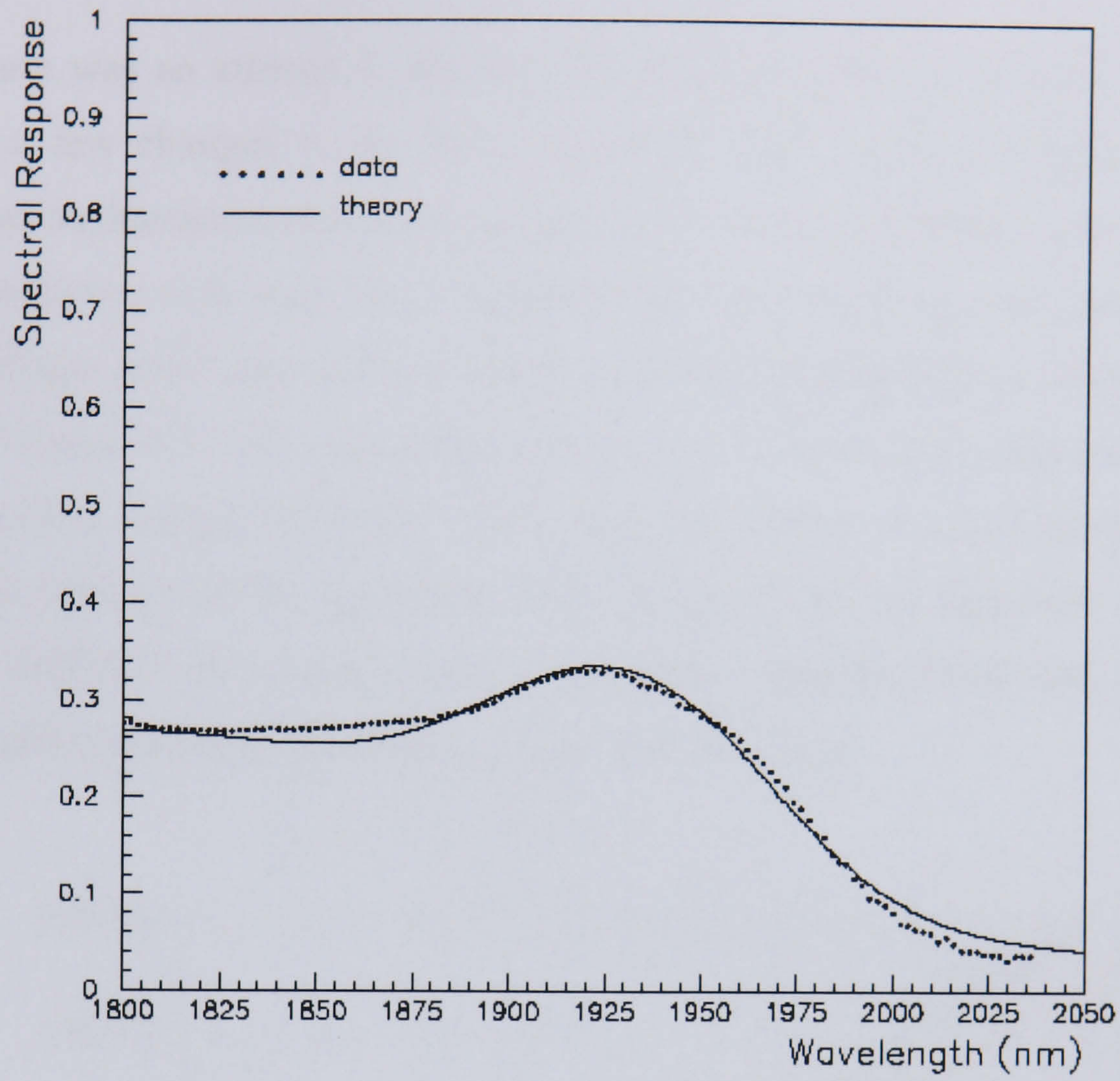

Figure 4.14: SOL modelled longer wavelength quantum efficiency of AR coated E1055 with no rear surface reflection.

As E1055 successfully demonstrates the ability to grow a large number of highly strained quantum wells and also extends the absorption wavelength sufficiently to absorb across the majority of the thulia emission wavelength range, this material was chosen as the structure for the final TPV system cells.

4.2. Sheffield grown structures

As was revealed in Chapter 2, all devices from Sheffield were 1mm mesa devices. These structures were grown and processed over the same time period as the IQE structures. The chronology of the Sheffield devices relative to those from IQE should be clear from the text.

4.2.1. MR1665 – Absorption edge: 1800nm

This structure was an attempt to recreate the good performance of E012, hence there were only a few changes to the E012 structure. The lateral conduction layer was removed and the barrier composition was altered as in structure E016. Also, to alleviate possible problems with quaternary material, this was replaced with lattice-matched InGaAs. Many small area devices were received, roughly half of which were AR coated. In Figure 4.15 the lowest dark currents of MR1665 are compared with E012 and the previous sample MR1288. E012 and MR1288 have identical quantum well regions with MR1665 differing only in barrier composition, see Appendix A. The dark currents of MR1665 were well bunched, with only a handful of devices, all of which were AR coated, having levels slightly higher than the others.

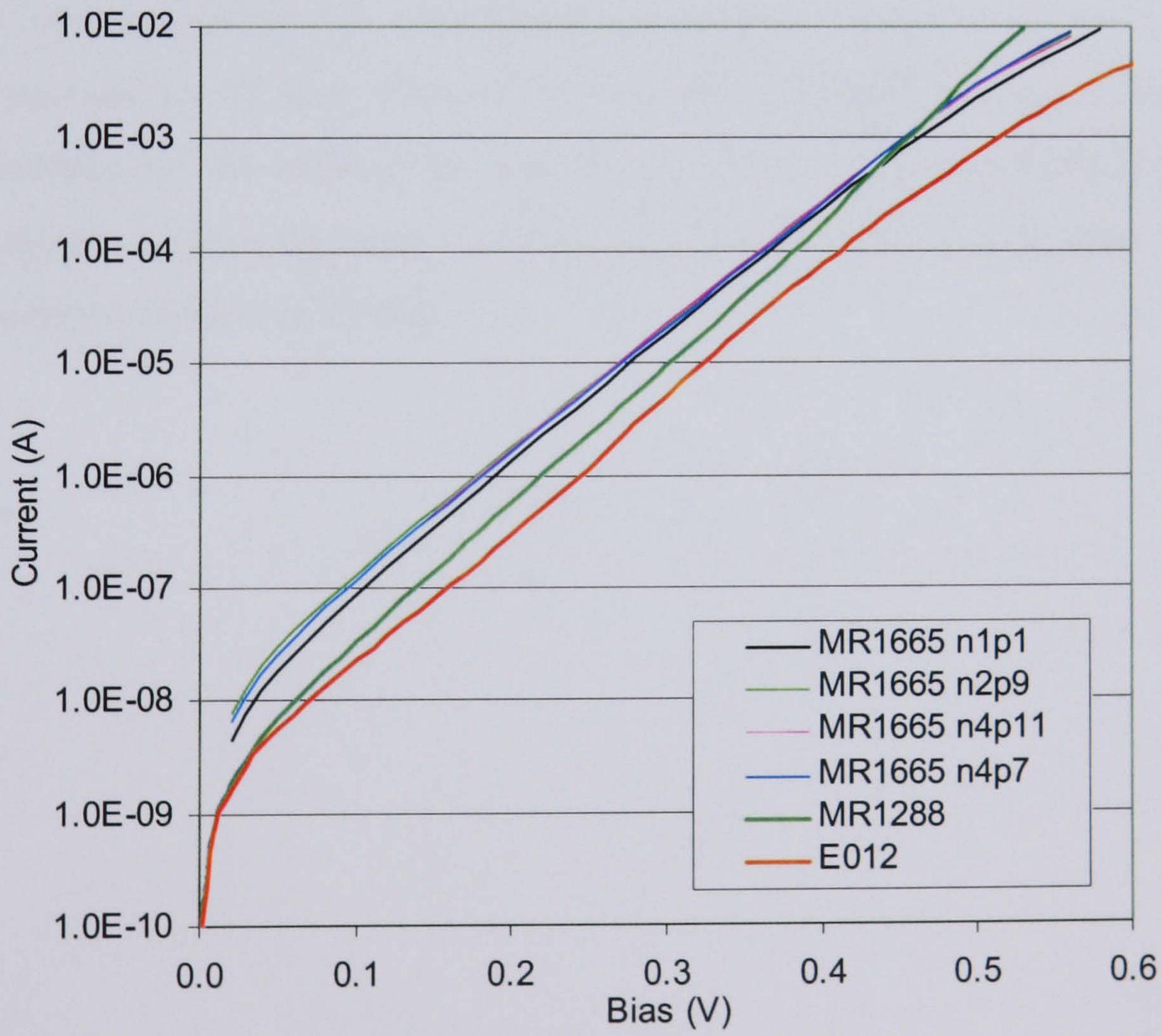

Figure 4.15: Dark currents of MR1665 devices compared with E012 and MR1288. The quantum wells in all the structures are identical in composition and thickness.

The quantum efficiencies and reflectivities of AR and non-AR devices from MR1665 compared to E012 are shown in Figure 4.16 and Figure 4.17 respectively. The absorption edge is at a slightly shorter wavelength than E012, which may be connected with the changes in nominal composition in the quantum well region. Also, at first sight the sample MR1665 is disappointing in that even the AR coated sample does not display a response as high as the non-AR E012. However, it must be remembered that E012 showed clear evidence of a rear surface reflector, something which Figure 4.17 strongly suggests is not present in MR1665. Sheffield substrates are generally only single-sided polished wafers and so reflections from the unpolished rear are not expected.

The performance of this structure can again be understood by modelling its exciton peak as was carried out for E012 and E1055. Starting from the non-AR E012 device with a 65% reflecting mirror, if this reflectivity is set to zero to simulate the absence of this reflector, the exciton peak reduces from 30% to 19%, which is approximately the level of the MR1665 non-AR device. Furthermore, if the front surface reflectivity is reduced to 2% to simulate an AR coat, the exciton quantum efficiency becomes 25%, which is again approximately the level of the AR device. Once again, the material quality of MR1665 appears to be comparable to E012, with the shortfall in absorption due to the lack of a reflector at the rear surface.

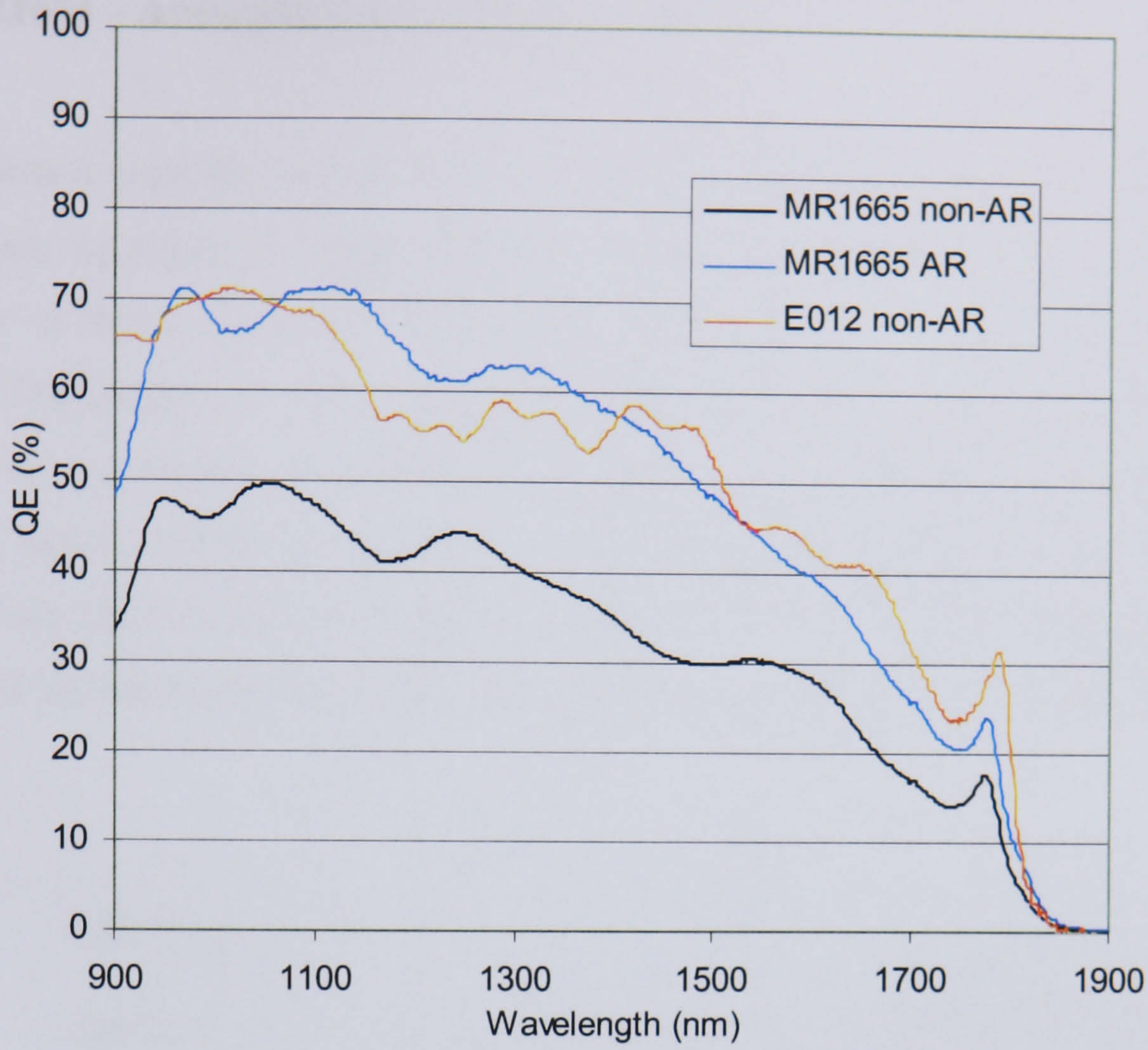

Figure 4.16: MR1665 AR and non-AR quantum efficiencies compared to E012.

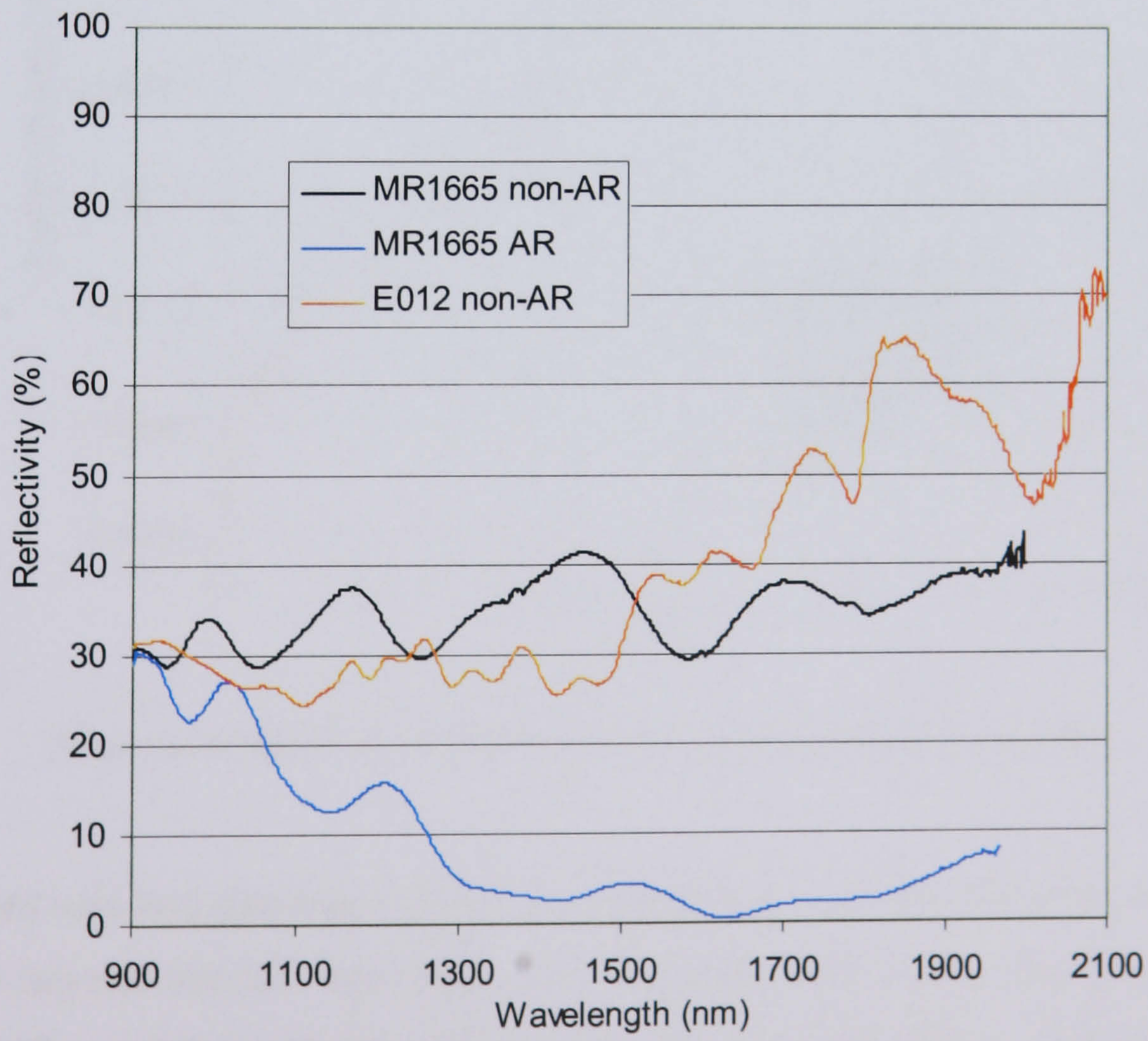

Figure 4.17: Reflectivity comparison between MR1665 AR and non-AR devices and E012 non-AR.

4.2.2. MR1674 – Absorption edge: Beyond 2000nm

MR1674 was a quantum well structure intended to demonstrate absorption out to 2μm, and as such incorporated highly strained InGaAs compositions. To minimise the possibility of strain relaxation in the initial structure only two quantum wells were present. The number of wells could be increased once the strain compensation was shown to be successful. A number of AR and non-AR samples were received with, generally, well bunched dark currents. The AR samples tended to have lower dark current levels than the non-AR samples, suggestive of surface passivation effects. As Figure 4.18 shows the lowest levels are comparable to MR1665 and slightly higher than E012.

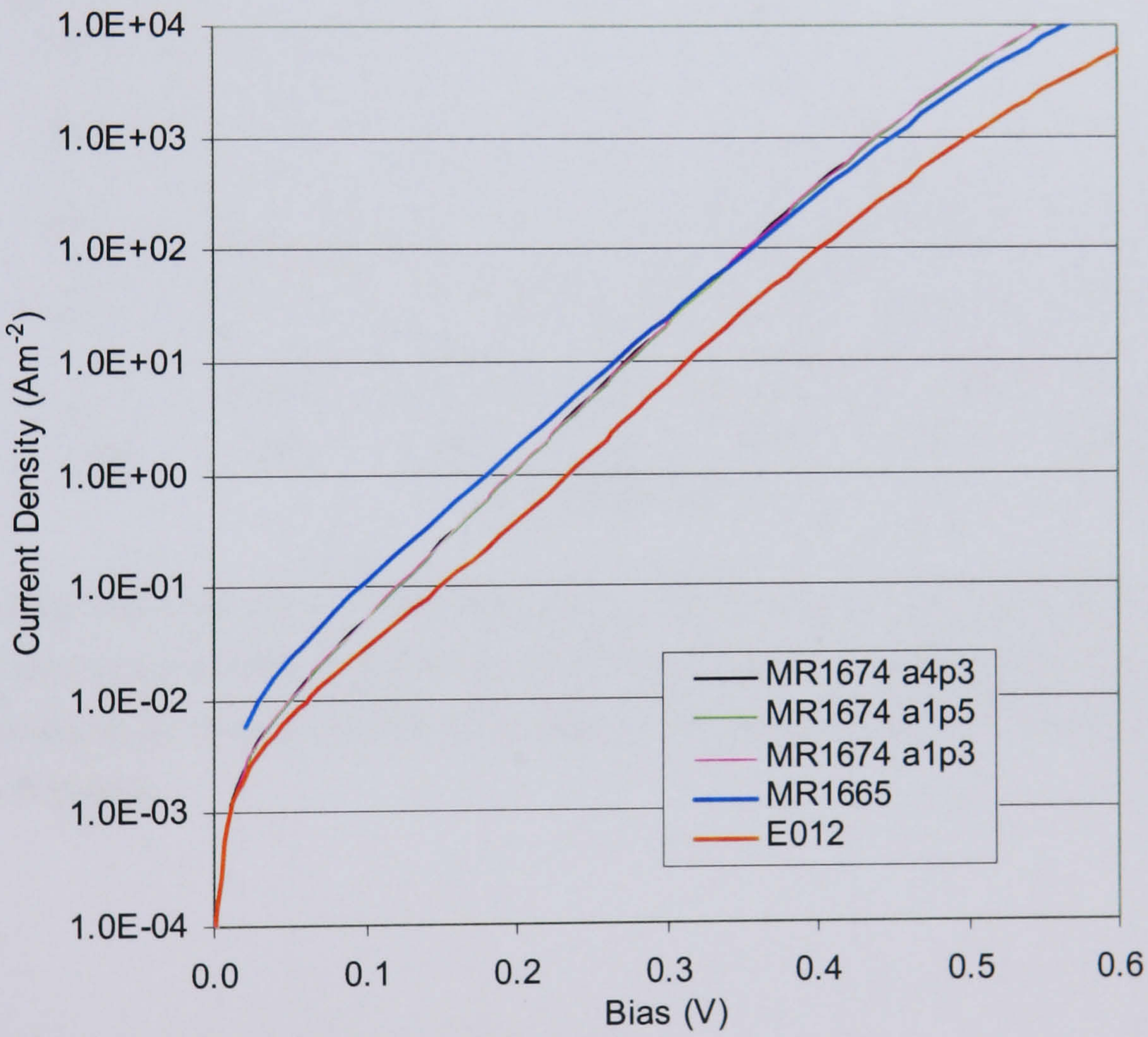

Figure 4.18: MR1674 dark currents compared with MR1665 and E012.

As there are only two quantum wells in the structure the quantum efficiency is expected to be low beyond the InP band-edge, and as Figure 4.19 shows, the level is much reduced with respect to the 30-well samples MR1665 and E012. However in this particular structure the signal becomes so small beyond around 1800nm that the exact

level cannot be measured with the experimental set-up, which is why the data ends abruptly. In addition, the figure shows that there is strong bias and temperature dependence to the quantum efficiency. In order to further study these dependencies, the carrier escape is examined in Section 4.4.3.

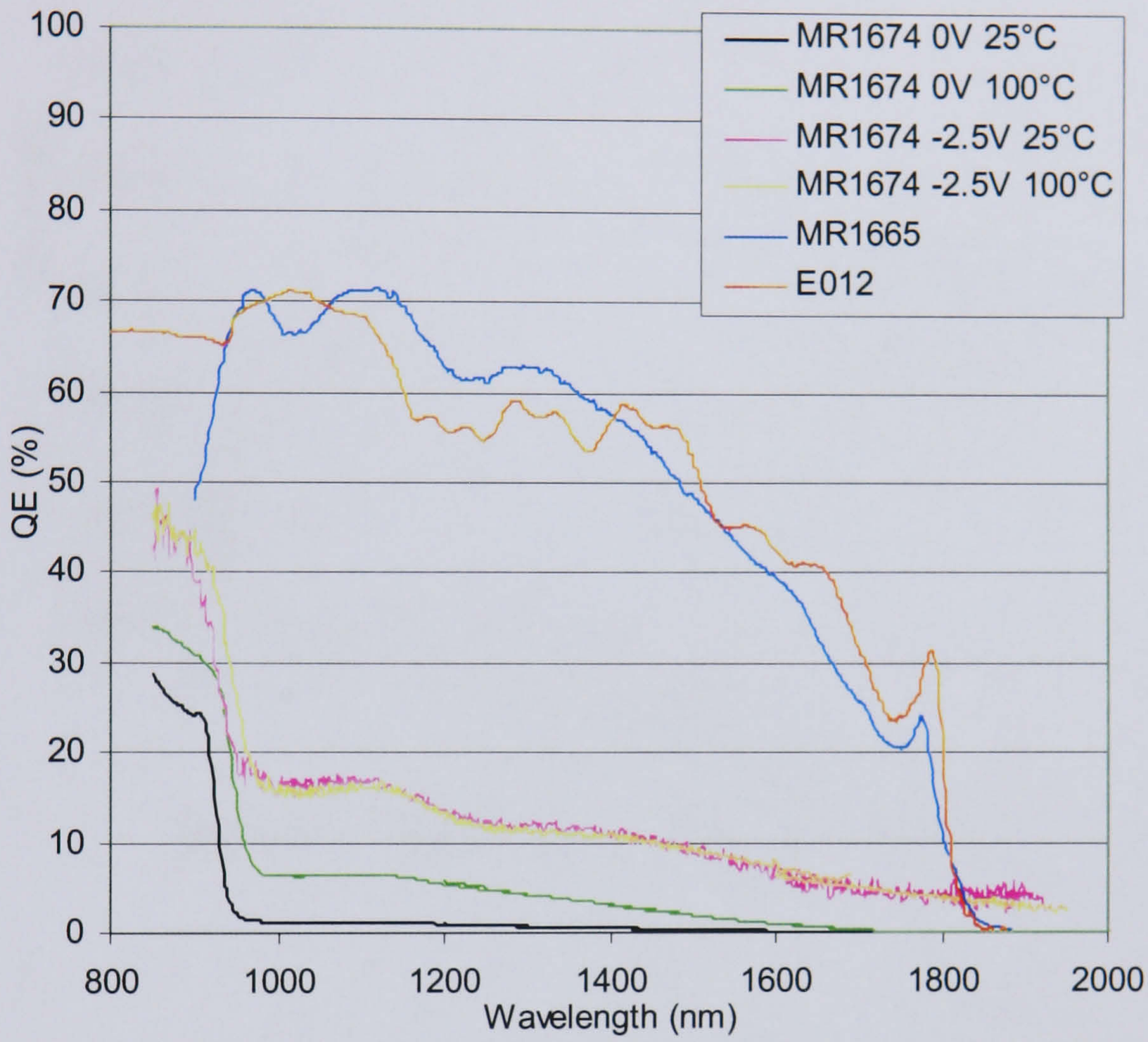

Figure 4.19: Bias and temperature dependent quantum efficiency of an AR coated MR1674 sample. The level is clearly much reduced compared with MR1665 and E012 as there are fewer wells. However, the signal becomes so small that the quantum efficiency cannot be accurately determined at longer wavelengths.

4.2.3. MR1845 – Absorption edge: 1840nm

For the structure MR1845 the well and barrier compositions were chosen such that the strain is intermediate between that of MR1674 and E012. As the strain is reduced, 30 quantum wells were included. For this structure only small area devices were received, both AR and non-AR. The dark currents were well bunched and the lowest are shown in Figure 4.20, only around a factor of two greater than the successful E012.

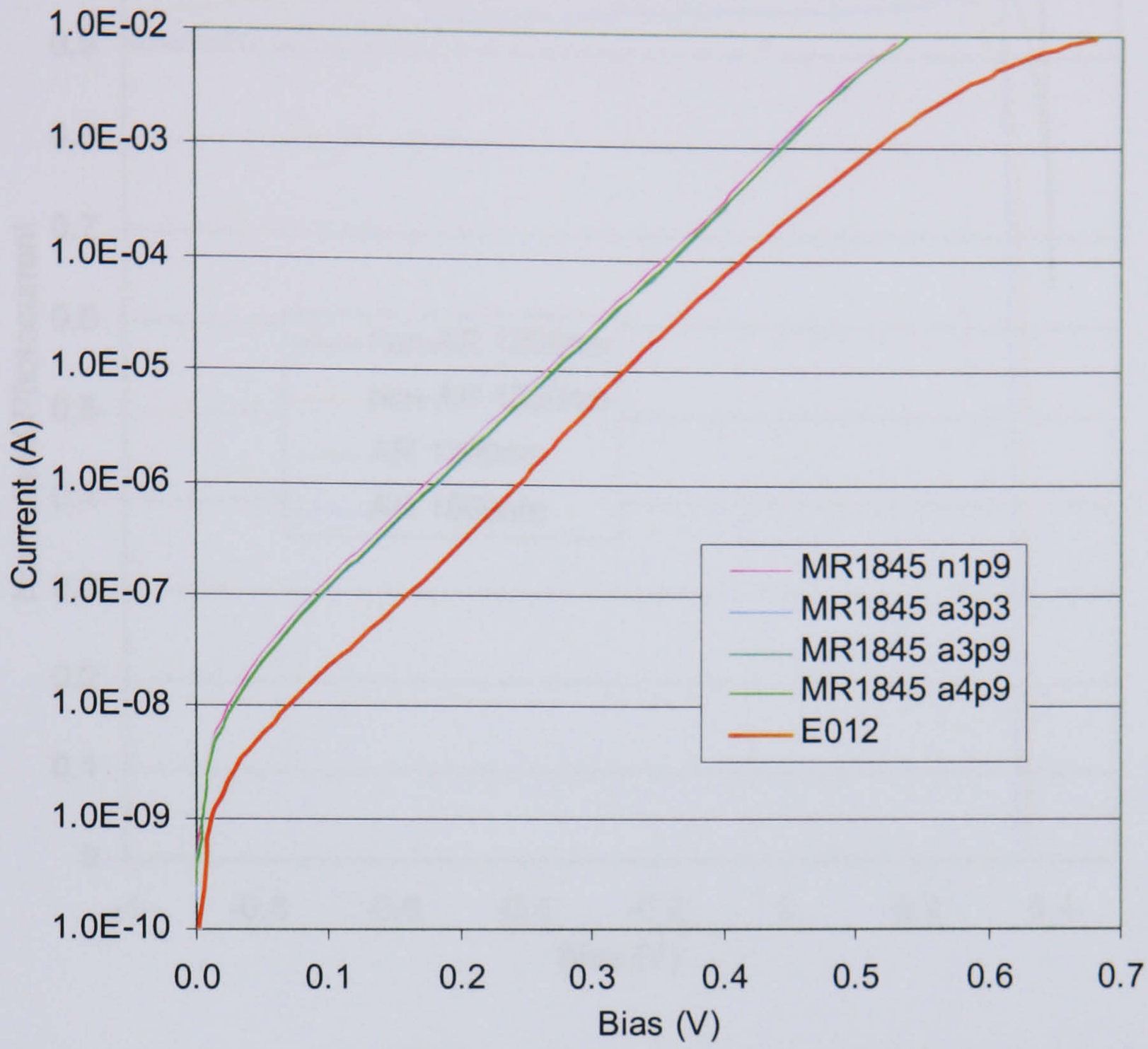

Figure 4.20: MR1845 dark currents compared to E012.

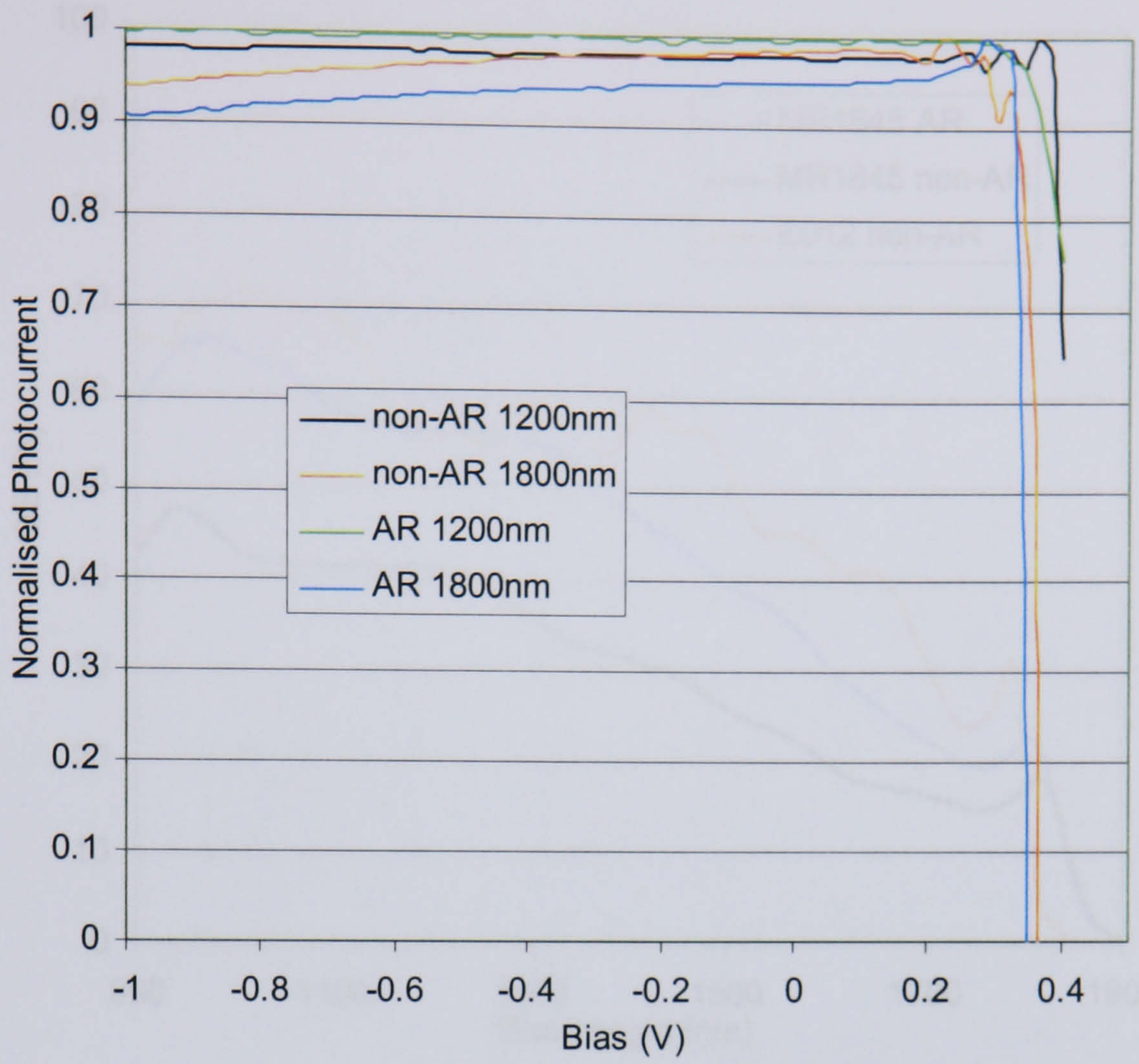

Figure 4.21: Monochromatic I-V of MR1845 samples. The flatness of the curves indicates low background doping in the quantum well region.

In Figure 4.21 the monochromatic I-Vs are given for an AR and a non-AR sample at two different wavelengths above and below the barrier band-gap. The measurements indicate good quality samples with little background doping. The increase in response from the quantum wells as the bias decreases could be a consequence of the quantum confined Stark effect, where the peaks in the conduction and valence band wavefunctions move apart spatially, reducing the overlap.

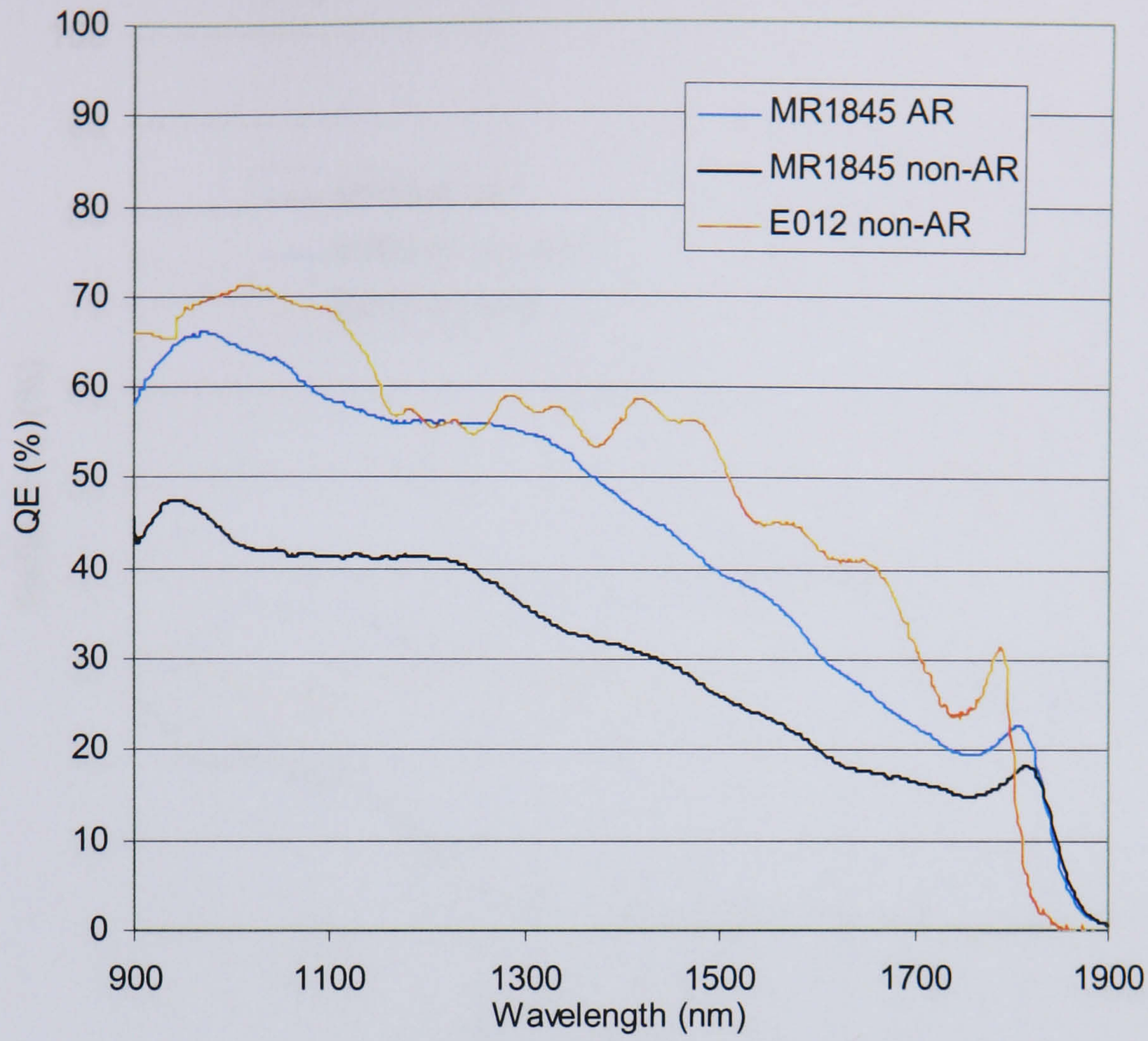

Figure 4.22: MR1845 compared with E012. Again, apart from a rear surface mirror, the response at the exciton wavelength is as good as E012.

Figure 4.22 shows the quantum efficiencies of MR1845 AR and non-AR samples compared with E012. The levels are similar to those of MR1665 in Figure 4.16, suggesting that the response is also as good as E012, apart from the lack of a rear surface mirror. This lack is confirmed by Figure 4.23, where the MR1665 reflectivities do not rise at wavelengths beyond the absorption edge.

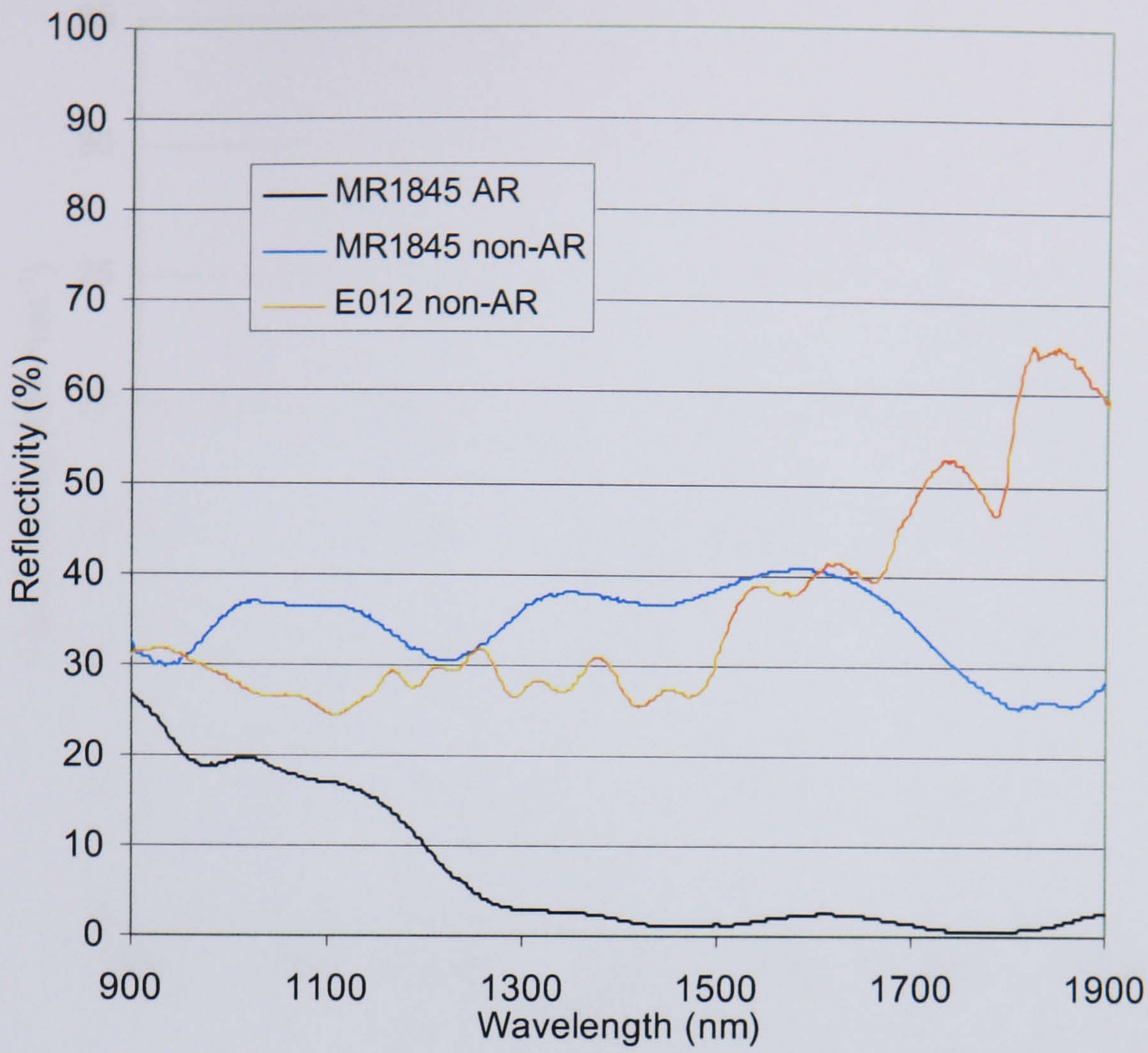

Figure 4.23: MR1845 and E012 reflectivities. The MR1845 devices do not appear to have a rear surface mirror because, unlike E012, there is no rise in reflectivity beyond the absorption edge.

4.3. Light I-V characterisation

The analysis of devices in this section follows the same pattern as for the lattice-matched devices as discussed in Section 3.2. The spectrum used to analyse the strain-compensated structures is a thulia emitter measured at a temperature of 1310°C at the University of Lecce in Italy [4]. thulia emits out to wavelengths of at least 5μm, and peaks at around 1750nm, but there will be a quartz shield between emitter and the cells. The quartz is also expected to be given a coating to reflect back longer wavelengths to the emitter. Therefore, the spectrum is only considered to 2100nm and it is shown in Figure 4.24. The power density of this spectrum at the emitter surface is 19.6kWm^{-2}, which would translate into 8.45kWm^{-2} at the surface of the cells if no funnels were used. As with the lattice-matched devices, the spectrum given in the figure will be used in the calculations.

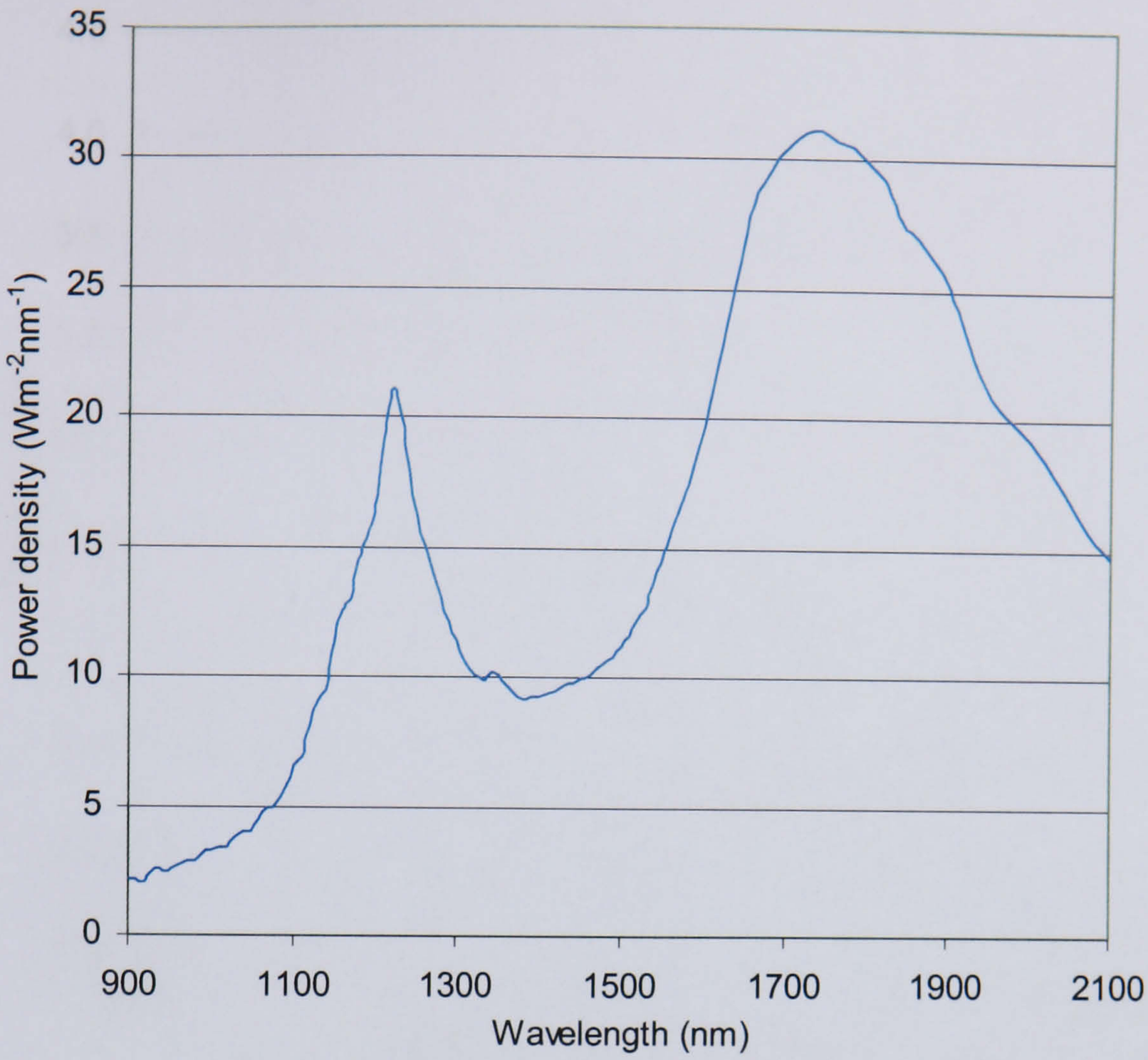

Figure 4.24: Measured thulia emitter spectrum, cut off at 2100nm.

As with the lattice-matched devices, the illumination was supplied by a 150W tungsten bulb on a movable stage. Measurements were performed on small area AR coated devices from wafers E1055, MR1665 and MR1845, whose short-circuit currents under this spectrum are predicted to be 2.88mA, 1.80mA and 1.66mA respectively. As explained in Section 4.1.2, there are no high intensity E012 measurements, primarily because all the devices with initially acceptable dark currents had since deteriorated to the point of being unusable.

4.3.1. Results

As was performed in Section 3.2 for the lattice-matched structures, a series of light I-Vs at differing intensities were taken for each strain-compensated structure. Using the short-circuit currents predicted from the spectrum in Figure 4.24 and comparing with those measured, a plot of efficiency against intensity can be constructed. For the three structures in question this is shown in Figure 4.25.

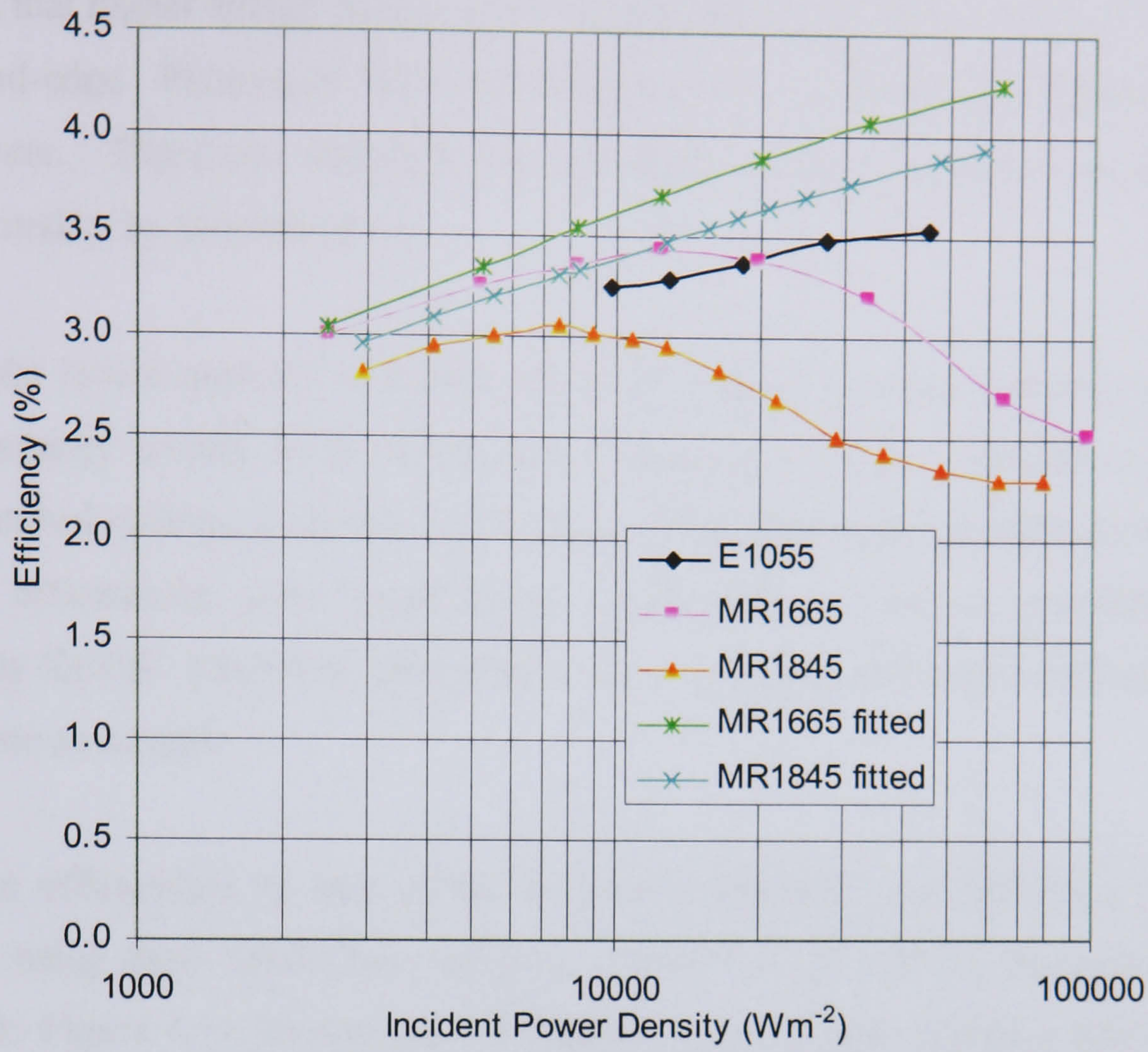

Figure 4.25: Light I-V measurements for E1055, MR1665 and MR1845, plus results modelled from the fitted dark currents of MR1665 and MR1845.

The general features of Figure 4.25 mirror those of Figure 3.25, the equivalent result for the lattice-matched structures. Initially the efficiency rises with the intensity, but due to series resistances the efficiency peaks and then begins to fall. Unlike in Figure 3.25, the efficiencies of these three devices peak at different intensities, yet all three devices were processed as small area mesas. Barring significant differences in the spreading resistance of the top layers, which are slightly different in the three cases, the three devices should possess similar resistances. The differences in the levels and the positions of the peak intensities could be due to the differences in the quantum efficiencies of the three structures.

The spectrum used for all the high intensity light I-V experiments (tungsten bulb) is unlike either of the two spectra used for the lattice-matched and the strain-compensated calculations (erbia and thulia emitters). In terms of the calculation, an absorbed photon of long wavelength light from the selective emitter produces a single electron-hole pair, as does an absorbed photon of shorter wavelength light from the tungsten bulb.

However, that higher energy photon releases more heat into the devices as it thermalises to the band-edge. Photons of different energies are also absorbed in different layers of the structure. Therefore, although the calculation treats all photons as equal, they cannot in reality be considered so.

Because the lattice-matched structures all have roughly the same quantum efficiency, any discrepancy arising from the spectral differences may be expected to affect the lattice-matched structures equally. In the case of the strain-compensated structures, the quantum efficiencies vary significantly, particularly at longer wavelengths and particularly E1055. Therefore, the changes due to spectral differences may not be equal for the three structures.

Again, the efficiencies of two of the structures, MR1665 and MR1845, have been modelled using their fitted dark currents. E1055 could not be modelled because, referring to Figure 4.11, its dark current displays a low ideality factor at low bias and a high factor at higher bias. As with the lattice-matched structures, the performances of the devices are much worse at higher intensities than are predicted from the dark currents alone. This again could be explained by additional spreading resistance encountered by photo-generated current in reaching the contacts, that cannot be detected by dark current measurements.

4.4. Quantum Well Carrier Escape

For THE REV, the purpose of incorporating quantum wells into p-i-n structures is to extend the absorption of the cells to match a selective emitter spectrum, which lies at wavelengths beyond the band-gap of lattice-matched materials. Therefore, it is to be expected that the majority of the absorption will occur in the quantum wells. The ability of the photo-generated carriers to escape from the quantum wells and be collected is a critical factor in the performance of the cells and the system. In this section two quantum well structures are investigated to discover how efficiently carriers escape and are collected.

4.4.1. Theory

A photo-generated carrier that is produced in a quantum well has a number of paths available to it. The preferred route for the photovoltaic application is that it leaves the well (it may overcome this barrier thermally or by tunnelling through it) and is swept to the relevant contact by the electric field and collected. It may recombine in the well, and this it can do radiatively or non-radiatively. In the case of the former, the photon produced may be absorbed somewhere else within the cell and may not be lost. Non-radiative recombination is invariably a loss. A further route for the carrier to follow, in the case of multiple quantum wells, is to tunnel into a neighbouring well.

The simplest structure to investigate is a single quantum well device. There is clearly no inter-well tunnelling and also minimising the number of wells can minimise the amount of tunnelling out of wells. In this case the remaining method for escape, the one of interest, is thermally assisted escape. A number of studies have been conducted into single quantum well structures [5, 6]. In these papers, measurements of collected photocurrent are combined with those of photoluminescence, leading to derivations of the non-radiative recombination efficiency as a function of bias and temperature and the activation energy for carrier escape.

4.4.2. Experimental Details

The investigations in this thesis are concerned with collected carrier efficiency only. The experiment is ideally carried out as a monochromatic I-V, exciting at a single wavelength within the quantum well to measure the photocurrent produced. In some devices there is a large wavelength region at energies slightly higher than the exciton, known as the continuum, where the response is fairly constant. By focussing on this area the absorption can be assumed to be relatively unaffected by temperature and bias. Unfortunately, as most of the quantum efficiency plots in this thesis show, the absorption in multi-well devices does not tend to be constant over large enough ranges for a single wavelength to be chosen for all temperatures. Therefore, a full quantum efficiency scan is taken across the range of the exciton and the data from the continuum

level can then be isolated and analysed. A heating stage was used for above room temperature measurements and a cryostat was used for lower temperatures. Relating the results from the two separate set-ups is discussed where applicable. Sections 4.4.3 and 4.4.4 will contain the specific experimental requirements of the structures under investigation and the results obtained.

One assumption can be used to normalise the measurements. At high reverse biases the band edges in a multi-quantum well cell tilt to such an extent that the barrier to escape for a carrier becomes narrow enough to tunnel through. If high reverse bias is applied at high temperature, where thermal escape is most likely, then the current collected can be taken as indicative of 100% escape, ie. no recombination. It is this point to which all the other data points are normalised.

4.4.3. MR1674

MR1674 contains the deepest quantum wells of any structure in this thesis and, as such, is the most interesting in terms of how successfully the carriers are able to escape from the wells. The structure contains only two wells, in attempt to minimise the risk of strain relaxation. This will also have the effect of reducing inter-well tunnelling. As was seen in Figure 4.19, beyond the InP band-gap the response of the device becomes very small and quite noisy. Therefore, it was necessary to remove the pinhole from the monochromator, in order to increase the amount of light reaching the device.

As the structure exhibited a rather flat response over a large wavelength range, MR1674 was investigated at a single wavelength, 1800nm. Shown in Figure 4.26 is a plot of normalised photocurrent against inverse temperature. As has been discussed, the photocurrent collection efficiency can be taken to be unity at high reverse bias and high temperature. The plot is normalised to this point. The slight dip in the fifth data point from the left in some of the curves is due to correcting for the separate results from the temperature stage and the cryostat. As is seen in Refs 2 and 3, there is a region with a strong temperature dependence, from which the activation energy of the thermal escape can be calculated. The rate of a thermally activated process with activation energy E_A is given by

$$\text{Rate} = A \exp\left[\frac{-E_A}{kT}\right] \tag{4.1}$$

where k is Boltzmann's constant, T is the temperature and A is a constant. A plot of ln[Rate] against 1/T gives a gradient from which the activation energy can be calculated. The activation energy of escape from MR1674 ranges from 12meV at –2V bias to 270meV at zero bias. For comparison, if a conduction band offset of 60% between InP and InGaAs is assumed, the total energy barrier that an electron in the quantum well must overcome to fully escape the structure is around 480meV. It appears from the measurement that the activation energy approaches this value as the band structure becomes flatter in forward bias.

It is clear that carrier escape is incomplete around room temperature and only approaches unity in reverse bias. This bias dependence is unacceptable for photovoltaic purposes where the cell operates in forward bias, but the increased temperatures present in TPV applications may have a slight positive effect in increasing the probability of escape from the quantum wells.

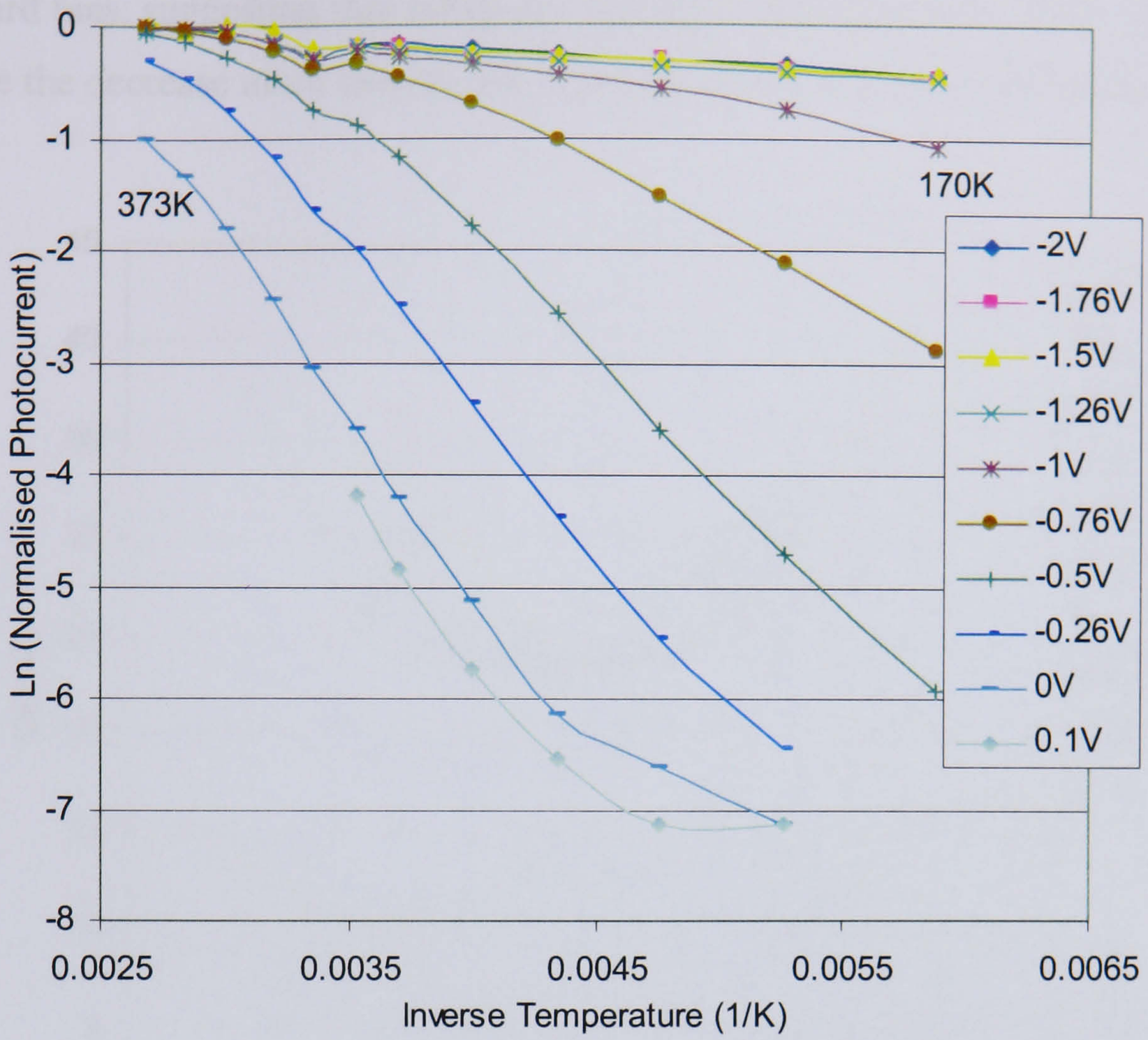

Figure 4.26: Arrhenius plot of normalised photocurrent against inverse temperature for MR1674 at 1800nm. The choice of axes aids the calculation of the activation energy for escape.

4.4.4. E1055

E1055 has been chosen as the nominal structure for the final TPV system, and as such collection efficiency will be an important factor in its performance within the system.

Figure 4.12 shows that the quantum efficiency of E1055 does not possess a flat continuum region at higher energies than the exciton. As the temperature changes, the response at a given wavelength would also be expected to change. For this reason, a series of quantum efficiency measurements were taken at different biases, at each temperature. The measurements made at –2V bias are shown in Figure 4.27. As expected, the quantum efficiency, most noticeably the exciton, moves to shorter wavelengths as the temperature decreases. The first continuum level at energies just higher than the exciton appears to remain at a constant level over most of the temperature range, before dropping sharply around 180K. This pattern is also repeated

into forward bias, suggesting that collection is complete at and above 180K. In order to investigate the decrease more closely, the experiment was repeated, starting from 180K.

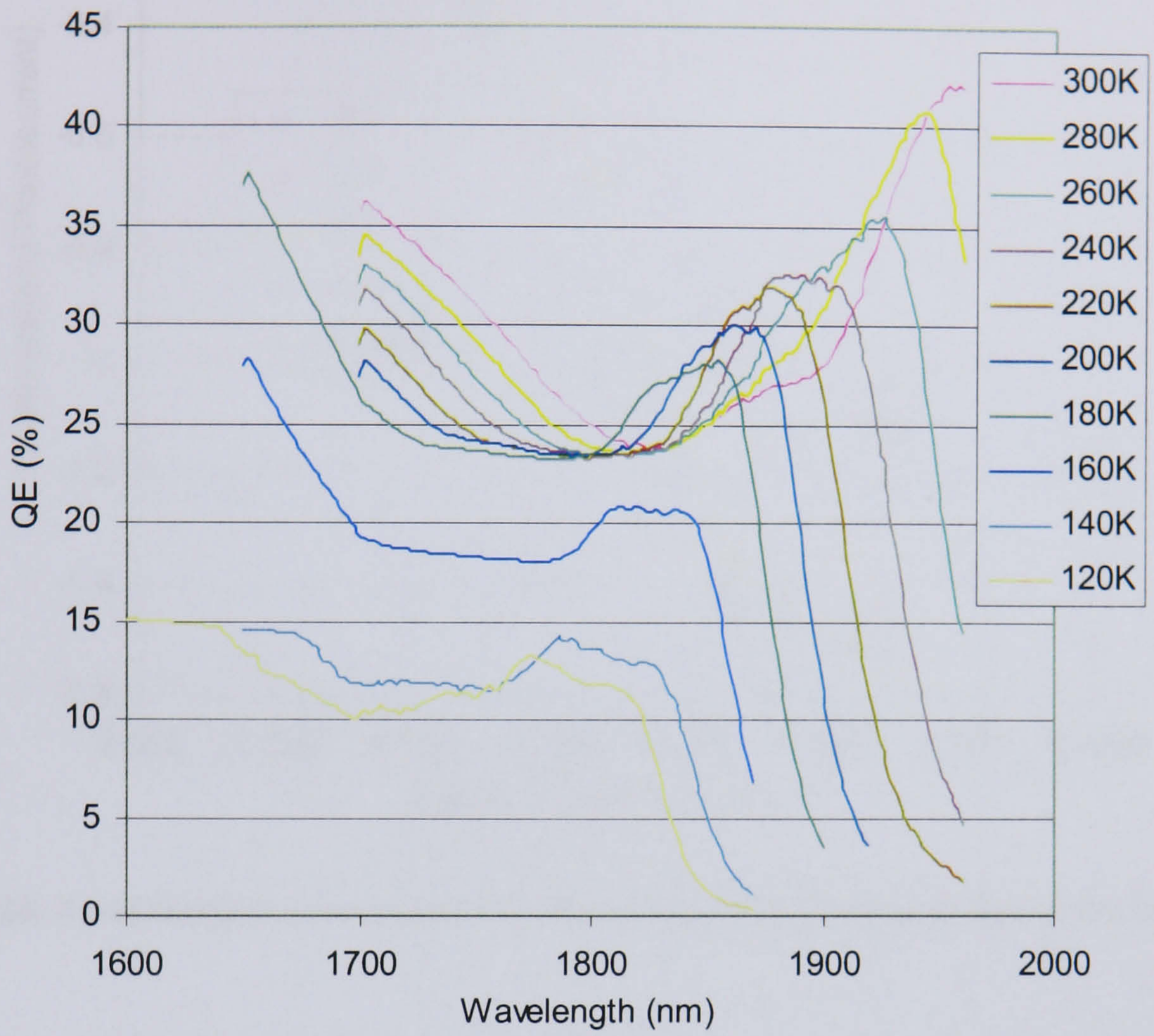

Figure 4.27: Temperature dependent quantum efficiency of E1055 at -2V applied bias.

The results are shown in Figure 4.28. They indicate a distinctive decrease in response from 180K to 130K. The 0.15V bias measurement yields an activation energy of 96meV, much lower than the zero bias figure for MR1674 and much lower than the 483meV barrier that is found between the bottom of the well and the InP in the conduction band using the same assumption that was made for the MR1674. It is notable that the temperature 180K corresponds to a thermal energy of 15meV, far below the activation energies calculated from the data. It could be suggested that escape from the quantum wells in this sample is aided by the multi-well structure, where inter-well tunnelling can occur. However, a lower thermal energy than the calculated activation energy is also seen in Refs. 2 and 3, using single quantum well structures.

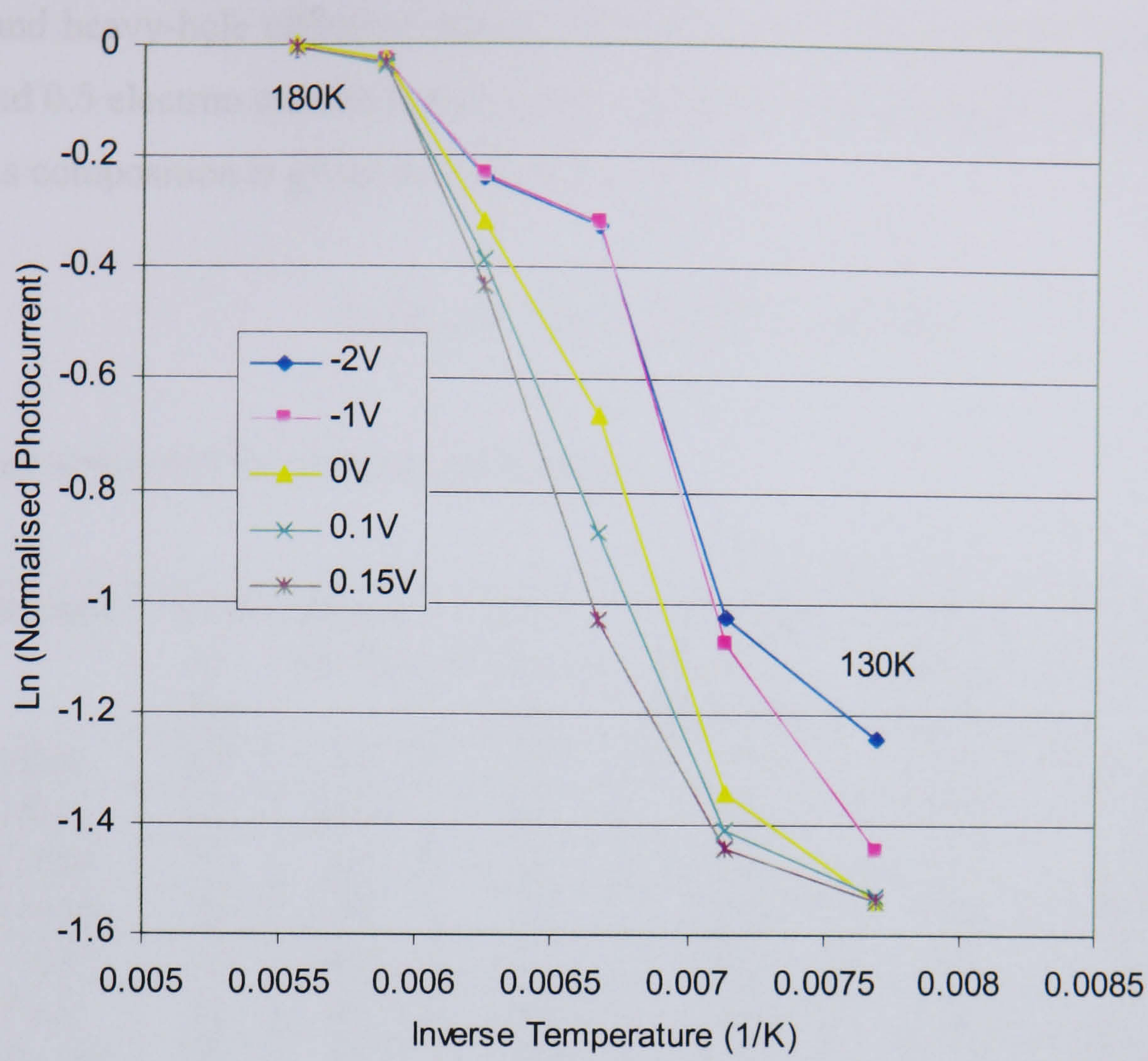

Figure 4.28: Arrhenius plot of normalised photocurrent against inverse temperature for E1055.

Although the reduction in carrier collection below 180K has been investigated, the important result for the TPV system itself is that the collection appears to be complete above this temperature, even in forward bias. As the cells will operate at a far higher temperature in the system, these results are compelling evidence to show that the quantum well region is of good quality and that all photo-generated carriers will be successfully collected.

4.5. A Study of Strain-Compensated Quantum Well Structures

Table 4.1 contains a breakdown of each of the strain-compensated structures characterised in this thesis. The measured band-edge is taken as the wavelength at which the quantum efficiency is half that at the exciton. The expected band-edge is calculated as the energy difference between the first electron level in the conduction band quantum well and the first heavy-hole level in the valence band quantum well. An offset of 60% is assumed in the conduction band between InP and InGaAs. The

electron and heavy-hole effective masses in InGaAs are taken from the model SOL to be 0.05 and 0.5 electron masses respectively. The band-edge energy (E_g) of an $In_{1-x}Ga_xAs$ composition is given by Equation 4.2.

$$E_g \text{ (in eV)} = 0.35 + 0.592x + 0.478x^2 \tag{4.2}$$

Strain is not accounted for in these calculations.

Structure	Well In (%)	Barrier In (%)	Well thickness (nm)	Calculated absorption edge (μm)	Measured absorption edge (μm)	Error (%)
E012	62	47	12	1.85	1.80	2.70
E016	62	44.9	12	1.85	1.75	5.41
E1054	75	45	8	2.12	1.95	8.02
E1055	75	45	8	2.12	1.97	7.08
E1057	75	45	8	2.12	1.97	7.08
Final	74	45	8	2.09	1.96	6.22
MR1665	62	45	12	1.85	1.80	2.70
MR1674	74	36	10	2.13	>1.95	N/A
MR1845	68	40.6	10	1.97	1.84	6.60

Table 4.1: Calculated and measured absorption edges for all the strain-compensated structures received. All thicknesses and indium compositions are the nominal values.

The lattice constant of lattice-matched $In_{0.53}Ga_{0.47}As$ is 5.86Å. As the illustration of strain compensation in Figure 1.10 shows, the quantum well material has a larger natural lattice constant. When it is compressed laterally to the substrate lattice constant this results in an increase in lattice spacing normal to the substrate. Hence, the spacing between quantum well layers as they are grown is larger than 5.86Å, not only naturally, but also due to the compression. The quantum well thicknesses in the table above range from 80Å to 120Å, ie. roughly between 13 and 20 atomic layers. A single grown atomic layer more or less can result in up to a 7% change in well thickness.

The structures with the least deviation between calculated and measured absorption edges are the early structures containing the least strain, E012, E016 and MR1665, which are all nominally similar. From the TEM image in Figure 4.6, the thickness of the well/barrier period in E012 is seen to be as requested, 24nm. Therefore, by varying

the composition of the wells only, it is possible to obtain the absorption edge that was measured by decreasing the indium fraction from 62% to 60%, a 3.2% relative change in composition. Although no TEM is available to definitively ascertain the cause of the absorption edges in E016 and MR1665, well composition would appear most likely to be responsible as it does have the most significant effect: a decrease in well thickness from 120Å to 110Å (an 8.3% relative change, roughly 2 atomic layers) only shifts the calculated absorption edge from 1.85μm to 1.84μm. Clearly, growing exact numbers of atomic layers is difficult and large percentage variations in quantum well thickness are possible. However, in calculations it would appear that well thickness has a relatively minor effect on absorption edge compared to variations in well composition.

As a result of the difficulties in measuring the response of MR1674 at long wavelengths, no comment may be made about the absorption edge, except that the quantum efficiency (Figure 4.19) does appear to extend beyond the limit of the measurement. MR1845 is similar to E012, E016 and MR1665 in that the large difference between the calculation and the measurement can only realistically be explained by a change in composition of the quantum wells. The measured absorption edge can be modelled by reducing the indium content of the wells from 68% to 65%, a 4.4% change. Again, changing quantum well thickness (in multiples of 0.5nm) has a much smaller effect on the absorption edge, which does not rule out thickness changes, but shows that they cannot be solely responsible for the measured absorption edge.

The structures showing the largest differences between the calculated and measured absorption edges are the final three structures, E1054, E1055 and E1057, from which the final structure was designed. These structures possess not only the thinnest quantum wells, but also the highest indium fraction in those wells. It is to be expected of such thin quantum wells (containing around 13 atomic layers) that there will be variations in the number of atomic layers throughout the well region. Indeed the quantum efficiencies in Figure 4.12 exhibit excitons with multiple peaks, strongly suggesting variations in well thickness. Despite such thin wells however, it is again only changes in quantum well composition that can successfully model the measured absorption edges. Reducing the indium content of the wells from 75% to 70% (a 6.6% change) moves the calculated absorption edge from 2.12μm to 1.95μm. In addition, varying the

well thickness between 7.5nm and 8.5nm (± one atomic layer) produces an absorption edge range of 1.93-1.96μm. This range includes all the measured structures' absorption edges.

4.5.1. Summary on quantum well structures

By comparing the measured absorption edges of all the quantum well structures with the predictions of a theoretical calculation, it has been found that the all structures cease to absorb at shorter wavelengths than expected. By considering changes in quantum well thickness and composition, the calculations shows that the well thickness has a much smaller effect on absorption edge. This is despite the fact that large percentage variations are possible due to the small number of atomic layers present in each individual quantum well. The measured absorption edges of all the structures can be modelled by decreasing the percentage of indium within the quantum wells. The TEM image of structure E012, see Figure 4.6, illustrates that the thicknesses of such thin layers can be achieved with good levels of accuracy, which suggests that it is composition that is subject to less control during growth.

4.6. Conclusions

In this chapter all the strain-compensated structures received were characterised. The first structure received exhibited the promising characteristic of absorption at longer wavelengths than the best lattice-matched structure, whilst also possessing a lower dark current. It also showed the presence of a rear surface reflector, which enhances the quantum efficiency and returns unused photons to the TPV heat source. The magnitude of the rear surface reflection was calculated separately by two complimentary models and was found by both to be 65%. By modelling, the significance of the effect of this reflection could be seen in that when it was reduced to zero, the modelled quantum efficiency dropped significantly.

The large positive effect of the rear surface reflector is also seen in later structures, whose measured quantum efficiencies are much lower than the structure exhibiting the

effect. In these structures the reflectivities show that the reflector is absent. If the quantum efficiencies are modelled to include the rear surface reflector then the levels can be increased such that they are comparable to the original structure.

As with the lattice-matched structures, large area devices displayed poorer dark currents than their small area counterparts, although a few of the later large area devices were comparable. The light I-V characteristics of the large area devices were generally poor, with the modelled I-Vs overestimating the measured I-Vs. A number of small area devices were measured at high intensity, with results similar to those from the lattice-matched structures: the efficiency peaks at a lower intensity than would be the case if the front contact design was optimised for the minimum series and spreading resistance.

In addition to I-V and quantum efficiency, temperature dependent monochromatic I-V studies have also been conducted on quantum well carrier escape, a vital factor in the ability to collect photocurrent. The structure with the deepest quantum wells (MR1674) showed poor collection, with high temperatures and reverse bias required to extract a significant proportion of the photocurrent. Although a temperature above room temperature would be present within the TPV system, devices must operate in forward bias, and this would result in a greatly reduced collected current.

The structure E1055 showed much better temperature characteristics. For this structure, the lowest temperature that produced maximum photocurrent was over 100°C below that which the device would be exposed to in the system. This complete collection was also maintained into forward bias, suggesting that this structure will not compromise the TPV system by failing to produce current.

The success of the strain-compensated quantum well growth in achieving absorption edges calculated from the nominal structures has been assessed. All the grown structures have a shorter wavelength absorption edge than expected. This appears to be attributable to quantum well composition rather than well thickness; changing the indium fraction of the wells has a much larger effect on the calculated absorption edge than changing the well thickness. All of the quantum wells in this thesis are between 8-12nm thick. This corresponds to between 13-20 atomic layers in each well. One quantum well more or less is equivalent to up to a 7% change in well thickness, yet the

calculations suggest that this only causes a minimal shift in absorption edge. The TEM image of one of the structures (E012) shows that layer thicknesses can be very accurate, which is a further indication that it is quantum well composition that is mostly responsible for the variations in absorption edge.

The structure that was decided upon for the final thulia TPV generator was based on E1055, which had been successful in extending the absorption to wavelengths where the majority of the thulia spectrum would be absorbed.

4.7. References

[1] P Abbott et al., Characterisation of Strain-Compensated InGaAs/InGaAs Quantum Well Cells for TPV Applications. In Coutts et al [Ref 23 in Chapter 1], pp.213-221. Rome, Italy, September 2002.

[2] C Rohr, InGaAsP Quantum Well Cells for Thermophotovoltaic Applications, PhD Thesis, Imperial College of Science, Technology and Medicine, 2000.

[3] N J Ekins-Daukes et al., Strain-Balanced Criteria for Multiple Quantum Well Structures and Its Signature in X-ray Rocking Curves. *Crystal Growth and Design,* **2**, (4), pp.287-292, 2002.

[4] D Diso, Private Communication.

[5] A Zachariou et al., A carrier escape study from InP/InGaAs single quantum well solar cells, *J. Appl. Phys.*, **83**, 877-881, 1998.

[6] J Nelson et al., Steady-State Carrier Escape from Single Quantum Wells, *IEEE J. Quantum Electron.*, **QE-29**, 1460, 1993.

5. Alternative Processing Techniques

In this chapter a number of alternative, and supplementary, processing techniques are discussed. The main focus is the need for low resistance layers under the contact fingers and across the whole device for the conduction of the photo-generated current, leading to a novel design whereby the device is inverted and light enters through the substrate. The motivation for this new design is discussed in Section 5.1. An important consideration for an inverted device structure is the below band-gap absorption of the InP substrate, which does not form the active region but through which the light will now be required to travel. The absorption of InGaAs is also considered and the theory and experiment involved in the determination of these absorption coefficients form Section 5.2. Section 5.3 contains the experimental investigation into the potential of this design. A further processing technique that can increase the efficiency of the devices is an anti-reflection (AR) coat. Section 5.4 discusses these techniques and also the consequences of system design on potential AR coats.

5.1. Inverted Cell Processing

5.1.1. The Present Design

One of the considered advantages of combustion driven TPV is a high incident power density of the order of $1Wcm^{-2}$ [1]. Given efficient cells, this would manifest itself as a high current density within the cell, of the order of $1Acm^{-2}$; the current density is hoped to be as high as $14Acm^{-2}$ in THE REV. As this current must travel laterally to reach the top contact fingers it is necessary for the spreading resistance of these top layers to be as low as possible. This must, of course, be achieved without compromising the optical performance of the cell.

Resistance within a doped semiconductor layer can be reduced by increasing either the layer thickness or the doping concentration [2]. All of the device structures reported in this thesis are grown as p-on-n devices (see Appendix A1), in order to reduce zinc

doping in the p-region. In the majority of cases the uppermost layers are an InP emitter with an InGaAs top contact layer. A schematic of the current device structure is shown in Figure 5.2. In all the previous test structures grown for THE REV the p-region has not been of sufficiently low resistance to be suitable for high current operation, although it is satisfactory for laboratory test conditions where the metallisation is much higher. It therefore must be altered if the existing device structure is to be retained.

The maximum doping concentration for zinc in InP is set by the point at which the zinc ceases to be substitutional and becomes interstitial. This maximum concentration (around $3\times10^{18}cm^{-3}$ [3]) is not of a high enough level to produce the required conductivity in the 0.5μm thick emitter. This suggests that an increase in thickness is required. However, the layer thickness would need to be increased to around 5μm in order to achieve such low resistance. Growth of such thick layers is problematic; a good surface morphology is more difficult to obtain, particularly if this extended growth takes place on a highly strained stack of quantum wells. In addition, the increased time required to grow the thicker layer could allow further unwanted dopant diffusion to occur. The conclusion here is that a simple adjustment of the existing structure is not sufficient.

The main reason that lattice-matched InGaAs is used as the top contact layer is that it can be doped to around five times the concentration of InP, and hence possesses a lower resistance. This would suggest that a possible solution would be to not remove this contact layer from the optical window in the device, leaving it as a complete layer to aid carrier transport. However, the absorption edge of InGaAs is around 1660nm, which would result in absorption of the high energy tail of the selective emitter spectrum. This loss of spectral intensity is illustrated in Figure 5.1, where a thulia spectrum is compared to InGaAs absorption, here represented by the quantum efficiency of E004. The overlap is substantial. Using tabulated data for the absorption of p-doped InGaAs [4], the effect of a 2μm thick InGaAs top layer is a reduction in incident power density over the range 1000-1700nm of 40%. This wavelength range is that over which the absorption data extends, but there would clearly be further loss at shorter wavelengths.

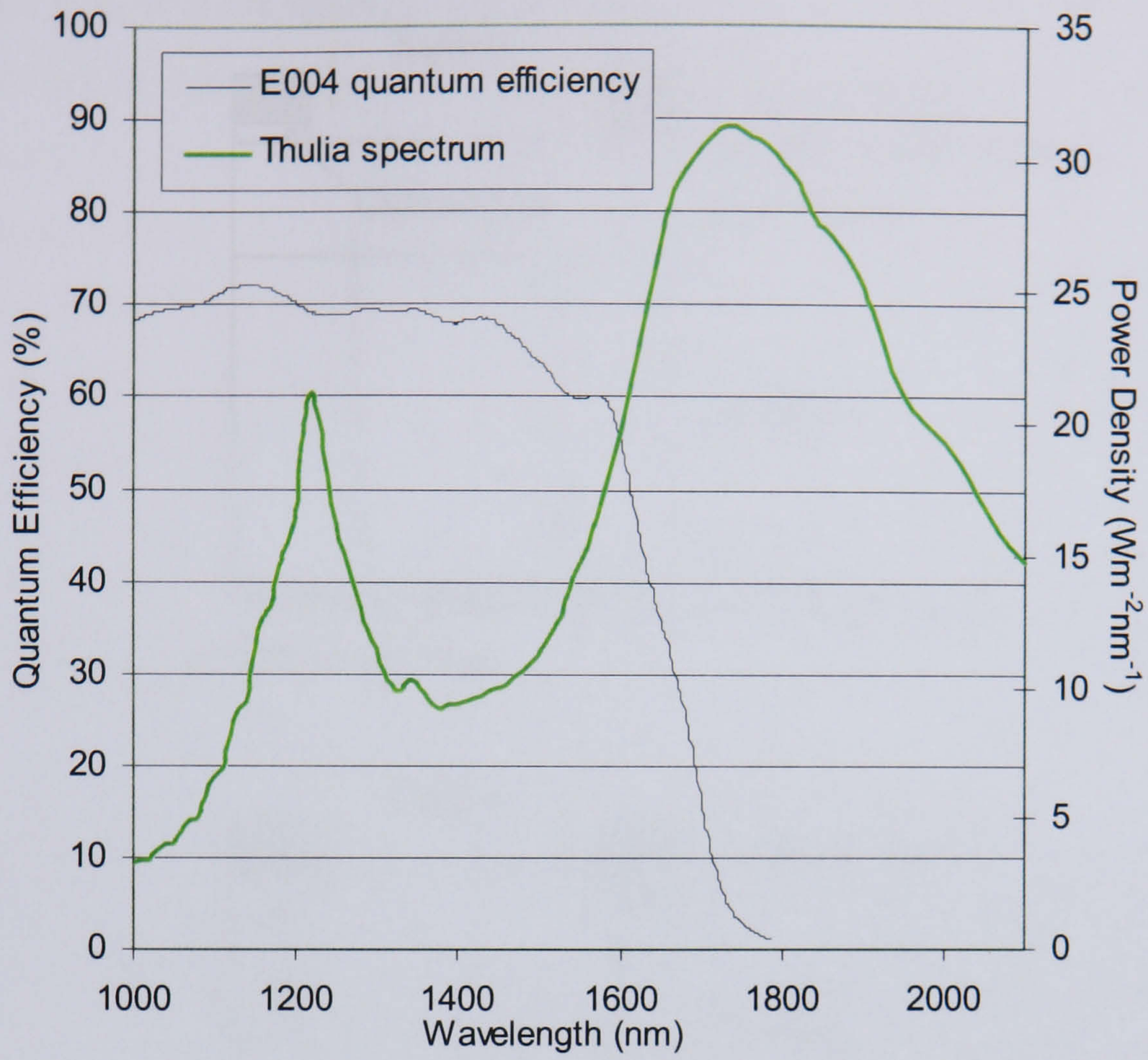

Figure 5.1: An illustration of the overlap between the thulia spectrum and InGaAs absorption, here represented by E004. Much of the high energy spectrum would be lost if there was an InGaAs layer over the optical window.

5.1.2. The Inverted Cell Design

A low level of spreading resistance within the uppermost layers can be realised by simply inverting the wafer prior to processing. In this configuration the contact fingers are placed on the substrate and light enters from the 'bottom' of the cell, see Figure 5.2, which compares this new structure with the existing design.

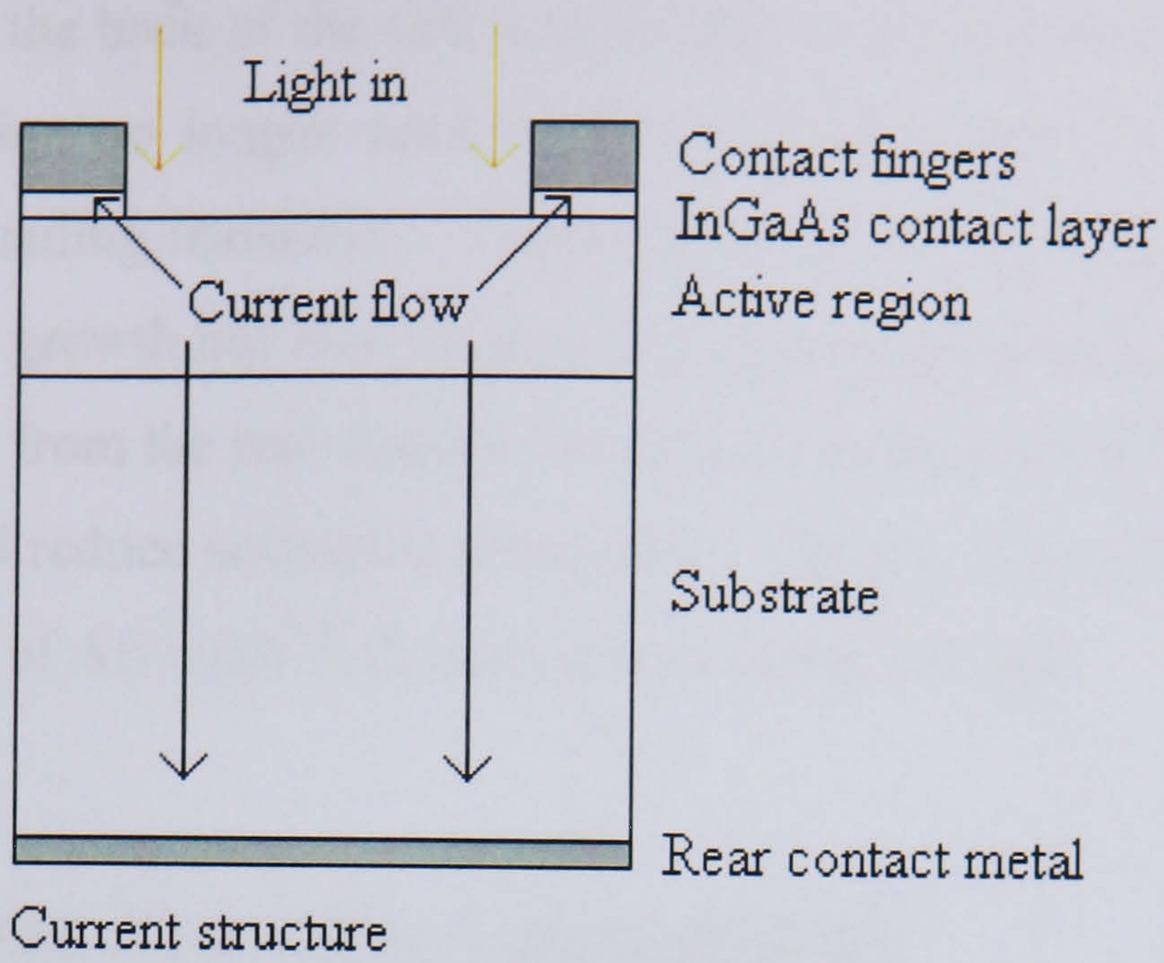

a) Current structure

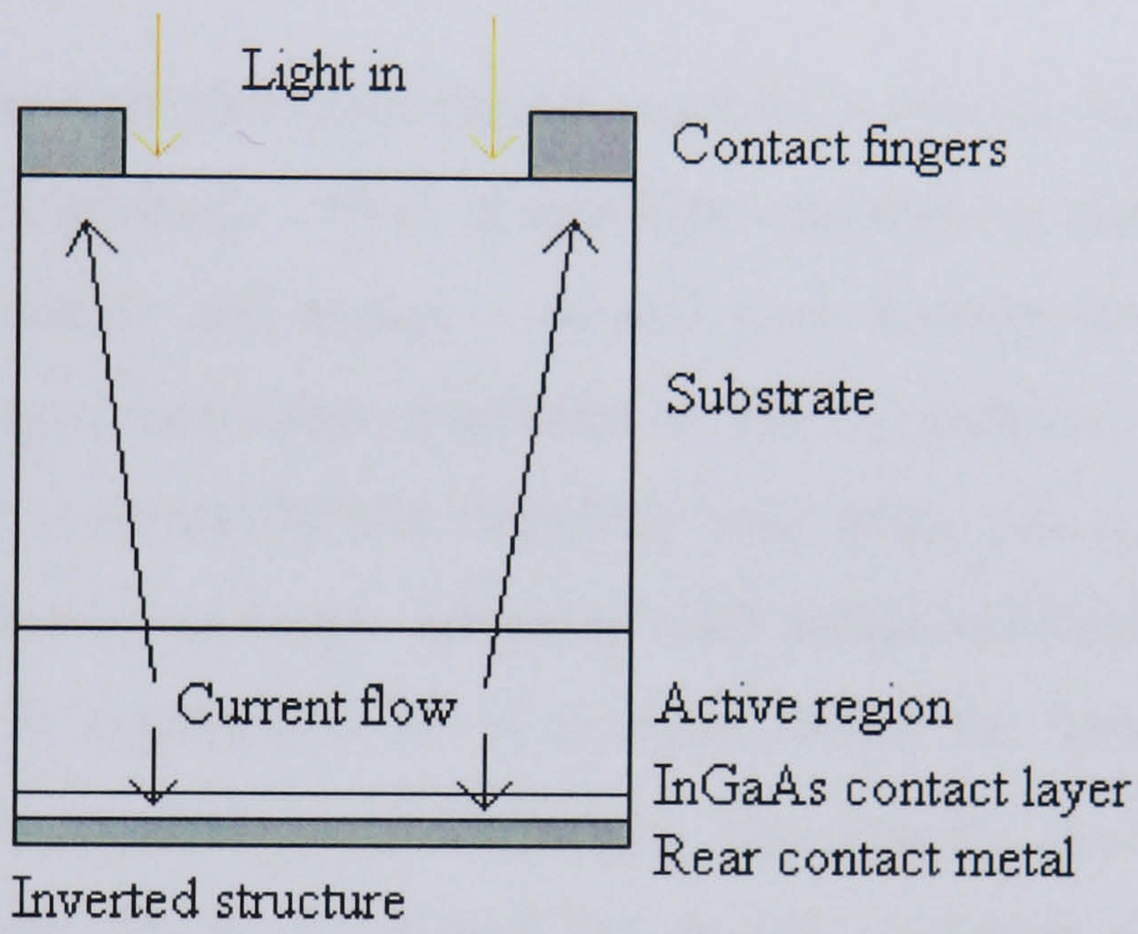

b) Inverted structure

Figure 5.2: The current 'normal' structure of processed devices, a), is compared with the proposed inverted structure, b). The thick substrate allows the carriers moving laterally upwards to the finger contacts to move along a path of lower resistance. The figures are not to scale.

This design has a number of positive aspects. Clearly no changes are required in the growth. With regard to processing, the obvious change is that all the steps, with the exception of the mesa etch, are now performed on the opposite side of the wafer. This does not introduce additional work or difficulty per se, provided that the lithographic alignment can be carried out sufficiently accurately that the mesa etch (now on the rear) is aligned correctly with the front contact pattern.

The 350μm thick n-doped InP substrate now forms the top layer of the cell structure, with sufficiently low resistance for efficient carrier collection. The InGaAs contact

layer, which is now at the back of the cell, can be fully metallised and, because carriers collected in the p-region no longer need to travel laterally, may be thinned without compromising the spreading resistance. Thinning would be advantageous not only in requiring less material growth but also because any light making a second pass through the cell after reflecting from the rear contact would need to pass twice through this layer and a thinner layer will reduce unwanted absorption. The fact that the InP front surface allows for the addition of AR coats is discussed later in this chapter.

5.2. Below Band-Gap Absorption Considerations

Clearly, the fact that the light must now pass through the substrate makes knowledge of the absorption of InP important. Also, if any light unabsorbed during the first pass reflects off the rear contact and makes a second pass through the device then the InGaAs rear contact layer must also contribute as little absorption as possible. The absorption edge of InP is around 920nm, therefore little of the selective emitter spectra will be absorbed across the band-gap. Similarly with lattice-matched InGaAs, most of the incident spectrum is expected to be of energies below the band-gap. However, knowing the absorption at these below band-gap wavelengths, and in particular the effect of passing through 350μm of n-doped InP, is still useful for accurate modelling and predictions for the performance of the new design.

5.2.1. Sample Descriptions

The absorption of InP was determined using a 350μm thick double-sided polished sulphur n-doped (concentration of 2×10^{18} – 8×10^{18} cm^{-3}) InP wafer supplied by IQE. The InGaAs used in the investigation forms part of a previously grown photovoltaic device structure called MR1181 [5]. This structure was grown in Sheffield and is a lattice-matched InGaAs structure grown on a similar InP substrate with orientation (100) offset 0.35° to (110). The nominal structure is shown in Table 5.1. The individual properties of the differently doped InGaAs layers are expected to be indistinguishable in the measurements, but the result, possibly a weighted mean of the

individually doped layers, should still be sufficient for predicting the performance of the inverted structure.

Thickness (nm)	Material	Doping type	Dopant	Concentration (cm^{-3})
150	InGaAs	p	Zn	3×10^{18}
1277	InGaAs	i	-	-
500	InGaAs	n	Si	8×10^{17}
300	InP	n	Si	3×10^{18}
Substrate	InP	n	S	

Table 5.1: Nominal structure of MR1181, which contains 1927nm of InGaAs lattice-matched to InP.

5.2.2. Theory

The calculations of absorption coefficient, which mirror the model described in Section 2.2.6, follow those of Humphreys et al [4], in that the wafer is treated as a uniform absorbing medium bounded to air by flat parallel surfaces. The assumption of flat surfaces is justified particularly for the bare double-polished InP substrate. Normal incidence is assumed throughout. An iteration is used to simulate multiple reflections and passes through the structure. In this way expressions for the total reflection (R_{tot}) and transmission (T_{tot}) of the InP wafer can be derived as functions of absorption, and are given as in Ref. 4:

$$T_{tot} = \frac{(1-R_s)^2 \exp(-\alpha_s l_s)}{1-R_s^{\,2} \exp(-2\alpha_s l_s)} \tag{5.1}$$

$$R_{tot} = R_s\left(1 + T_{tot} \exp[-\alpha_s l_s]\right) \tag{5.2}$$

R_s is the reflection at an air/InP surface and l_s is the thickness of the substrate, leaving the absorption coefficient of the InP substrate (α_s) as the only free parameter.

As transmission is a more accurate measurement than reflection, the absorption is initially calculated from Equation 5.1. The reflection is then predicted from Equation

5.2 and compared with the measured reflection, giving a further indication of the validity of the theory.

As in Ref. 4 the InGaAs here is present as an epitaxially grown layer on an InP substrate, and it is also treated in the same manner as above. However, whereas Humphreys has neglected reflection at the internal InP/InGaAs boundary, it is included here. The inclusion of this boundary requires that the 1.927μm thick InGaAs layer is treated as a thin film, where interference effects now become important. Subsequently, the first step in treating this structure is to derive the reflection and transmission of a thin layer of InGaAs bounded on each side by semi-infinite air and InP. Clearly, the sum of reflection and transmission is expected to be less than one and this shortfall is assumed to be absorption within the InGaAs. The whole wafer can then be treated as before as simply an InP wafer, but with a modified reflection and transmission at its front surface. The theory of reflection and transmission of layers of thin films is fully described by Macleod [6] and is given in Section 5.4. The calculations in this case are simplified by the facts that there is only one thin layer and that normal incidence is used throughout.

Once expressions for the reflection R_l and transmission T_l of the InGaAs layer on InP have been derived, the MR1181 wafer can be treated as an InP substrate with an air interface at the rear, reflection R_s as before, and a front interface with reflection R_l and transmission T_l. By iterating multiple reflections within the structure, expressions for the total transmission T_{tot} and reflection R_{tot} of the wafer can be derived:

$$T_{tot} = \frac{T_l(1-R_s)\exp(-\alpha_s l_s)}{1-R_l R_s \exp(-2\alpha_s l_s)} \tag{5.3}$$

$$R_{tot} = R_l + \frac{R_s T_l T_{tot} \exp(-\alpha_s l_s)}{1-R_s} \tag{5.4}$$

The reader is reminded that α_s is the absorption coefficient of InP and that the absorption coefficient of InGaAs is contained within the terms T_l and R_l. Again, the transmission measurement will be used for initial determination of the InGaAs

absorption with a comparison of extracted and measured reflections being used to confirm the results.

5.2.3. InP and InGaAs absorption results

The results obtained with the InP wafer are shown in Figure 5.3. The measured transmission is used in Equation 5.1 to yield the absorption coefficient of InP (also shown in Figure 5.3. The measurement stops slightly short of 900nm because the absorption increases rapidly and the transmitted signal becomes too small to measure accurately. As discussed earlier, the transmission measurement is the more accurate and thus is used to extract the absorption. Equation 5.2 gives the expected reflectivity of the wafer with respect to transmission and absorption and this is shown on Figure 5.3 along with the measured reflectivity. The close agreement gives confidence in this method. InP absorption data from a tabulated source is shown in Figure 5.3 [7]. However, towards the band-edge the data becomes very sparse before falling to zero, hence there are only two data points shown in the figure, which are in good agreement with the experimentally determined data.

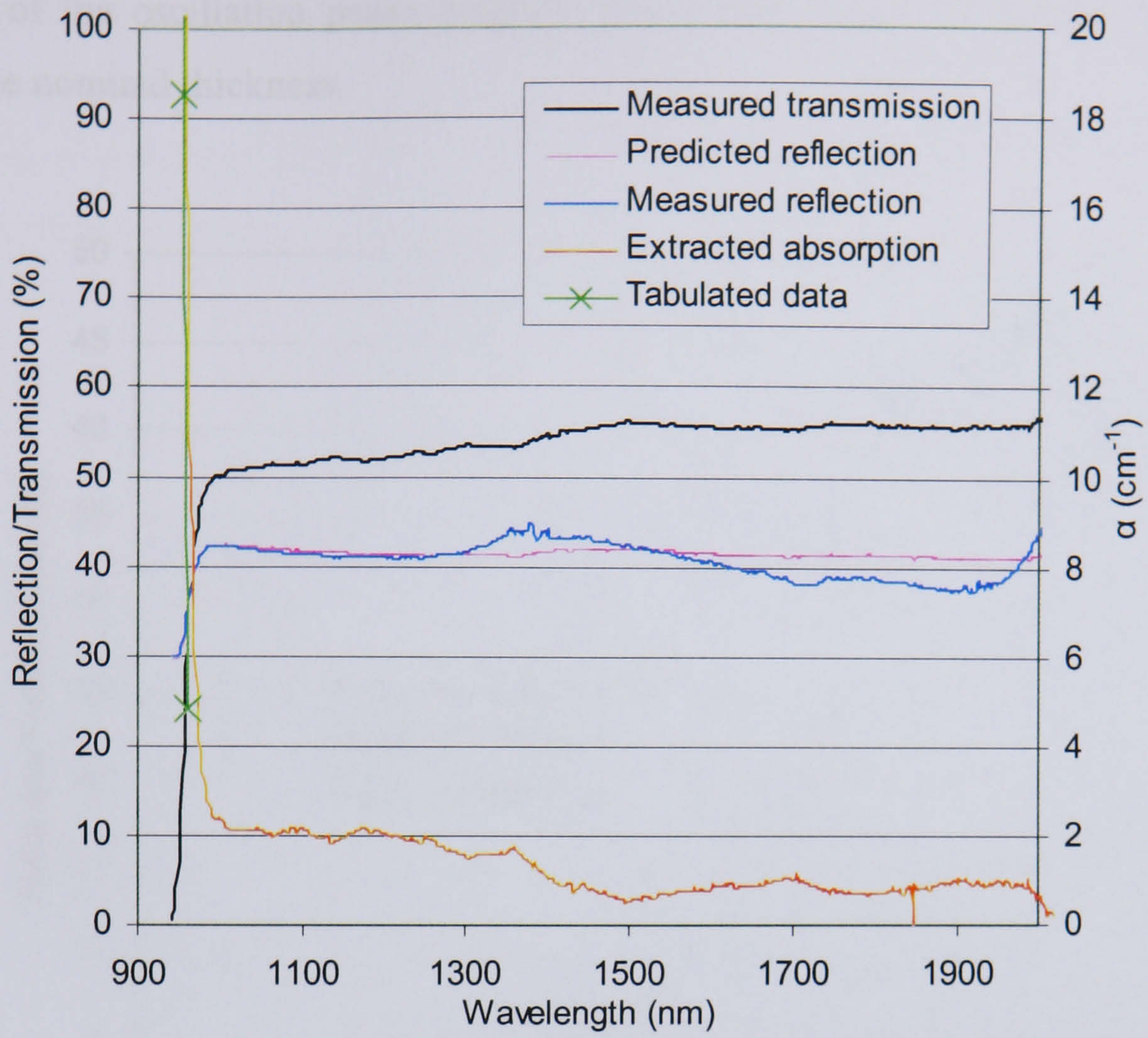

Figure 5.3: The measured transmission of the InP wafer yields the absorption coefficient (right-hand axis). The theory also predicts the reflectivity of the wafer, which is confirmed by experiment. Also included is tabulated data from Ref. 7, although only two data points are available over the range of the experiment.

The below band-gap absorption is very low. For illustration, at wavelengths beyond 1500nm the absorption is $1cm^{-1}$, which corresponds to a loss of about 3.5% through a 350μm wafer. If the surfaces of the wafer were not perfectly flat and parallel, a proportion of the light would be expected to escape from the wafer yet not be detected by either the reflectivity or transmission measurements, say by diffuse reflections. This would result in an overestimation of the absorption within the wafer, and hence the absorption results obtained should be considered to be an upper limit.

Figure 5.4 shows the measured transmission of the wafer MR1181, the InP substrate with a 2μm epitaxial layer of lattice-matched InGaAs. By using this data in Equations 5.3 and 5.4, the absorption can be calculated. The predicted reflection can also be calculated and this is also shown in Figure 5.4, along with the actual measured reflection. The measurement is again close to the theory, with the discrepancy in the

positions of the oscillation peaks possibly due to the total InGaAs layer not having exactly the nominal thickness.

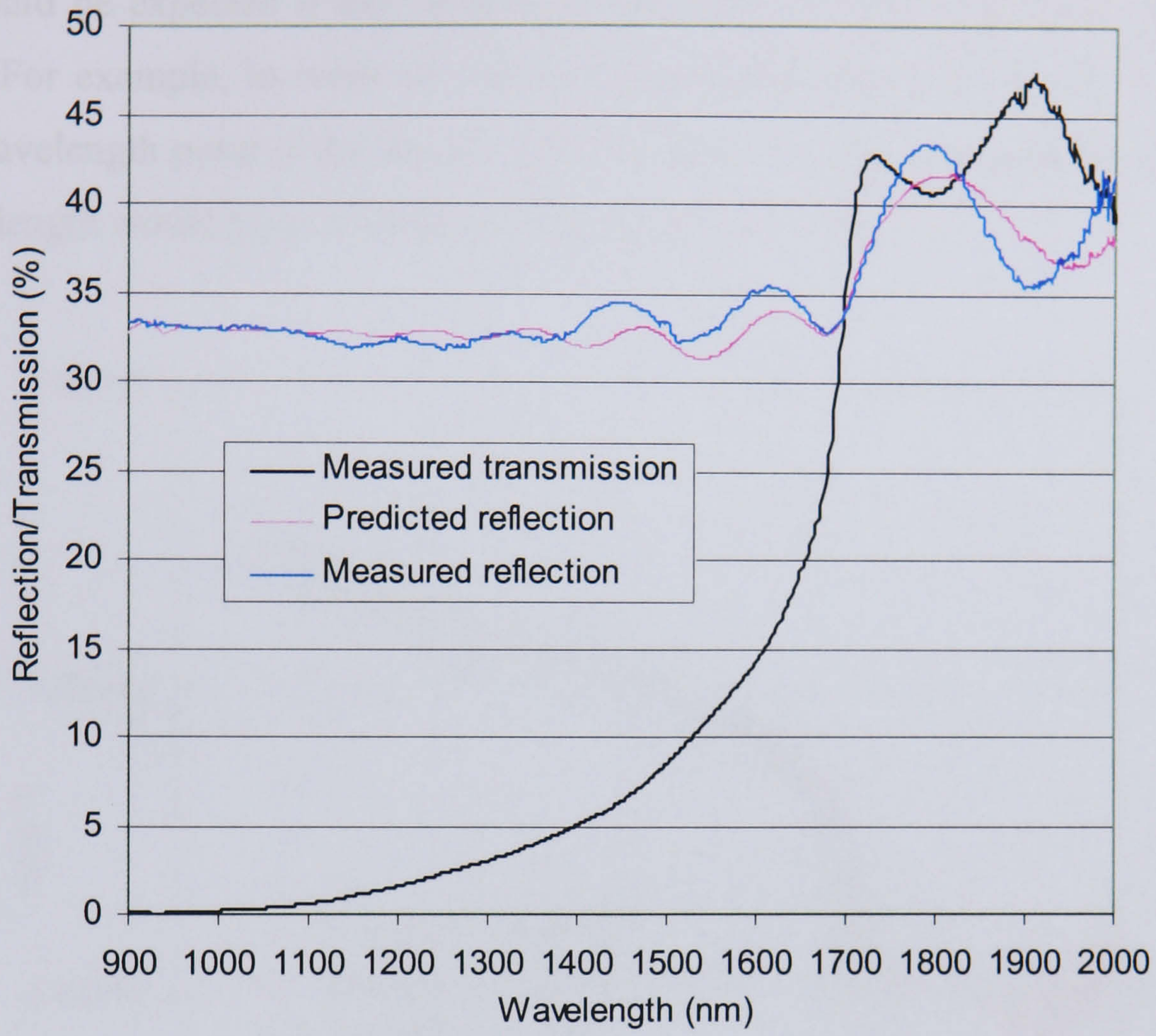

Figure 5.4: Measured transmission of MR1181. The expected reflection is also shown compared to the measured reflection.

The experimentally determined absorption of InGaAs, extracted from Equation 5.3, is shown in Figure 5.5. Also in the figure are four other sets of published data. Three were calculated in Ref. 4 for n-, p- and p+ doped InGaAs. As was discussed, this data was produced by neglecting the internal InP/InGaAs boundary. The fourth data set was calculated by Bacher et al. also using a thin-film theory [8]. If the internal boundary is neglected then the calculations follow the same method as for the InP wafer and these are given in Ref. 4. The absorption obtained by neglecting this boundary is also shown in Figure 5.5.

Up to the InGaAs absorption edge the calculated data agrees well with the other published data, showing that the internal boundary is indeed negligible. The published data does not extend beyond the absorption edge, suggesting that the absorption reduces

to levels below that measurable; certainly the sharp drop is clear. That the experimental data remains at a relatively high level is a possible limitation of the experiment. One cause for an overestimation of the absorption is an underestimation of the transmission, which would be expected if the surfaces of the wafer were not perfectly smooth and parallel. For example, in order to reduce the extracted absorption to the level of the longest wavelength point of the Bacher data in Figure 5.5, the measured transmission at that wavelength would have to increase from 42.3% to 51.0%.

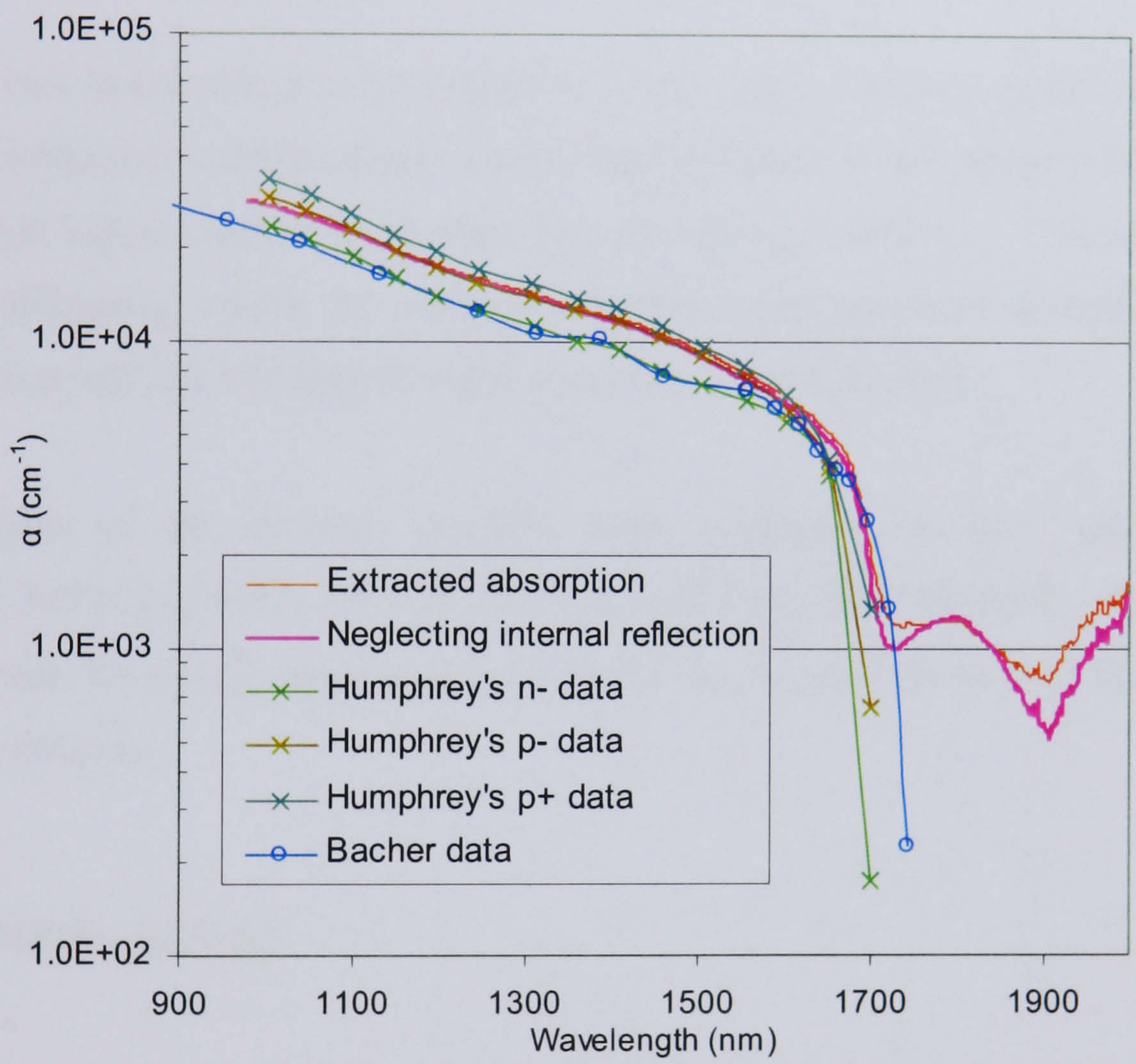

Figure 5.5: Calculated InGaAs absorption coefficient. This is compared with three data sets where the internal InP/InGaAs boundary was ignored (Ref. 4), and another using a different thin-film theory (Ref. 8). The calculated absorption if the internal boundary is ignored is also shown for comparison.

5.2.4. Summary On Absorption Measurements

The below band-gap absorption of InP is very low, of the order of a 3.5% loss over 350μm of substrate. The experimental data for InGaAs agrees with existing data up to the absorption edge, where the measurement becomes unreliable. It seems not

unreasonable to assume that the actual absorption of InGaAs below band-gap is at a similar low level to InP. If the inverted structure is to be a suitable design, the measurements conducted in the next section should show that the collected photocurrent is only reduced by about 4% when illuminated from the reverse compared to the front.

5.3. Investigation of the Inverted Structure

There are two characteristics of proposed inverted structure which require investigation. The first is the dark current, where the inverted structure should display a lower series resistance at higher current levels than the conventional structure. The second is the quantum efficiency, where the substrate absorption, as measured in Section 5.2.3, is expected to result in a 4% drop in signal from the inverted devices.

Investigations of the inverted structure were conducted on four separate device structures: MR1020, E012, MR1091 and the final THE REV material. The details of each material, the experimental method used and the results obtained are all given in the following sections.

5.3.1. MR1020 and E012

The simplest way to examine the effect of reversing the wafer on quantum efficiency is by using a device which can be illuminated from both sides, in order to determine how the amount of collected photocurrent is affected when the device is turned around. For this, an unprocessed wafer with the appropriate contacts can be used. In order that the test is as fair as possible, the wafer under investigation must have two smooth surfaces.

Two wafers were located which satisfied the requirements for the quantum efficiency investigation. The first was a previous Sheffield wafer MR1020 [5]. On visual inspection it appeared to possess a rear surface as smooth as the front. The structure of MR1020 is given in Table 5.2. The second sample was a piece of IQE grown wafer E012.

Repeats	Thickness (Å)	Material	Dopant	Type	Concentration (cm^{-3})
1	1000	InGaAs	Zn	p	3×10^{18}
1	2500	InP	Zn	p	8×10^{17}
1	2500	InP	-	i	-
60	70	Q1.1	-	i	-
60	100	Q1.6	-	i	-
1	70	Q1.1	-	i	-
1	5000	InP	Si	n	3×10^{18}
Substrate		InP		n	

Table 5.2: Nominal structure of MR1020. Q1.1 and Q1.6 are InGaAsP lattice-matched to InP with band-edges of 1.1μm and 1.6μm respectively.

5.3.1.1. Experimental Details

Both pieces of wafer were of roughly $2cm^2$ area. To simulate the optical window of a fully processed device the InGaAs top contact layer was etched away over a large area of each wafer. The etchant was that used in Sheffield: 1 H_2SO_4: 8 H_2O_2: 40 H_2O for approximately 13 seconds. Metal contacts were then evaporated onto both sides of each wafer in the area where the contact layer remained. The procedure used is given as steps 1 and 2 in Section 2.1.1. The wafers were then mounted on a copper disc with a hole; the area of wafer without the contact layer was suspended over the hole. External contacts were then made as described for large area devices in Section 2.1. The layout is shown in Figure 5.7. Clearly, this is not optimum processing and this form of device can be used to investigate relative quantum efficiency but not dark current.

A determination of whether illuminating the wafer from the rear significantly affected the amount of collected photocurrent could in theory have been achieved simply by taking a photocurrent measurement, then turning around the stage on which the wafer is mounted and repeating the measurement. However, it could not be guaranteed that reversing the stage would illuminate the wafer at exactly the same point. And in view of the non-ideal contacts that were made to the wafers, in particular the lack of contact fingers, it was possible that there would be significant variation in response due to spreading resistance as the beam moves across the wafer, particularly with the distance to the contact.

The experiments on MR1020 and E012 were conducted on the quantum efficiency set-up, with the copper disc mounted on the three axis translational stage. The stage could be rotated 180° through a vertical axis to expose either side of the wafer to the light from the monochromator.

5.3.1.2. MR1020 Results

The first experiments conducted on the MR1020 wafer were reflectivity and transmission. These were taken from the front and the rear of the wafer, and the results are shown in Figure 5.6. The results from the front of the wafers vary little from those from the back, especially the transmission measurements. The similarities indicate that both surfaces are indeed smooth. Had only one surface been smooth then the reflectivity from that side would have been around 30%, with direct reflectivity from the rough side being much lower due to the scattering. These results show that whatever difference in collected photocurrent is found between front and rear, it is unlikely to be caused by variations in reflectivity or transmission.

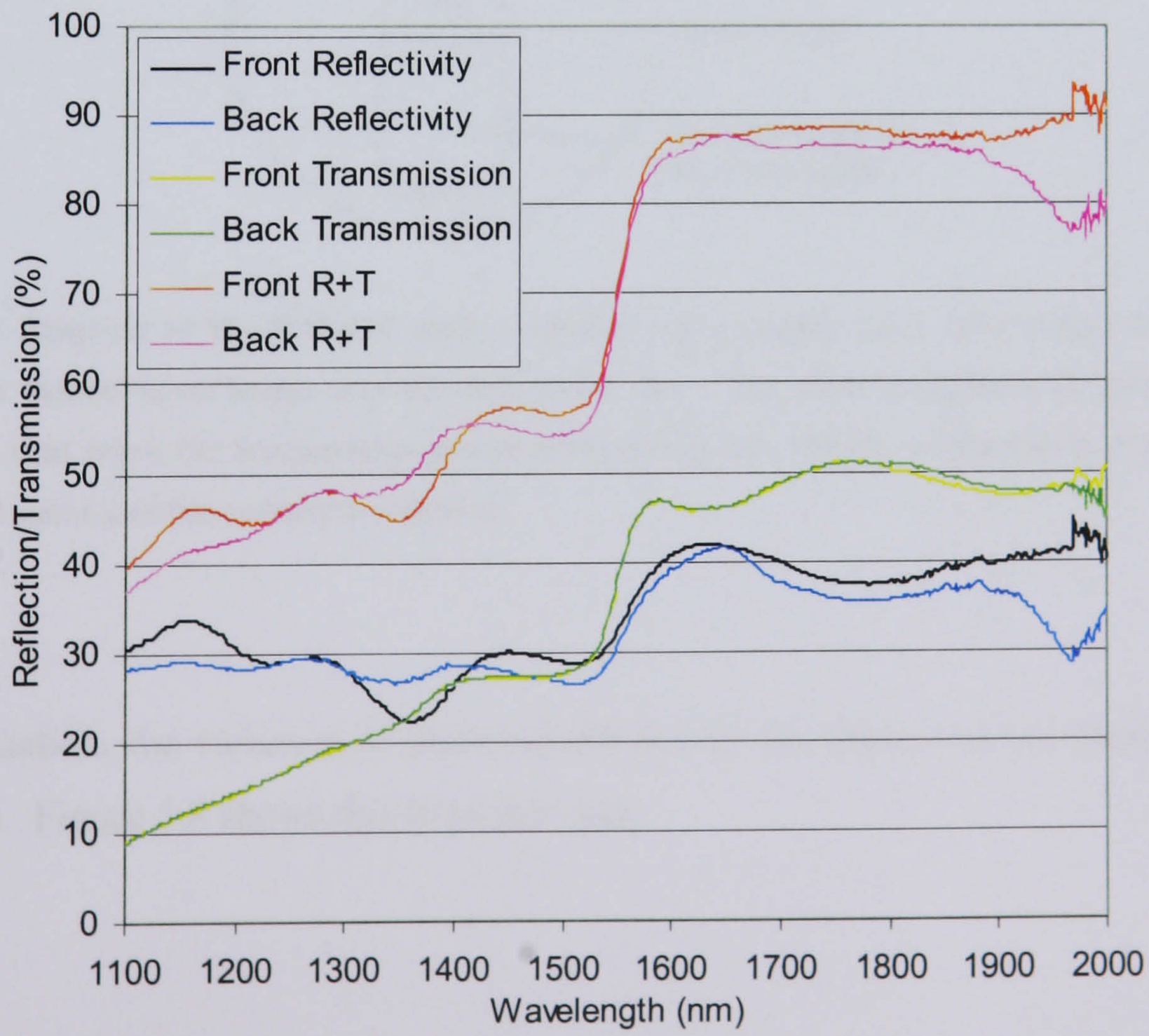

Figure 5.6: Reflectivity and transmission of MR1020 taken from the front and the rear of the wafer.

To examine the two sides of the wafer the translational stage is simply turned through 180° about a vertical axis. Therefore, there can be little question that, in the vertical direction, the illumination will fall in the same place on both sides of the wafer. The only doubt about positioning front and rear concerns the horizontal position of the beam for the two measurements.

The following experiment conducted on MR1020 was a series of quantum efficiencies taken at a number of positions along the wafer in the horizontal direction. This was performed on the front of the wafer, with each position related by a single turn of the dial controlling the stage; a single turn corresponded to 0.5mm of movement. The copper disc was in an orientation such that the contact was above the area being scanned and thus the change in distance from the illuminated point to the contact was minimised. This situation is illustrated in Figure 5.7.

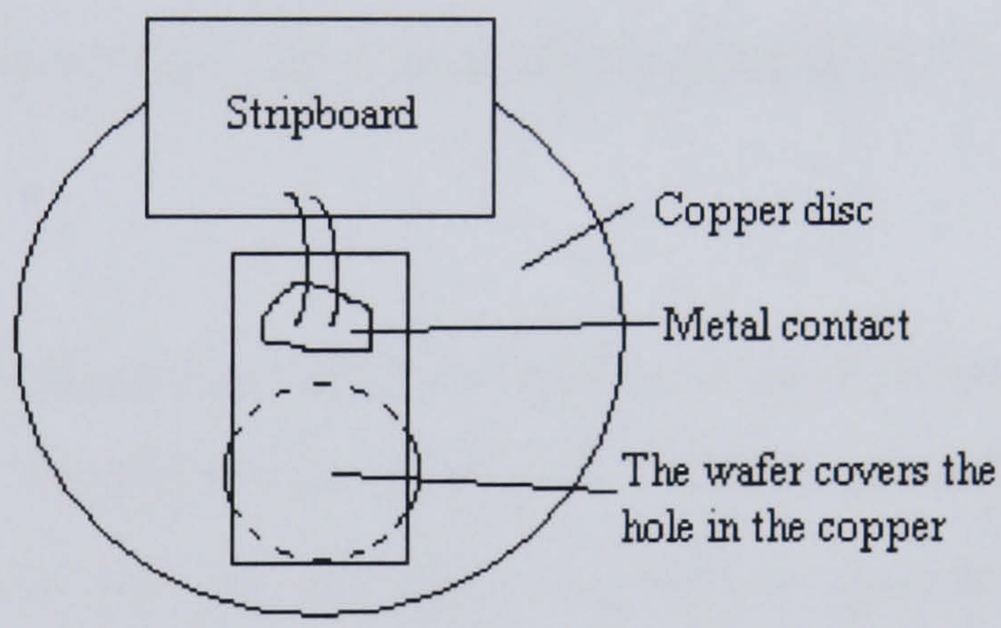

Figure 5.7: Diagram of the MR1020 wafer mounted on a copper disc. The region of the wafer without the contact layer hangs over the hole in the disc. The contact region is directly above the wafer such that when the illumination moves horizontally any change in the distance between the illuminated point and the contact is minimal.

In this situation, the variation of photocurrent across the scans was not expected to be very large. Figure 5.8 shows this to be the case.

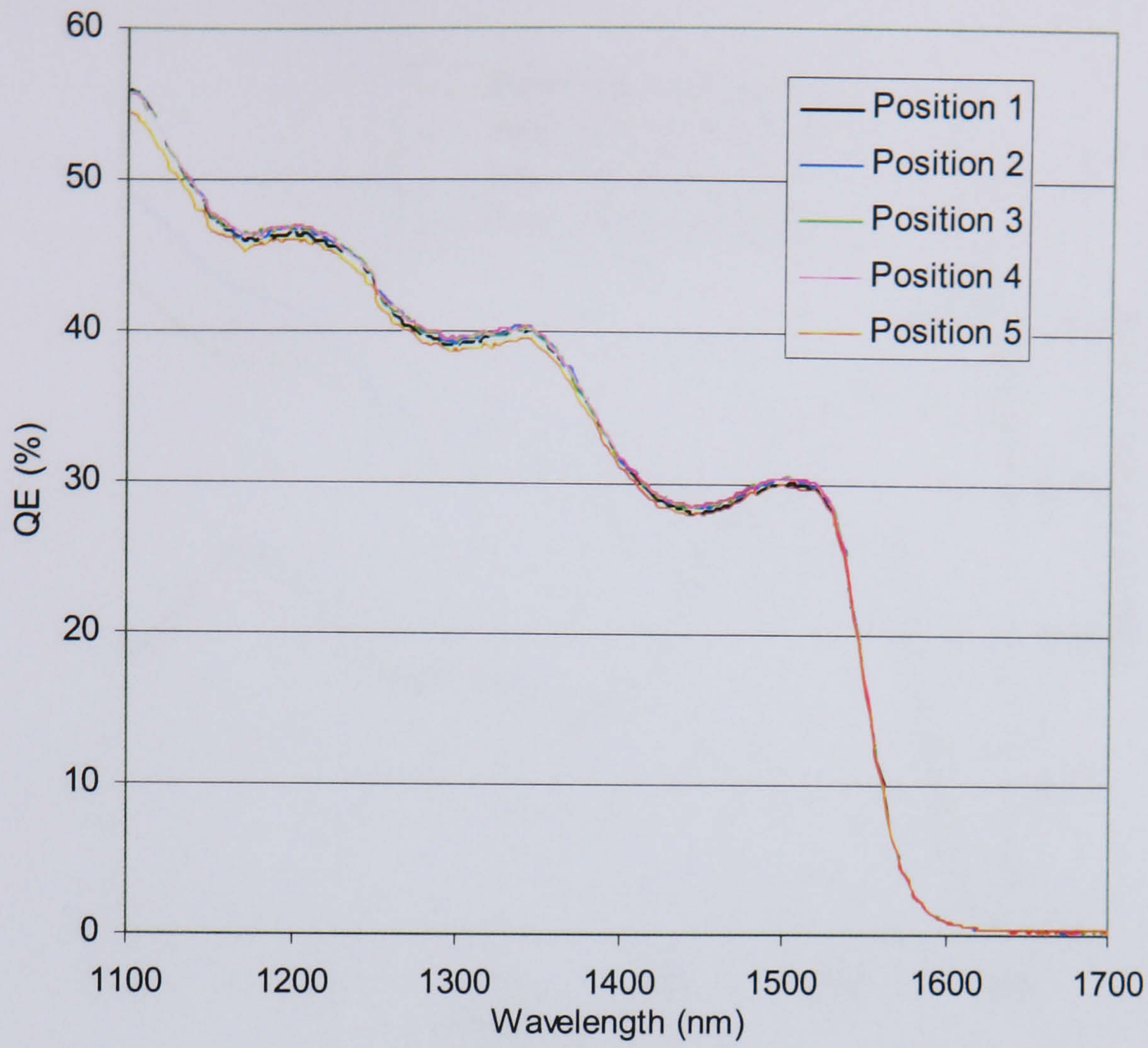

Figure 5.8: Quantum efficiency scans taken from various positions in a horizontal line on the front of wafer MR1020.

By using a visible wavelength, it could be seen that the movement in spot position on the stage caused by revolving the stage was almost unnoticeable. Thus, having determined that there would be minimal variation in photocurrent signal over this distance, it was decided that quantum efficiencies from the front and rear, related by simply revolving the stage, would be sufficient to examine the effect of reverse processing. The front and rear quantum efficiencies of the MR1020 device were measured and are shown in Figure 5.9. The right-hand axis gives the rear signal as a fraction of the front signal. For comparison, the figure also shows the quantum efficiency of a small area non-AR device, measured when the structure was originally received [5].

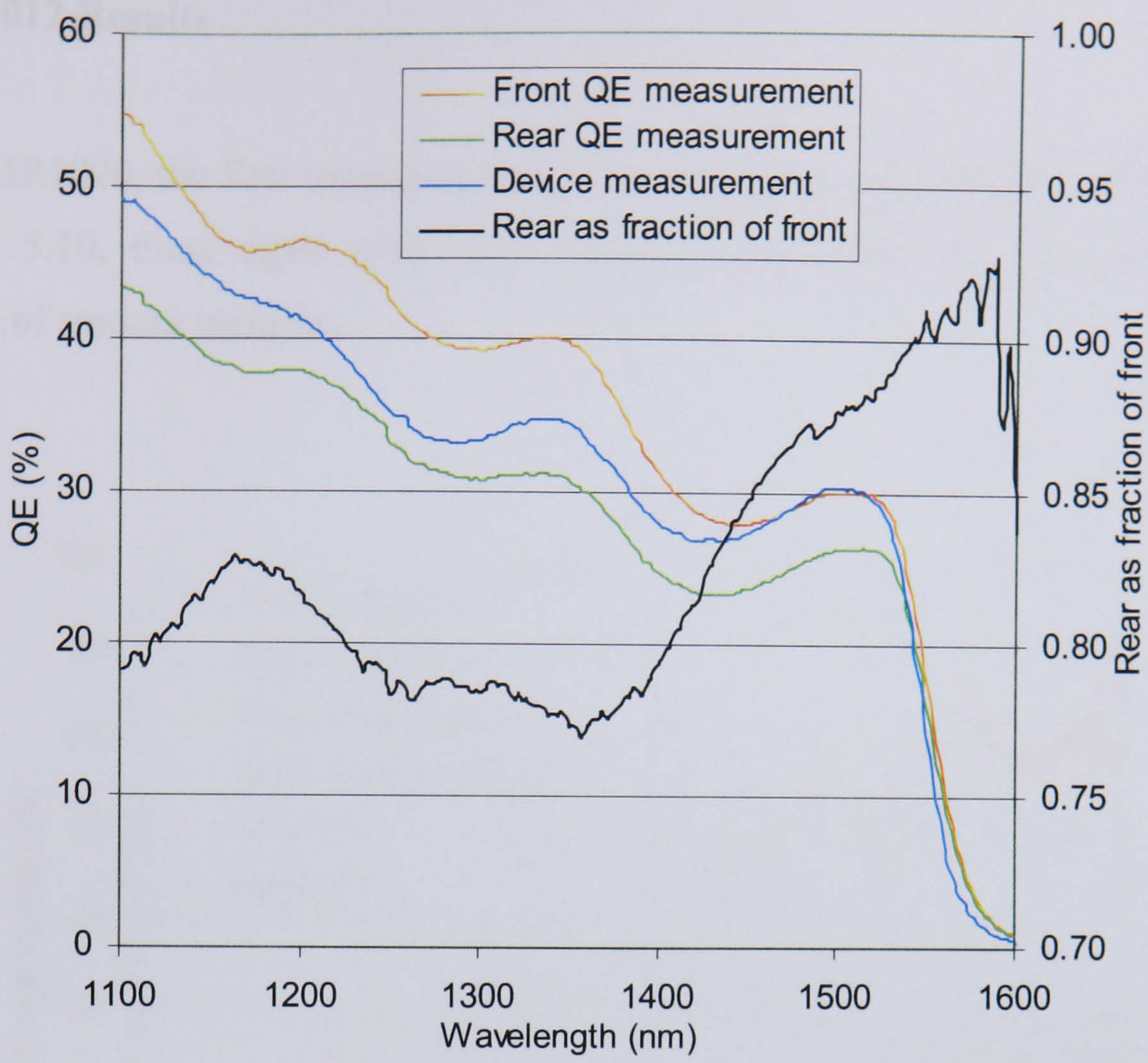

Figure 5.9: Quantum efficiencies of wafer MR1020 taken from the front and the rear. The right-hand axis shows the response of the rear as a fraction of that from the front. Also included is an original measurement on an MR1020 small area non-AR device.

The measurement on the front of the wafer shows a quantum efficiency which is as good as the fully processed device in the wavelength region of the exciton, although it is higher at shorter wavelengths. However, the two measurements are similar, indicating that there is no significant loss in signal compared to a processed device and that the most accurate comparison can be made between the front and rear measurements.

From 1100-1400nm, the amount of photocurrent collected from the rear of the wafer is approximately 80% of that collected through the front. This rises to 90% towards the absorption edge around 1550nm. Although the decrease in photocurrent through the rear is greater than the experimentally determined prediction of a 4% loss for a single pass through the substrate, the fact that around 90% of the response remains at the wavelengths of interest is still encouraging.

5.3.1.3. E012 Results

As with MR1020, the first measurements were of reflectivity and transmission. Shown in Figure 5.10, these again give very similar results from the front and the rear, indicative of smooth surfaces.

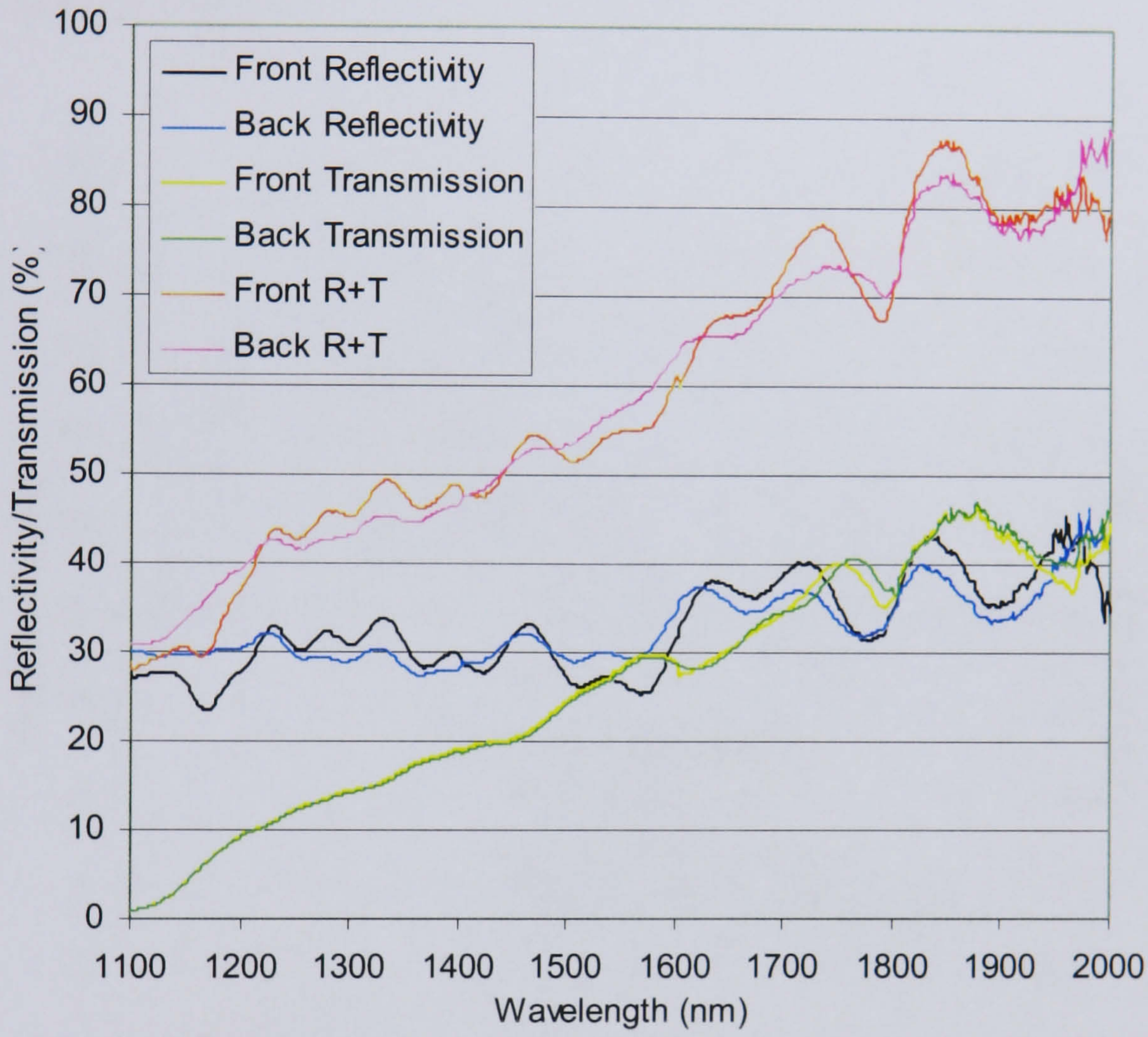

Figure 5.10: Front and rear reflectivity and transmission of wafer E012.

As the measurements on MR1020 had shown minimal variation in photocurrent due to small movements in the position of the light beam, wafer E012 was examined by simply taking a photocurrent scan from the front and the rear, related by turning the mounting stage around. The results are shown in Figure 5.11, where it should be noted that it is only the collected photocurrent that is shown and not the quantum efficiency. The signal from the rear of the wafer reaches 90% of that from the front at 1300nm and remains roughly constant for all longer wavelengths.

By referring to the structure of E012 (see Appendix A) a number of observations can be made. The fraction of the rear signal compared to the front begins to rise towards its peak level at around 1100nm, the wavelength corresponding to the absorption edge of the quaternary InGaAsP that is present. The shortfall in the rear photocurrent at wavelengths below 1300nm could be explained by noting that, ignoring the depletion regions within the p- and n-regions, light entering from the front must pass through 0.2μm of InGaAsP before reaching the field region, whereas light entering from the rear must pass through 0.5μm.

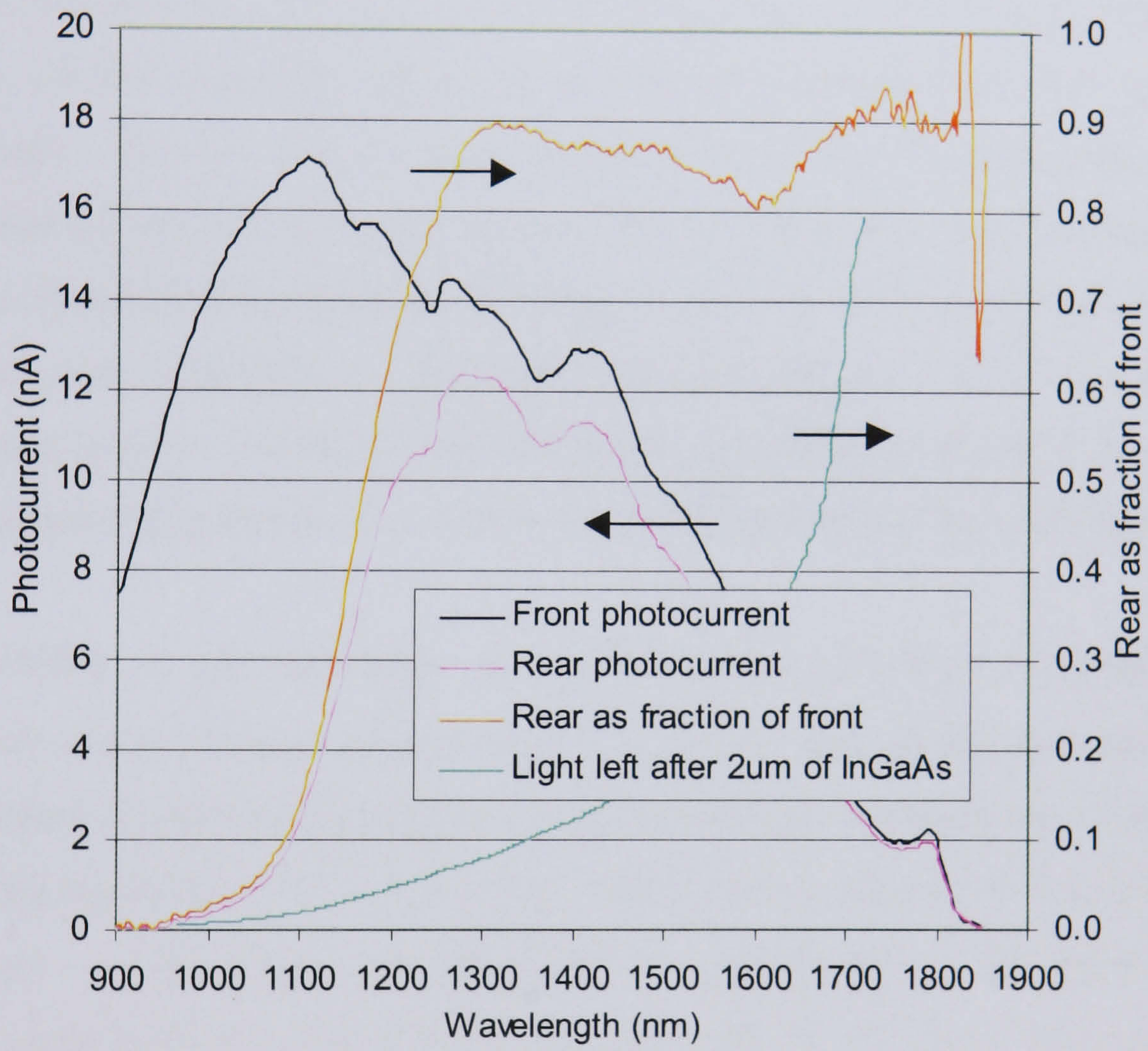

Figure 5.11: Front and rear photocurrents of wafer E012. The rear signal as a fraction of the front is given along with the fraction of light intensity unabsorbed after passing through 2μm of InGaAs.

The nominal structure of E012 has a 2μm thick lattice-matched InGaAs layer as the first non-InP layer above the substrate. There is a high band-gap InP window layer between this InGaAs and the active region, therefore carriers generated in the InGaAs would not be expected to pass through this window and contribute to the collected photocurrent.

Lattice-matched InGaAs absorbs strongly out to its absorption edge of 1660nm. Indeed, the fourth line plotted in Figure 5.11 shows the fraction of light intensity remaining at each wavelength after passing through 2μm of InGaAs. Given such a low transmission through this InGaAs layer it is surprising that the rear measurement should be able to contribute such a high photocurrent, in the range 1100-1650nm, with respect to the front measurement. It is inconceivable that of the large number of carriers generated in the InGaAs layer, a sizeable proportion is passing through the window layer and being collected.

The curve showing the amount of light remaining after 2μm of InGaAs gives a rough indication of the maximum level that would be expected from the transmission measurement. The fact that so much more light is able to pass through the wafer suggests that the InGaAs layer is not actually present. If it were simply missing then the quaternary layer below the quantum well region would be the first non-InP layer to have been grown, see Appendix A. However, the TEM image of E012, see Figure 4.6, clearly shows a layer of different material below the 100nm thick InP at the bottom of the picture, indicating that there is indeed a non-InP layer below the quaternary.

One possibility is that the layer is lattice-matched quaternary InGaAsP, of the composition used elsewhere in the structure. A further 2μm of this material at the rear of the structure would certainly explain the significant rise in photocurrent from the rear and the high transmission beyond 1100nm, whilst also giving rise to the contrast in the TEM image. To investigate this possibility, the transmission of the wafer E012 was modelled using the model SOL [9], but the 2μm thick InGaAs layer was replaced with the lattice-matched quaternary. This is shown in Figure 5.12, compared with the experimentally measured transmissions from the front and the rear of the wafer. The fourth curve in the figure is the modelled transmission of the nominal E012 wafer (including the InGaAs layer), produced using the author's model (see Section 2.2.6).

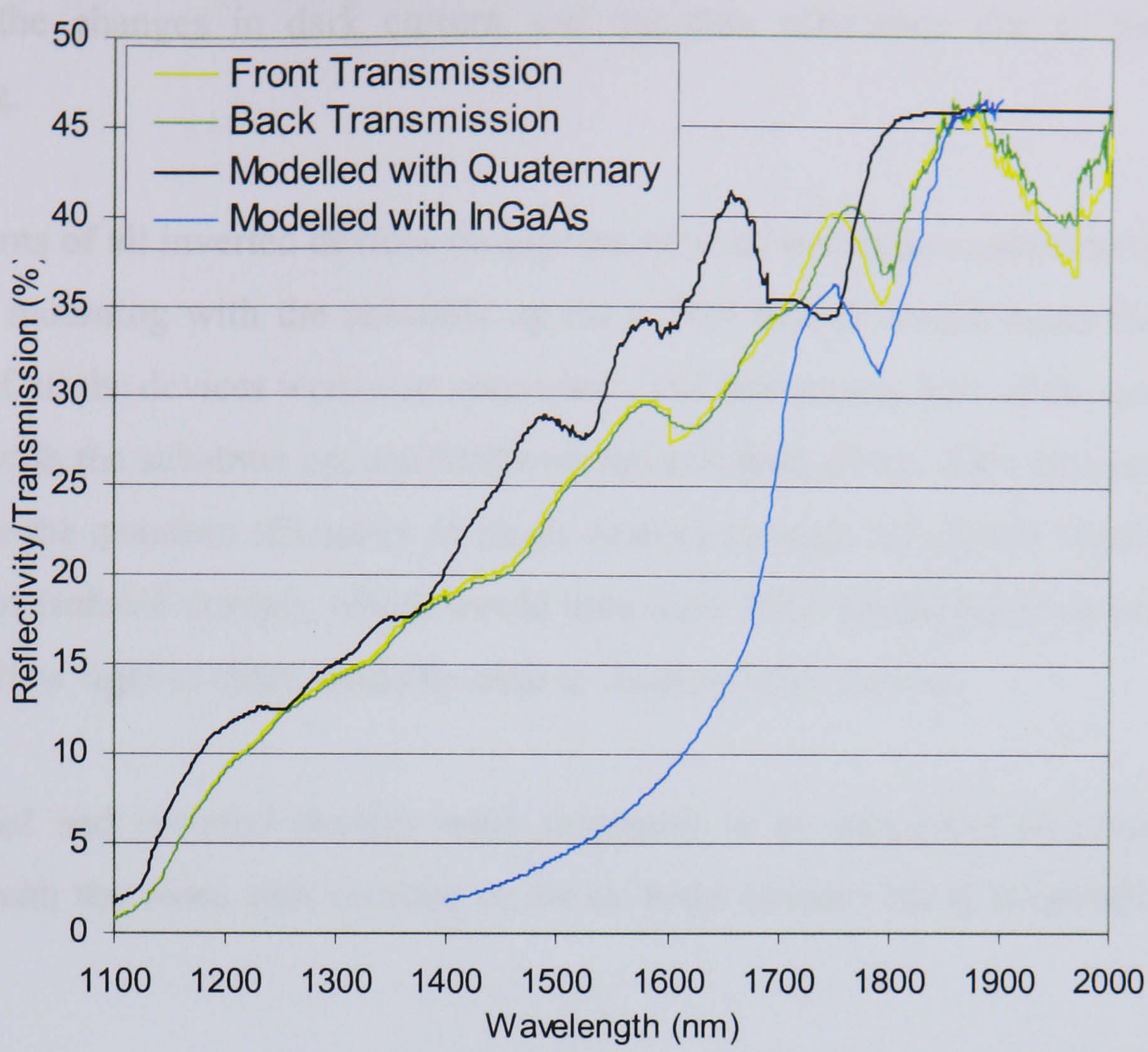

Figure 5.12: Wafer E012 transmission comparison. The experimental measurements are compared with the modelled transmission of the wafer using the author's model (blue line). The black line is the SOL modelled transmission of E012 if the 2μm thick InGaAs below the quantum wells is replaced with lattice-matched quaternary of the composition used elsewhere in the structure.

The modelled transmissions definitely rule out InGaAs as the layer below the quantum wells, and also strongly suggest that the layer was actually grown as lattice-matched quaternary.

5.3.2. MR1091

MR1091 is a barrier control structure that was designed for comparison with a quantum well structure. It was grown in Sheffield and is described in Ref. 5. It was chosen as there was available a significant amount of wafer that appeared to be visibly smooth on both sides. Both normal and inverted processed small area mesa devices were produced by the author. The normal devices were produced following the processing steps in Section 2.1.1, with the inverted devices following a similar route apart from necessary changes concerning the mesa etching. These two sets of devices were then used to

examine the changes in dark current and quantum efficiency due to the inverted processing.

As the fronts of all inverted devices on a given piece of wafer are connected through the substrate, mounting with the substrate up on a TO5 header would mean that the rear surfaces of all the devices were also connected. For this reason, half of the devices were mounted with the substrate up, and half with the substrate down. One set could be used to measure the quantum efficiency of single devices through the optical window and the other set of isolated devices, which would then have fully metallised front contacts and thus not allow light to enter, could be used to measure dark current.

The normal and inverted devices were originally to be processed in parallel, but a problem with the mesa etch resulted in the inverted devices being produced in a later run.

5.3.2.1. MR1091 Results

The dark currents from the normal and inverted processed sets of devices were slightly spread out. The best device from each set is shown in Figure 5.13, along with the best dark current from the original set of normal devices produced by Sheffield.

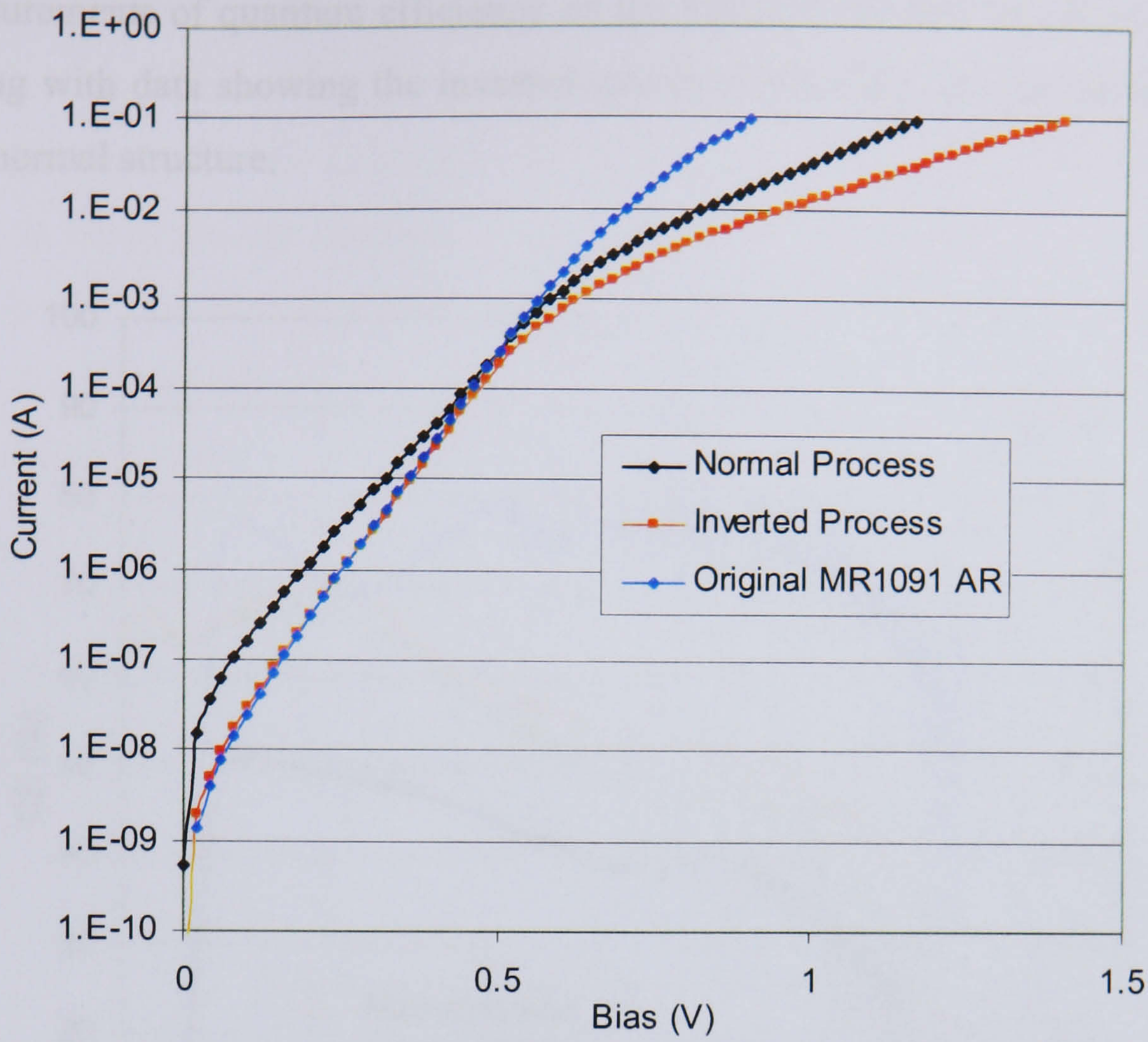

Figure 5.13: Dark current comparison of MR1091 normal and inverted devices processed by the author and an original AR coated device processed in Sheffield.

The inverted processed devices are expected to display a lower level of series resistance at higher current levels than the normal devices. Unfortunately, both of the author's devices display the form of dark current that has been seen in a number of previous devices, namely a low ideality factor at low bias and a higher ideality factor at high bias. The high bias region of both dark currents cannot be fitted with dark current models. This could be indicative of problems with the processing of the devices. The original Sheffield device also displays a dark current that appears to yield to series resistance, but that cannot be fitted as such. Even if processing issues are indeed masking the most interesting section of the dark current, preventing a study of series resistance of being made, an encouraging conclusion that can be drawn from the dark currents is that the processing technique for producing inverted devices, despite being novel, has not had a detrimental effect on the overall level.

The measurements of quantum efficiency on the MR1091 devices are shown in Figure 5.14, along with data showing the inverted quantum efficiency as a percentage of that from the normal structure.

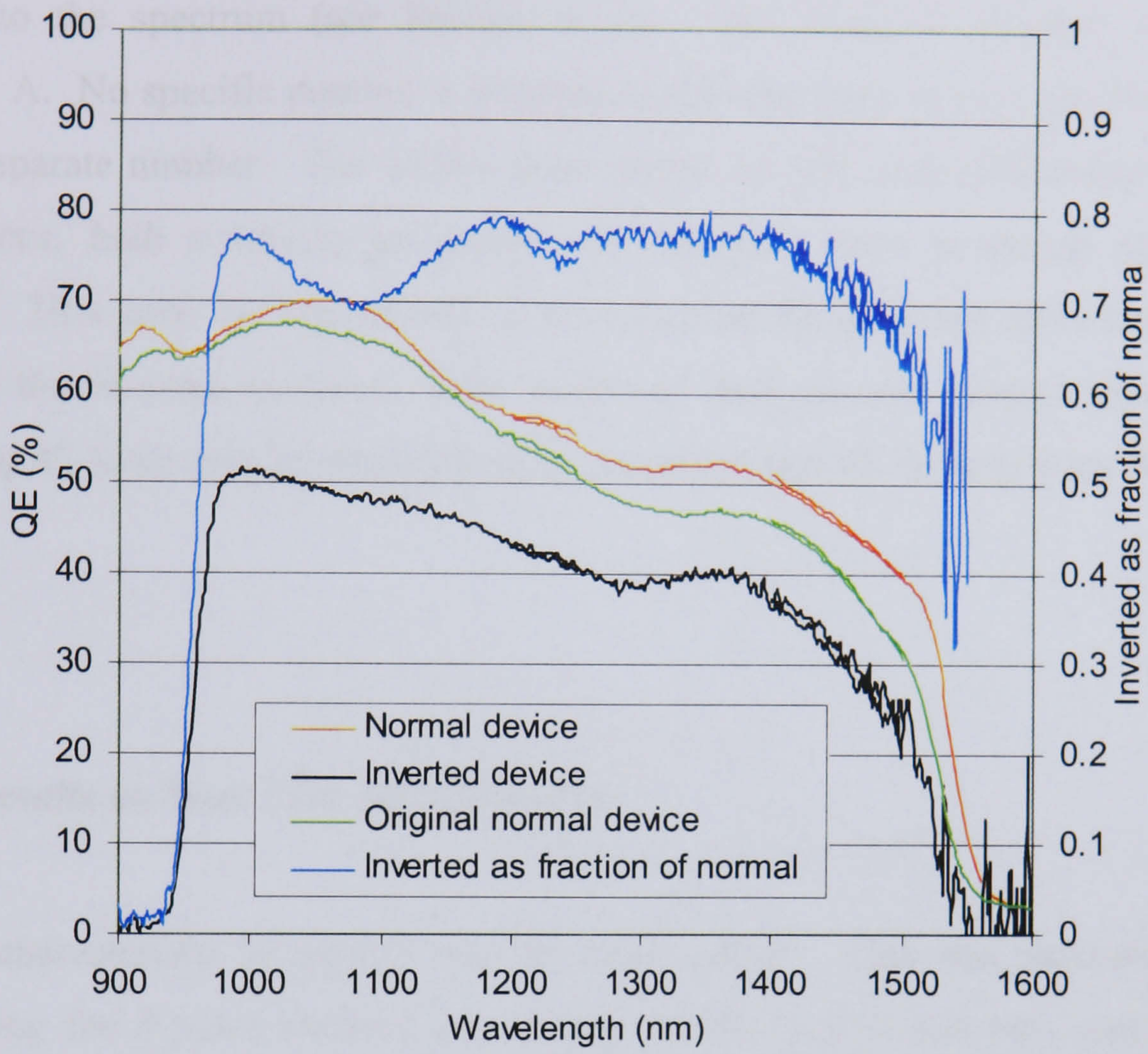

Figure 5.14: Quantum efficiency measurements of normal and inverted processed MR1091 devices. The quantum efficiency of the inverted structure as a percentage of the normal structure, using the same axis, shows a loss of around 20%. Also shown for comparison is a quantum efficiency of one of the original normally processed non-AR devices from Sheffield.

As with both MR1020 and E012, the loss in quantum efficiency with the inverted structure beyond 1200nm is in the region of 20%, although slightly higher at longer wavelengths. Figure 5.14 also shows a quantum efficiency taken from an original Sheffield device. This device was non-AR and was processed normally. The similarity between this quantum efficiency and that measured on the author's normal device gives a degree of confidence in the measurements. Reflectivity measurements of the author's two devices show that both devices have similar characteristics, such that reflectivity cannot be the cause of the 20% loss in the inverted device.

5.3.3. Final THE REV material

The device structure for the final THE REV system, to be matched to the thulia emitter spectrum, is based on the structure E1055, which gave the quantum efficiency best matched to the spectrum (see Section 4.1.4). The nominal structure is given in Appendix A. No specific number is attached to this structure as each grown wafer was given a separate number. The wafers were grown by IQE and preliminary 1cm large area devices, both normally processed and inverted, were produced by RWE in Germany. This gave the opportunity of investigating the quantum efficiency and dark current of the inverted structure. Four wafers of each process method were received, comprising 42 large area devices normally processed and 48 devices from the inverted process.

5.3.3.1. Results on final THE REV material

The first characteristic of interest was the dark current. This was measured on each device using the 4-point method: two probes on the busbar and two contacts to the copper block on which the device was laid. There was spread in the dark currents of both the normal and the reverse processed devices, although the spread was considerably larger in the inverted devices. The best three dark currents from each of the two process methods are shown in Figure 5.15. The normal and reverse processed devices appear to possess different ideality factors, which could be process related, but the most positive aspect of these dark currents is that there are no indications of series resistance, either in the normal or the inverted devices up to a current level of 1A. Dark currents of some of the devices were repeated up to 3A and series resistance remained absent. This is the current level expected with the final TPV system. Although this cannot therefore show an advantage with the reverse processed devices, it does give assurance that such high current levels are achievable with the conventional design.

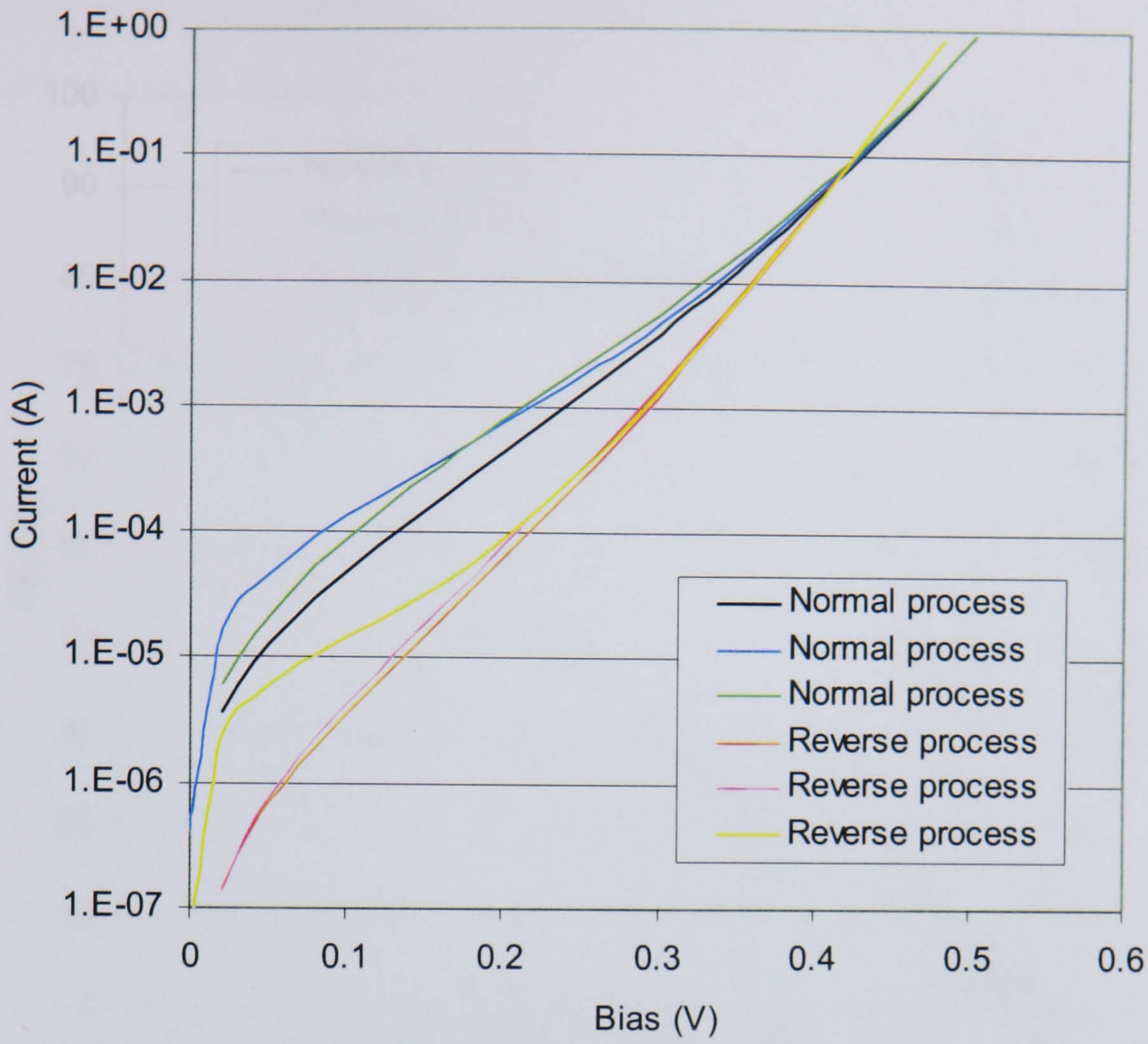

Figure 5.15: Dark current comparison of normal and reverse processed devices produced from the final THE REV material.

The second characteristic to be investigated is the quantum efficiency. Measured quantum efficiencies of two of the better normal and reverse processed devices are shown in Figure 5.16. The exciton peaks in structure E1055 were around 1920nm, whereas those in the final structure are only at 1850nm, about 70nm shorter than expected. This is found for both the normal and the inverted structures and is also consistent with the results of cathodoluminescence (CL), which has been performed on a number of the wafers. Also shown in Figure 5.16 is the ratio between the quantum efficiencies of the inverted and the normal devices. Apart from the anomalous drop at longer wavelengths, the inverted device is collecting around 70% of the photocurrent of the normal device. Measurements of device reflectivity, although they are complicated by the presence of the contact fingers, indicate that the normal and inverted devices are very similar, again suggesting that reflectivity is not responsible for the loss.

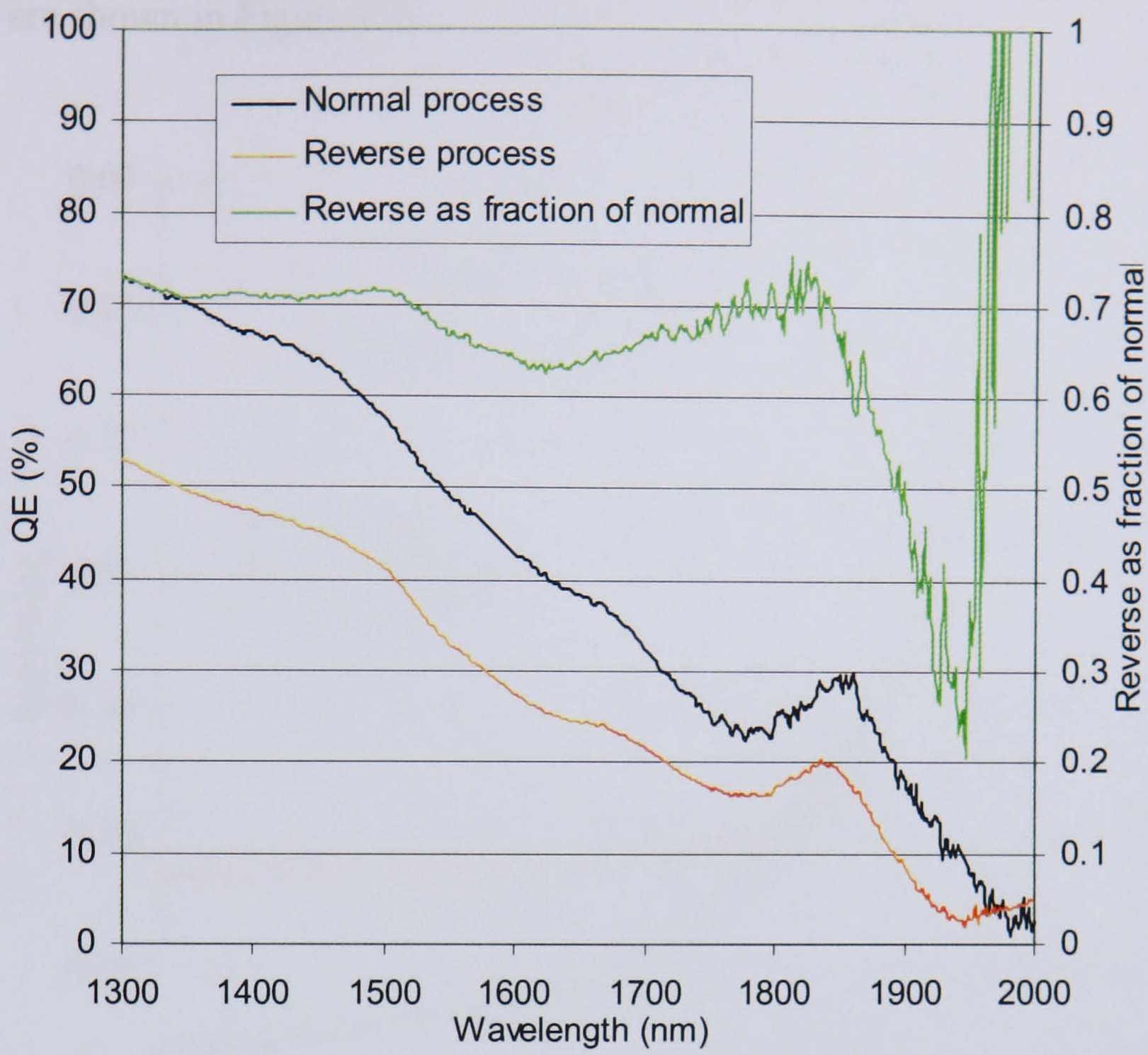

Figure 5.16: Quantum efficiencies of normal and reverse processed devices from the final THE REV material. The ratio between the reverse and the normal quantum efficiencies shows a 30% drop in signal with the inverted device.

One explanation for the reduced quantum efficiency in the inverted devices is that in these devices the rear contact is between the metal and the original InGaAs contact region. Whereas the contact to the InP substrate has been seen to possess reflectivities of up to 65% (see Section 4.1.2 for example), the reflectivity of the InGaAs contact may not be as good. This could result in less light making a second pass through the structure.

Using the tungsten bulb, as described for high intensity illumination in Section 2.2.2, light I-V measurements were performed on two of the best devices, one normal and one inverted. This experiment was unshuttered because of space limitations due to the probes. For comparison, in order to recreate the loss of 20% of the photocurrent in the inverted structure, intensities for the two measurements were chosen such that the short-

circuit current of the inverted device was 80% of that from the normal device. The two light I-Vs are shown in Figure 5.17.

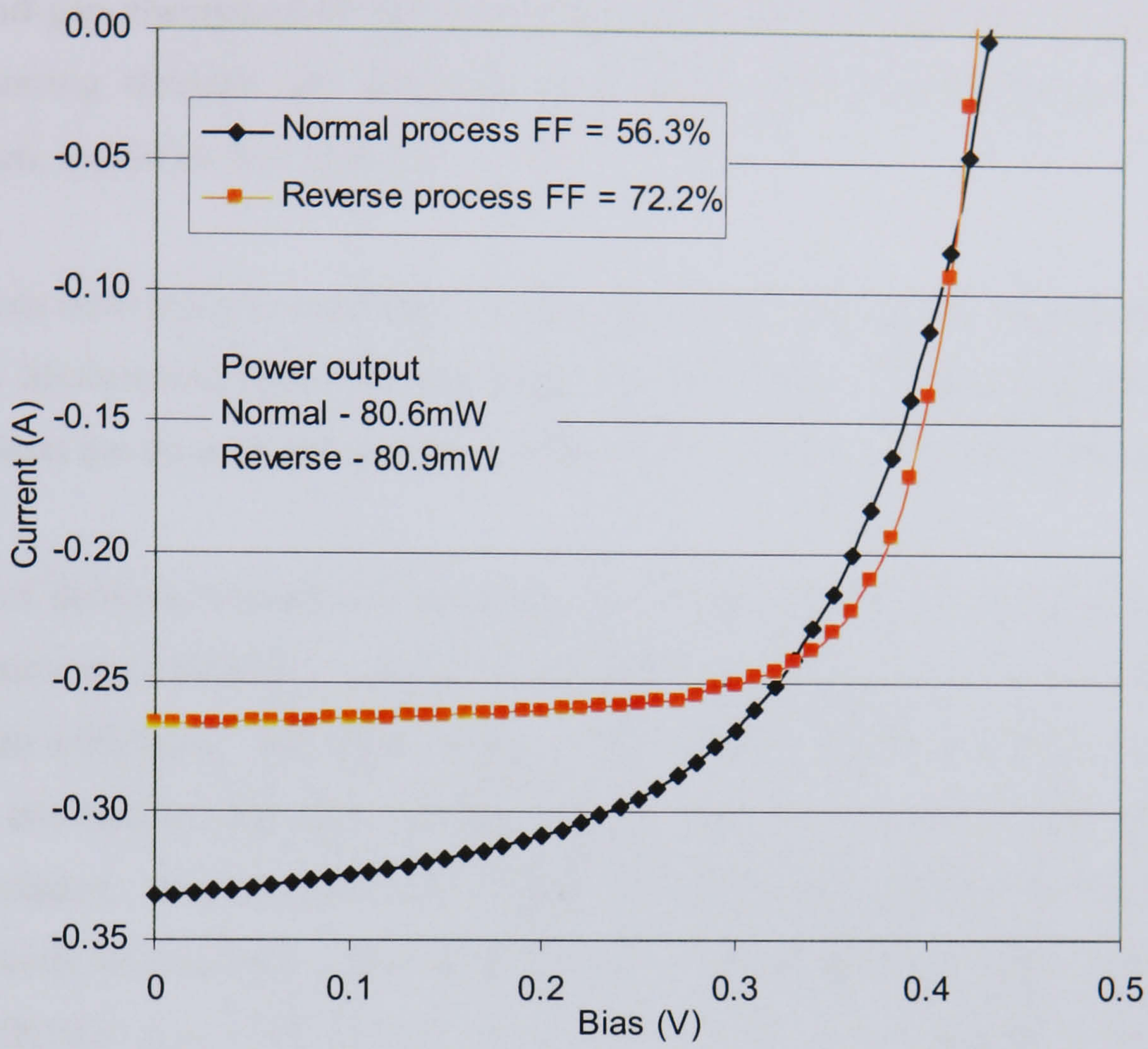

Figure 5.17: Light I-Vs of one normal and one inverted device from THE REV final material.

It is clear that the inverted structure gives a much higher fill factor, which can be attributed to better series and parallel resistance values. Although at these current densities the power outputs are approximately equivalent, at the higher intensities anticipated in THE REV system (approximately ten times more photocurrent) the inverted structure will give superior results.

5.3.4. Conclusions on inverted structure

A number of devices and structures have been investigated to determine the feasibility of the proposed inverted processing method for THE REV. Pieces of wafer from E012 and a Sheffield wafer MR1020 were used to explore the quantum efficiencies produced

by illumination from the front and the rear. By forming contacts to the front and rear of each piece, mounting on a copper block and wire bonding contacts to the front metal, devices were created that could be illuminated from both sides. Measurements on the below band-gap absorption of InP were used to predict that the loss in light intensity due to passing through the substrate, and hence the photocurrent loss with rear illumination, would be less than 4%.

Results from both MR1020 and E012 wafers show, at wavelengths longer than 1300nm, that when illuminating from the rear there is a loss in photocurrent compared to that obtained from the front of no more than 20% and as little as 10% in the case of E012.

Two sets of devices, normal and inverted, were produced by the author using another Sheffield structure MR1091. Fully processed devices of both kinds allow investigations of quantum efficiency and dark current. The dark currents produced by the two processes are similar, and both exhibit a low ideality factor at high bias, rather than series resistance. This characteristic is also present in the original devices from this material, made in Sheffield. Quantum efficiency measurements on these devices show, as with MR1020 and E012, that there is around 20% loss in signal in the inverted devices.

The most important structure that has been examined is the final material for THE REV system with the thulia selective emitter. The structure is based on E1055, the previous structure which was well matched to the emitter spectrum. Numerous 1cm devices processed in Germany, both normal and inverted, have been characterised to study dark current and quantum efficiency. The dark currents of neither the normal nor the inverted structures exhibit any signs of series resistance up to around 3A, which is extremely encouraging. Measurements of the quantum efficiency of the two structures show that the loss produced in the inverted devices is around 30%, slightly higher than is found for the other structures.

In order to decide which structure will be used for the final TPV system there are a number of factors to be considered. Firstly, InP absorption predicts only a 4% loss in photocurrent for the inverted structure, whereas it has been found experimentally to be much larger. Secondly, for the final system material, at high currents in the dark the

normal structure shows no signs of series resistance problems, a characteristic that the inverted structure had been intended to improve upon. However, under illumination, the normal devices were seen to display a much greater level of resistance problems than the inverted devices. The dark currents of the inverted devices had a much greater spread than the normal devices which can be attributed to the inverted process being a much newer and less developed technology. If the variation in quality of the inverted devices can be reduced by optimisation of the process then the inverted device could produce a significant increase in system efficiency.

5.4. Anti-Reflection Coatings

The change in refractive index between air and III-V semiconductors means that, in the absence of an anti-reflection (AR) coat, only around 70% of incident light enters a photovoltaic device. This represents an unacceptable loss, but one that AR coats can help to minimise. An ideal coat would provide low reflectivity over a large wavelength range, in order to maximise the amount of light that can be absorbed. The TPV system adds another requirement because the cells are in such close proximity to the emitter: the AR coat must also deliver low reflectivity over a wide range of incident angles. Analysis of the layout of THE REV system predicts that radiation will be incident on the cells at angles up to 50°.

All results in this report were theoretically modelled, either by the programme Multilayer [10] or by another model written by David Bushnell at Imperial College [11]. As the devices produced for THE REV have InP top surfaces unless stated all AR coats were modelled as being applied to an infinite layer of InP.

5.4.1. Basic Theory

The following theory applies to thin films, which are defined as those thin enough compared to the wavelength of the light in question for interference effects to become relevant [6]. Each of the applied layers in the structure has a characteristic matrix:

$$M_j = \begin{bmatrix} \cos\delta_j & (i\sin\delta_j)/\eta_j \\ i\eta_j \sin\delta_j & \cos\delta_j \end{bmatrix} \tag{5.5}$$

where
$$\delta_j = \frac{2\pi n_j d_j \cos\theta_j}{\lambda}, \tag{5.6}$$

$$\eta_j = \sqrt{\frac{\varepsilon_0}{\mu_0}} n_j \cos\theta_j \qquad \text{for s-polarisation,} \tag{5.7}$$

and
$$\eta_j = \frac{\sqrt{\frac{\varepsilon_0}{\mu_0}} n_j}{\cos\theta_j} \qquad \text{for p-polarisation.} \tag{5.8}$$

Terms are defined as:

n_j - The real refractive index of the layer material.

θ_j - The angle of travel of the light ray through the layer.

λ - The wavelength of interest.

d_j - The thickness of the film.

Each layer's characteristic matrix is independent of those of other layers. All the matrices are then multiplied into a single matrix, which describes the whole system:

$$M = \prod_{j=1}^{q} M_j \qquad \text{for q layers.} \tag{5.9}$$

This single matrix relates the electric and magnetic fields which are incident on the structure to those which emerge from it and gives an equation of the form

$$\begin{bmatrix} B \\ C \end{bmatrix} = M \begin{bmatrix} 1 \\ \eta_m \end{bmatrix} \tag{5.10}$$

where the subscript m denotes the substrate. The components B and C then give the reflectivity:

$$R = \left(\frac{\eta_o B - C}{\eta_o B + C}\right)\left(\frac{\eta_o B - C}{\eta_o B + C}\right)^* \tag{5.11}$$

5.4.2. Single layer AR coats

Light reflecting from the front layer of the AR material will undergo a 180° phase shift, because the refractive index of the film is greater than one. Providing that the index of the film is lower than that of the substrate, reflection at the back of the coat will also suffer this 180° shift. In order for these two rays to be entirely destructive in their interference the total path length through the film must correspond to a phase shift of 180°. This is the basis of the quarter-wavelength film. Complete cancellation requires that the amplitudes are equal. For this, the refractive index ratios between air and film, and film and substrate, must be equal.

Therefore, in order to achieve a zero minimum in reflectivity at normal incidence, the refractive index of the coat (n_1) as a function of the refractive indices of the incident medium (n_o) and the substrate (n_s) must satisfy:

$$n_1 = \sqrt{n_o . n_s} \tag{5.12}$$

For InP with a refractive index of n_s=3.16 at 1.6μm, the ideal single layer AR coat material would have a refractive index of n_1=1.77, given that n_o=1 for air. It is to be expected that in reality the available materials are unlikely to have precisely the properties required and that any AR coat will not be ideal. However, in this case the material aluminium oxide (Al_2O_3) has refractive index data very similar to that required. The modelled reflectivity of this single coat is shown in Figure 5.18.

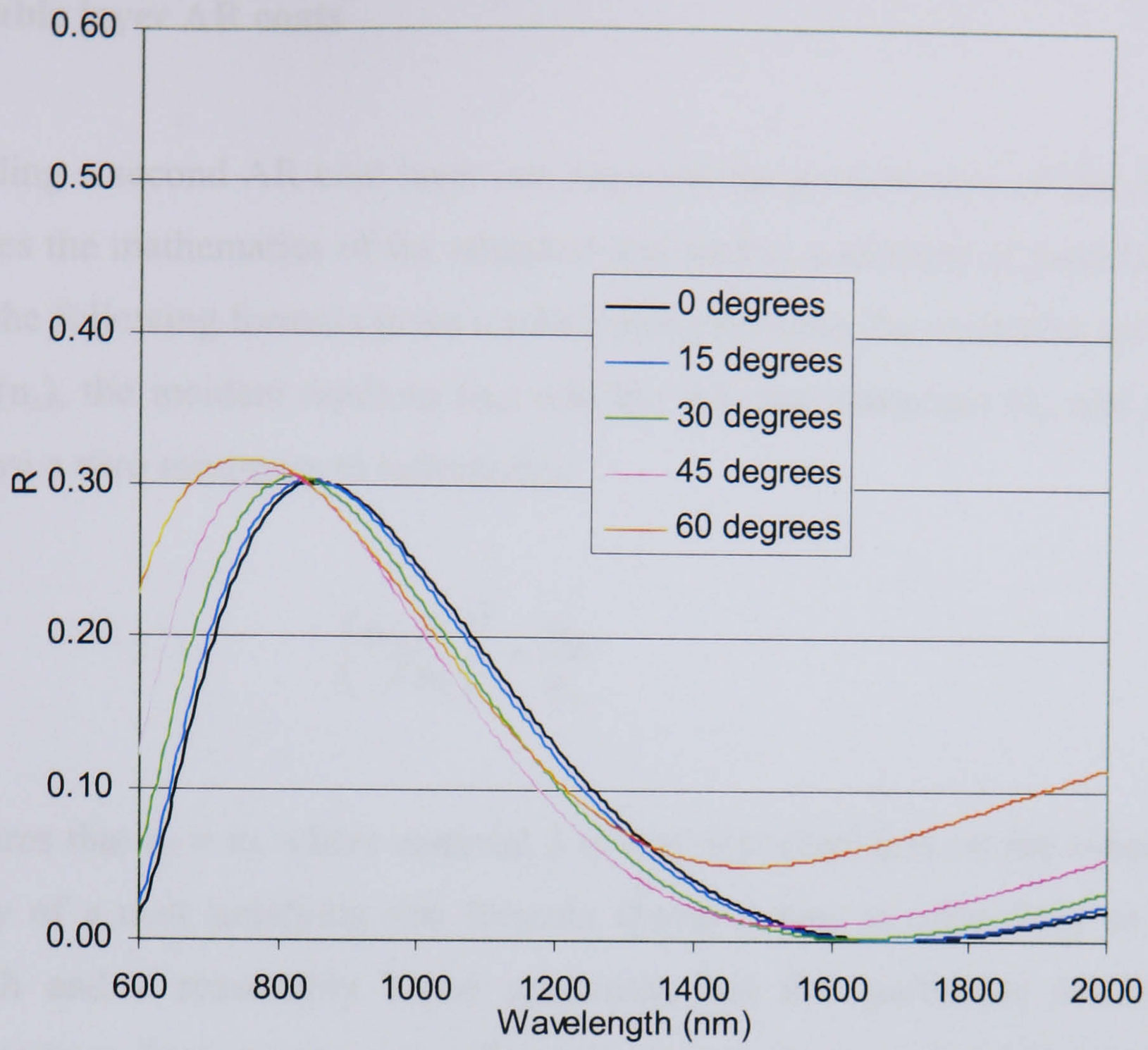

Figure 5.18: Modelled angular reflectivity of an Al_2O_3 coat optimised at 1700nm.

This single layer coat gives a minimum in reflectivity at the chosen wavelength and remains below 10% over a large range for normal incidence. At larger angles the minimum moves to shorter wavelengths and the reflectivity rises over the whole range.

Albeit counterintuitive, the minimum moves to shorter wavelengths with increasing angle as a result of Equation 5.6. The cosine term in the phase factor means that as the angle increases the phase shift due to one pass through the film decreases. The condition of 180° phase shift can then only be satisfied by a shorter wavelength.

By optimising the coat for a wavelength of 1700nm, the effect of increasing the angle is to move the reflectivity minimum towards the 1500nm target for the erbia selective emitter. Not until the highest angles does the reflectivity around 1500nm rise above 5%.

5.4.3. Double layer AR coats

While adding a second AR coat layer can improve the performance of the coat, it also complicates the mathematics of the situation and lead to a number of possibilities. For instance, the following formula gives a relationship between the refractive indices of the substrate (n_s), the incident medium (n_o) and the AR coat materials (n_1 and n_2), which will achieve a zero minimum in reflectivity:

$$\left(n_2/n_1\right)^2 = \frac{n_s}{n_o} \tag{5.13}$$

This requires that $n_2 > n_1$ where material 2 is that deposited first on the substrate. The reflectivity of a coat satisfying this formula shows a zero in reflectivity at the target wavelength and a reasonably broad minimum, but this particular combination of refractive indices does not give a significant improvement over a single layer coat.

In order to achieve zeroes at more than one wavelength, materials are needed to satisfy the following equation:

$$\frac{n_1}{n_0} = \frac{n_2}{n_1} = \frac{n_s}{n_2} \tag{5.14}$$

This can be expressed as

$$n_s n_0 = n_1 n_2 \tag{5.15}$$

Despite the assumed difficulties in finding matching materials, for InP with n≈3.15, the materials magnesium fluoride (MgF_2, n=1.37) and zinc sulphide (ZnS, n=2.27) are almost perfect, and their predicted performance is shown in Figure 5.19.

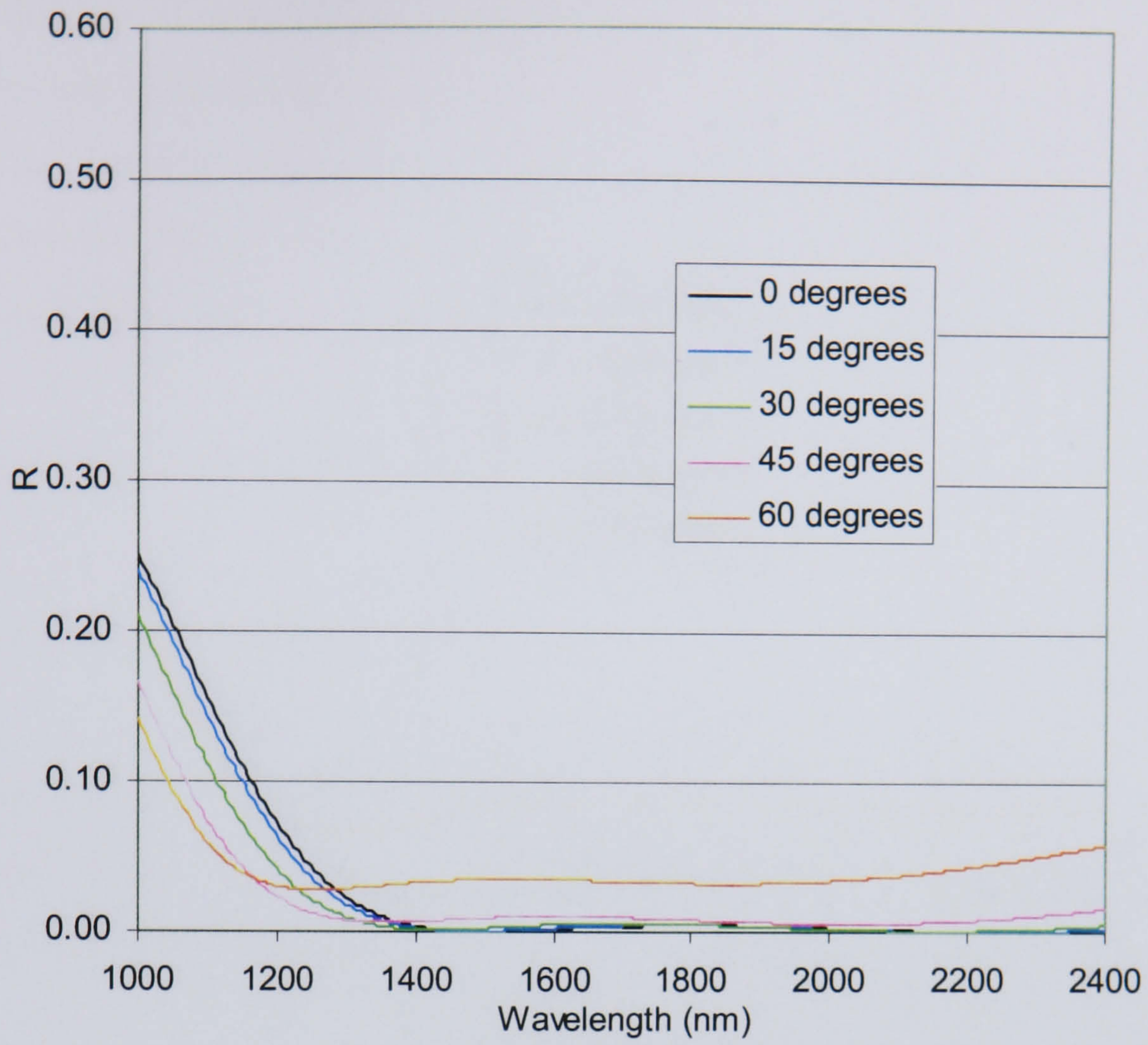

Figure 5.19: Modelled angular reflectivity of a MgF_2/ZnS AR coat optimised for 1800nm.

As Figure 5.19 shows, the coat offers exceptional performance, not only over a wide wavelength range but also at large incident angles. Given the additional effort involved in applying an increasing number of AR coats, this combination offers excellent value.

The processing of the devices for the working prototypes is performed by RWE Solar (formerly ASE) in Germany. The AR coat regularly used there is titanium dioxide (TiO_2, n=2.59) and aluminium oxide (Al_2O_3, n=1.75). The performance of this coat is very similar to that of the MgF_2/ZnS coat, but with a slightly higher level of reflectivity. This is shown in Figure 5.20. However, another set of materials being considered by RWE is silicon nitride and silicon oxynitride. Unlike the titanium and aluminium oxides, they can be used to passivate the edges of the cells as the deposition is conformal. These materials have refractive indices that are dependent on factors such as the processing method. Therefore, if refractive indices of n=1.37 and n=2.27 can be achieved then a double layer coat with the performance as good as that shown in Figure 5.19 should be possible.

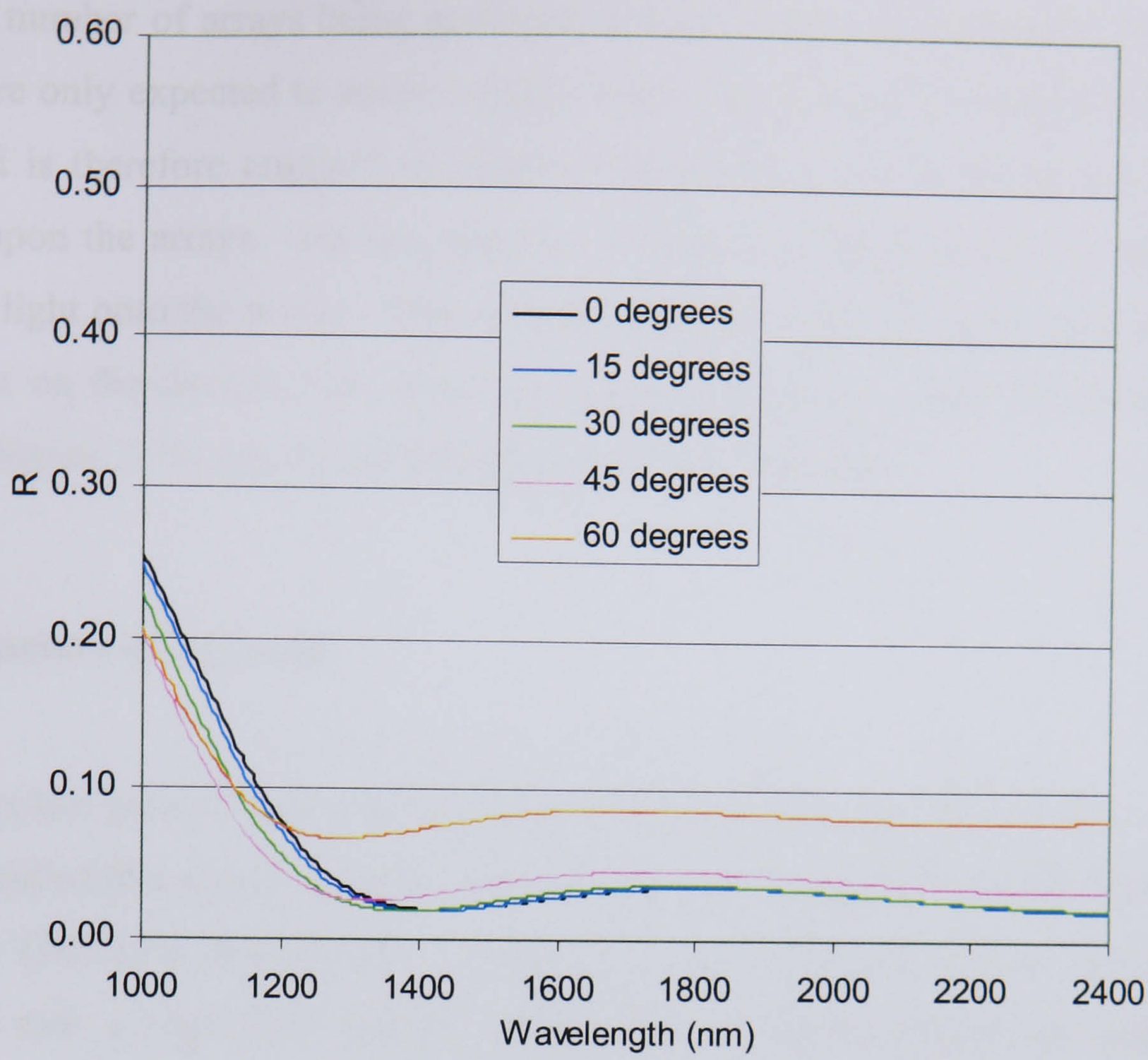

Figure 5.20: Modelled angular reflectivity of the RWE double layer Al203/TiO2 coat optimised at 1800nm.

5.4.4. System Considerations

Included in the TPV system are two quartz shields between the emitter and the cells. One of their functions is to prevent convective heat transfer to the cells. Quartz also has the added intrinsic property of absorbing at wavelengths longer than 3μm, thus preventing this radiation from reaching and potentially heating the cells. However, quartz has a non-unity refractive index and would therefore reflect back a proportion of all radiation incident on it. In a THE REV report from August 2001 [12], details were given of an infra-red (IR) filter which is applied to the quartz shields. This filter passes the wavelengths required by the cell whilst reflecting the unwanted longer wavelengths back to the source, increasing system efficiency and reducing unwanted heating of the cells and the quartz.

From the number of arrays being produced and the radius of the system, the arrays of devices are only expected to cover roughly half of the area of the inside of the system. A method is therefore required of utilising the photons which would not be directly incident upon the arrays. For this purpose, a series of reflectors will be employed, to guide the light onto the arrays. This may increase the range of angles from which light is incident on the devices, but with such good performance from AR coats, such as shown in Figure 5.19, this should not pose a particular problem.

5.4.5. Summary of AR coats

This report has given a brief outline of the theory of thin-film anti-reflection coatings and has applied this theory to single and double layer coatings for the InP based cells to be used in THE REV demonstrator. It has been shown that, given an air interface at the top of the cell, a MgF_2/ZnS quarter wavelength coat offers exceptional performance. Also, if the material system of silicon nitride/silicon oxynitride can be produced with the refractive indices of magnesium fluoride and zinc sulphide then the performance can be repeated with the additional benefit of edge passivation.

The theory of AR coats extends beyond two layers, and the ideal minimum in reflectivity can be broadened and given better angular dependence. However, the theory places further restrictions on the relationships between the refractive indices of the layers, which become more difficult to satisfy with existing materials. Despite this there are double layer coats that can exhibit very good reflectivities, as Figure 5.19 and Figure 5.20 show. These reflectivities can be achieved over a broad wavelength range and at high incident angles. It does not seem appropriate to consider increasing the complexity of device processing with more than two coats when such good characteristics can be demonstrated with two.

5.5. Conclusions

In this chapter two different processing techniques were investigated with the potential for incorporation into the final THE REV system: reverse processing and AR coatings.

Due to the high current levels expected during operation of the system and the subsequent need for low spreading resistance in the top layers, the wafers can be inverted and processed such that the substrate is the top layer. This structure has the advantage of allowing current to reach the contact fingers via the thicker substrate rather than a thinner contact layer. A study on the below band-gap absorptions of InP and lattice-matched InGaAs has concluded that the loss of light intensity due to a single pass through the substrate should be around 4%, and that this should also be the loss of photocurrent if the reverse method is employed.

A number of structures have been investigated to compare the dark currents and quantum efficiencies of normal and inverted device structures. Pieces of bare wafer from the structure E012 and the existing MR1020 were contacted to such that photocurrent comparisons could be conducted. In both structures, the loss in photocurrent when illuminating from the rear, compared to front illumination, is between 10-20%. This is larger than the loss predicted for a single pass through the substrate. Devices processed by the author also showed a loss of around 20% in the inverted structure.

The most interesting results were obtained from normal and inverted devices that had been processed in Germany from wafers of the material that will be used in the final TPV system. The dark currents of both structures appeared to be free of series resistance problems up to a current level of 3A, whereas the inverted devices had been expected to show reduced series resistance at higher current levels. Also, the inverted dark currents were much more spread, which could be expected of a newer and less developed processing technique. In terms of quantum efficiency, the inverted devices showed a loss of roughly 30% compared to the normal devices, an increase even on the figures found previously. However, when light I-V measurements were performed the normal devices were seen to suffer from much greater resistance problems than the inverted devices. Optimisation of the inverted processing is needed to fully realise the potential of this structure.

Anti-reflection (AR) coatings are used to reduce the reflectivity of the front surfaces of devices, ensuring that a greater amount of light reaches the active regions. Multiple

coatings can improve performance but at the cost of increased processing and the need for greater accuracy in growth. A modelling study of potential single and double coatings that can be applied to InP has been undertaken. The materials which are commonly used by the processors involved in THE REV project have been shown to display excellent characteristics.

The impressively low reflectivities achieved with a double layer coating suggests that no extra layers need to be considered. It is unlikely that a coating consisting of more than two layers could be good enough to justify the additional work involved in its production.

5.6. References

[1] T J Coutts, A review of progress in thermophotovoltaic generation of electricity. *Renewable and Sustainable Energy Review,* **3**, p80, 1999.

[2] S M Sze, Physics of semiconductor devices, 2nd edition, Wiley Interscience, 1981.

[3] A W Nelson and L D Westbrook, A study of p-type dopants for InP grown by adduct MOVPE, *J. Cryst. Growth*, **68**, pp.102-110, 1984.

[4] D A Humphreys et al., Measurement of absorption coefficients of $Ga_{0.47}In_{0.53}As$ over the wavelength range 1.0-1.7μm, *Electronics Letters.* **21**, pp.1187-1189, 1985.

[5] C Rohr, InGaAsP Quantum Well Cells for Thermophotovoltaic Applications, PhD Thesis, Imperial College of Science, Technology and Medicine, 2000.

[6] H A Macleod, Thin-Film Optical Filters, 3rd Edition, IoP Publishing, 2001.

[7] E D Palik ed., Handbook of Optical Constants of Solids Vol I, Academic Press, Boston, 1985.

[8] F R Bacher et al., Optical-absorption coefficient of $In_{1-x}GaAs/InP$, *Phys. Rev. B*, **37**, (5), p2551, 1988.

[9] J P Connolly et al., Modelling Multi Quantum Well Solar Cell Efficiency. *Proc. 17th European Solar PV Energy Conf.* Munich, Germany, 2001.

[10] Randy Geels, formerly Spectra Diode Labs, San José, CA, 1993.

[11] David B Bushnell, PhD Thesis, Imperial College of Science, Technology and Medicine, 2001.

[12] Peng Ruwen, IR filters for Erbia based sources, EU Framework V project THE REV, Internal Report, August 2001.

6. Conclusions and Discussion

The world's energy requirement is predicted to rise dramatically over the next few decades, and to counter the expected rise in greenhouse gas emissions renewable sources must begin to contribute significantly to overall energy production. As costs fall and efficiencies increase, photovoltaics can play an increasingly important role in reducing a nation's reliance on fossil fuels. A topic closely related to photovoltaics, thermophotovoltaics (TPV) can provide a portable, quiet and reliable source of heat and electricity utilising a number of possible fuels. The introduction of thin low band-gap layers into a p-i-n structure to create multi-quantum well (MQW) solar cells can enhance the efficiency of bulk solar cells, while in conjunction with strain-compensation their advantage for TPV is clear: the effective band-gap can be engineered to match the emission spectra of narrow band selective emitters such as erbia and thulia.

In this thesis the primary focus of the work was TPV cells, which have been developed as part of a European collaboration to produce a TPV generator system to be used as a range extender for an electric car. Two such systems were to be produced. The first includes erbia selective emitter, which operates at 2000K and produces a narrow band of radiation around 1500nm. For this purpose, lattice-matched InGaAs p-n cells were designed and characterised. Although none of the later lattice-matched cells performed as well as the initial structure a number of modifications were made to the design for the final system cell structure. It was decided that Monolithic Interconnected Module (MIM) design was not necessary, therefore a lateral conduction layer was not required. Also, the need to reduce series resistance led to a threefold increase in the thickness of the top contact layer. In view of problems that were discovered in some of the structures, and of an optical study that was carried out, quaternary material was not used in any of the later cell designs. The best lattice-matched cells were found to possess a significant rear surface reflector, which manifests itself in a dramatic increase in reflectivity below the band-gap of the InGaAs active region. Quantum efficiency measurements were consistent with this reflectivity in a number of cases. This reflection allows more light to be absorbed in the active region, while returning unused

photons to the heat source is vital for maintaining the temperature and improving system efficiency. Problems were encountered with the large area devices, which displayed higher dark currents and also parallel conductivity problems. Comparisons between small and large area devices is desirable but was not possible because of the poor quality of the larger devices. The processing of large area devices is less well developed than for small area devices and so further work is required to produce large area devices to the same high standard.

The second system includes a thulia emitter, operating at 1700K and radiating around 1700nm. Photovoltaic cells to match this spectrum must contain lattice-mismatched materials. Strain compensation can enable these materials to be incorporated into the cells without causing strain relaxation and subsequent loss of performance. Beginning from a previous successful structure, the design of the cells was modified to extend the absorption out to the emission wavelength of the thulia emitter. Again, the later cells failed to match the performance of the first structure. In some of these structures however, this shortfall was not caused by material quality or design, but by the lack of a rear surface reflection from the back contact, which was again present in the better cells. Again, some problems were seen with the large area devices, with high dark currents and poor light I-Vs.

In strain-compensated devices, quantum well carrier escape and collection is an important factor in determining the performance and efficiency. Measurements of photocurrent at various biases and temperatures were conducted on two devices. One device, which exhibited a poor quantum efficiency possessed incomplete carrier collection in reverse bias and above room temperature. This is clearly unsatisfactory as photovoltaic cells must operate in forward bias. However, the TPV system is clearly above room temperature and this may itself have a positive effect on carrier escape. The second structure gave complete collection into forward bias and down to temperatures as low as 180K. The thermal requirements of carriers in this structure would easily be satisfied in a TPV system.

For both lattice-matched and strain-compensated structures, the best devices were investigated under high intensity illumination, in order to simulate the environment of the TPV system. Device efficiency rises as the intensity increases, providing the short-

circuit current remains proportional to the incident intensity and the forward diode current remains at the same level that can be measured in the dark. However, as the current in the device increases series resistance becomes more important. Indeed, it is responsible for an eventual decrease in efficiency at higher intensities. For this reason, front metal contacts must be specifically designed for the current that will flow in the cell. Due to the problems with the large area devices – specifically the fact that the photocurrent did not saturate at zero bias, invalidating the assumption that the short-circuit current is the photocurrent – the large area devices could not be included in a comparison between devices and could only be used for illustration.

The feasibility of processing wafers such that the radiation enters through the substrate was also investigated. This research was stimulated by the high resistance of the top layers of the standard design, which would reduce system efficiency at the light intensities expected in these systems. In view of the thickness of material through which light would be expected to pass in the inverted configuration, the above and below band-gap absorptions of InP and lattice-matched InGaAs were determined. At selective emitter wavelengths, 1500-2000nm, the absorption of InP is very low, equivalent to a loss of 3.5% through a 350μm substrate. An accurate measurement of the below band-gap absorption of InGaAs was not possible due to experimental limitations and also the fact that the InGaAs used formed part of a photovoltaic cell structure and hence there were differently doped regions of InGaAs. A more conclusive investigation of InGaAs absorption could be conducted using a single doped InGaAs layer and a double polished wafer, in order for the assumption of smooth parallel surfaces to be fully valid.

Despite the low photocurrent loss of less than 4%, predicted for the inverted structure, experimental results on numerous different devices have shown the loss to be around 20%. This is particularly evident in measurements of normal and inverted devices processed from the material that is to be used in the final TPV system. In addition, the dark currents of the inverted devices had a greater spread than the normal devices. This is indicative of inverted devices being a much less developed technique, and one which would require optimisation to realise its full potential. Most notably, the dark currents of the normal devices appeared to be free from series resistance problems up to current

levels of at least 3A. This result could not be reproduced in the light where the normal structure suffered from resistance problems and the inverted structure gave a much higher fill factor. Further investigation is needed to decide between the two processing methods, although the time constraints of the project may prevent a prolonged period of optimisation.

Appendix A: Sample Descriptions

All the dimensions given in these descriptions are the nominal values as requested of the grower. InGaAs is lattice-matched to InP unless an indium composition is given. All InGaAsP quaternary materials are grown lattice-matched to InP with a band-edge of the wavelength given. Where necessary comments are included with each structure.

A.1. IQE Grown Samples

A.1.1. Lattice-Matched InGaAs Samples

E004 and E006:

Layer	Material	Thickness (nm)	Doping (cm^{-3})	Type	Dopant
Contact	InGaAs	100	1e19	p	Zn
Window	InP	100	2e18	p	Zn
Emitter	InGaAs	300	1e19	p	Zn
Base	InGaAs	2000	5e17	n	Si
Window	InP	100	1e18	n	Si
Conduction	InGaAs	1000	2e19	n	Si
Buffer	InP	200	2e19	n	Si
Substrate	InP		n-type (E004) and SI (E006)		
Comment:	InGaAs p-n structure.				

E005 and E007:

Layer	Material	Thickness (nm)	Doping (cm^{-3})	Type	Dopant
Contact	InGaAs	100	1e19	p	Zn
Window	InP	50	2e18	p	Zn
Etch-stop	InGaAsP (λ=1.3μm)	100	1e18	p	Zn
Emitter	InGaAs	300	1e18	p	Zn
Base	InGaAs	2000	5e17	n	Si
Window	InP	100	1e18	n	Si
Conduction	InGaAs	2500	2e19	n	Si
Buffer	InP	200	2e19	n	Si
Substrate	InP		n-type (E007) and SI (E005)		
Comment:	As E004 with etch-stop included for process testing.				

E008:

Layer	Material	Thickness (nm)	Doping (cm^{-3})	Type	Dopant
Contact	InGaAs	100	1e19	p	Zn
Window	InP	100	2e18	p	Zn
Emitter	InGaAsP (λ=1.1μm)	200	1e18	p	Zn
Buffer	InGaAsP (λ=1.1μm)	250	-	-	-
Intrinsic	InGaAs	1030	-	-	-
Base	InGaAsP (λ=1.1μm)	500	5e17	n	Si
Window	InP	100	1e18	n	Si
Conduction	InGaAs	2000	2e19	n	Si
Buffer	InP	200	2e19	n	Si
Substrate	InP		n-type		
Comment:	InGaAs p-i-n with quaternary base and emitter to reduce dark current but allow InP windows to be retained. Buffer included to reduce emitter dopant diffusion into the i-region.				

E014:

Layer	Material	Thickness (nm)	Doping (cm^{-3})	Type	Dopant
Contact	InGaAs	100	1e19	p	Zn
Window	InP	100	2e18	p	Zn
Emitter	InGaAs	300	5e18	p	Zn
Base	InGaAs	3000	5e17	n	Si
Buffer	InP	100	1e18	n	Si
Buffer	InP	200	2e19	n	Si
Substrate	InP		n-type		

Comment: Repeat of E004 with lower p-doping and thicker n-region to increase the n response. Lateral conduction layer also removed.

E015:

Layer	Material	Thickness (nm)	Doping (cm^{-3})	Type	Dopant
Contact	InGaAs	300	1e19	p	Zn
Window	InP	100	2e18	p	Zn
Emitter	InGaAs	300	1e19	p	Zn
Base	InGaAs	3000	5e17	n	Si
Window	InP	100	1e18	n	Si
Buffer	InP	200	2e19	n	Si
Substrate	InP		n-type		

Comment: As E014 but with higher p-doping and thicker contact layer to improve contacting.

E042, Structure for the 6-month demonstrator:

Layer	Material	Thickness (nm)	Doping (cm^{-3})	Type	Dopant
Contact	InGaAs	300	1e19	p	Zn
Window	InP	100	2e18	p	Zn
Emitter	InGaAs	300	1e19	p	Zn
Base	InGaAs	2000	5e17	n	Si
Window	InP	100	1e18	n	Si
Buffer	InP	200	2e19	n	Si
Substrate	InP		n-type		

Comment: As E004 with thicker contact layer and no conduction layer.

A.1.2. Strain-balanced InGaAsP samples

E010 and E011:

Layer	Material	In content	Thickness (nm)	Doping (cm^{-3})	Type	Dopant
Contact	InGaAs		100	1e19	p	Zn
Window	InP		100	2e18	p	Zn
Emitter	InGaAsP (λ=1.1μm)		200	1e18	p	Zn
Buffer	InGaAsP (λ=1.1μm)		250	-	-	-
Barrier x 30	InGaAs	In N/A	N/A	-	-	-
Well x 30	InGaAs	In N/A	N/A	-	-	-
Barrier x 30	InGaAs	In N/A	N/A	-	-	-
Base	InGaAsP (λ=1.1μm)		500	5e17	n	Si
Window	InP		100	1e18	n	Si
Conduction	InGaAs		2000	2e19	n	Si
Buffer	InP		200	2e19	n	Si
Substrate	InP			n-type (E010) and SI (E011)		

Comment: Well and barrier compositions and thicknesses were not specified for this attempt to achieve maximum extension of absorption and thus these parameters are unknown.

E012 and E013:

Layer	Material	In content	Thickness (nm)	Doping (cm^{-3})	Type	Dopant
Contact	InGaAs		100	1e19	p	Zn
Window	InP		100	2e18	p	Zn
Emitter	InGaAsP (λ=1.1μm)		200	1e18	p	Zn
Buffer	InGaAsP (λ=1.1μm)		250	-	-	-
Barrier x 30	InGaAs	47%	6	-	-	-
Well x 30	InGaAs	62%	12	-	-	-
Barrier x 30	InGaAs	47%	6	-	-	-
Base	InGaAsP (λ=1.1μm)		500	5e17	n	Si
Window	InP		100	1e18	n	Si
Conduction	InGaAs		2000	2e19	n	Si
Buffer	InP		200	2e19	n	Si
Substrate	InP			n-type (E012) and SI (E013)		
Comment:	Based on successful previous design MR1288, see section 4.1.2.					

E016:

Layer	Material	In content	Thickness (nm)	Doping (cm^{-3})	Type	Dopant
Contact	InGaAs		300	1e19	p	Zn
Emitter	InP		300	2e18	p	Zn
Buffer	InP		200	-	-	-
Barrier x 30	InGaAs	44.9%	6	-	-	-
Well x 30	InGaAs	62%	12	-	-	-
Barrier x 30	InGaAs	44.9%	6	-	-	-
Buffer	InGaAs		20	-	-	-
Base	InP		500	1e18	n	Si
Substrate	InP			n-type (E012) and SI (E013)		
Comment:	Repeat of E012 with better strain compensation but without quaternary and conduction layer.					

E1054:

Layer	Material	In content	Thickness (nm)	Doping (cm^{-3})	Type	Dopant
Contact	InGaAs		300	1e19	p	Zn
Emitter	InP		300	2e18	p	Zn
Buffer	InP		200	-	-	-
Barrier x 40	InGaAs	45%	8	-	-	-
Well x 40	InGaAs	75%	8	-	-	-
Barrier x 40	InGaAs	45%	8	-	-	-
Buffer	InP		20	-	-	-
Base	InP		500	1e18	n	S
Substrate	InP			n-type		
Comment:	E1054/5/7 to investigate the effect of barrier thickness.					

E1055:

Layer	Material	In content	Thickness (nm)	Doping (cm^{-3})	Type	Dopant
Contact	InGaAs		300	1e19	p	Zn
Emitter	InP		300	2e18	p	Zn
Buffer	InP		200	-	-	-
Barrier x 40	InGaAs	45%	8.9	-	-	-
Well x 40	InGaAs	75%	8	-	-	-
Barrier x 40	InGaAs	45%	8.9	-	-	-
Buffer	InP		20	-	-	-
Base	InP		500	1e18	n	S
Substrate	InP			n-type		

E1057:

Layer	Material	In content	Thickness (nm)	Doping (cm^{-3})	Type	Dopant
Contact	InGaAs		300	1e19	p	Zn
Emitter	InP		300	2e18	p	Zn
Buffer	InP		200	-	-	-
Barrier x 40	InGaAs	45%	7	-	-	-
Well x 40	InGaAs	75%	8	-	-	-
Barrier x 40	InGaAs	45%	7	-	-	-
Buffer	InP		20	-	-	-
Base	InP		500	1e18	n	S
Substrate	InP			n-type		

Final THE REV system material:

Layer	Material	In content	Thickness (nm)	Doping (cm^{-3})	Type	Dopant
Contact	InGaAs		100	1e19	p	Zn
Emitter	InP		150	1e18	p	Zn
Buffer	InP		200	-	-	-
Barrier x 30	InGaAs	45%	9	-	-	-
Well x 30	InGaAs	74%	8	-	-	-
Barrier x 30	InGaAs	45%	9	-	-	-
Buffer	InP		20	-	-	-
Base	InP		250	1e18	n	S
Substrate	InP			n-type		

Comment: Based on E1055 as the best match to the thulia spectrum.

A.2. Sheffield Grown Samples

MR1665:

Layer	Material	In content	Thickness (nm)	Doping (cm^{-3})	Type	Dopant
Contact	InGaAs		100	1e19	p	Zn
Emitter	InP		700	2e18	p	Zn
Buffer	InGaAs		6	-	i	-
Barrier x 30	InGaAs	45%	6	-	i	-
Well x 30	InGaAs	62%	12	-	i	-
Barrier x 30	InGaAs	45%	6	-	i	-
Buffer	InGaAs		6	-	i	-
Base	InP		500	1e18	n	Si
Substrate	InP			n-type		

Comment: Near repeat of E012, without quaternary or conduction layer. Also, the compositions are altered to improve the strain compensation.

MR1674:

Layer	Material	In content	Thickness (nm)	Doping (cm^{-3})	Type	Dopant
Contact	InGaAs		100	1e19	p	Zn
Emitter	InP		200	2e18	p	Zn
Buffer	InP		200	-	-	-
Barrier x 2	InGaAs	36%	5	-	-	-
Well x 2	InGaAs	74%	10	-	-	-
Barrier x 2	InGaAs	36%	5	-	-	-
Buffer	InGaAs		20	-	-	-
Base	InP		500	1e18	n	Si
Substrate	InP			n-type		

Comment: Grown to demonstrate absorption at longer wavelengths.

MR1845:

Layer	Material	In content	Thickness (nm)	Doping (cm^{-3})	Type	Dopant
Contact	InGaAs		100	1e19	p	Zn
Emitter	InP		200	2e18	p	Zn
Buffer	InP		200	-	-	-
Barrier x 30	InGaAs	40.6%	5	-	-	-
Well x 30	InGaAs	68%	10	-	-	-
Barrier x 30	InGaAs	40.6%	5	-	-	-
Buffer	InGaAs		20	-	-	-
Base	InP		500	1e18	n	Si
Substrate	InP			n-type		

Comment: Grown to investigate intermediate strain values between E012 and the highly strained MR1674.

Appendix B: High Intensity Light I-V Electronics

In order to investigate devices under the high illumination intensities predicted for THE REV TPV system a new series of electronics was constructed and a computer programme written to control the electronics, a mechanical shutter (if required) and a data-acquisition card (DAC) within the computer. This experimental set-up was developed because the Source-Measure Unit (SMU) previously used for I-V measurements possesses a current limit of 1A and is also too slow for the experiments that are to be conducted. All electronic components were selected in order for currents up to 10A to be measured.

The circuit diagram of the electronics is shown in Figure B.1.

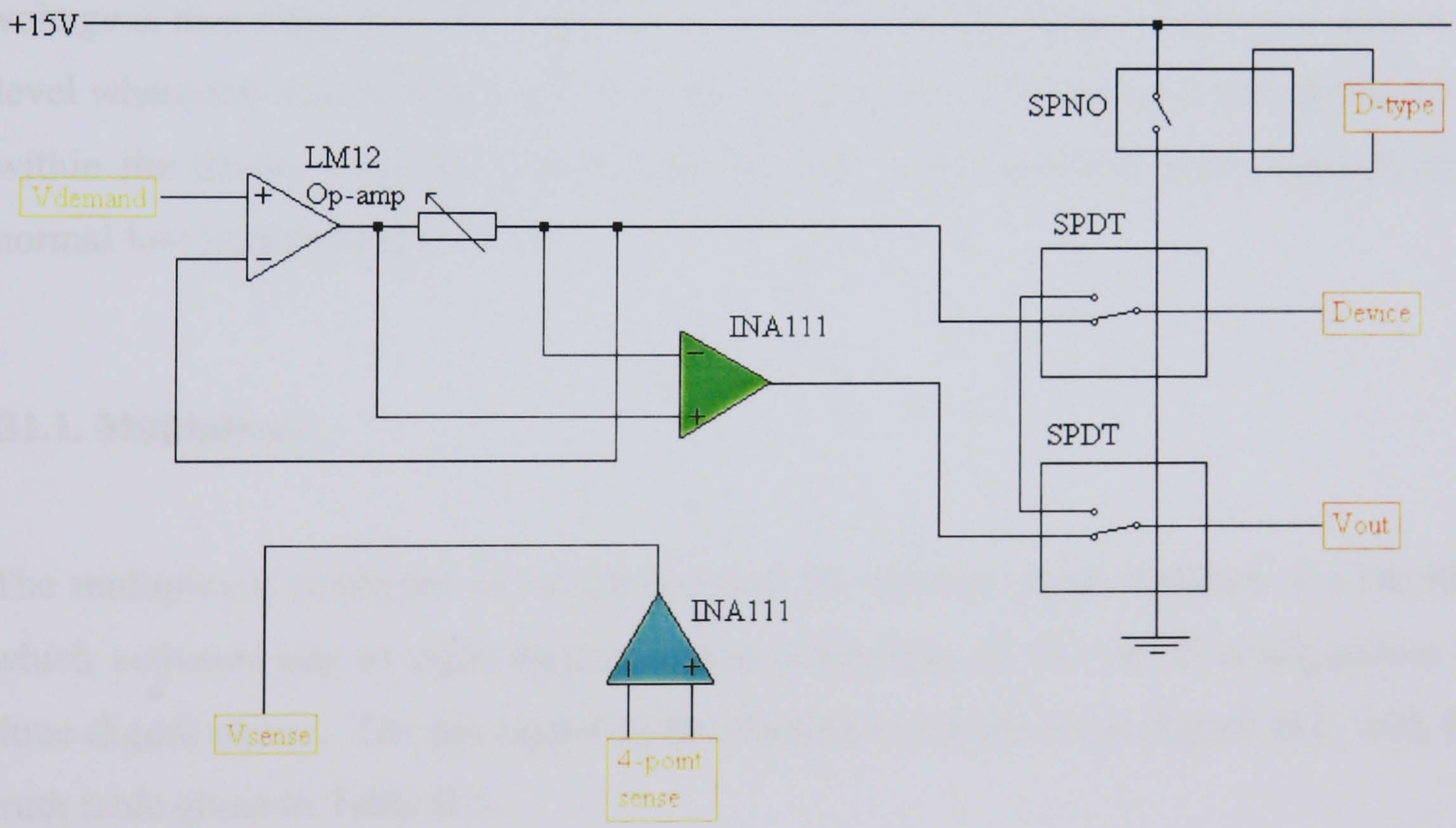

Figure B.1: Circuit diagram of the high current pulsed source-measure unit.

The red boxes denote external inputs to the circuit. Apart from the D-type connector, all connections are via BNC cable.

B.1. Operation of the Electronics

The electronics are designed to measure up to ±10V, which is the limit of the DAC. However, using a single measurement resistor, as is shown in Figure B.1, only a limited voltage range could be measured accurately. Therefore, in order to accurately measure a large range of currents up to 10A, the variable resistor depicted in the circuit diagram is actually six separate resistors. The most suitable resistor for each individual reading is controlled by the programme through the DAC and the D-type connection into a multiplexer (see section B1.1) inside the box. The electronics allow the user to perform dark I-V and light I-V shuttered and unshuttered. Shuttered light I-V can be used for very high intensity illumination where the minimum exposure time is required. For unshuttered light I-V, with the device at the required temperature, the shutter opens and the programme records the maximum open-circuit voltage that the device displays, before rising device temperature causes it to decrease. The real-time open-circuit voltage is then displayed, allowing the user to decrease the temperature of the stage to a level where the original open-circuit voltage is regained. This ensures that the junction within the device is at the intended temperature. The operation then proceeds as a normal low intensity light I-V.

B1.1. Multiplexer

The multiplexer employed to switch between the measurements resistors is a DG508, which activates one of eight digital outputs depending on the on/off configuration of three digital inputs. The pin layout of the multiplexer is shown in Figure B.2, with the truth table given in Table B.1.

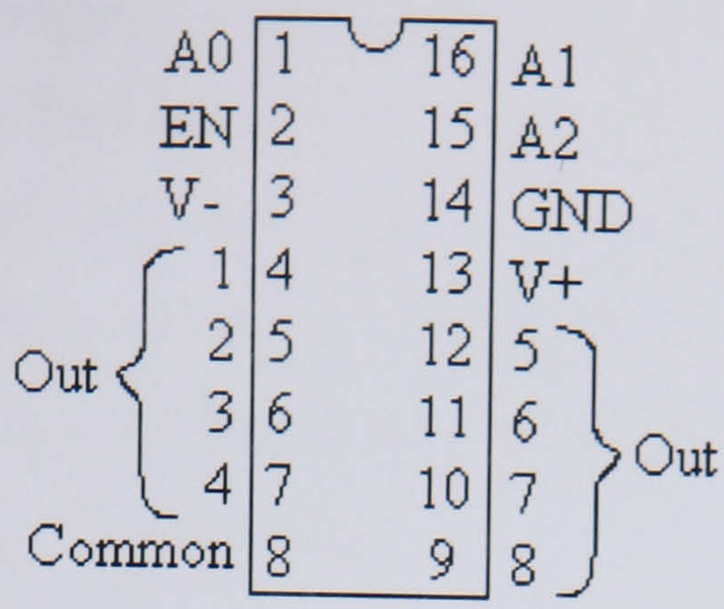

Figure B.2: DG508 multiplexer pin layout.

A_2	A_1	A_0	En	On
0	0	0	1	1
0	0	1	1	2
0	1	0	1	3
0	1	1	1	4
1	0	0	1	5
1	0	1	1	6
1	1	0	1	7
1	1	1	1	8

Table B.1: DG508 multiplexer truth table.

B1.2. 4-point measurement

In their current form, the electronics may take 4-point measurements. Two sets of connections to the device are required. The first connection is used to pass the current through the device and the measurement resistor, while the 'sense' connection is fed into the INA111 instrumentation amplifier, coloured blue in the figure. The feedback to the op-amp ensures that the point beyond the resistor is at the demanded bias. The actual voltage across the device is fed directly into the DAC. It is this voltage that is then recorded as data, rather than the voltage that was originally requested. Because of this it can be necessary to widen the range of a scan in order that the required voltages are reached.

The original intention with regards 4-point measurements had been to feed the 4-point sense input directly into the feedback input of the op-amp. This would ensure that the voltage across the device was that demanded and that only one signal line to the DAC was needed. The voltage range recorded would then have been exactly the range that was required. However, in this configuration, the feedback loop began to oscillate and it was then not possible to take measurements.

B1.3. Open-circuit voltage

The single pole normally open (SPNO) relay, which is also controlled by the multiplexer through the D-type connector, activates the two single pole double throw (SPDT) relays. When this section of the circuit is unactivated, in the configuration shown in the circuit diagram, I-V measurements may be taken. If this section is activated the Vout connection to the DAC is connected directly to the device, independent of the remaining electronics. As no current flows into the card, this is effectively a measurement of the device's open-circuit voltage. This section of the circuit is only used for unshuttered light I-V measurements.

Appendix C: SOL Device Modelling

The model SOL has been developed over a number of years at Imperial College. Although it also performs dark I-V modelling, it is used in this thesis only to model multi-quantum-well device quantum efficiency. The explanation given in this appendix is a brief summary of the description of SOL as given in Ref. 2 of Chapter 3.

Separate contributions from the p-, i- and n-regions are calculated. Quantum efficiency is calculated by solving the carrier transport equations. A number of assumptions are made to accomplish this: room temperature, uniform doping with abrupt composition changes, low injection, depletion approximation.

Equation C.1 gives the rate of generation of electron-hole pairs at a distance x from the surface, for light of wavelength λ.

$$G(\lambda,x) = \alpha(\lambda,x)\Phi(\lambda,x)[1-R(\lambda)]\exp\left(-\int_0^x \alpha(\lambda,x')dx'\right) \qquad (C.1)$$

In the i-region, carriers drift under the influence of the built-in electric field. With the depletion approximation this field is maintained and recombination is zero. Carriers are collected with 100% efficiency. In the p- and n-regions, transport is dominated by diffusion, dictated by variations in carrier concentration. In the p-region where there is no electric field the excess electron concentration n(x) is given by

$$\frac{d^2n(x)}{dx^2} - \frac{n(x)}{l_n^2} + \frac{G(\lambda,x)}{D_n} = 0 \qquad (C.2)$$

Here, l_n and D_n are the electron diffusion length and diffusion constant respectively. The low injection condition allows electron recombination to be approximated by $n(x)/\tau_n$, where the bulk electron lifetime $\tau_n = l_n^2/D_n$ includes radiative, non-radiative and Auger recombination mechanisms. The excess hole concentration in the n-region, p(x), is derived in the same way because carriers and current must be conserved.

Two boundary conditions are used to obtain an analytical solution. Firstly, the excess carrier concentration is zero at the boundary of the depletion zones within the p- and n-regions, with depths w_p and w_n respectively.

$$n(x) = 0 \quad \text{at} \quad x = x_p - w_p \tag{C.3}$$

$$p(x) = 0 \quad \text{at} \quad x = x_p + x_i + w_n \tag{C.4}$$

where x_p and x_i are the widths of the p- and i-regions respectively. The second condition is that the surface recombinations determine the current at both the front and the back surface with respective surface recombination velocities S_n and S_p.

$$D_n \frac{dn(x)}{dx} = S_n n(x) \quad \text{at} \quad x = 0 \tag{C.5}$$

$$D_p \frac{dp(x)}{dx} = S_p p(x) \quad \text{at} \quad x = x_p + x_i + x_n \tag{C.6}$$

The diffusive currents at the first boundary condition give the contributions to photocurrent from the p- and n-regions, Jn and Jp.

$$J_n(\lambda) = q\, D_n \frac{dn(x)}{dx} \quad \text{at} \quad x = x_p - w_p \tag{C.7}$$

$$J_p(\lambda) = q\, D_p \frac{dp(x)}{dx} \quad \text{at} \quad x = x_p + x_i + w_n \tag{C.8}$$

where q is the electronic charge.

The cap and window layer can be approximated by a reduced surface recombination velocity and their contribution to photocurrent is neglected. The contribution to photocurrent from the depletion region ($w_p + x_i + w_n$) is given by

$$J_i(\lambda) = q\Phi(\lambda)[1 - R(\lambda)]\exp\left(-\sum x_j \alpha_j(\lambda)\right)\left[1 - \exp\left(-\alpha_p(\lambda)w_p - \alpha_i(\lambda)w_i - \alpha_n(\lambda)w_n\right)\right] \tag{C.9}$$

The first exponential term accounts for light attenuation in the layers before the depletion region. If quantum wells are present in the i-region, the $\alpha_i(\lambda)x_i$ term is replaced by $N(\alpha_w(\lambda)L_w + \alpha_b(\lambda)L_b)$, where α_w, L_w, α_b and L_b are the absorption

coefficients and thicknesses of the well and barrier respectively, and N is the number of periods. Carrier escape from quantum wells is assumed to be 100%.

The total photocurrent as a function of wavelength is the sum of the contributions from the p-, i- and n-regions.

$$J_{tot}(\lambda) = J_p(\lambda) + J_i(\lambda) + J_n(\lambda) \tag{C.10}$$

The most recent improvement to the model has been the inclusion of strain effects in order to account for the strain compensation technique. The most relevant reference for SOL is Ref. 3 of Chapter 2.

Appendix D: THE REV Project

THE REV project is scheduled to run for three years in order to produce a thermophotovoltaic (TPV) range extender for an electric car. The main aims of the project are:

- to deliver 6kW of electrical energy using a TPV system powered by the combustion of a fossil fuel.
- to produce a system no larger than 800x300x220mm, in order to fit inside the car itself.
- to produce an overall system efficiency of 25%.
- to achieve zero carbon oxide emission and NO_x emission below the best internal combustion engine.

This European project gathers collaborators from a number of countries. Here, the role of each collaborator within the project is given.

Imperial College – The institute of the author, the co-ordinator of the photovoltaic cell part of the project, utilising its expertise in this field.

National Microelectronics Research Centre (NMRC) – Located in the Republic of Ireland, responsible for the processing of all devices up to the final system devices.

IQE (Europe) Ltd – Located in Wales, responsible for the growth of all device material for the project.

RWE – Located in Germany, responsible for the fabrication and packaging of the final system devices.

CNR-IME – Located in Italy, responsible for material characterisation and development of the selective emitters and the institute of the overall project co-ordinator.

CNR-MASPEC – Located in Italy, also responsible for material characterisation such as electron microscopy and X-ray diffraction.

University of Lecce – Located in Italy, responsible for research into combustion and the overall system design

MASMEC – Located in Italy, responsible for assembling and testing the final system.

FIAT-ELASIS – Located in Italy, responsible for the final installation of the system into the vehicle.

BIBL. LONDIN. UNIV.